Modeling of near-wall flame dynamics in laminar and turbulent combustion

Modellierung der wandnahen Flammendynamik in laminarer und turbulenter Verbrennung
Zur Erlangung des akademischen Grades Doktor-Ingenieur (Dr.-Ing.)
Genehmigte Dissertation von Matthias Steinhausen aus Darmstadt
Tag der Einreichung: 27.11.2023, Tag der Prüfung: 14.02.2024

1. Gutachten: Prof. Dr.-Ing. Christian Hasse
2. Gutachten: Prof. Dr. Andrea Gruber
Darmstadt, Technische Universität Darmstadt

TECHNISCHE
UNIVERSITÄT
DARMSTADT

Modeling of near-wall flame dynamics in laminar and turbulent combustion
Modellierung der wandnahen Flammendynamik in laminarer und turbulenter Verbrennung

Accepted doctoral thesis by Matthias Steinhausen

Date of submission: 27.11.2023
Date of thesis defense: 14.02.2024

Darmstadt, Technische Universität Darmstadt

Bitte zitieren Sie dieses Dokument als:
URN: urn:nbn:de:tuda-tuprints-269573
URL: http://tuprints.ulb.tu-darmstadt.de/26957
Jahr der Veröffentlichung auf TUprints: 2024

Dieses Dokument wird bereitgestellt von tuprints,
E-Publishing-Service der TU Darmstadt
http://tuprints.ulb.tu-darmstadt.de
tuprints@ulb.tu-darmstadt.de

Urheberrechtlich geschützt / In Copyright
https://rightsstatements.org/page/InC/1.0/

To science!

Preface

The work presented in this dissertation was conducted during my time as a doctoral candidate at the Institute for Simulation of reactive Thermo-Fluid Systems (STFS) at the Technical University of Darmstadt. The gained scientific insights were published in internationally recognized journals with peer review. In chronological order, these publications are:

- [P1] **M. Steinhausen**, Y. Luo, S. Popp, C. Strassacker, T. Zirwes, H. Kosaka, F. Zentgraf, U. Maas, A. Sadiki, A. Dreizler, and C. Hasse. "Numerical Investigation of Local Heat-Release Rates and Thermo-Chemical States in Side-Wall Quenching of Laminar Methane and Dimethyl Ether Flames". In: *Flow Turbul. Combust.* 106 (2021), 681–700. DOI: 10.1007/s10494-020-00146-w
- [P2] **M. Steinhausen**, T. Zirwes, F. Ferraro, S. Popp, F. Zhang, H. Bockhorn, and C. Hasse. "Turbulent Flame-Wall Interaction of Premixed Flames Using Quadrature-based Moment Methods (QbMM) and Tabulated Chemistry: An a Priori Analysis". In: *Int. J. Heat Fluid Flow* 93 (2022), 108913. DOI: 10.1016/j.ijheatfluidflow.2021.108913
- [P3] **M. Steinhausen**, F. Ferraro, M. Schneider, F. Zentgraf, M. Greifenstein, A. Dreizler, C. Hasse, and A. Scholtissek. "Effect of Flame Retardants on Side-Wall Quenching of Partially Premixed Laminar Flames". In: *Proc. Combust. Inst.* 39 (2023), 3745–3754. DOI: 10.1016/j.proci.2022.07.207
- [P4] **M. Steinhausen**, T. Zirwes, F. Ferraro, A. Scholtissek, H. Bockhorn, and C. Hasse. "Flame-Vortex Interaction during Turbulent Side-Wall Quenching and Its Implications for Flamelet Manifolds". In: *Proc. Combust. Inst.* 39 (2023), 2149–2158. DOI: 10.1016/j.proci.2022.09.026
- [P5] Y. Luo, **M. Steinhausen**, D. Kaddar, C. Hasse, and F. Ferraro. "Assessment of Flamelet Manifolds for Turbulent Flame-Wall Interactions in Large-Eddy Simulations". In: *Combust. Flame* 255 (2023), 112923. DOI: 10.1016/j.combustflame.2023.112923

During my time as a research associate at STFS, I co-authored additional publications, which are not directly included in this cumulative dissertation, but have a close scientific connection to it. These publications, listed in chronological order, encompass:

- [A1] T. Zirwes, T. Häber, F. Zhang, H. Kosaka, A. Dreizler, **M. Steinhausen**, C. Hasse, A. Stagni, D. Trimis, R. Suntz, and H. Bockhorn. "Numerical Study of Quenching Distances for Side-Wall Quenching Using Detailed Diffusion and Chemistry". In: *Flow Turbul. Combust.* 106 (2021), 649–679. DOI: 10.1007/s10494-020-00215-0
- [A2] A. Stagni, Y. Luo, **M. Steinhausen**, A. Dreizler, and C. Hasse. "Chemistry Effects in the Wall Quenching of Laminar Premixed DME Flames". In: *Combust. Flame* 232 (2021), 111529. DOI: 10.1016/j.combustflame.2021.111529
- [A3] F. Zentgraf, P. Johe, **M. Steinhausen**, C. Hasse, M. Greifenstein, A. D. Cutler, R. S. Barlow, and A. Dreizler. "Detailed Assessment of the Thermochemistry in a Side-Wall Quenching Burner by Simultaneous Quantitative Measurement of CO_2, CO and Temperature Using Laser Diagnostics". In: *Combust. Flame* 235 (2022), 111707. DOI: 10.1016/j.combustflame.2021.111707
- [A4] P. Johe, F. Zentgraf, M. Greifenstein, **M. Steinhausen**, C. Hasse, and A. Dreizler. "Characterization of Flow Field and Combustion Dynamics in a Novel Pressurized Side-Wall Quenching Burner Using High-Speed PIV/OH-PLIF Measurements". In: *Int. J. Heat Fluid Flow* 94 (2022), 108921. DOI: 10.1016/J.IJHEATFLUIDFLOW.2021.108921
- [A5] D. Kaddar, **M. Steinhausen**, T. Zirwes, H. Bockhorn, C. Hasse, and F. Ferraro. "Combined Effects of Heat Loss and Curvature on Turbulent Flame-Wall Interaction in a Premixed Dimethyl Ether/Air Flame". In: *Proc. Combust. Inst.* 39 (2023), 2199–2208. DOI: 10.1016/j.proci.2022.08.060
- [A6] H. Böttler, H. Lulic, **M. Steinhausen**, X. Wen, C. Hasse, and A. Scholtissek. "Flamelet Modeling of Thermo-Diffusively Unstable Hydrogen-Air Flames". In: *Proc. Combust. Inst.* 39 (2023), 1567–1576. DOI: 10.1016/j.proci.2022.07.159
- [A7] J. Bissantz, J. Karpowski, **M. Steinhausen**, Y. Luo, F. Ferraro, A. Scholtissek, C. Hasse, and L. Vervisch. "Application of Dense Neural Networks for Manifold-Based Modeling of Flame-Wall Interactions". In: *Appl. Energy Combust. Sci.* 13 (2023), 100113. DOI: 10.1016/j.jaecs.2023.100113
- [A8] M. Greifenstein, F. Zentgraf, P. Johe, B. Boehm, **M. Steinhausen**, C. Hasse, and A. Dreizler. "Measurements of the Local Equivalence Ratio and Its Impact on the Thermochemical State in Laminar Partially Premixed Boundary Layer Flames". In: *Exp. Fluids* 65 (2023), 7. DOI: 10.1007/s00348-023-03747-z

This work has been funded by the Deutsche Forschungsgemeinschaft (DFG, German Research Foundation) – Project Number 237267381 – TRR 150. The calculations were conducted on the Lichtenberg high-performance computer of the Technical University of Darmstadt and the national supercomputer HAWK at the High-Performance Computing Center Stuttgart (HLRS).

Abstract

For the transition to a CO_2-neutral energy economy, it is necessary to adapt technical combustion systems for low-emissions and highly efficient operation with alternative fuels from renewable sources. In the design of these novel combustors, numerical simulations can be a powerful tool. However, the key to a simulation-aided design process is the comprehension of the fundamental physical processes and their integration into predictive combustion models. The interaction of flames with combustor walls is one of these crucial physical phenomena. Flame-wall interactions result in heat losses that decrease the combustion efficiency and increase pollutant formation.

In this thesis, the modeling of flame-wall interactions with chemistry manifolds is investigated in several generic configurations. The starting point is the investigation of laminar, premixed flame-wall interaction under atmospheric conditions. Previous findings of methane-air flames are extended to more complex oxygenated fuels. Subsequently, the complexity of the configuration is progressively increased. In a second configuration, the effect of turbulence on the quenching flame is addressed. On the one hand, flame-vortex interaction is analyzed. This mixing phenomenon is caused by the interaction of turbulent vortices with the flame tip and alters the near-wall flame structure and pollutant formation. A novel chemistry manifold is presented and validated that captures the effect of flame-vortex interactions by an additional manifold dimension. On the other hand, a novel turbulence-chemistry interaction closure model is presented. The model accounts for the effect of unresolved fluctuations in Reynolds-averaged Navier-Stokes and large eddy simulations. In two further configurations, the impact of external mixture stratification and pressure effects is investigated. The relevant physical phenomena, that must be integrated into existing closure models, are identified. The insights gained provide the foundation for future model development.

In conclusion, this thesis presents significant advancements in the modeling of flame-wall interaction using chemistry manifolds that pave the path toward the simulation of partially premixed, turbulent flame-wall interactions under pressurized conditions within technical combustors.

Kurzfassung

Für den Umstieg zu einer CO_2-neutralen Energiewirtschaft ist es zwingend erforderlich technische Verbrennungssysteme für einen emissionsarmen und hocheffizienten Betrieb mit alternativen Brennstoffen aus erneuerbaren Quellen anzupassen. Beim der Entwicklung dieser neuen Brennkammern können numerische Simulationen ein sehr mächtiges Werkzeug sein. Jedoch liegt der Schlüssel für eine simulationsgestützte Auslegung dieser Brennkammern im Verständnis der grundlegenden physikalischen Prozesse und deren Integration in prädiktive Verbrennungsmodelle. Die Wechselwirkung von Flammen mit Brennkammerwänden ist eines dieser entscheidenden physikalischen Phänomene. Flamme-Wand-Wechselwirkungen führen zu Enthalpieverlusten, die den Wirkungsgrad verringern und die Schadstoffbildung erhöhen.

In dieser Arbeit wird die Modellierung der Flamme-Wand-Wechselwirkung mithilfe von Chemietabellen in verschiedenen generischen Konfigurationen untersucht. Der Startpunkt ist die Analyse der laminaren, vorgemischten Flamme-Wand-Wechselwirkung unter atmosphärischen Bedingungen. Hier werden die bisherigen Erkenntnisse über Methan-Luft-Flammen auf komplexere sauerstoffhaltige Brennstoffe erweitert. Anschließend wird die Komplexität der Konfigurationen schrittweise erhöht. In einer zweiten Konfiguration wird der Einfluss von Turbulenz auf die Flamme-Wand-Wechselwirkung untersucht. Zunächst wird die Flamme-Wirbel-Interaktion analysiert. Dieses Mischungsphänomen wird durch die Interaktion turbulenter Wirbelstrukturen mit der Flammenspitze verursacht und beeinflusst die wandnahe Flammenstruktur und die Schadstoffbildung. Eine neuartige Chemietabelle wird vorgestellt und validiert, welche die Wirkung von Flamme-Wirbel-Interaktionen durch eine zusätzliche Tabellendimension abbildet. Des Weiteren wird ein Schließungsmodell für die Turbulenz-Chemie-Interaktion präsentiert. Das Modell berücksichtigt den Einfluss nicht aufgelöster turbulenter Fluktuationen in Reynolds-gemittelten Navier-Stokes und Grobstruktursimulationen. In zwei weiteren Konfigurationen wird der Einfluss von einer externen Flammenstratifizierung und Druckeffekten auf die Flamme-Wand-Wechselwirkung untersucht. Dabei werden relevante physikalische Prozesse herausgearbeitet, die in die bestehenden Schließungsmodelle integriert werden müssen. Die gewonnenen Erkenntnisse bilden die Grundlage für zukünftige Modellentwicklungen.

Zusammenfassend stellt diese Arbeit einen bedeutenden Fortschritt in der Modellierung der Flamme-Wand-Wechselwirkung mit Hilfe von Chemietabellierung dar. Die Erkentnisse ebnen den Weg für prädiktive Simulationsmodelle für partiell vorgemischte, turbulente Flamme-Wand-Wechselwirkungen unter Druck, wie sie in technischen Brennkammern vorkommen.

Table of contents

List of figures

List of tables

Acronyms

ATF Artificially thickened flame

CFD Computational fluid dynamics

CQMOM Conditional quadrature method of moments

DME Dimethyl ether

DMMP Dimethylmethylphosphonat

DNS Direct numerical simulation

EGR Exhaust gas recirculation

FBLI Flame-boundary layer interaction

FDF Filtered density function

FGM Flamelet-generated manifold

FPI Flame prolongation of intrinsic low-dimensional manifold

FPV Flamelet/Progress variable

FRC Finite-rate chemistry

FRS Flame-resolved simulation

FSD Flame surface density

FVI Flame-vortex interaction

FWI Flame-wall interaction

HOQ Head-on quenching

IC Interal combustion

IEM Interaction by exchange with the mean

ILDM Intrinsic low-dimensional manifold

LES Large eddy simulation

LIF Laser-induced fluorescence

PDF Probability density function

QbMM Quadrature-based moment method

QFM Quenching flamelet-generated manifold

QFM-EGR Quenching flamelet-generated manifold with exhaust gas recirculation

QMOM Quadrature method of moments

RANS Reynolds-averaged Navier-Stokes

REDIM Reaction-diffusion manifold

SWQ Side-wall quenching

TC Tabulated chemistry

TCI Turbulence-chemistry interaction

1 Introduction

The emission of greenhouse gases needs to be drastically reduced to mitigate the effects of global warming [1]. While the increase of renewable energy resources and the electrification of the transport sector and industrial processes are essential for the transition to a CO_2-neutral energy system [2], the development of low-emission and highly efficient combustion applications remains to be of utmost importance. In that respect, chemical energy carriers are promising options for energy storage to compensate for temporal fluctuations of wind and solar power [3]. Further, the high energy density of chemical energy carriers is beneficial for a range of applications, like heavy-duty and aero engines [2]. In this context, alternative fuels generated from renewable sources, like hydrogen, ammonia, or oxygenated fuels, can be used for CO_2-neutral energy conversion [2]. These fuels have different combustion properties that require the adaption of technical combustion systems [4, 5]. In the redesign of these combustors, computational fluid dynamics (CFD) is a powerful tool that can yield profound insights into the technical combustors. However, to enable a simulation-driven design process, first, the fundamental physical processes need to be understood and incorporated into predictive combustion models [6, 7].

One particularly important phenomenon is flame-wall interaction (FWI) [7, 8]. Technical combustors for power generation, such as internal combustion (IC) engines or gas turbines, are typically enclosed by walls. The interaction of flames with combustor walls leads to heat losses that inhibit the chemical reactions within the flame and, finally, result in flame extinguishment, the so-called quenching. This lowers combustion efficiency and enhances pollutant formation [9]. The complex interplay between the (turbulent) flow, the combustion chemistry, and the combustor walls has to be understood to accurately predict the impact of FWI on the combustion process.

In the literature, generic FWI scenarios are used to study the underlying physics of the quenching processes in technical combustors [7]. Figure 1.1 illustrates the most prominent canonical FWI scenarios that incorporate two types of quenching:

1. **Head-on quenching (HOQ):** In a HOQ scenario, the flame propagates perpendicular to the wall. In the vicinity of the wall, the flame gradually loses heat to the wall until it finally extinguishes [9]. The quenching process is transient and occurs at a certain instance, the quenching time. In HOQ, the amount of heat loss peaks at the quenching time.
2. **Side-wall quenching (SWQ):** In a SWQ scenario, the flame propagates tangential to the wall into the wall boundary layer. The flame quenching occurs locally at a certain quenching distance at the near-wall flame edge [9]. While in HOQ, the heat loss increases with time, in SWQ, the heat loss increases with decreasing wall distance. Note that laminar SWQ is a stationary process.

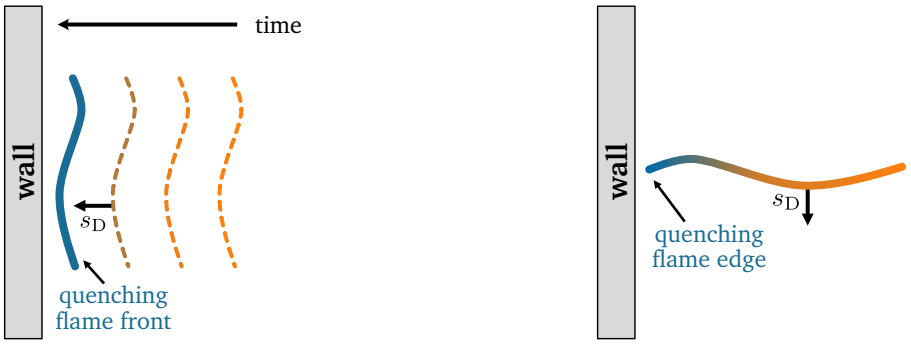

(a) Transient head-on quenching (HOQ) flame (b) Stationary side-wall quenching (SWQ) flame

Fig. 1.1: Schematic depiction of generic FWI scenarios. The dashed lines show different time instances of the flame. The flame front is colored by the amount of heat loss: undisturbed (orange) $\rightarrow$ quenched (blue) and s_D shows the propagation direction.

In the past, various aspects of FWI were investigated in generic FWI configurations. The review article of Dreizler and Böhm [7] presents experimental studies and corresponding numerical investigations emphasizing laser diagnostic applications. Luo and Liu [10] summarize studies of FWI in the context of soot and pollutant formation. The experimental studies related to this work conducted measurements of the flame front topologies, the local heat release rates, and the near-wall thermochemical states in both laminar [A3, 11–13] and turbulent [13, 14] SWQ flames. In addition to the experimental investigations, *numerical experiments* of FWI were carried out using flame-resolved simulations (FRSs) with single-step and finite-rate chemistry (FRC). Starting with one-dimensional simulations of laminar, transient HOQ [15–19], wall heat fluxes, surface reactions, the formation of unburnt hydrocarbons and pollutants, as well as the impact of the employed transport model, were studied. With increasing computational resources, studies of turbulent HOQ [20–28] became possible and gave deeper insights into the interplay of the combustion chemistry with the turbulent flow field. Similar studies also exist for laminar [A1, A2, 29–32] and turbulent [A5, 26, 33–37] SWQ.

While the FRSs give detailed insights into the underlying physics, the simulations require high computational efforts, which restricts them to generic cases and simple geometries. For the simulation of combustors employed in technical systems, Reynolds-averaged Navier-Stokes (RANS) and large eddy simulations (LESs) coupled with chemistry manifold approaches [38–42] are often employed. For this kind of simulation, two major modeling challenges are faced:

1. **Modeling of the chemical source terms:** In FRC simulations, the chemical source terms are determined by analytical models that describe the chemical system. While this approach has low modeling efforts, a large (and stiff) set of equations needs to be solved, which results in high computational costs. To overcome these limitations, chemistry manifold approaches [38–42], also known as tabulated chemistry (TC), aim to combine the model accuracy of FRC with reduced computational costs. In the models, the chemical system is precalculated and stored in a chemistry manifold that is parametrized by a reduced number of scalars, the control variables. Instead of solving the whole chemical system, only the

transport equations for the control variables are solved. The remaining thermochemical quantities are then retrieved from the manifold.

Recent studies [43–45] of fully premixed laminar SWQ methane-air flames showed that the chemistry manifolds need to be adjusted to accurately capture the near-wall flame structure, especially the pollutant formation. This work extends these findings to different operation conditions, like oxygenated fuels, turbulent FWI, and, partially premixed FWI. A more detailed overview of the different modeling approaches for the description of the chemical system, in general, and chemistry manifolds for FWI, in particular, is given in Section 2.2.

2. **Turbulence-chemistry interaction (TCI) closure:** In turbulent flames, the turbulence introduces small-scale fluctuations that need to be accounted for in the simulation. In FRSs, these fluctuations are resolved by a fine computational grid that results in large computational efforts. To overcome these limitations, RANS and LESs capture the impact of unresolved temporal and spatial fluctuations in TCI closure models. This lowers the resolution requirements and computational costs of these simulations.

   In the literature, studies of FWI using RANS [46] and LESs [47–49] coupled with chemistry manifolds exist. However, a detailed assessment of the capabilities of TCI closure models to capture the near-wall flame dynamics and pollutant formation was not performed previously but is addressed in this thesis. A detailed overview of TCI closure models, in general, and studies of TCI closure models for FWI, in particular, is given in Section 2.4.

Aim and structure of this work

This dissertation elucidates modeling approaches and challenges for the simulation of FWI using chemistry manifolds. Specific aspects of turbulent, partially premixed FWI under pressurized conditions in technical combustors are analyzed in simplified configurations.

The main focus of this work is the investigation of fully premixed FWI under atmospheric conditions. Starting from a laminar flow (→ laminar, premixed FWI), the complexity is increased by considering a more complex flow field caused by turbulence (→ **turbulent**, premixed FWI). The corresponding publications [P1, P2, P4, P5] cover the entire range of model development from the analysis of physical phenomena and the derivation of closure models to model validation and application in LESs. The remaining part focuses on the physical analysis of additional phenomena occurring in technical combustors, namely mixture stratification from an active wall (→ **partially premixed** FWI) and pressure effects (→ **pressurized** FWI). The incorporation of these phenomena in manifold closure models will be the next step toward predictive models for FWI effects in technical combustors.

Figure 1.2 shows an overview of the publications that originated from this thesis, classified by the configurations investigated. The scientific objectives of the investigated configurations are:

- Configuration 1: **Laminar, premixed flame-wall interaction** (see Section 3.1)
  The first configuration is a fully premixed, laminar SWQ burner under atmospheric conditions, which was also used in previous studies of methane-air flames [11, 30, 43–45, 50]. In these

studies, the main modeling challenge was to capture the effect of heat losses to the wall on the near-wall flame structure, particularly, the prediction of the near-wall CO formation. For this, the classical manifold approaches need to be adapted (see Section 2.3). The investigations performed in the context of this thesis [P1, A1–A3, A6, A7] extend previous findings of methane flames to the more complex oxygenated fuels. In particular, dimethyl ether (DME) air flames are investigated.

- Configuration 2: **Turbulent, premixed flame-wall interaction** (see Section 3.2)
  In the second configuration, the physical complexity is increased by a more complex flow field due to turbulence. An FRS of a stationary premixed methane-air flame in a fully developed turbulent channel flow is performed. The FRS is investigated to gain a more profound understanding of the complex phenomena in turbulent, premixed FWI and to derive and validate corresponding closure models. The first phenomenon considered is flame-vortex interaction (FVI) [14]. FVI is caused by the interaction of the flame tip with the near-wall vortices, which results in an additional mixing phenomenon that does not occur in the laminar counterpart. To capture these effects, a novel manifold is presented [P4] and validated [P4, P5] by comparing to the FRS reference data. Further, when applying these manifolds in RANS and LESs, the unresolved fluctuations of the control variables need to be considered. These are analyzed in [P2] and a TCI closure model based on the conditional quadrature method of moments (CQMOM) [51] is derived. Finally, in [A5] an FRS with DME as fuel is performed and the characteristics of the oxygenated fuel are analyzed and outlined.
- Configuration 3: **Partially premixed flame-wall interaction** (see Section 3.3)
  In the third configuration, the laminar SWQ configuration (Section 3.1) is extended by an inlet in the wall that allows the seeding of additional gases. Using this configuration, the combined effects of heat loss and flame stratification are analyzed in the context of fire safety. More specifically, additional fuel is seeded from the wall, resulting in a partially premixed SWQ flame that is characterized both experimentally [P3, A8] and numerically [P3]. In the second part of publication [P3], the effect of flame retardants on the near-wall flame structure is considered.
- Configuration 4: **Pressurized flame-wall interaction** (see Section 3.4)
  The final configuration is the subject of an ongoing investigation elucidating FWI in enclosed combustion vessels, like IC engines. In these enclosed vessels, the combustion occurs under pressure-rising conditions. Consequently, the strong coupling of pressure, local temperature, and flame structure and propagation must be taken into account. The study explores the resulting physical effects that need to be considered in the closure models for isochoric FWI in IC engines.

This thesis is structured in the following manner: Firstly, the fundamental concepts crucial to this thesis are outlined in Chapter 2. Then the findings derived from each simplified configuration are examined in Chapter 3. Lastly, in Chapter 4 an overall conclusion is given.

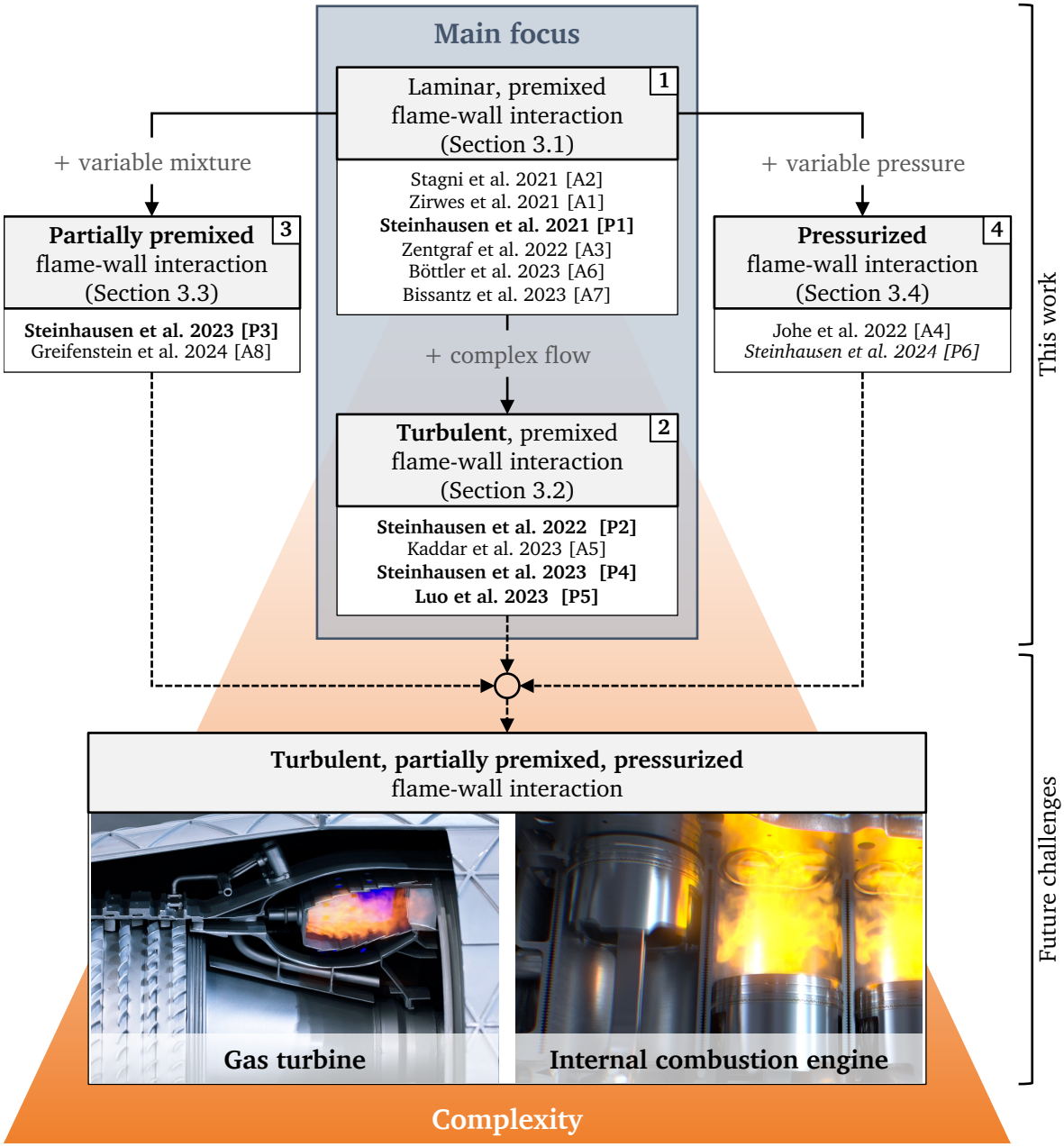

Fig. 1.2: Overview of the four simplified FWI configurations investigated in this thesis and the corresponding main [P1–P5] and related co-author [A1–A8] publications.[1] Publication [P6], written in a cursive font, is an ongoing work. The complexity of the configurations increases from top to bottom. The graphics are taken from [52].

[1] In the references of this dissertation the leading "P" denotes the main publications [P1–P5], which form the basis of this thesis and the leading "A" marks related co-author publications [A1–A8].

2 Fundamentals

In this chapter, the most relevant fundamentals for this dissertation are briefly outlined. More detailed descriptions can be found in the literature of chemically reacting flows [6, 9, 53, 54]. In the following, the instantaneous conservation equations for mass, momentum, species mass fraction, and energy are outlined in Section 2.1. Building upon these equations, the description of the chemically reacting system is discussed in Section 2.2. Section 2.3 delves into the chemistry manifold approaches for FWI that are used in [P1, P2, P4, P5]. Finally, Section 2.4 addresses turbulence-chemistry interaction (TCI) closure. In addition to the descriptions presented here, more specific fundamentals are provided in the publications associated with this thesis.

2.1 Instantaneous conservation equations

Mass and momentum conservation

In the publications included in this work, Newtonian fluids are considered. In addition, low Mach number is assumed and all body forces except gravity are neglected. Given these assumptions, the equations for mass and momentum read

$$\frac{\partial \rho}{\partial t} + \frac{\partial}{\partial x_i}\left(\rho u_i\right) = 0 \,, \tag{2.1}$$

$$\frac{\partial}{\partial t}\left(\rho u_j\right) + \frac{\partial}{\partial x_i}\left(\rho u_i u_j\right) = \frac{\partial}{\partial x_i} \underbrace{\left(\rho\nu\left(\frac{\partial u_i}{\partial x_j} + \frac{\partial u_j}{\partial x_i}\right) - \frac{2}{3}\rho\nu\frac{\partial u_k}{\partial x_k}\delta_{ij}\right)}_{\text{stress tensor: } \tau_{ij}} - \frac{\partial p}{\partial x_j} + \rho g_j \,, \tag{2.2}$$

where ρ is the density, u the flow velocity, p the pressure, x_i the i-th component of the spatial coordinate, g_j the j-th component of the gravitational acceleration and ν the kinematic viscosity.

Species conservation

In addition to the mass and momentum conservation, the composition of the fluid is described by additional transport equations for the species mass fractions Y_k

$$\frac{\partial}{\partial t}\left(\rho Y_k\right) + \frac{\partial}{\partial x_i}\left(\rho u_i Y_k\right) + \frac{\partial}{\partial x_i}\left(\rho Y_k V_{k,i}^{\text{tot}}\right) = \dot{\omega}_k \,, \tag{2.3}$$

with Y_k being the mass fraction, $\dot{\omega}_k$ the source term and $V_{k,i}^{\text{tot}}$ the i-th component of the diffusion velocity of species k. For the description of the species diffusion velocity, multiple closure models are reported in the literature [9]. In this work, the diffusion velocity of the species is modeled using two different approaches:

- **Unity Lewis number diffusion:** In this approach, the species and enthalpy diffusion are assumed to be equal. As the name suggests, the Lewis number that describes the ratio of the thermal diffusivity α and species diffusivity ρD_k is assumed to be unity:

$$\text{Le} = \frac{\alpha}{\rho D_k} = 1 \quad \rightarrow \quad \rho D_k = \alpha \tag{2.4}$$

  Using Fick's Law [55], the species diffusion flux $\rho Y_k V_{k,i}^{\text{tot}}$ is given by

$$\rho Y_k V_{k,i}^{\text{tot}} = -\alpha \frac{\partial Y_k}{\partial x_i} \, . \tag{2.5}$$

- **Mixture-averaged diffusion:** In mixture average diffusion, the Hirschfelder and Curtiss approximation [56] is employed. Given this approximation, the diffusive flux $\rho Y_k V_{k,i}$ is given by

$$\rho Y_k V_{k,i} = \underbrace{-\rho D_k^{\text{mix}} \frac{\partial Y_k}{\partial x_i} - \rho D_k^{\text{mix}} Y_k \frac{1}{\overline{W}} \frac{\partial \overline{W}}{\partial x_i}}_{\text{Species diffusion}} - \underbrace{D_k^{\text{therm}} \frac{1}{T} \frac{\partial T}{\partial x_i}}_{\text{Thermal diffusion}} \, , \tag{2.6}$$

  with $\overline{W}$ being the mean molecular mass of the mixture, T the temperature and D_k^{mix} and D_k^{therm} the mixture-averaged and thermal diffusion coefficient of species k, respectively. The equation above is a first-order approximation, hence, a correction velocity V_i^{corr} is employed to ensure mass conservation and the total species mass flux $\rho Y_k V_{k,i}^{\text{tot}}$ is given by

$$\rho Y_k V_{k,i}^{\text{tot}} = \rho Y_k V_{k,i} - \rho Y_k V_i^{\text{corr}} \, , \tag{2.7}$$

  with

$$\rho Y_k V_i^{\text{corr}} = Y_k \sum_{k=1}^{N_{\text{s}}} \rho Y_k V_{k,i} \, . \tag{2.8}$$

  In this work, the diffusion coefficients are calculated either with the open-source chemistry library Cantera in version 2.6 [57] or the EGLIB transport library [58].

Energy conservation

Finally, the energy balance needs to be considered. Among other things, the energy balance accounts for heat losses (e.g., at cold walls) and mixing processes of gases with different energy levels (e.g., fresh gases and cold exhaust gases) and, hence, has a major significance in processes involving FWI. In this work, the energy is described by either the enthalpy h (TC) or the sensible enthalpy h_s (FRC) that are defined as

$$h = h_s + \Delta h_\mathrm{f}^\mathrm{ref} \quad \text{with} \quad h_\mathrm{s} = \int_{T_\mathrm{ref}}^{T} c_\mathrm{p} dT \quad \text{and} \quad \Delta h_\mathrm{f}^\mathrm{ref} = \sum_{k=1}^{N_\mathrm{s}} Y_k \Delta h_{\mathrm{f},k}^\mathrm{ref} \,. \tag{2.9}$$

In the equation above $\Delta h_\mathrm{f}^\mathrm{ref}$ is the enthalpy of formation of the mixture at the reference temperature T_ref. Following the derivation by Poinsot et al. [9], the transport equation for the enthalpy h reads

$$\frac{\partial}{\partial t}\left(\rho h\right) + \frac{\partial}{\partial x_i}\left(\rho u_i h\right) = \frac{Dp}{Dt} - \frac{\partial q_i}{\partial x_i} + \tau_{ij}\frac{\partial u_i}{\partial x_i} + \dot{Q} + \rho \sum_{k=1}^{N_\mathrm{s}} Y_k f_{k,i} V_{k,i}^\mathrm{tot} \,, \tag{2.10}$$

with $\dot{Q}$ being the heat source term from external sources, q_i the enthalpy flux and $f_{k,i}$ volume forces acting on species k. In the configurations considered in this work, some of these terms can be neglected

$$\underbrace{\dot{Q} \approx 0}_{\text{No external heat source}} \quad \text{and} \quad \underbrace{\tau_{ij}\frac{\partial u_i}{\partial x_i} \approx 0}_{\text{Low Mach}} \quad \text{and} \quad \rho \sum_{k=1}^{N_\mathrm{s}} Y_k f_{k,i} V_{k,i}^\mathrm{tot} = \rho g_i \underbrace{\sum_{k=1}^{N_\mathrm{s}} Y_k V_{k,i}^\mathrm{tot}}_{=0} = 0 \,.$$

Finally, the transport equation for the enthalpy h and the sensible enthalpy h_s read

$$\frac{\partial}{\partial t}\left(\rho h\right) + \frac{\partial}{\partial x_i}\left(\rho u_i h\right) - \frac{Dp}{Dt} - \underbrace{\frac{\partial}{\partial x_i}\left(\lambda \frac{\partial T}{\partial x_i}\right)}_{\text{Heat diffusion}} + \underbrace{\left(\frac{\partial}{\partial x_i}\rho \sum_{k=1}^{N_\mathrm{s}} \left(h_k Y_k V_{k,i}^\mathrm{tot}\right)\right)}_{\text{Species diffusion}} = 0 \,, \tag{2.11}$$

$$\frac{\partial}{\partial t}\left(\rho h_\mathrm{s}\right) + \frac{\partial}{\partial x_i}\left(\rho u_i h_\mathrm{s}\right) - \frac{Dp}{Dt} - \underbrace{\frac{\partial}{\partial x_i}\left(\lambda \frac{\partial T}{\partial x_i}\right)}_{\text{Heat diffusion}} + \underbrace{\left(\frac{\partial}{\partial x_i}\rho \sum_{k=1}^{N_\mathrm{s}} \left(h_{\mathrm{s},k} Y_k V_{k,i}^\mathrm{tot}\right)\right)}_{\text{Species diffusion}} = \dot{\omega}_{h_\mathrm{s}} \,. \tag{2.12}$$

Note that in the equation for the sensible enthalpy an additional source term $\dot{\omega}_{h_\mathrm{s}}$ appears, which is the heat release rate due to combustion that is defined as

$$\dot{\omega}_{h_\mathrm{s}} = -\sum_{k=1}^{N_\mathrm{s}} \Delta h_{f,k}^\mathrm{ref} \dot{\omega}_k \,. \tag{2.13}$$

2.2 Description of the chemical system

In the simulation of chemically reacting flows, one of the central challenges is the accurate description of the chemical system [9]. In general, such a chemical system consists of N_s species that react with one another through N_r reactions

$$\sum_{k=1}^{N_\mathrm{s}} \nu'_{k,j} \mathcal{X}_k \rightleftharpoons \sum_{k=1}^{N_\mathrm{s}} \nu''_{k,j} \mathcal{X}_k \quad \text{for} \quad j = 1, \dots, N_\mathrm{r} \; . \tag{2.14}$$

In the equation above, $\mathcal{X}_k$ denotes the chemical formular for species k while ν'_{kj} and $\nu''_{k,j}$ are the molar stoichiometric coefficients of species k in reaction j. In a chemical reaction flow simulation, the relevant species $\mathcal{X}_k$ and their reaction pathways are defined in reaction mechanisms that are tailored for specific fuel-oxidizer compositions, as well as, specific operation conditions.

Given the reaction mechanism, the thermochemical state Ψ of the chemical system can be described by the species composition Y_k, sensible enthalpy h_s and the pressure p

$$\Psi = f\left(Y_1, \dots, Y_{N_\mathrm{s}}, h_\mathrm{s}, p\right) \; . \tag{2.15}$$

From the thermochemical state, the mixture properties consisting of the thermophysical and transport properties and the reaction rates $\dot{\omega}_k$ can be calculated.[1]

2.2.1 Finite-rate chemistry (FRC) closure

In FRC simulations, all variables that describe a full thermochemical state $[Y_1, \dots, Y_{N_\mathrm{s}}, h_\mathrm{s}, p]$ are directly transported. This means, in addition to the flow field, a transport equation for each species Y_k and the sensible enthalpy h_s is solved that are given in Eq. (2.3) and (2.12), respectively. The resulting system of differential equations is stiff with complex dependencies on the thermochemical state. Furthermore, the temporal and spatial scales that need to be considered in the simulations cover a wide range leading to temporal and spatial resolution requirements that can be orders of magnitude higher than in non-reacting flows [9].

While FRC simulations provide a detailed description of the interaction between flow and chemistry with few modeling assumptions, they necessitate high computational costs. This restricts FRC simulations to simple fuels or generic configurations. In the publications included in this thesis, FRC simulations are used to (i) gain detailed insights into the underlying physics of FWI that need to be captured by chemistry manifold models and (ii) for the model validation of novel chemistry manifolds for FWI.

[1] The dependency of the thermochemical states will be denoted by $\Psi\left(Y_1, \dots, Y_{N_\mathrm{s}}, h_\mathrm{s}, p\right)$ in the following.

2.2.2 Chemistry manifold closure

Chemistry manifold models aim to combine the model accuracy of FRC with reduced computational costs. In the literature, multiple approaches for the generation of chemistry manifolds are reported, including intrinsic low-dimensional manifolds (ILDM) [38], flame prolongation of ILDM (FPI) [39], reaction-diffusion manifolds (REDIMs) [40], flamelet-generated manifolds (FGMs) [41] and the flamelet/progress variable (FPV) approach [42]. In all of the approaches, a separation of chemical and flow time scales is assumed. While in chemical systems, a broad range of time scales ranging from 10^{-9} to 10^{2} s are present, flow time scales are usually in a much smaller range [38]. The ratio of the flow τ_{flow} and the chemical time scales $\tau_{\text{chemistry}}$ is described by the Damköhler number

$$\text{Da} = \frac{\tau_{\text{flow}}}{\tau_{\text{chemistry}}} \, . \tag{2.16}$$

The tabulated chemistry (TC) approaches assume fast chemical time scales when compared to the flow time scales ($\text{Da} \gg 1$). Given this assumption, the interaction of the flow with the inner flame structure is neglectable which leads to a *thin flame sheet*. The changes perpendicular to the flame are significant, while in the tangential direction, only small changes are expected. One-dimensional structures known as flamelets emerge along the normal direction of the flame sheet. As a result, the thermodynamic state of a multidimensional turbulent flame can be precalculated using simplified (flamelet) configurations. Note that during FWI the heat loss at the wall introduces non-neglectable changes in the flame tangential direction. Therefore, one-dimensional flame structures are not sufficient to capture the thermodynamic state during FWI and the chemistry manifold models need to be extended to account for these two-dimensional effects. This is discussed in Section 2.3.

The precalculated thermochemical states are represented by a reduced set of input parameters, the control variables ξ_i, i.e.,

$$\Psi\left(Y_1, \ldots, Y_{N_\text{s}}, h_\text{s}, p\right) \approx \Psi\left(\xi_1, \ldots, \xi_M\right) \quad \text{with} \quad M \ll N_\text{s} \, . \tag{2.17}$$

Typically, these manifolds are stored in normalized look-up tables for fast and efficient retrieval of the thermochemical states during simulation runtime. Therefore, the control variables are normalized to allow the storage of the output variables on a rectilinear M-dimensional grid from which they can be extracted with non-searching algorithms. The main challenges in the construction of chemistry manifolds are the selection of a simplified configuration that incorporates the relevant physical effects, and the parametrization of the reduced thermochemical state space on the rectilinear grid.

In comparison to FRC simulations, in the simulations with chemistry manifolds a lower number of transport equations needs to be solved and, additionally, the chemical system and mixture properties are not calculated during runtime. This results in significantly reduced computational costs that can be orders of magnitude lower than in FRC simulations.

2.2.3 Numerical implementation

Figure 2.1 illustrates the numerical procedure followed in FRC simulation (top) and simulations with chemistry manifolds (bottom). In the FRC simulation, the source terms and mixture properties are calculated from the thermochemical state in each time iteration while in chemistry manifold closure, the chemical system is determined in a pre-processing step in which the thermochemical state is approximated using simplified configurations. The reduced state space is stored in a look-up table, from where the source terms and mixture properties are retrieved during simulation runtime.

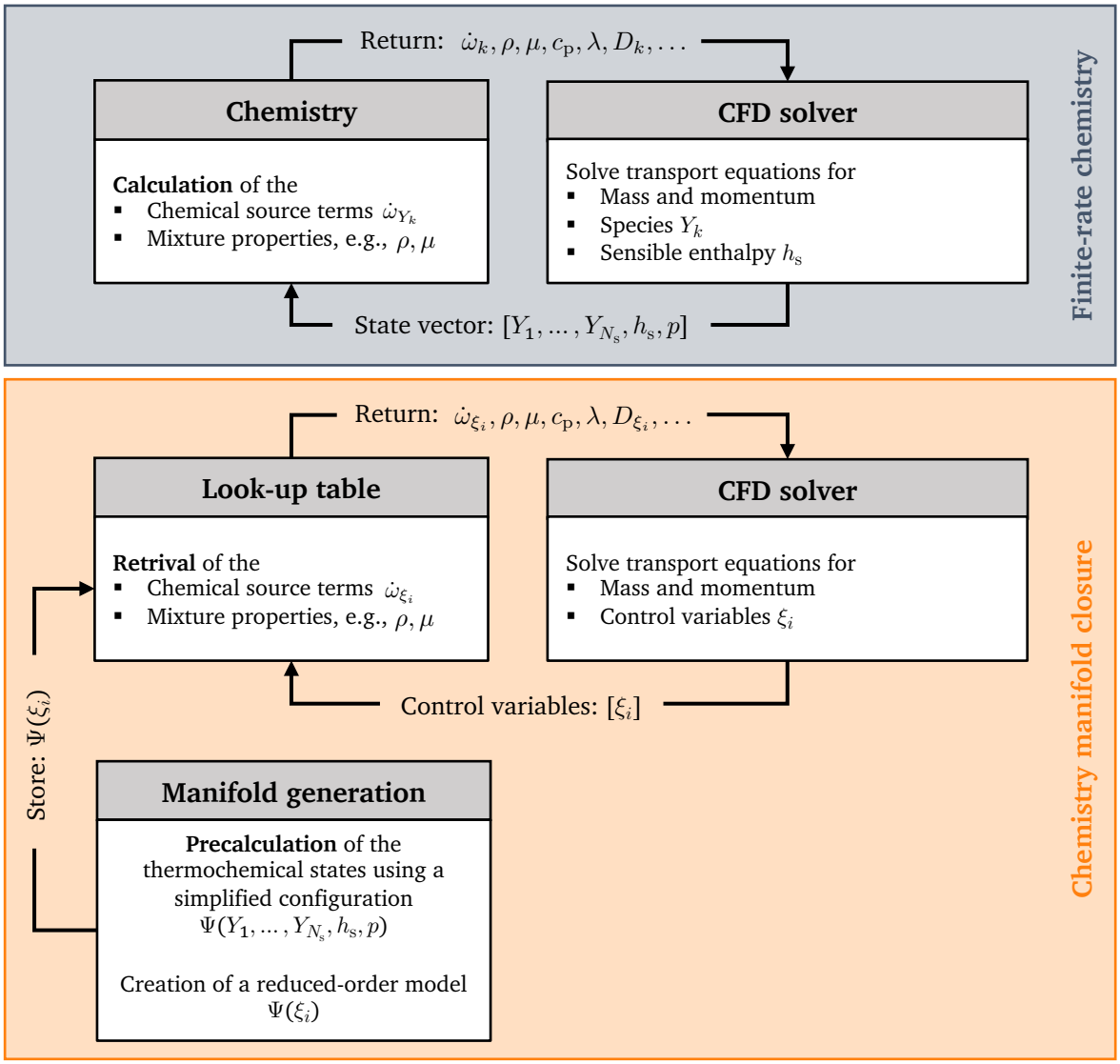

Fig. 2.1: Schematic depiction of the numerical procedure followed in FRC simulations (top) and simulations using chemistry manifolds (bottom). Note that the chemistry manifold generation is a pre-processing step that is performed prior to the simulation.

2.3 Chemistry manifolds for flame-wall interaction

As stated before, FWI requires more advanced manifold generation techniques, particularly addressing heat loss effects. Before describing the corresponding modeling approaches of the present work in Section 2.3.2 and 2.3.3, it is worthwhile to briefly revisit the state of the art of manifold generation for FWI documented in the literature.

2.3.1 Literature review

An early approach for the incorporation of heat loss effects in chemistry manifolds was presented by van Oijen et al. [41, 59]. In the studies, a two-dimensional FGM, parametrized by a progress variable Y_c and the enthalpy h, was employed. For the enthalpy variation, a series of one-dimensional, adiabatic flames with different enthalpy levels was calculated using two different approaches: (i) exhaust gas recirculation (EGR) [41], i.e., different amounts of cooled exhaust gases are mixed with the fresh gases and (ii) burner-stabilized flames with varying mass flow rates [59].[2] The FGMs were validated in one-dimensional and two-dimensional burner-stabilized flames and a ceramic-foam surface burner. Fiorina et al. [60] followed a similar approach and extended a two-dimensional FPI model based on mixture fraction Z and a progress variable Y_c to a three-dimensional FPI including the enthalpy h as an additional dimension. Similar to van Oijen et al. [59] the enthalpy variation was achieved by a series of burner-stabilized flames. The manifold was successfully applied for the calculation of a one-dimensional flame influenced by radiative heat loss and fully premixed and partially premixed laminar bunsen-like burners. Subsequently, Ketelheun et al. [61] extended the standard FGM approach to allow for the representation of non-adiabatic boundaries. At these boundaries, the wall heat flux and the enthalpy are typically unknown, while the wall temperature is more accessible. Therefore, an inverse tabulation procedure was presented that obtains the unknown enthalpy, density and viscosity using a boundary look-up table parametrized by the temperature instead of the enthalpy. The new approach was validated in bunsen-like flames and the LES of three-dimensional, turbulent premixed swirl flames with heat losses to cold walls.

Following the methodology introduced by Ketelheun et al. [61], Heinrich et al. [50] performed both two-dimensional and three-dimensional simulations of a laminar methane-air flame in an SWQ burner [11]. The simulations showed a good agreement with experimental measurements of the global flame properties, such as the temperature. However, the near-wall CO formation was significantly underpredicted. Using the detailed insights from FRC simulations, Ganter et al. [30, 43] found that the high amount of CO at the wall originates from diffusive transport processes that accumulate CO produced in regions away from the wall in the near-wall region.

To further elaborate on the findings of Ganter et al. [30, 43], Fig. 2.2 illustrates the CO distribution in state space for a FGM similar to the ones employed in [41, 50, 59–61] (left) and a transient HOQ (right) for a methane-air flame.[3] Since the FGM is based on a series of adiabatic flames, the enthalpy gradient along the progress variable is implicitly set to the gradient present in a freely propagating flame. In the case of Unity Lewis transport, this gradient is zero ($\partial h / \partial Y_\mathrm{c} = 0$). Hence,

[2] While the flamelet configurations of these two approaches differ, they lead to a similar thermochemical state [59].
[3] Transport model: Unity Lewis, Equivalence ratio: $\Phi = 1$, Wall temperature: $T_\mathrm{wall} = 300$ K, Pressure: $p = 1$ atm

the progress variable and the enthalpy dimension are fully decoupled. During FWI, however, the reaction progress and the heat loss to the wall are closely coupled ($\partial h/\partial Y_c \neq 0$). This results in non-neglectable changes tangential to the progress variable dimension. In contrast to the FGMs, the transient HOQ simulation spans an inherently two-dimensional manifold over space and time, see also Fig. 2.4. In this configuration, the species diffusion along the enthalpy direction, i.e., from regions far off the wall (high enthalpy) to the near-wall region (low enthalpy), is captured. The impact of these changes perpendicular to the flame front on the near-wall CO formation becomes apparent when comparing the CO mass fractions of the FGM with the transient HOQ simulation in Fig. 2.2. Since the species diffusion in the enthalpy direction cannot be captured with adiabatic flames, the FGM underpredicts the near-wall CO formation significantly.

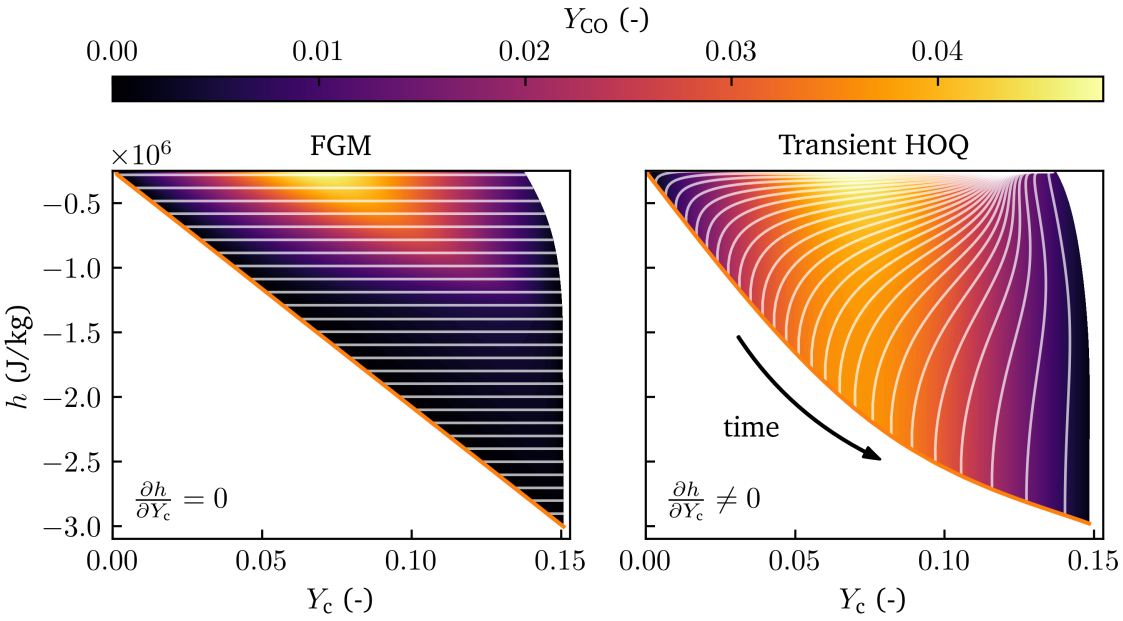

Fig. 2.2: Mass fraction of CO in the state space for an FGM based on adiabatic flames (left) and a transient HOQ (right). The white lines correspond to the flamelets that are used for manifold generation that are also shown in physical space in Fig. 2.3 and 2.4. The solid orange line depicts the temperature isoline that corresponds to the wall temperature.

Based on the findings of Ganter et al. [30, 43], novel chemistry manifolds [44, 45] for the prediction of FWI phenomena were presented, namely a REDIM [44] and the quenching flamelet-generated manifold (QFM) [45]. Instead of using a series of adiabatic one-dimensional laminar flames, the manifolds are based on transient one-dimensional HOQ flames that incorporate diffusive transport processes in the enthalpy direction. This leads to a significant improvement in the prediction of the near-wall CO formation. The novel manifolds were validated with FRC simulations and measurements of the near-wall thermochemical states in premixed, laminar SWQ and HOQ flames and showed very good prediction accuracy [44, 45]. In the following, the manifold generation for the FGM and QFM used in in [P1, P2, P4, P5] is described in more detail.

2.3.2 Flamelet-generated manifold (FGM) generation

As described above, the FGM is based on a series of adiabatic one-dimensional freely propagating flames with varying enthalpy levels. Similar to [41], in [P1, P5] the enthalpy variation is achieved by EGR. For each flame, different amounts of exhaust gases at fresh gas temperature are mixed into the fresh gases resulting in an inflow mixture with a lower enthalpy. The ratio of exhaust and fresh gases in the inflow mixture Y_{EGR} is described by

$$Y_{\mathrm{EGR}} = \frac{m_{\mathrm{exhaust}}}{m_{\mathrm{fresh}} + m_{\mathrm{exhaust}}} \,, \tag{2.18}$$

with m_{fresh} and m_{exhaust} denoting the amounts of fresh and cooled exhaust gases in the inflow mixture, respectively. Additionally, the upper enthalpy limit of the manifold can be expanded using one-dimensional preheated freely propagating flames with $Y_{\mathrm{EGR}} = 0$ and increased fresh gas temperatures.

Figure 2.3 shows an exemplary mixture fraction plane of the flamelet database used for the manifold generation for a methane-air flame. The physical state space is spanned along the axial coordinate x and the ratio Y_{EGR}. At a certain percentage of EGR, the flammability limit is reached and no burning flame simulations can be performed. Beyond this point, the calculation of the state space simplifies into a mixing problem. These remaining thermodynamic states can be calculated by an interpolation in state space using the last burning flamelet and the point of exhaust gases at fresh gas temperature ($Y_{\mathrm{EGR}} = 1$).

The reaction progress, represented by a progress variable Y_{c}, changes along the axial direction x along each flamelet. The enthalpy, however, is constant along the flame and only changes in the Y_{EGR}-direction. This makes the coordinate transformation from the physical space $\Psi\left(Y_{\mathrm{EGR}}, x\right)$ to the state space stored in the manifold $\Psi\left(H, C\right)$ straightforward. For the generation of the look-up table, the normalized enthalpy H and the normalized progress variable C are calculated

$$H = \frac{h - h_{\mathrm{min}}\left(Z\right)}{h_{\mathrm{max}}\left(Z\right) - h_{\mathrm{min}}\left(Z\right)} \,, \tag{2.19}$$

$$C = \frac{Y_{\mathrm{c}} - Y_{\mathrm{c,\,min}}\left(Z, H\right)}{Y_{\mathrm{c,\,max}}\left(Z, H\right) - Y_{\mathrm{c,\,min}}\left(Z, H\right)} \,, \tag{2.20}$$

with h_{min} and h_{max} being the minimum and maximum value of the enthalpy h for a given mixture fraction Z, respectively. The minimum $Y_{\mathrm{c,\,min}}$ and maximum $Y_{\mathrm{c,\,max}}$ of the progress variable Y_{c} depend on the mixture fraction Z and normalized enthalpy H. Finally, two independent coordinate transformations are performed. First, the axial coordinate x is mapped to the normalized progress variable

$$\Psi\left(Z, Y_{\mathrm{EGR}}, x\right) \rightarrow \Psi\left(Z, Y_{\mathrm{EGR}}, C\right) \,. \tag{2.21}$$

Then, the Y_{EGR} coordinate is transformed into the normalized enthalpy H, leading to the final representation of the manifold

$$\Psi\left(Z, Y_{\mathrm{EGR}}, C\right) \rightarrow \Psi\left(Z, H, C\right) \ . \tag{2.22}$$

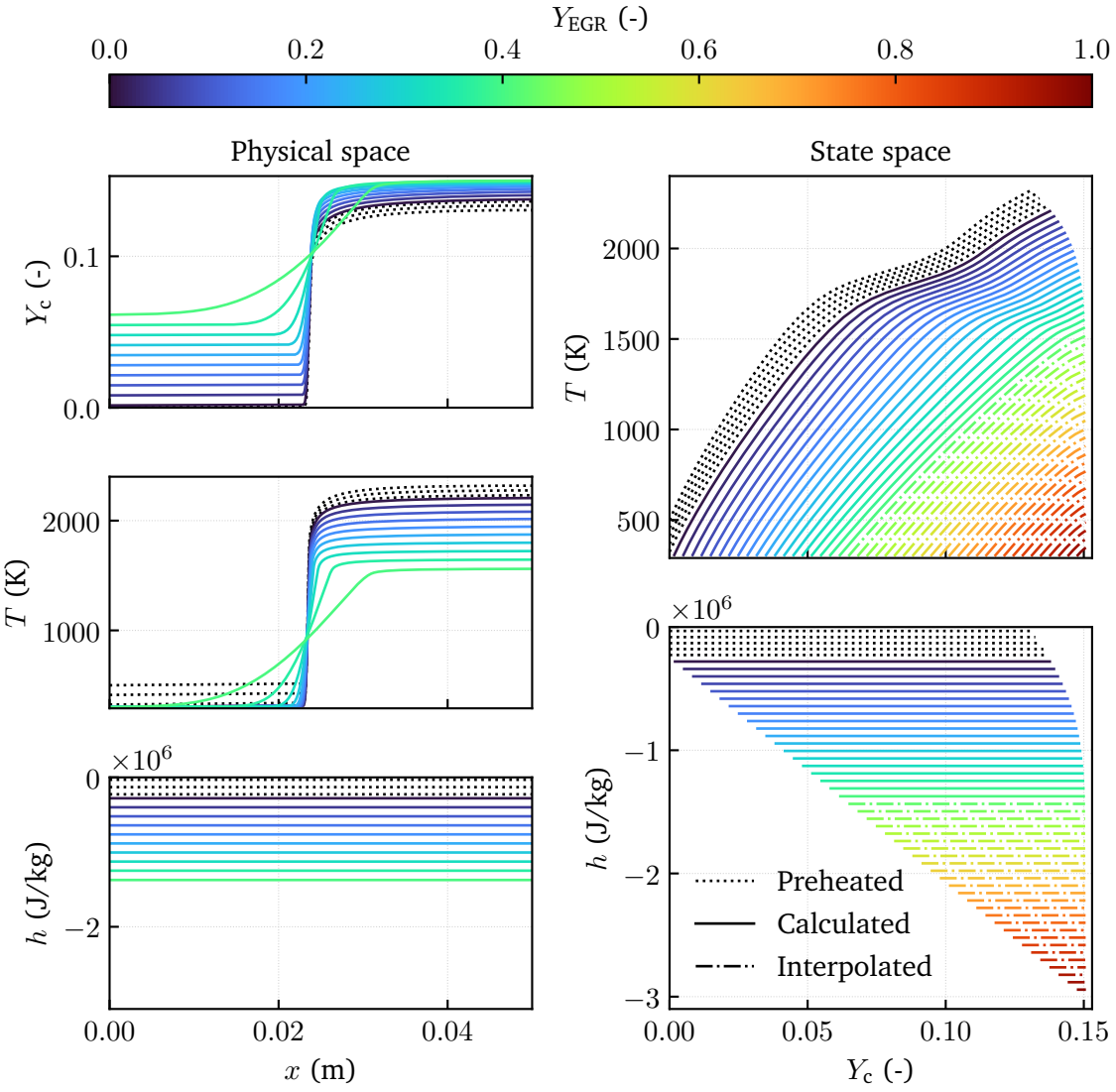

Fig. 2.3: Flamelet database for a mixture fraction slice of an FGM in physical space $\Psi\left(x, Y_{\mathrm{EGR}}\right)$ (left) and state space (right). The interpolated flamelets are calculated in state space and, therefore, are not shown in physical space.

2.3.3 Quenching flamelet-generated manifold (QFM) generation

For the generation of QFMs [45], one-dimensional, transient HOQ flames are employed. Again, the upper enthalpy limit of the manifold can be expanded using one-dimensional freely propagating flames with increased fresh gas temperatures. Figure 2.4 shows the numerical results of a transient HOQ in physical (left) and state space (right). In the plot, t_q is the time relative to the time of quenching, i.e., the time instance of the maximum wall heat-flux. The HOQ simulation spans a two-dimensional space $\Psi\left(x,t\right)$ along the axial coordinate x and time t. In the simulation, the reaction progress and heat loss are closely related to one another during the quenching process. As a result, changes tangential to the flame front, like the species diffusion in the enthalpy direction, can be captured by the HOQ configuration.

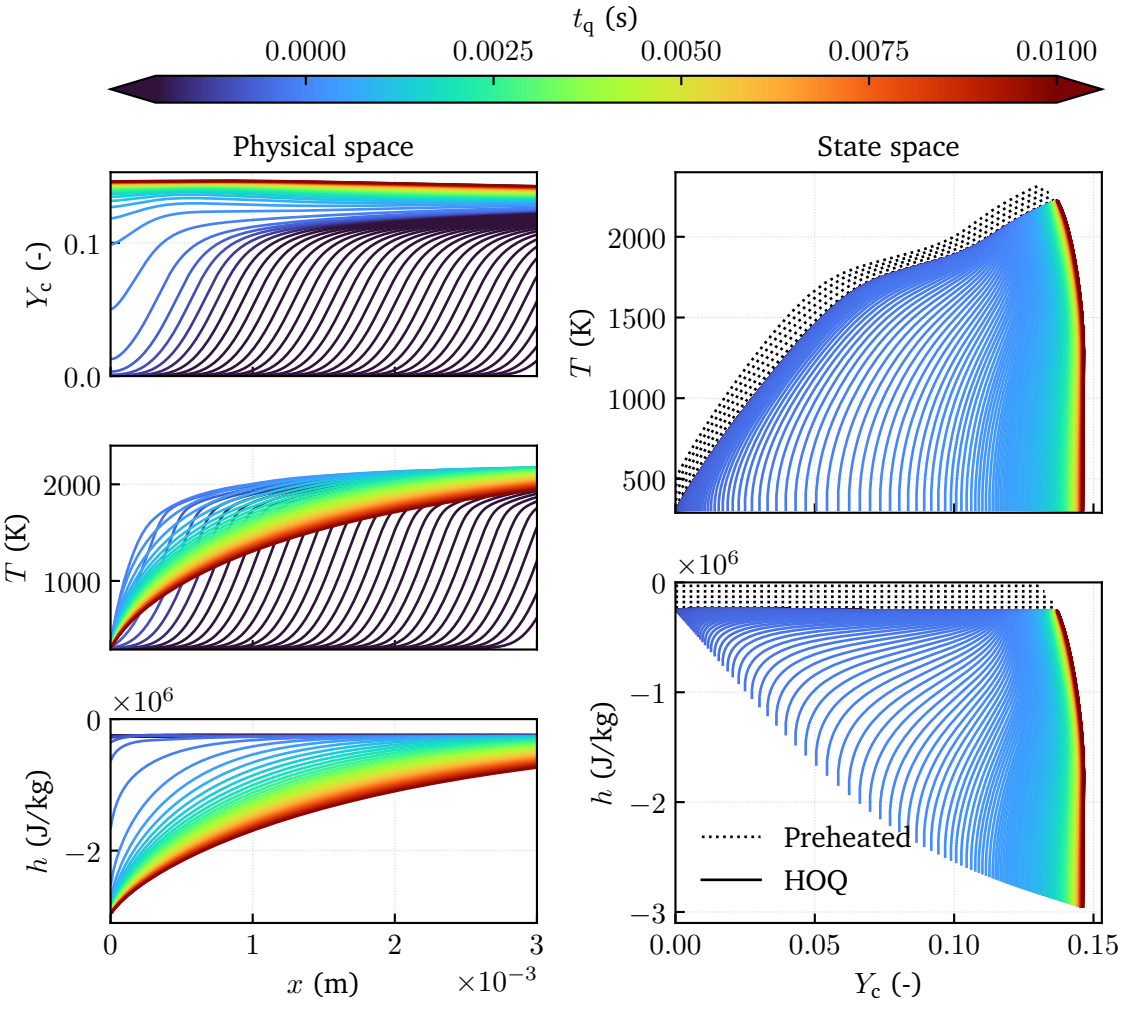

Fig. 2.4: Flamelet database for a mixture fraction slice of a QFM in physical space $\Psi\left(x,t\right)$ (left) and state space (right). t_q is the time relative to the time of quenching.

While the two-dimensional nature of the transient HOQ enables the incorporation of FWI effects into the manifold, it poses additional challenges during table generation. For the FGMs presented above, the coordinate transformation from the physical into the state space could be performed as two individual one-dimensional transformations. Unfortunately, this is not possible for the QFMs, because the enthalpy and the progress variable are a function of both space and time (see Fig. 2.4). Therefore, a two-dimensional coordinate transformation needs to be performed

$$\Psi\left(Z, x, t\right) \rightarrow \Psi\left(Z, H, C\right) \ . \tag{2.23}$$

The procedure used for the manifolds used in this thesis [P1, P2, P4] consists of multiple steps:

1. Extract the position of the enthalpy isolines from the physical space: $[x_i, t_i] = f\left(h_{\text{iso}}\right)$.
2. Calculate the thermodynamic state along the isoline: $\Psi_i\left(h_{\text{iso}}\right) = f\left([x_i, t_i]\right)$.
3. Calculate the normalized progress variable C and interpolate the thermodynamic state onto the normalized progress variable grid assuming $\Psi_i = f\left(C_i\right)$ along the enthalpy isoline.

2.3.4 Closing remarks

Even though the QFM and the FGM have similar dimensions in state space and are used similarly in a coupled simulation, the two manifolds incorporate different ways of heat loss to the flame. While the FGM flamelets experience enthalpy variations caused by a change in the unburnt mixture composition, the QFM incorporates quenching-induced heat losses. In publications [P4, P5], a novel manifold is validated in turbulent FWI that incorporates both causes of enthalpy loss at the cost of an additional manifold dimension. More details are given in Section 3.2.

2.4 Turbulence-chemistry interaction (TCI) closure

The simulation approaches for turbulent (reacting) flows are usually characterized based on the range of resolved length and time scales in the simulations:

- **Flame-resolved simulations (FRSs)**[4] resolve all relevant time and length scales and no additional closure models are required. For a turbulent reacting flow, the instantaneous balance equations given in Section 2.1 are solved and the complex interplay of turbulence and combustion chemistry is resolved by the simulation.
- **Large eddy simulations (LESs)** resolve the large turbulent structures, while the effect of small-scale turbulence is accounted for in subgrid-scale closure models. The scale separation in LES is achieved by spatially filtering the instantaneous balance equations given in Section 2.1. A filtered quantity $\overline{f}$ is given by

$$\overline{f}\left(\boldsymbol{x}\right) = \int f\left(\boldsymbol{x'}\right) F\left(\boldsymbol{x} - \boldsymbol{x'}\right) d\boldsymbol{x'} \; . \tag{2.24}$$

  For the LES filter operation $F\left(\boldsymbol{x} - \boldsymbol{x'}\right)$, different formulations exist both in physical and spectral space and an overview is given in [9, 62].[5]
- **Reynolds-averaged Navier-Stokes (RANS)** simulations solve for the time-averaged flow fields and corresponding reactive and non-reactive scalars. The balance equations are obtained by temporally averaging the instantaneous balance equations given in Section 2.1.

In RANS and LESs of turbulent flames, not only the effect of turbulence needs to be modeled, but also the two-way interaction of turbulence and chemistry [9]. On the one hand, turbulence is influenced by the combustion process. The heat release in the flame front results in a change in viscosity and temperature and, finally, leads to a strong flow acceleration that affects the turbulent flow. On the other hand, turbulence alters the flame structure, which can enhance the chemical reaction, but in extreme cases can also inhibit it, leading to flame quenching.

Due to the highly non-linear dependency of the reaction rates on the reaction progress, i.e., the mean reaction rate $\overline{\dot{\omega}}_{Y_\mathrm{c}}$ is unequal to the reaction rate $\dot{\omega}_{Y_\mathrm{c}}$ of the mean reaction progress variable $\overline{Y_\mathrm{c}}$

$$\overline{\dot{\omega}_{Y_\mathrm{c}}\left(Y_\mathrm{c}\right)} \neq \dot{\omega}_{Y_\mathrm{c}}\left(\overline{Y_\mathrm{c}}\right) \; , \tag{2.25}$$

it is necessary to account for the effect of the unresolved fluctuations caused by turbulence on the combustion chemistry in RANS and LESs. Therefore, numerous TCI closure models are reported in the literature [6, 9, 63–65]. In the following, only a short overview of TCI closure models that were applied to FWI scenarios is given.

[4] In the literature for this kind of simulation often the term direct numerical simulation (DNS) is employed.

[5] In this thesis, the notation from Vervisch and Veynante [6] is followed, with $\overline{Q}$ and Q' denoting the Reynolds mean and fluctuations of a quantity Q, respectively, while $\widetilde{Q}$ and Q'' correspond to the Favre-averaged counterparts. The definitions are connected by $\widetilde{Q} = \overline{\rho Q}/\overline{\rho}$.

In the existing literature, multiple TCI closure models were applied to FWI phenomena:

- **Geometrical closure:** In geometrical closure models, the flame is described as a geometrical surface. In a premixed flame, the flame surface is envisioned as an interface between the fresh and exhaust gases. The geometrical closure models account for the effect of unresolved wrinkling on the burning velocity to ensure correct flame propagation.
    - **Flame surface density (FSD):** The FSD model describes the flame as a propagating surface and an FSD that defines the flame area per unit volume. In recent studies, FRSs of turbulent HOQ [21, 23, 25, 26] and SWQ [26, 36, 37] were used to analyze the validity of the FSD closure in the vicinity of the wall. Based on the findings, wall-adapted formulations of the FSD model were derived.
    - **Artificially thickened flame (ATF):** The ATF [66] model is often employed for the TCI closure in LES of premixed flames. In the model, the reaction zone of the flame is artificially thickened to allow the resolution on a coarser grid. In a turbulent flow, the unresolved wrinkling of the flame surface is then accounted for by an efficiency function. The ATF model was used for the simulation of FWI phenomena [P5, 47–49] in the past. However, in all of the studies, the wall boundary layer is highly resolved and, therefore, the artificial thickening is only applied in the free flame branch unaffected by the wall. In the near-wall region no artificial flame thickening, i.e., no TCI closure, is used.
- **Statistical closure:** Statistical approaches model the effects of the unresolved fluctuations of the reactive and non-reactive scalars[6] by their statistical behavior that is captured by probability density functions (PDFs) and filtered density functions (FDFs) in the context of RANS and LES, respectively. They can be classified as:
    - **Presumed PDF:** In presumed PDF approaches, the PDF/FDF shape is determined prior to the simulation and parameterized by low-order moments of the control variables ξ_i, e.g., the mean and the variance that are calculated during runtime. In the context of FWI, multiple studies [46, 67, 68] used presumed PDF closure models for the simulation of turbulent premixed flames with enthalpy losses. However, only Fiorina et al. [46] focused particularly on FWI. In the study, a RANS simulation was performed and the prediction accuracy of global flame parameters, like the temperature and major species, was assessed. The pollutant formation, which is very sensitive to FWI effects, however, was not considered.
    - **Transported PDF:** In transported PDF models, the PDF/FDF is solved during runtime [69]. Hence, in contrast to presumed PDF approaches, these models do not need to prescribe the PDF/FDF shape prior to the simulation. This makes transported PDF approaches suitable for the description of complex PDFs/FDFs. Multiple transported PDF models exist that rely on Monte-Carlo-based methods, like the Lagrangian approach [70] and the Eulerian stochastic fields approach [71]. In this thesis, an alternative and very efficient mathematical approach to solve PDF-based systems is employed, namely quadrature-based moment methods (QbMMs) [72] that describe the unknown PDF/FDF by a set of integral PDF properties, the moments.

[6] When coupled to a chemistry manifold these scalars correspond to the control variables of the manifold ξ_i.

Recently, Pollack et al. [73] successfully applied QbMMs for the simulation of a one-dimensional premixed turbulent flame. In [P2], a novel TCI closure approach is presented that extends the work of Pollack et al. [73] to turbulent FWI. The closure approach is based on CQMOM. The CQMOM approach is then compared to a presumed PDF approach [46]. These two closure approaches are briefly outlined in the following.[7]

2.4.1 Presumed probability density function (PDF) closure

In the presumed PDF methods, the filtered transport equations of the control variables ξ_k are solved

$$\frac{\partial}{\partial t}\left(\overline{\rho}\widetilde{\xi}_k\right) + \frac{\partial}{\partial x_i}\left(\overline{\rho}\widetilde{u}_i\widetilde{\xi}_k\right) + \frac{\partial}{\partial x_i}\left[\left(\overline{\rho}D_{\xi_k} + \frac{\mu_t}{\mathrm{Sc}_t}\right)\frac{\partial\widetilde{\xi}_k}{\partial x_i}\right] = \overline{\dot{\omega}}_{\xi_k} \ , \tag{2.26}$$

with D_{ξ_k} being the diffusion coefficient of the k-th control variable, μ_t the eddy viscosity that is determined by the turbulence model employed, and, Sc_t the turbulent Schmidt number. The unclosed filtered quantities, like the mean density $\overline{\rho}$ or the mean source term $\overline{\dot{\omega}}_{\xi_k}$, are calculated based on an integral in state space $\mathcal{R}_{\boldsymbol{\xi}}$

$$\widetilde{Q} = \int_{\mathcal{R}_{\boldsymbol{\xi}}} Q\left(\boldsymbol{\xi}\right)\widetilde{P}\left(\boldsymbol{\xi}\right)d\boldsymbol{\xi} \tag{2.27}$$

or

$$\overline{Q} = \overline{\rho}\int_{\mathcal{R}_{\boldsymbol{\xi}}}\frac{Q\left(\boldsymbol{\xi}\right)}{\rho\left(\boldsymbol{\xi}\right)}\widetilde{P}\left(\boldsymbol{\xi}\right)d\boldsymbol{\xi} \quad \text{with} \quad \overline{\rho} = \left[\int_{\mathcal{R}_{\boldsymbol{\xi}}}\frac{1}{\rho\left(\boldsymbol{\xi}\right)}\widetilde{P}\left(\boldsymbol{\xi}\right)d\boldsymbol{\xi}\right]^{-1} \ , \tag{2.28}$$

assuming a sub-grid distribution $\widetilde{P}\left(\boldsymbol{\xi}\right)$ with $\boldsymbol{\xi}$ being the vector of the control variables of the chemistry manifold employed. The main modeling effort for this method is to find a proper description for the joint presumed PDF $\widetilde{P}\left(\boldsymbol{\xi}\right)$ that represents the distribution of the unresolved fluctuations. Here, usually, the unknown PDF is described as the product of individual marginal scalar PDFs

$$P\left(\xi_1, \xi_2, \ldots, \xi_N\right) \approx \prod_{k=1}^{N} P\left(\xi_k\right) \ , \tag{2.29}$$

assuming the statistical independence of the control variables.

In the studies of premixed flames with heat losses [46, 67, 68], the distribution of the progress variable Y_c is modeled by a β-PDF described by the mean $\widetilde{Y}_\mathrm{c}$ and the variance $\widetilde{Y_\mathrm{c}''^2}$, while for the remaining control variables a δ-peak is used.

[7] For better readability, the term PDF will be used interchangeably for both PDFs and FDFs in the following.

2.4.2 Quadrature-based moment methods (QbMMs)

Instead of assuming the distribution of the control variables directly, the QbMMs solve for integral properties of the unknown distribution $\widetilde{P}(\boldsymbol{\xi})$. These mixed moments $\widetilde{M}_{\boldsymbol{k}}$ are given by

$$\widetilde{M}_{\boldsymbol{k}} = \widetilde{M}_{k_1,k_2,\ldots,k_M} = \int_{\mathcal{R}_{\boldsymbol{\xi}}} \xi_1^{k_1}, \xi_2^{k_2}, \ldots, \xi_M^{k_M} \widetilde{P}(\boldsymbol{\xi})\, d\boldsymbol{\xi}\,, \tag{2.30}$$

with k_i being the order of the moment for the control parameter ξ_i and M the dimension of the control variable vector $\boldsymbol{\xi}$, i.e., the dimension of the chemical manifold employed. The transport equation for the moments can be derived from the transport equation of the Favre-averaged joint PDF $\widetilde{P}(\boldsymbol{x}, t; \boldsymbol{\xi})$. Under the assumption of unity Lewis-number and the gradient-diffusion hypothesis this transport equation reads [74]

$$\begin{aligned} &\frac{\partial}{\partial t}\left(\overline{\rho}\widetilde{P}(\boldsymbol{\xi})\right) + \frac{\partial}{\partial x_i}\left(\overline{\rho}\widetilde{u}_i\widetilde{P}(\boldsymbol{\xi})\right) + \frac{\partial}{\partial x_i}\left[\left(\overline{\rho}D + \frac{\mu_t}{\mathrm{Sc}_t}\right)\frac{\partial \widetilde{P}(\boldsymbol{\xi})}{\partial x_i}\right] \\ &\qquad = \underbrace{\frac{\partial}{\partial \xi_d}\left(\overline{\rho}\dot{\omega}_d(\boldsymbol{\xi})\,\widetilde{P}(\boldsymbol{\xi})\right)}_{\text{Mean chemical source term}} - \underbrace{\frac{\partial^2}{\partial \xi_d \xi_{d'}}\left(\left\langle D\frac{\partial \xi_d}{\partial x_i}\frac{\partial \xi_{d'}}{\partial x_i}\middle|\, \boldsymbol{\Xi} = \boldsymbol{\xi}\right\rangle \widetilde{P}(\boldsymbol{\xi})\right)}_{\text{Micro mixing term}}\,, \end{aligned} \tag{2.31}$$

with $\dot{\omega}_d$ being the source term of the control variable ξ_d and $\boldsymbol{\Xi}$ indicating an instance of the control variable vector $\boldsymbol{\xi}$. The transport equation of the moments is obtained by applying the moment definition of Eq. (2.30) to Eq. (2.31)

$$\begin{aligned} &\frac{\partial}{\partial t}\left(\overline{\rho}\widetilde{M}_{\boldsymbol{k}}\right) + \frac{\partial}{\partial x_i}\left(\overline{\rho}\widetilde{u}_i\widetilde{M}_{\boldsymbol{k}}\right) - \frac{\partial}{\partial x_i}\left[\left(\overline{\rho}D + \frac{\mu_t}{\mathrm{Sc}_t}\right)\frac{\partial \widetilde{M}_{\boldsymbol{k}}}{\partial x_i}\right] \\ &\qquad = \underbrace{k_d \int_{\mathcal{R}_{\boldsymbol{\xi}}} \xi_d^{k_d-1}\xi_{d'}^{k'_d}\overline{\rho}\dot{\omega}_d(\boldsymbol{\xi})\,\widetilde{P}(\boldsymbol{\xi})\, d\boldsymbol{\xi}}_{\text{Mean chemical source term } \widetilde{\dot{\omega}}_{M_{\boldsymbol{k}}}} + \mathcal{MM} \qquad \forall k'_d \neq k_d\,, \end{aligned} \tag{2.32}$$

with $\mathcal{MM}$ indicating the micro-mixing contribution. In the transport equation, the chemical source term and the micro-mixing term appear in unclosed form.

Closure of the micro-mixing term

For the description of the micro-mixing term, different closure models exist [53]. In this work, the well-established interaction by exchange with the mean (IEM) [75] model was employed. The IEM model relies on a mixing time scale τ_{MM} that is dependent on the description of the turbulent flow field by the turbulence model employed.

Closure of the mean chemical source term

The mean chemical source term $\widetilde{\dot{\omega}}_{M_{\boldsymbol{k}}}$ contains the unknown distribution $\widetilde{P}(\boldsymbol{\xi})$. In the quadrature method of moments (QMOM) closure [72], such integral quantities $\widetilde{Q}$ are approximated using Gaussian quadrature

$$\widetilde{Q} = \int_{\mathcal{R}_\Psi} \widetilde{P}(\boldsymbol{\xi})\, f_Q(\boldsymbol{\xi})\, d\boldsymbol{\xi} \approx \sum_{\alpha=1}^{N} w_\alpha f_Q(\boldsymbol{\xi}_\alpha) \ , \tag{2.33}$$

with w_α being the integration weights and $\boldsymbol{\xi}_\alpha$ the corresponding integration nodes. The function $f_Q(\boldsymbol{\xi})$ describes the dependency of the parameter Q on the integration nodes. Note that the function $f_Q(\boldsymbol{\xi})$ corresponds to a table lookup when a chemistry manifold is employed.

The integration nodes w_α and weights $\boldsymbol{\xi}_\alpha$ are obtained by a moment conversion based on the Wheeler algorithm [53, 76] using the transported system of moments $M_{\boldsymbol{k}}$ as input parameters. Thereby, the number of transported moments determines the accuracy of the integral approximation. Additional information on the system of moments and QbMM closure is given in [53, 77].

Finally, Fig. 2.5 shows a presumed PDF approach (top) in comparison with a QMOM closure (bottom) for a one-dimensional manifold with the control variable ξ. In the presumed PDF approach, the mean $\widetilde{\xi}$ and variance $\widetilde{\xi''^2}$ of the control variable are solved. They parametrize the presumed β-PDF that is prescribed prior to the simulation. In the QMOM approach, a certain number of moments $\widetilde{M}_k$ are transported. From these moments, integration nodes and weights are determined to approximate the integral quantities. Here, the PDF shape is not fixed and the approximation accuracy can be increased by transporting a higher number of moments.

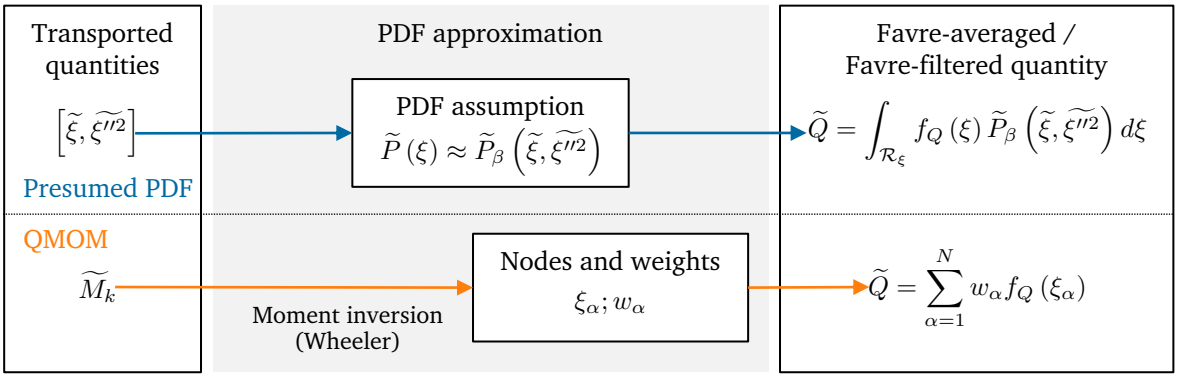

Fig. 2.5: Schematic comparison of presumed PDF (top) and QMOM (bottom) closure.

3 Results and discussion

In the following, the publications that are included in this thesis are embedded in their respective scientific context. The results are discussed in terms of four simplified configurations each incorporating a particular challenge for the simulation of near-wall combustion using chemistry manifolds. Each section first presents the simplified configuration and the scientific challenges related to it. This is followed by an analysis of physical phenomena, that clarifies the essential factors that must be incorporated into the combustion models. Given the physical insights, the implications for chemistry manifold models are elucidated and novel closure models are presented. Finally, future challenges for chemistry manifold simulations in the respective configuration are shortly discussed.

For a detailed description of the scientific results, the reader is referred to the original publications. This chapter is intended as a review that highlights the overall scientific progress that has been made during the period of the dissertation with particular emphasis on publications included or related to this thesis. If not explicitly mentioned, one can recognize the main publications [P1–P5] by the leading "P", and the publications that have been co-authored [A1–A8] by the leading "A".

3.1 Laminar, premixed flame-wall interaction

Figure 3.1 shows the first configuration investigated. From the bottom, a fully premixed fuel-air mixture enters through the nozzle and a flame is stabilized at a ceramic rod. The flame propagates towards a temperature-controlled wall where it undergoes SWQ. The laminar SWQ burner was investigated both experimentally [A3, 11–13] and numerically using FRC [P1, A1, A2, 30, 43] and chemistry manifold approaches [P1, A7, 44, 45, 50, 78, 79]. In most of the numerical studies, a reduced two-dimensional subdomain that covers the quenching flame branch is employed. This subdomain was first introduced by Ganter et al. [30] and is depicted in Fig. 3.1.

The scientific challenge in this configuration is to understand the interplay between the heat losses to the wall, species diffusion and combustion chemistry and to capture these effects in suitable chemistry manifolds. The quenching of the flame at the wall significantly influences the chemical reaction pathways and thereby alters the flame structure and the formation of pollutants. Previous investigations that were focused on methane flames are summarized in Section 2.3. The investigations in this section focus on laminar DME flames.

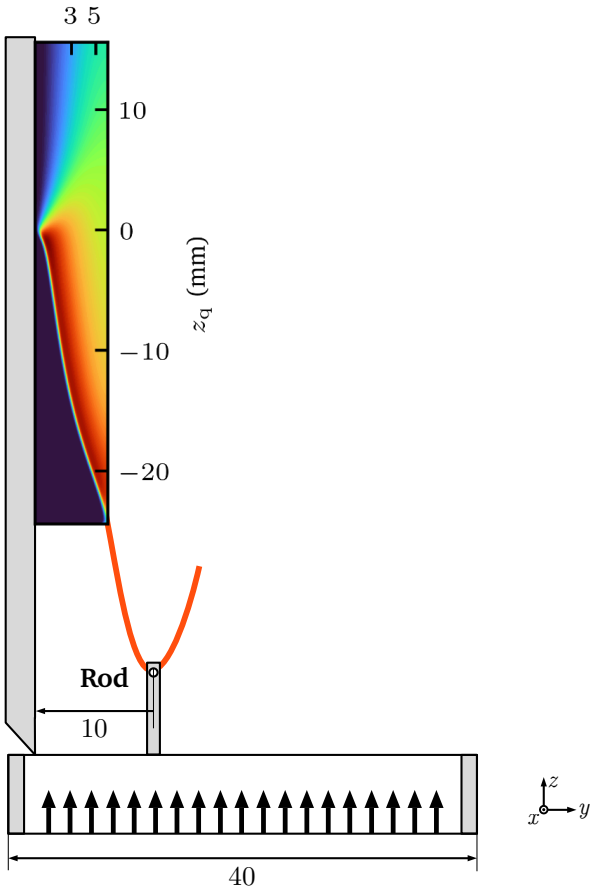

Fig. 3.1: Setup of the laminar, premixed SWQ burner configuration adapted from [P1]. The numerical subdomain is depicted by the contour plot of the OH mass fraction. The dimensions are given in units of mm.

Physical phenomena

Publication [P1] extends previous investigations of methane-air flames [30, 43, 50] to more complex oxygenated fuels. In the study, FRC simulations are performed and compared to measurements of the local heat release rate [13], as well as simultaneous measurements of the temperature and CO mass fraction [12]. In the experimental study [13], the local heat release rate is determined using the normalized product of OH-LIF (laser-induced fluorescence) and CH_2O-LIF measurements. In [P1], the validity of the experimental heat release rate definition is confirmed using computed signals that calculate the OH-LIF and CH_2O-LIF signal based on the full thermochemical state of the simulations. A very good agreement between the experimental heat release rate definition $\mathrm{HHR}_{\mathrm{exp}}$ based on the computed signal $S_{\mathrm{OH\text{-}LIF}}$ and $S_{\mathrm{CH_2O\text{-}LIF}}$

$$\mathrm{HHR}_{\mathrm{exp}} = \frac{\langle S_{\mathrm{OH\text{-}LIF}} \rangle \cdot \langle S_{\mathrm{CH_2O\text{-}LIF}} \rangle}{\max\left(\langle S_{\mathrm{OH\text{-}LIF}} \rangle \cdot \langle S_{\mathrm{CH_2O\text{-}LIF}} \rangle \right)}$$

and the numerical heat release rate definition $\mathrm{HHR}_{\mathrm{num}}$ based on the species source term $\dot{\omega}_k$ and the enthalpy of formation $\Delta h_{\mathrm{f},k}$

$$\mathrm{HHR}_{\mathrm{num}} = \frac{\sum_{k=1}^{N_\mathrm{s}} \dot{\omega}_k \Delta h_{\mathrm{f},k}}{\max\left(\sum_{k=1}^{N_\mathrm{s}} \dot{\omega}_k \Delta h_{\mathrm{f},k}\right)}$$

was found in the SWQ configuration. Further, the flame structure and CO formation in the simulations and experiments are similar. Nonetheless, the simulations predict a higher quenching distance compared to the experiments, resulting in a shift in the wall-normal direction. The shift is consistent in both the heat release profiles, as well as in the thermochemical states of the flame. Multiple measurement uncertainties were considered and superimposed onto the simulations, however, the shift in the wall-normal direction could not be explained.

Zirwes et al. [A1] observed similar deviations comparing simulations of methane-air and propane-air flames to corresponding experimental measurements [11, 80]. In their study, the quenching distance of the experiments and simulations differed by a factor of 1.8, independently of the fuel and equivalence ratio employed. A systematic parameter variation was conducted to elucidate the effect of multiple influence factors on the quenching distance. However, none of the investigated phenomena could explain the observed deviations.

Subsequently, Zentgraf et al. [A3] performed novel measurements of the thermochemical state of DME-air flames in the SWQ configuration and compared them to FRC simulations based on the numerical setup used in [P1].[1] In the measurements, a much better agreement of the experimental and numerical wall-normal flame position is observed. The shift in wall-normal direction decreased from 150 µm to only 20 µm. Zentgraf et al. [A3] explain the remaining shift by beam steering. In the subsequent comparison between the experiments and numerical results in state space, this shift is accounted for.

The main novelty of the study presented in [A3] is the extension of the two-scalar measurements (X_{CO}, T) that were performed in previous studies [11, 13] to three-scalar measurements of the CO_2 and CO mole fractions and gas phase temperature T. The inclusion of the CO_2 mole fraction presents a superior description of the near-wall thermochemical states compared to previous measurements. Figure 3.2 shows a comparison of the measurement data with two FRC simulations using a unity Lewis number diffusion model and the mixture-averaged approach. The results correspond to a wall distance of 120 µm. In the evaluation of numerical simulations against the experiments, the mixture-averaged transport approach shows an improved agreement compared to the unity Lewis number model. This reveals the importance of differential diffusion effects in oxygenated fuels, which is especially visible in the $X_{\mathrm{CO_2}}$-T and the $X_{\mathrm{CO_2}}$-X_{CO} space that was not available in previous measurements [12].

[1] The numerical simulations in [A3] were provided by the author of this thesis.

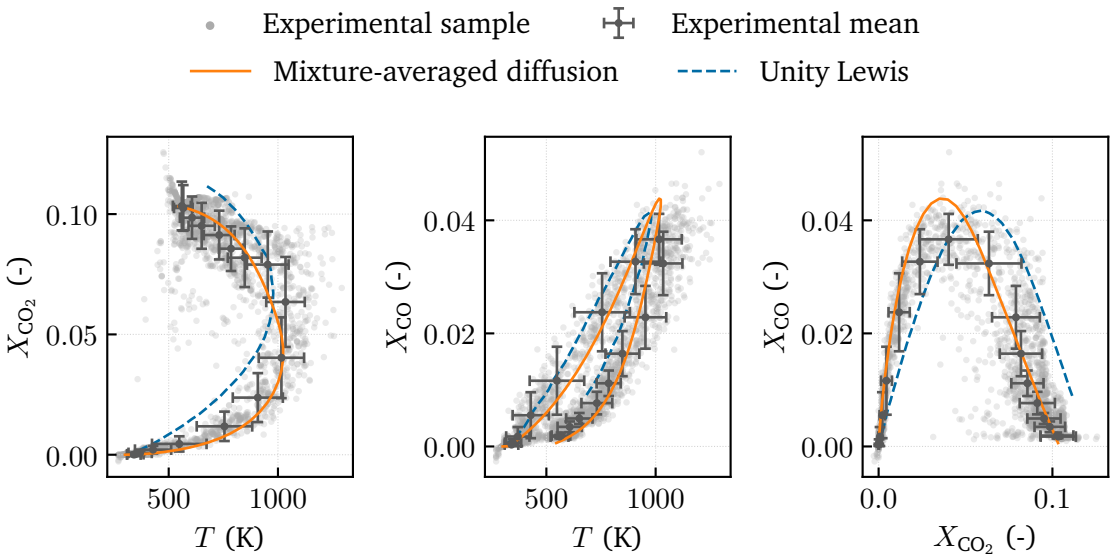

Fig. 3.2: Thermochemical state of laminar SWQ of a DME-air flame at a wall distance of 120 µm based on the data published in [A3]. The experimental data is shifted by 20 µm to match the numerical T-X_{CO_2} profiles. The experimental means are calculated along the wall-parallel direction and the error bars show the respective standard deviations.

Finally, Stagni et al. [A2] investigated the role of low-temperature chemistry in the near-wall region. They found that the decomposition pathways of the low-temperature and high-temperature chemistry exhibit similar significance. However, due to the overall low reactivity in the near-wall region, the flame structure is dominated by convective and diffusive processes and not chemical reactions. As a result, the low-temperature chemistry does not affect the near-wall flame structure and the quenching parameter, like the quenching distance or the wall heat flux, to a significant extent. Based on these findings, a reduced reaction mechanism with 20 species and 93 reactions is derived that allows the simulation of DME flames with FRC closure with a high degree of accuracy and relatively low computing cost. Further, a similar mechanism was also created for methane flames with 24 species and 165 reactions. These mechanisms were later employed in the FRSs of turbulent FWI [P2, P4, P5, A5] in Section 3.2.

Modeling using chemistry manifolds

In addition to the physical analysis, simulations using chemistry manifolds were conducted in publication [P1], marking the first analysis of the laminar SWQ of a DME flame with chemistry manifold closure. With the FRC simulations as a reference, the validation of three chemistry manifold models, namely a flamelet-generated manifold (FGM) [61], a reaction-diffusion manifold (REDIM) [44] and a two-dimensional quenching flamelet-generated manifold (QFM) [45], is performed.[2] The latter two are based on a HOQ flame and were specifically designed to capture the effects of FWI. Note that publication [P1] contains the first direct comparison of all three

[2]A more detailed description of the manifold generation is given in Section 2.3.

manifolds: the FGM, the REDIM, and the QFM. Figure 3.3 shows the temperature and the CO mass fraction profiles in the vicinity of the quenching point from the FRC reference and the simulations using chemistry manifolds. While all three manifolds show a good agreement for the major flame structure characterized by the local heat release rate or the temperature, only the QFM and REDIM can capture the CO formation in the near-wall region. This finding extends the previous knowledge based on laminar methane-air flames [30, 43–45] to more complex oxygenated fuels.

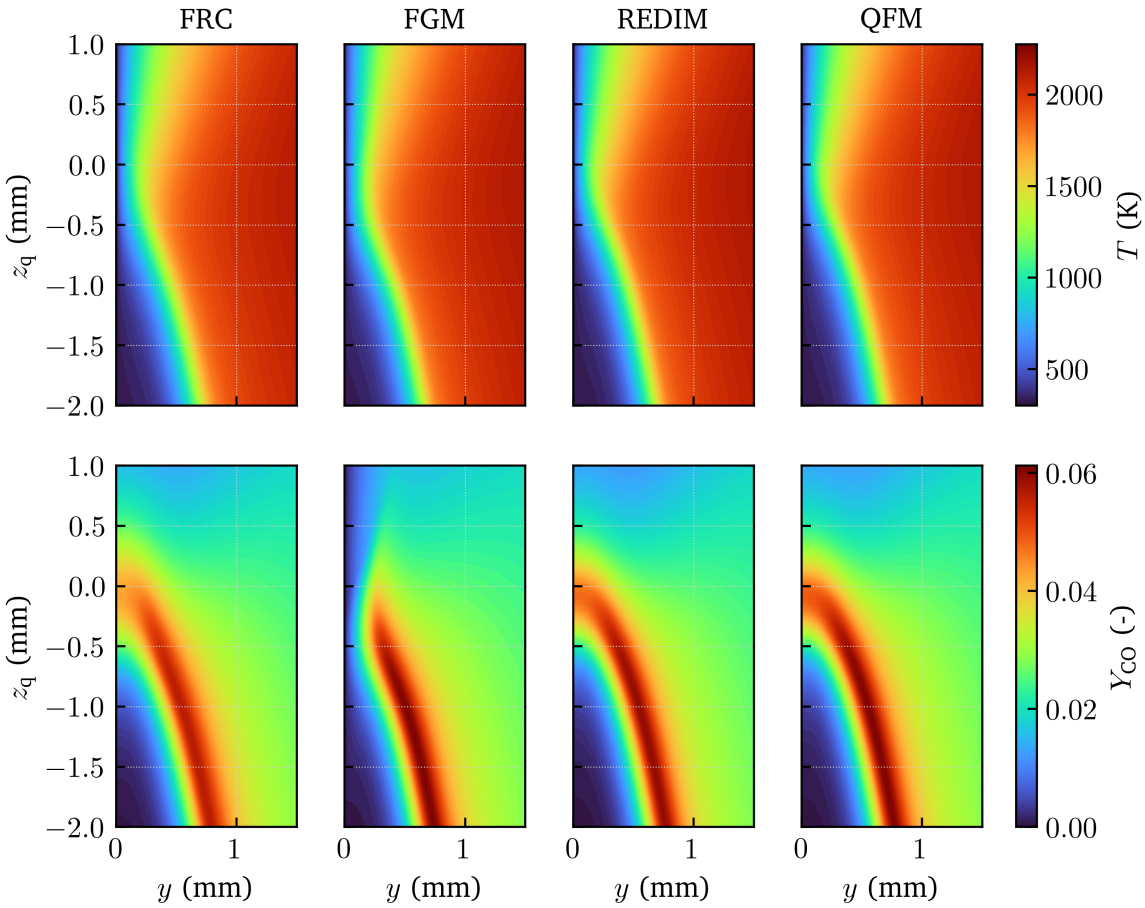

Fig. 3.3: Temperature and CO mass fraction profiles in laminar SWQ of FRC simulations and simulations using chemistry manifolds. The plot shows a zoom of the quenching region shown in Fig. 3.1 and is based on the results published in [P1].

Future challenges

Considering the transition to a CO_2-neutral energy conversion, the chemistry manifold models need to be adapted for alternative fuels. While the impact of differential diffusion is already noticeable in oxygenated fuels, it is particularly important in hydrogen combustion. Here, the mixture stratification caused by differential diffusion induces additional physical phenomena, such as thermo-diffusive instabilities.

Different chemistry manifold approaches [A6, 81–83] were recently presented that aim to account for the effect of differential diffusion in laminar hydrogen flames. These novel manifold approaches [A6, 81–83] aim to capture the effect of ignition, local mixture stratification, and curvature effects. In [A6, 83] the enthalpy h is also included as a manifold dimension. However, in none of these studies, FWI was considered. To incorporate the effects of FWI in the manifolds, a better physical understanding of the interplay between differential diffusion effects and heat losses at the walls is required as a first step. In the second step, the relevant physical phenomena need to be integrated into the existing manifold models. Achieving this likely involves increasing the dimensionality of the manifolds, leading to higher computational costs and increased memory requirements. Moreover, the manifold parametrization becomes progressively challenging due to the strong coupling of mixture stratification and enthalpy. As an example, Fig. 3.4 displays the state space that is spanned by a one-dimensional HOQ simulation of a hydrogen-air (left) and methane-air (right) flame over the progress variable Y_c, the enthalpy h and the local equivalence ratio Φ. While the methane flame is only slightly affected by mixture stratification induced by differential diffusion, the state space spanned by the hydrogen flame is inherently three-dimensional, which complicates the parametrization of the manifold in a normalized state space for efficient table access.

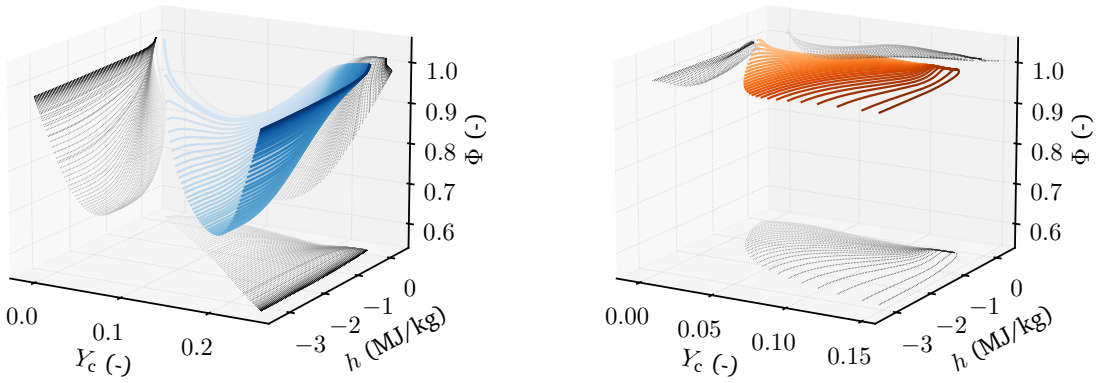

(a) Hydrogen-air flame

(b) Methane-air flame

Fig. 3.4: Three-dimensional state space $\Psi(\Phi, h, Y_c)$ of HOQ flames with differential diffusion. The grey lines show the projection of the colored lines in the 2D space. The lightness of the colored lines indicates the time (bright $\rightarrow$ dark).

To overcome these issues, in multiple studies [A7, 84–89] the manifold representation based on neural networks is analyzed. As universal approximators, neural networks can represent any given correlation between arbitrary control variables and corresponding outputs. In contrast to look-up tables, a normalization of the control variables is not necessary for the network inference. Further, the memory requirements to store the neural network change only slightly with an increasing number of control variables. These benefits of neural networks can be exploited to represent the increasingly complex thermochemical state space spanned by the chemistry manifold models for hydrogen flames. In the context of FWI, Bissantz et al. [A7] present a neural-network-based QFM for a methane flame that could be a promising alternative to the normalized look-up table representation in hydrogen flames.

3.2 Turbulent, premixed flame-wall interaction

In the second configuration, the physical complexity is increased by an intricate flow field induced by turbulence. Figure 3.5 depicts the turbulent SWQ configuration that is investigated in [P2, P4, P5, A5]. A fully premixed fuel-air mixture is stabilized in a fully developed turbulent channel flow with a friction Reynolds number of

$$\mathrm{Re}_\tau = \frac{U_\tau H}{\nu} = 180 \,, \tag{3.1}$$

with H being the channel half width, U_τ the wall shear velocity and ν the kinematic viscosity of the unburnt fuel-air mixture at inflow temperature. The setup is inspired by a previous study of Gruber et al. [34]. In the channel flow, a V-shaped flame is stabilized at a flame holder that is modeled as a cylindrical region with burnt gas temperature. Note that in contrast to the study of Gruber et al. [34], the flame holder is not placed in the middle of the channel at H, but $H/2$ above the lower channel wall.[3] The wall temperature is fixed and equal to the inflow temperature of the fresh gas mixture entering from the left ($T_\mathrm{wall} = T_\mathrm{inflow}$). From the flame holder, the lower flame branch propagates to the isothermal walls where it undergoes SWQ. In the context of this study, two FRSs are performed. Table 3.1 summarizes the most important operation conditions and closure models employed in the numerical studies. The fuel, equivalence ratio, and wall temperatures are chosen to allow a comparison of the physical phenomena with recent experimental investigations [11, 14]. While Zentgraf et al. [14] focus on DME flames, a stoichiometric methane-air flame was also investigated in the experimental campaign. In their study, the equivalence ratio of the DME flame was chosen to match the flame speed of a stoichiometric methane-air flame.

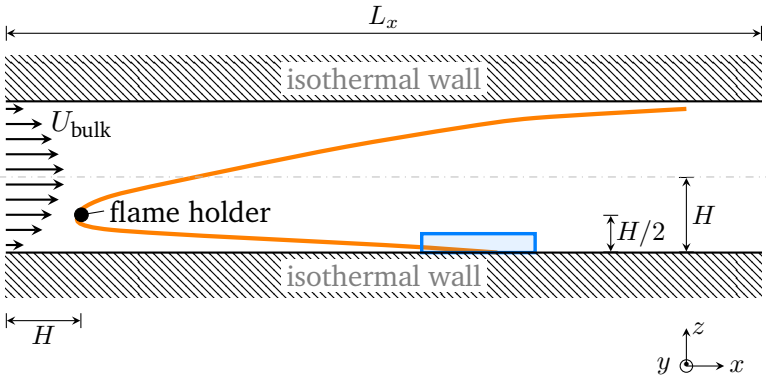

Fig. 3.5: Schematic illustration of the turbulent, premixed SWQ configuration adapted from [P4]. In the (statistically independent) lateral direction (y) the channel width is $3H$. The region shown in Fig. 3.6 is highlighted as a blue rectangle.

[3] The placement of the flame holder closer to the bottom wall allows a shorter channel width and thereby reduces the required grid size. The placement in the middle of the channel, however, results in two statistically independent flame branches (upper and lower) that can be used for the generation of flame statistics. Therefore, a reduced number of time steps is necessary to reach statistical convergence.

Tab. 3.1: Overview of the operation conditions and closure models for the turbulent SWQ simulations performed in this thesis.

Parameter	**Studies [P2, P4, P5]**	**Study [A5]**
Inlet / wall temperature	300 K	300 K
Friction Reynolds number	180	180
Gas mixture	Methane-air ($\Phi = 1$)	DME-air ($\Phi = 0.83$)
Diffusion model	Unity Lewis	Mixture-averaged
Reaction mechanism	Reduced CRECK [90] based on the findings in [A2] 24 species / 165 reactions	20 species / 93 reactions
Chemistry closure	FRC [P2, P4] Chemistry manifolds [P4, P5]	FRC
Turbulence closure	FRS [P2, P4] / CQMOM [P2] / ATF [P5]	FRS

The FRSs serve as the starting point for various analyses of turbulent SWQ. In the publications, the underlying physical processes are analyzed and compared to respective experimental findings [14]. Based on the insights, closure models for both chemistry manifolds and TCI are derived and validated. In the following, two modeling challenges are addressed that arise through the complex interplay between the turbulence, the combustion chemistry and the combustor walls, namely flame-vortex interaction (FVI) and the closure of the joint PDF in FWI.

3.2.1 Flame-vortex interaction (FVI)

The first investigated phenomenon is FVI, a mixing process during FWI in transient and turbulent flows. The additional mixing results in a change in the thermochemical state space that needs to be considered in the chemistry closure using chemistry manifolds.

Physical phenomena

In recent numerical [32, 35] and experimental [14] studies, FWI in transient flows was investigated. The studies show a high dependency of the near-wall flame structure and pollutant formation on the velocity perturbations interacting with the quenching flame tip. Palluli et al. [32] investigated two-dimensional SWQ flames distorted by velocity perturbations at the inlet over a range of different forcing frequencies. In the study the near-wall flame structures, more specifically, the local heat release rate and CO formation were analyzed. At low and high forcing frequencies the flame behaved similarly to a SWQ flame without velocity perturbations. However, at intermediate frequencies, the flame showed both HOQ and SWQ-like quenching that significantly affects the CO formation at the wall. Similar to the simulations performed in the context of this work [P2, P4, A5], Jiang et al. [35] investigated a turbulent SWQ flame stabilized in a fully developed turbulent channel flow. As a fuel, they employed methane diluted by hot combustion products. Among other findings, they reported that the near-wall CO formation is mainly influenced by diffusive and convective transport processes and not chemical reactions.

On the experimental side, Zentgraf et al. [14] investigated the thermochemical state during turbulent atmospheric SWQ. The thermochemical state is characterized by the simultaneous measurement of the CO and CO_2 mole fractions and gas temperature T. The observed thermochemical states in the turbulent scenario differed significantly from the laminar counterpart [A3]. Similar to the findings reported in [32], the turbulent flame showed HOQ and SWQ-like behavior, leading to different thermochemical states. In the study, an FVI mechanism is proposed that explains the differences between the observed laminar and turbulent states. In the vicinity of the wall, the interaction of the turbulent flow (vortices) with the flame tip results in the mixing of unburnt gases with cold exhaust gases. This so-called FVI results in thermochemical states that are not present in the laminar (stationary) flame. Figure 3.6 shows a time series of an FVI event adapted from [P4] that is in agreement with the mechanism reported in the experiments [14]. The flame front is visualized by an isocontour of the progress variable CO_2 that is shown in orange. In addition, the area of FVI is shown in blue and vortical structures in front of the flame are shown as grey isocontours.

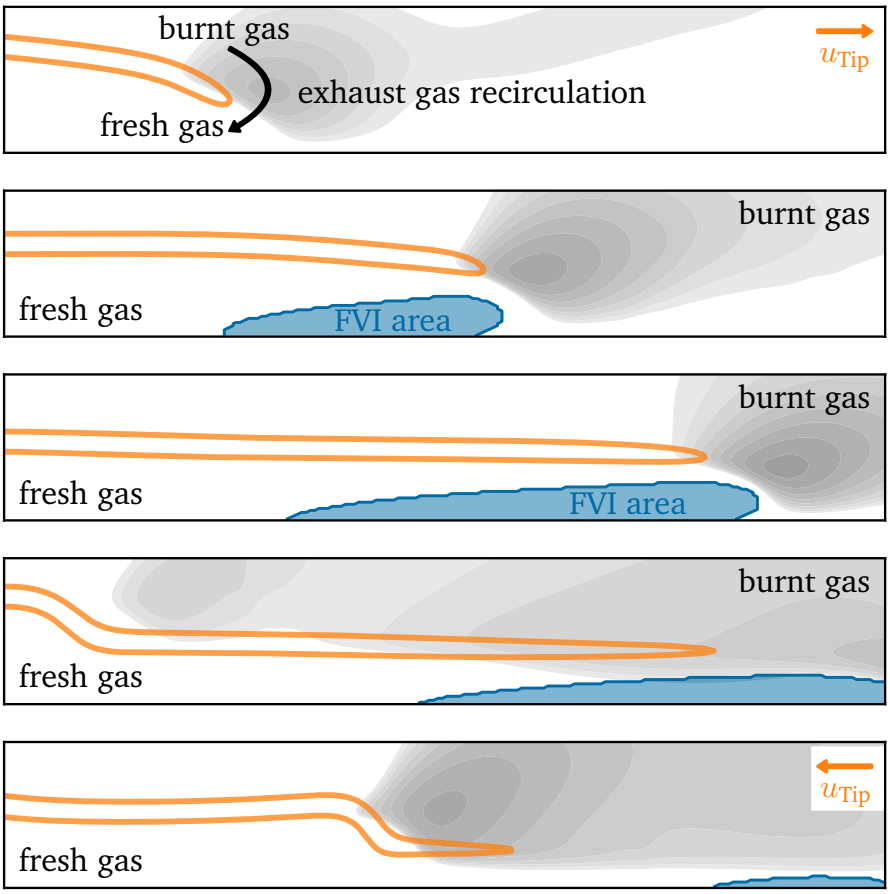

Fig. 3.6: Schematic illustration of FVI adapted from [P4]. The flame front visualized by a contour of $\dot{\omega}_{Y_c}$ is depicted in orange, while the area of FVI is colored in blue and the vortical structures are shown in grey. The time increases from top to bottom.

The mechanism depicted in Fig. 3.6 starts from a SWQ-like state with no EGR. However, a turbulent vortex is present downstream of the quenching flame tip. With increasing time, the flame tip propagates into the vortical structure and pushes the vortex in the streamwise direction. The forward motion results in an entrainment of hot exhaust gases at the wall that are cooled down and mixed with the fresh gases in the vicinity of the flame tip (blue FVI areas). The change in fresh gas composition results in a reduced reactivity of the flame, i.e., a lower heat release rate and local flame speed. Finally, the vortical structure spreads over a wide area above the flame and pushes the flame against the wall. The result is a HOQ-like event with the quenching region parallel to the wall. After the flame has been extinguished, it spreads out again in a SWQ-like manner and the described procedure repeats itself.

Modeling using chemistry manifolds

The interaction of the quenching flame with the transient flow in premixed FWI results in heat losses through two physical processes:

- **Exhaust gas recirculation (EGR):** Downstream of the reaction front, the burnt gases are cooled down when approaching the thermal boundary layer ($T_{\text{wall}} < T_{\text{burnt}}$). This lowers the enthalpy level of the burnt gases in the vicinity of the wall. A transient velocity field, for example, caused by turbulent vortices, can lead to the mixing of the cold burnt gases with the fresh gases in the vicinity of the quenching flame tip. This results in a change in the unburnt gas composition upstream of the flame. When these unburnt gases are ignited and form a reaction front, the thermochemical states differ from the flame observed when only fresh gases are present. During EGR, the heat loss and the chemical reactions are decoupled, i.e., the chemical reactions that take place in the flame front are not directly affected by heat losses, but only by the change in mixture composition. Hence, this kind of enthalpy loss can be well captured by the FGM based on adiabatic one-dimensional flames with EGR presented in Section 2.3.
- **Flame quenching:** During flame quenching, the CO formation at the wall is strongly influenced by species diffusion in the enthalpy direction [30]. During enthalpy-induced flame quenching, the effect of heat loss and the chemical reaction are very closely coupled. To capture the effect of flame quenching in laminar flames, QFM based on laminar HOQ flames are derived in [45]. These are presented in Section 2.3 and extended to oxygenated fuels in Section 3.1.

Both of the above causes of enthalpy loss need to be incorporated into the chemistry manifold for an accurate prediction of the thermochemical state during turbulent FWI. Following the work of Ganter et al. [91], in publication [P4] such a chemistry manifold is presented that is based on a series of HOQ flames. Each HOQ flame simulation is initialized with a freely propagating flame. Similar to the FGM presented in Section 2.3, the unburnt gas composition of the initial flame is adapted by mixing a certain amount of cold exhaust gases with the fresh gases given by the ratio Y_{EGR} in Eq. (2.18).

The initial flame front then propagates towards an isothermal wall where it undergoes HOQ spaning a two-dimensional state in space and time, that describes the effect of heat-loss-induced

flame quenching. The final flamelet database used to generate the novel manifold spans a three-dimensional state space Ψ depending on the position x, the time t and the ratio EGR Y_{EGR}

$$\Psi\left(x, t, Y_{\mathrm{EGR}}\right) \ . \tag{3.2}$$

The manifold is then mapped into state space using two normalized progress variables C' and C_2 and the normalized enthalpy H' that are defined as[4]

$$C' = \frac{Y_{\mathrm{c}} - Y_{\mathrm{c,\,min}}\left(Z\right)}{Y_{\mathrm{c,\,max}}\left(Z\right) - Y_{\mathrm{c,\,min}}\left(Z\right)} \ , \tag{3.3}$$

$$C_2 = \frac{Y_{\mathrm{c2}} - Y_{\mathrm{c2,\,min}}\left(Z, C\right)}{Y_{\mathrm{c2,\,max}}\left(Z, C\right) - Y_{\mathrm{c2,\,min}}\left(Z, C\right)} \ , \tag{3.4}$$

$$H' = \frac{h - h_{\mathrm{min}}\left(Z, C, C_2\right)}{h_{\mathrm{max}}\left(Z, C, C_2\right) - h_{\mathrm{min}}\left(Z, C, C_2\right)} \ . \tag{3.5}$$

The mapping from the physical into the normalized state-space is performed in a two-stage process that consists of two individual two-dimensional mapping procedures:

$$\Psi\left(x, t, Y_{\mathrm{EGR}}\right) \rightarrow \Psi\left(C', T_{\mathrm{norm}}, Y_{\mathrm{EGR}}\right) \rightarrow \Psi\left(C', C_2, H'\right) \ . \tag{3.6}$$

The novel manifold is first validated a-priori [P4] and finally a-posteriori in a LES [P5]. Thereby, the publications [P4, P5] cover the full range of chemistry manifold development. In [P4], first, physical analyses of the turbulent flame are performed to gain a deeper understanding of the significant physical phenomena. A novel manifold is presented that incorporates these effects and extends the work of Ganter et al. [91] to turbulent flames. Finally, in [P5] the manifold prediction capabilities are assessed and compared to existing counterparts in a fully coupled simulation. In this context, Luo et al. [P5] present the first LESs employing chemistry manifolds that were specifically designed for FWI, namely FGMs [60], QFMs [45] and the novel QFM with EGR (QFM-EGR) [P4]. The publication gives insights into the manifolds' prediction capabilities and, thus, guidance for the selection of a suitable manifold for the simulation of more complex combustion configurations affected by FWI.

Future challenges

The generic configurations of turbulent FWI that were investigated concerning FVI have a moderate turbulence level. The level of turbulence in technical combustors is usually much higher. That begs the question of how the FVI is influenced by higher levels of turbulence. In this context, it could be valuable to analyze if the importance of FVI is dependent on the ratio between the turbulent scales, i.e., the size of the small-scale vortices close to the wall, and the quenching distance of the fuel-air mixture. This would give an indication that can help to decide which manifold complexity is necessary for turbulent FWI.

[4] Note that the normalized progress variable and enthalpy are defined differently than in Section 2.3.

Finally, similar to the laminar case, the incorporation of differential diffusion effects in the chemistry manifolds needs to be considered, especially for highly diffusive fuels like hydrogen. The FRS of Kaddar et al. [A5] gives a first idea of the combined effects of heat loss and curvature in a turbulent DME flame. Figure 3.7 shows the normalized local heat release rate at the wall parallel plane in the undisturbed part of the flame and the near-wall region. The undisturbed part of the flame shows a negative correlation of flame curvature with the local heat release rate, i.e., a positive curvature leads to a decrease in the local heat release rate. This finding is similar to the experimental data from Kosaka et al. [12]. However, in the near-wall region, this correlation is no longer present due to the combined effect of heat loss and curvature. The incorporation of these effects in the chemistry manifolds not only results in additional manifold dimensions but, similar to the laminar flame, also leads to technical difficulties in the manifold generation. These start with the identification of suitable generic configurations for the table generation and end with the strong coupling of differential diffusion, curvature and enthalpy in the physical space.

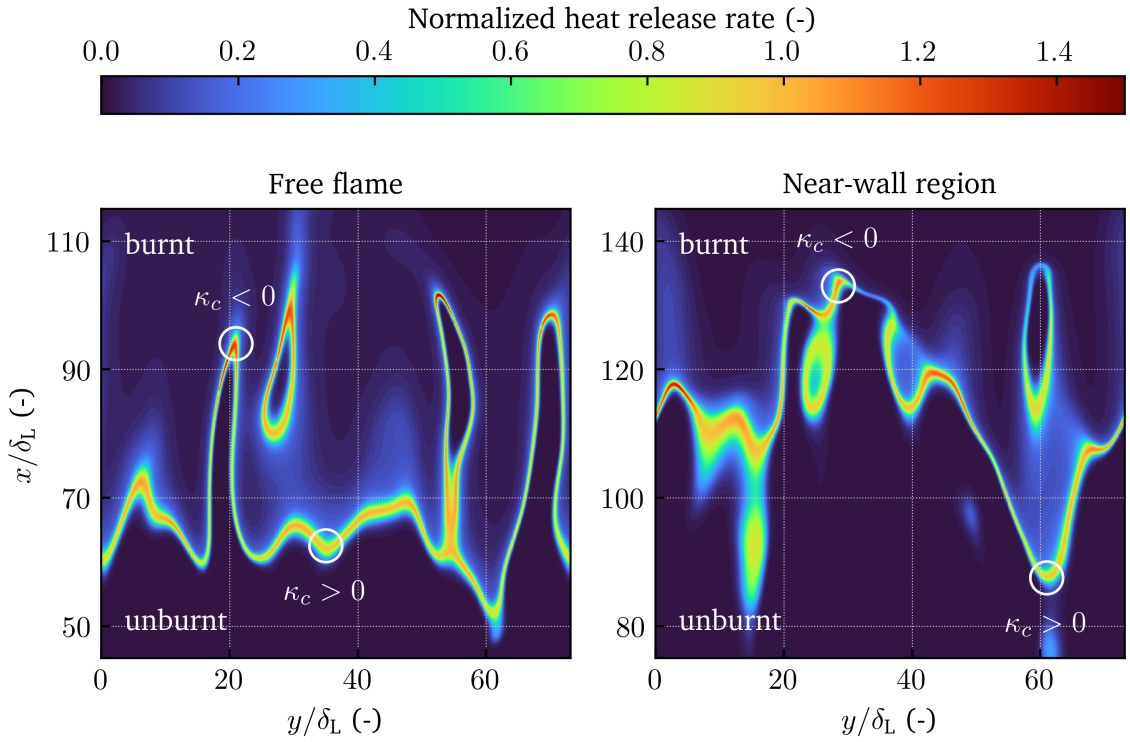

Fig. 3.7: Normalized heat release rate of a turbulent DME flame undergoing SWQ at different wall-parallel planes: undisturbed flame (left) and near-wall region (right). Regions of negative and positive curvature κ_c are indicated by the circles. The figure was adapted from [A5].

3.2.2 Closure of the joint PDF in flame-wall interaction

The second modeling challenge that is addressed in the turbulent SWQ configuration is the closure of the joint PDFs of the unresolved fluctuations of the control variables in RANS and LES. This closure is relevant in TCI closure models based on presumed or transported PDFs.

Physical phenomena

In publication [P2], a two-dimensional QFM for the chemistry closure is employed. Hence, the unresolved fluctuations are described by a multivariate PDF of the control variables

$$\widetilde{P}\left(H, Y_\mathrm{c}\right) \ , \tag{3.7}$$

with H being the normalized enthalpy and Y_c the progress variable. In presumed and transported PDF approaches this distribution is modeled to account for the effect of the unresolved fluctuations caused by turbulence on the flame structure and pollutant formation (see also Section 2.4). To gain insight into the complexity of the underlying distributions, i.e., the model complexity required to capture the flame structure, the PDFs are extracted from the FRS. Figure 3.8 shows the corresponding multivariate PDFs in the context of RANS. The PDFs are extracted at different representative locations in the turbulent flame. The positions correspond to a fixed wall distance z, while the streamwise direction is given by the position of the mean, normalized progress variable $\overline{C}$ at the given wall distance. In the core flow ($z = 2.0$ mm, top), the flame is unaffected by heat losses to the wall and a univariate PDF solely dependent on the progress variable can be observed. With decreasing wall distance ($z < 0.6$ mm), the PDF becomes bivariate varying in both the progress variable and enthalpy direction due to the increasing heat loss to the wall. These bivariate PDFs present a challenge for the TCI closure models in the near-wall region.

Modeling using presumed and transported PDFs

For an accurate prediction, the closure model needs to consider all of the manifestations of the unresolved fluctuations in the simulations, i.e., all of the possible PDF shapes need to be taken into account. Therefore, a novel closure approach is presented that is based on the CQMOM [51]. In the model, the bivariate PDFs are described by a conditional PDF

$$\widetilde{P}\left(H, Y_\mathrm{c}\right) = \widetilde{P}\left(Y_\mathrm{c}\right) \widetilde{P}\left(H|Y_\mathrm{c}\right) \ , \tag{3.8}$$

with $\widetilde{P}\left(Y_\mathrm{c}\right)$ being the distribution of the progress variable Y_c and $\widetilde{P}\left(H|Y_\mathrm{c}\right)$ the conditional PDF for the normalized enthalpy at a given value of the progress variable. In the simulation, the unknown PDFs are then described by their statistical moments

$$\widetilde{M}_{k,l} = \int_{\mathcal{R}_\psi} Y_\mathrm{c}^k H^l \widetilde{P}\left(H, Y_\mathrm{c}\right) dY_\mathrm{c} dH \ . \tag{3.9}$$

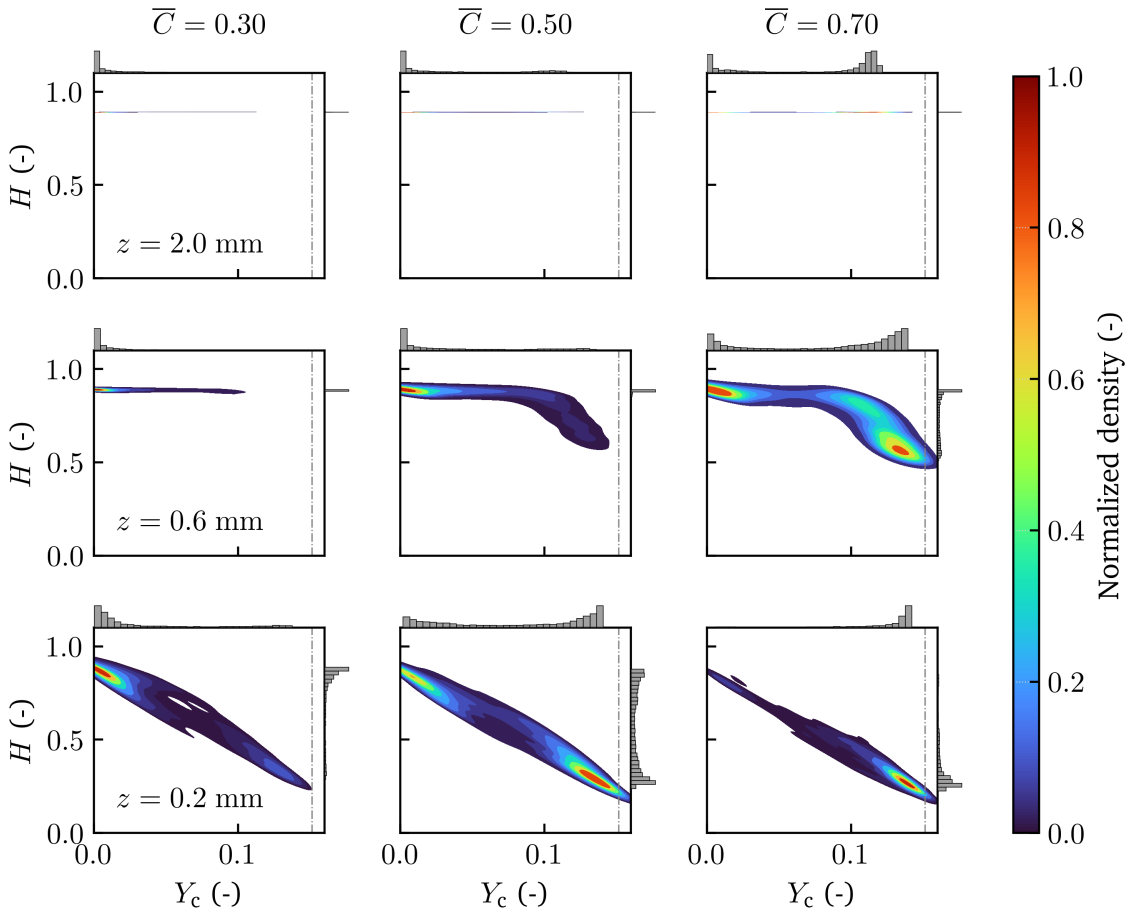

Fig. 3.8: PDF of the unresolved fluctuations of the control variables in the context of RANS [P2].

The unclosed terms in the moment transport equations, which contain the unknown distribution $\widetilde{P}(H, Y_c)$ are finally closed using Gaussian quadrature.[5]

$$\widetilde{Q} = \int_{Y_c} \int_{H} f_Q(Y_c, H)\, \widetilde{P}(Y_c, H)\, dY_c dH \approx \sum_{\alpha=1}^{N_\alpha} \sum_{\beta=1}^{N_\beta} w_\alpha w_{\alpha;\beta} f_Q(\xi_\alpha, \xi_{\alpha;\beta}) \ . \tag{3.10}$$

In the equation above, the primary ξ_α and secondary (conditional) $\xi_{\alpha;\beta}$ nodes approximate the PDF. The subscript α describes the index of the primary direction, while $(\alpha;\beta)$ reads as index β of the secondary direction for a given index in the primary direction α. For each N_α node in the primary direction, N_β nodes in the secondary direction are defined. Given Eq. (3.8) the primary and secondary (conditional) direction correspond to the progress variable Y_c and normalized enthalpy H, respectively. Finally, $f_Q(Y_c, H)$ is the approximation of the quantity Q from the chemistry manifold employed.

[5] For more information see Section 2.4.

Finally, the novel CQMOM approach is validated and compared to a presumed PDF approach [46] that uses a β-PDF for the normalized progress variable and a δ-peak for the enthalpy. While both models show a good prediction accuracy in the core flow region unaffected by wall heat losses, near the wall only the CQMOM approach can predict the complex distributions in the context of RANS and for coarse LES resolutions. These results give a good indication of the high prediction accuracy that can be achieved by the novel closure model.

Future challenges

The model validation that is presented in [P2] is based on an *a-priori* assessment, i.e., the moments $\widetilde{M}_{k,l}$ that describe the sub-grid fluctuations of the control variables are directly calculated from the FRS. In RANS or LESs that use the QMOM approach for TCI closure, a transport equation for the moments is solved. Given the moment transport equation (2.32), additional quantities that are dependent on the turbulent flow field need to be defined, like the turbulent diffusivity D_{T} or the decay time scale τ_{MM}. In a RANS or LES of turbulent FWI, these quantities are calculated based on the turbulence model employed. This means, that in a FWI configuration, not only the TCI closure needs to be considered, but also the description of the near-wall turbulence in the reacting boundary layer by the turbulence model applied.

Given the insights gained in [P4, P5], the chemistry manifold in [P2] needs to be extended by an additional dimension. This means, that instead of the two-dimensional PDF $\widetilde{P}\left(Y_{\mathrm{c}}, H\right)$ a three-dimensional PDF $\widetilde{P}\left(Y_{\mathrm{c}}, Y_{\mathrm{c},2}, H\right)$ needs to be modeled by the CQMOM model to capture the effect of FVI. When considering oxygenated fuels or hydrogen, additionally the effect of local mixture stratification needs to be considered.

Finally, similar to the FVI phenomena, the analysis performed in [P2] is based on a relatively low level of turbulence. If suitable FRSs can be conducted, the impact of higher turbulence intensities on the unresolved fluctuations of the control variables and the model accuracy of the CQMOM closure can be investigated.

3.3 Partially premixed flame-wall interaction

The third configuration that is investigated in this thesis addresses the combined effects of flame stratification and heat loss to the wall, namely partially premixed FWI. These quenching phenomena are relevant in different combustion applications, for example, in effusion cooling at low inflow rates or fire safety. In effusion cooling, the mixture stratification is caused by the cooling air that is inserted through the combustor walls while in a fire scenario, gases can be released from pyrolysis reactions at the burning surface. Figure 3.9 shows the configuration that is employed in this thesis to study these phenomena. The burner that was investigated in Section 3.1 is extended by an additional inlet in the wall. The wall inlet allows the seeding of additional gases and, thereby, a controlled mixture stratification in the near-wall region. Depending on the inflow from the wall, the operation conditions can be adapted to mimic effusion cooling effects or an active wall that releases burnable compounds. So far, the burner configuration was investigated in the context of fire safety both numerically [P3] and experimentally [A8, 92].

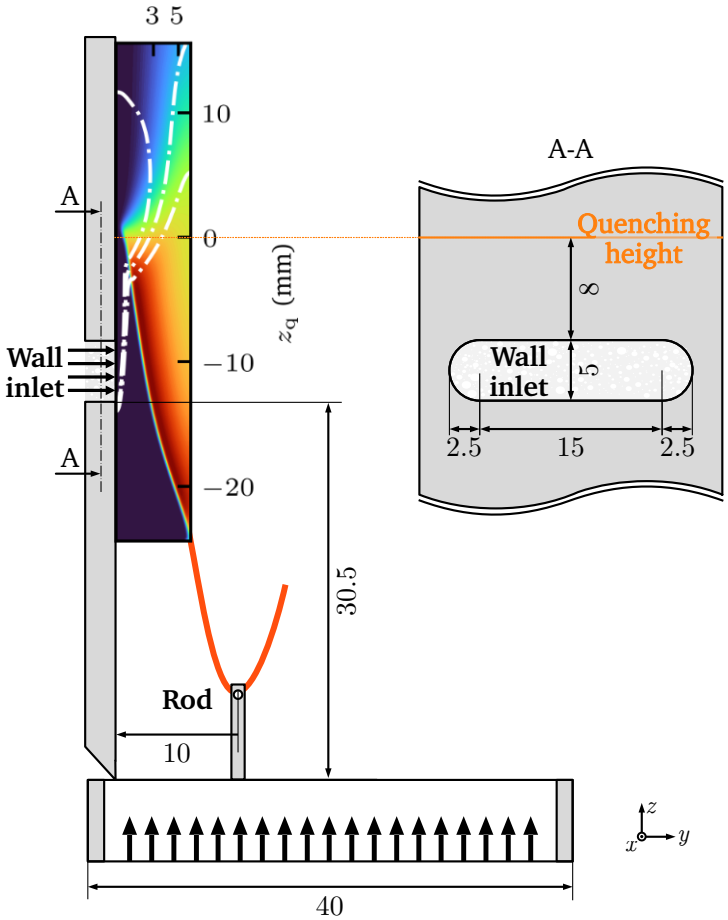

Fig. 3.9: Setup of the partially premixed SWQ burner configuration adapted from [P3]. The white dash-dotted lines correspond to isolines of the local mixture fraction.

Physical phenomena

In the first investigations of the novel burner configuration [P3, A8], pure methane is seeded from the wall at different flow rates to mimic the pyrolysis of a wall-embedded polymer. In contrast to a real polymer, the methane flow has a reduced chemical complexity, which results in well-controlled boundary conditions. This simplifies the interplay between experiments and simulations. In publication [P3], FRC simulations were performed that are compared to corresponding planar OH-LIF measurements [92] at different inflow rates. In a follow-up study, Greifenstein et al. [A8] extended the experimental data by measurements of the CO_2 mole fraction, gas temperature T and the local equivalence ratio Φ. The additional measurement data reveal discrepancies in the development of the concentration boundary layer between the experiments and simulations that originate from inhomogeneities in the inflow from the wall.[6] When accounting for these inhomogeneities, an excellent agreement between the numerical results and measurements is found.

Even with the simplified methane inflow from the wall, the high complexity of the configuration becomes apparent in the reported results. Figure 3.10 shows the flame structures in the configuration at increasing inflow rates (left $\rightarrow$ right) from the wall. In the top panel, isocontours of the local mixture fraction Φ depict the local mixture stratification. Further, the enthalpy loss that originates from heat losses to the wall is shown by the enthalpy difference Δh

$$\Delta h_i = h_i - h_{\mathrm{FP}}\left(\Phi_i, Y_{\mathrm{c},i}\right) \ , \tag{3.11}$$

with h_{FP} being the enthalpy of a freely propagating (FP) flame for the local equivalence ratio Φ_i and reaction progress variable $Y_{\mathrm{c},i}$ at a given point i. As individual phenomena, the impact of mixing and heat loss on the flame structure are well understood in laminar flames. However, the additional inflow from the wall results in a concentration boundary layer that is formed at the wall and affects the quenching flame branch. At high inflow rates (right; 4.5 L/h), a non-reactive boundary layer is formed at the wall and the flame is mostly quenched by mixture stratification. At intermediate inflow rates (middle; 2.0, 3.5 L/h), flame quenching and mixture stratification occur simultaneously, leading to a complex interplay between mixing and heat loss to the wall. This is reflected in the experimental results [A8] that show a significant change towards lower temperatures and CO_2 mole fractions in the near-wall thermochemical state compared to the fully premixed counterpart caused by the mixture stratification that results in a decrease in the local heat release rates. Further, the OH-LIF signal $S_{\text{OH-LIF}}$, which is usually used for flame front visualization, is not only affected by heat losses to the wall but also by the mixture stratification. Hence, an increasing methane inflow from the wall results in an increase in the deviation of the flame position indicated by the computed OH-LIF signal $S_{\text{OH-LIF}}$ and the actual flame front that is visualized by the local heat release rate in Fig. 3.10 (bottom). As a result, some of the established measurement techniques, e.g., the determination of the quenching point based on the gradient of $S_{\text{OH-LIF}}$, are not applicable in the novel configuration [P3, A8].

[6] The differences reported in [A8] are not reflected in the OH-LIF measurements in [P3]. Due to the low reactivity in this area, the normalized OH-LIF signal is not sensitive to the differences observed.

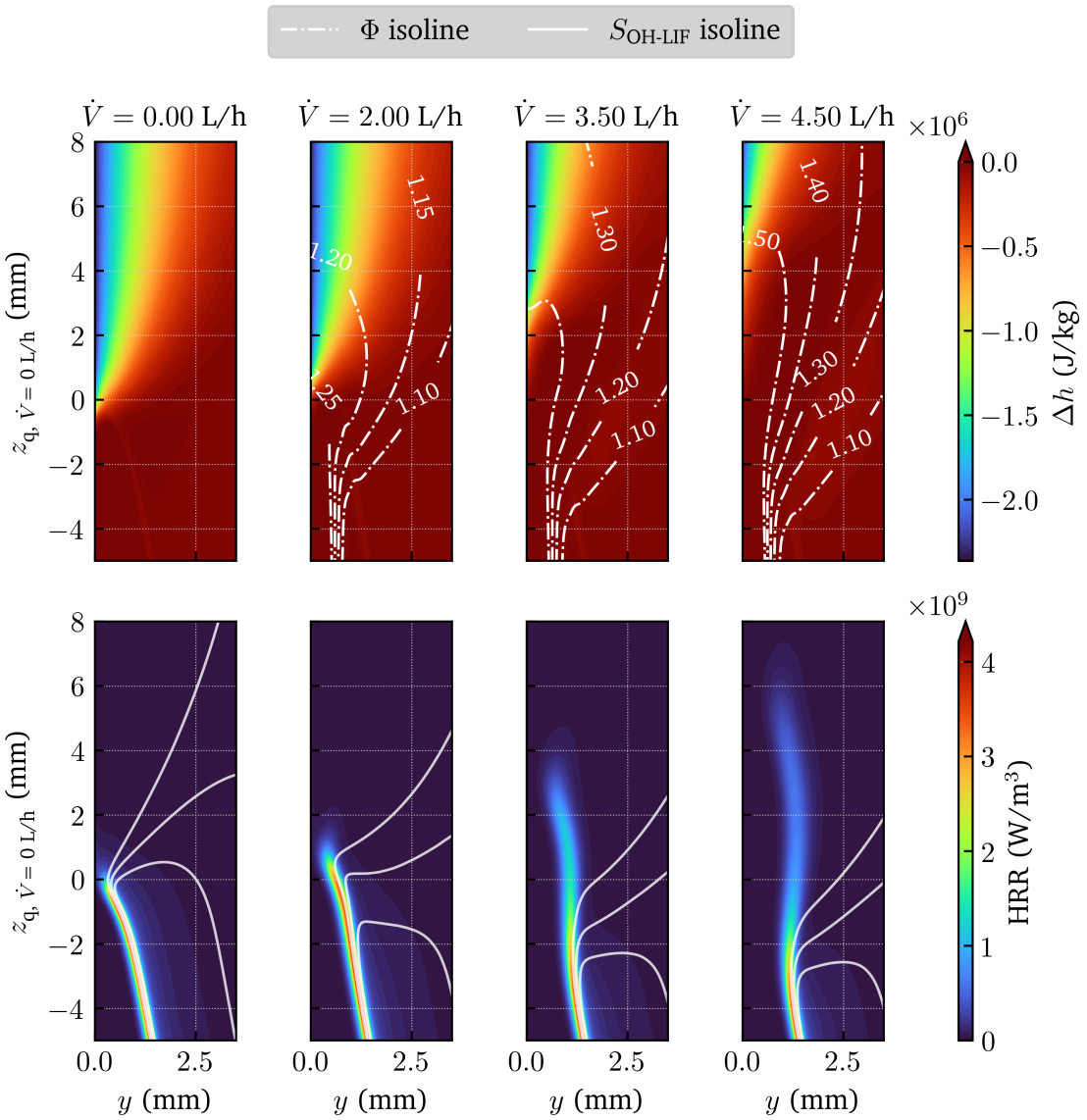

Fig. 3.10: Partially premixed SWQ at different inflow rates from the wall $\dot{V}$ adapted from [P3]. In the top panel the enthalpy difference Δh is shown together with isocontours of the local mixture fraction Φ. The bottom panel depicts the heat release rate (HRR) with isocontours of the OH-LIF signal $S_{\text{OH-LIF}}$. The data is plotted relative to the quenching point of the case without inflow from the wall.

In the second part of publication [P3], the effect of flame retardants is investigated numerically. Flame retardants are fire-suppressing substances that are used as polymer additives to reduce the ignition probability of the polymer and slow the fire spread [93]. This provides more time to escape or for fire suppression activities. Specifically, the effect of dimethylmethylphosphonat (DMMP), a phosphorous flame retardant, is analyzed. The methane inflow from the wall is replaced by a

mixture of methane and DMMP. The inflow rate is kept constant, while the amount of DMMP $Y_{\mathrm{DMMP}} = 1 - Y_{\mathrm{CH_4}}$ in the inflow mixture from the wall is gradually increased. This mimics the pyrolysis of a wall-embedded polymer with different amounts of flame retardant addition or a change in the pyrolysis gas composition over time.

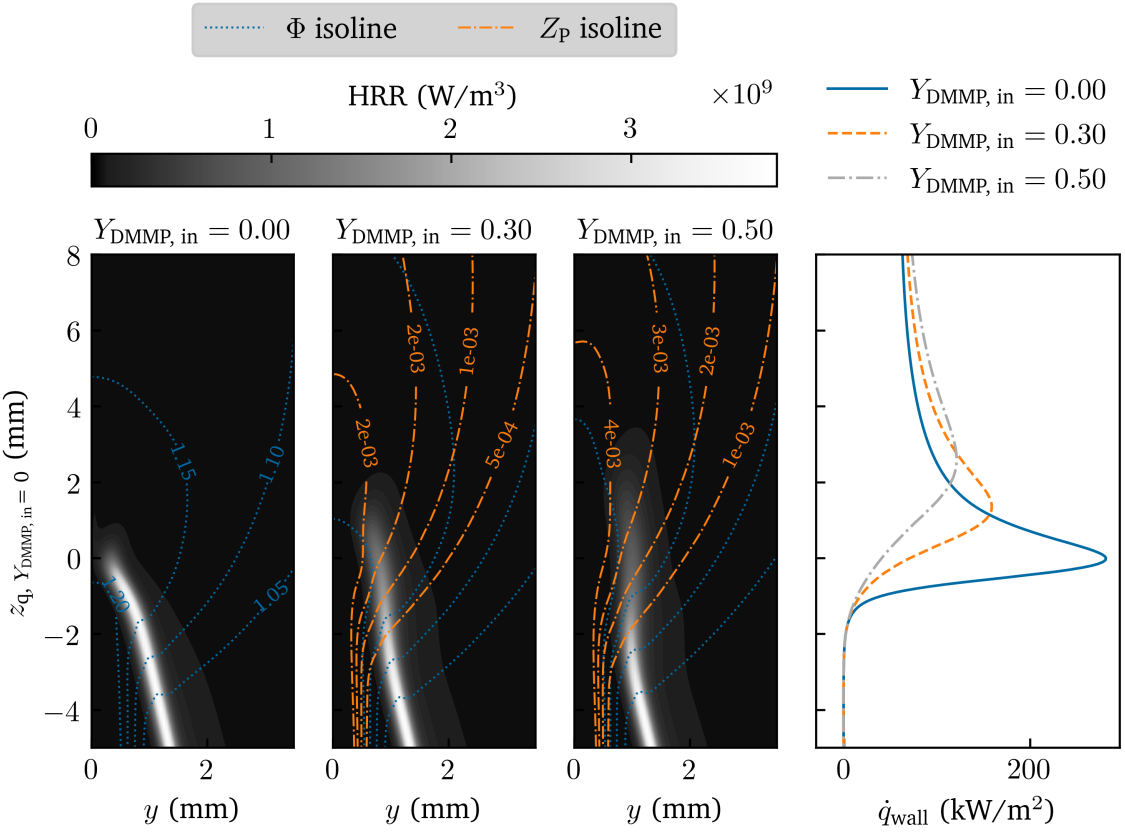

Fig. 3.11: Partially premixed SWQ with different amounts of flame retardants $Y_{\mathrm{DMMP,\,in}}$ added to the mixture entering from the wall at a fixed inflow rate $\dot{V} = 2$ L/h. The right part depicts the heat-release rate with isocontours of the local mixture fraction Φ and the elemental mass fraction of phosphor Z_{P}. On the left, the wall heat-flux $\dot{q}_{\mathrm{wall}}$ is depicted. The data is plotted relative to the quenching point of the case without DMMP addition.

Figure 3.11 shows the local heat release rate together with isocontours of the local equivalence ratio and the elemental mass fraction of phosphor (Z_{P}) that indicates the amount of flame retardant in the flame. Similar to the pure methane case, a concentration boundary layer is formed that influences the quenching flame branch. However, the addition of flame retardants results in a two-dimensional mixture stratification. Since the inflow rate from the wall is kept constant, the fuel-air ratio is mostly unaffected by the variation of inflow mixture composition. The major difference is the amount of flame retardant compounds that lower the reactivity of the flame in the near-wall region. This leads to a change in different quenching parameters, like an increased quenching distance or a decrease in the peak heat-flux to the wall $\dot{q}_{\mathrm{wall}}$ (right column in Fig. 3.11).

Note that the variation of mixture composition from the wall is a simplification of the processes that occur during the pyrolysis of a wall-embedded polymer. Here, both the mixture composition (Y_{DMMP}) and the rate at which burnable compounds are released from the wall ($\dot{V}$) are expected to change simultaneously. The decoupling of the two phenomena allows an easier analysis of the underlying physics, which is particularly important for future model development. The insights gained serve as a starting point for more detailed investigations of near-wall flame structures at active walls that release flame-retardant compounds and corresponding model development.

Future challenges

For the generation of chemistry manifolds that describe the effects in partially premixed FWI, multiple challenges need to be overcome. First, the combined effect of flame stratification and heat loss to the wall on the near-wall flame structure needs to be better understood. In this context, it is necessary to investigate which generic flame configurations, like adiabatic freely propagating flames or transient HOQ, can be used to capture the thermochemical state. These generic configurations can then be used to generate the flamelet database that is used for manifold derivation. In the context of flame-cooling-air interaction, Palluli et al. [31, 94] present such an analysis for the CO formation and compare the state space from a FRC simulation with freely propagating flames at different equivalence ratios. On the experimental side, Greifenstein et al. [95–98] investigated turbulent flame-cooling-air interaction in an effusion-cooled model gas turbine combustor. These measurement data can be used for the model verification of novel manifold approaches.

Once a flamelet database can be calculated that represents the thermochemical state, the state space needs to be represented by a suitable control variable vector $\boldsymbol{\xi}$. For a general description of the phenomena occurring in the case of flame retardant addition, the physical state space will be at least four-dimensional $\Psi\left(Y_{\mathrm{FR}}, Z, Y_{\mathrm{c}}, h\right)$, with Y_{FR} being the amount of flame retardant released into the mixture, Z describing the mixture stratification caused by the release of burnable gases that are not flame retardant compounds. The reaction progress is captured by Y_{c} and the heat loss to the walls by h. In this case, the amount of flame retardant can be seen as an additional co-flow with a different fuel composition. In the literature, multiple approaches [99–103] exist that describe such state spaces by a second mixture fraction. In turbulent operation conditions a similar extension to the manifolds as presented in Section 3.2 might be necessary to capture the mixing phenomena induced by FVI introducing an additional manifold dimension.

3.4 Isochoric, premixed flame-wall interaction

The final configuration is the subject of an ongoing investigation [P6]. Therefore, this section is intended as an outlook on the ongoing inquiries rather than a detailed discussion of the results. This planned investigation represents a crucial next step in modeling FWI processes with chemistry manifolds in technical combustion systems.

The previous sections focused on the examination of FWI under atmospheric pressure. However, many technical combustors operate in pressurized environments. For example, in an aero-engine, combustion takes place at constant, but elevated pressures. In this regard, Johe et al. [A4] introduced a novel SWQ burner designed to operate at pressures from 3 to 5 bar. The presented test rig allows the investigation of the influence of pressure on FWI phenomena, including the near-wall thermochemical states and pollutant formation. Additionally, the experimental measurements with the aforementioned novel burner [A4, 104] offer valuable reference data for model validation, like near-wall flow velocities, flame front imaging and FSD statistics. Moving beyond aero-engines, the complexity amplifies in enclosed combustion vessels like IC engines. Here, the combustion takes place in pressure-rising conditions which significantly influence chemical reactions, fluid dynamics, flame propagations and heat loss characteristics. In several FRSs [105–109] the effect of these pressure-rising conditions on FWI in isochoric configurations was explored, focusing on local heat release rates and flame propagation. However, the impact of pressure effects in isochoric combustion on pollutant formation, and whether it can be captured by existing manifold models has not been investigated yet. This gap is addressed by the planned publication [P6].

Therefore, a laminar, isochoric HOQ configuration is investigated, which is shown in Fig. 3.12. The one-dimensional domain is enclosed by isothermal walls. In the center of the domain, a flame kernel is initialized using the temperature and species profile of a freely propagating flame. The initial pressure p^0 is constant and for the velocity profile an initial guess is used that is depicted in Fig. 3.12. From the middle of the domain, the flame propagates toward the isothermal walls where it undergoes HOQ. For the FRC simulations the species diffusion is modeled using the mixture-averaged approach including thermal diffusion, see Section 2.1.

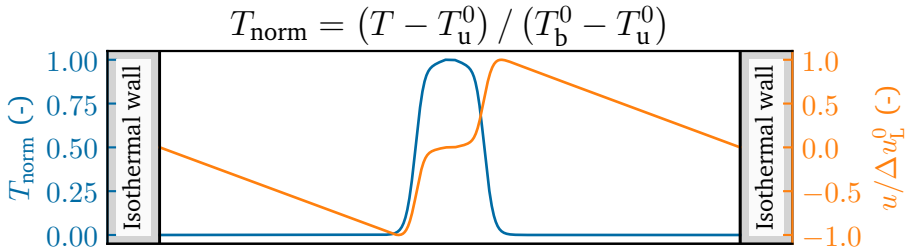

Fig. 3.12: Schematic depiction of the laminar, isochoric HOQ setup. A hot spot is initialized in the domain center using the temperature and species (not shown here) profiles of a freely propagating flame. Δu_{L}^0 is the difference between the fresh and burnt gas velocity of the freely propagating flame and T_{norm} the normalized temperature with T_{u}^0 and T_{b}^0 being the initial unburnt and burnt gas temperature, respectively.

Figure 3.13 shows the spatially averaged temperature $\overline{T}$ and pressure $\overline{p}$, the fresh gas temperature T_{u}, the wall heat flux $\dot{q}_{\mathrm{wall}}$ and the maximum heat release rate $\mathrm{HRR}_{\mathrm{max}}$ over time for the isochoric HOQ of a stoichiometric ammonia-hydrogen-air mixture[7].

The global quantities in Fig. 3.13 reveal certain aspects of isochoric FWI that complicate the modeling of isochoric quenching phenomena. In constant-volume vessels, the heat released by the combustion process increases the average temperature $\overline{T}$ in the combustion chamber. This temperature increase results in a rise in pressure $\overline{p}$, see the top panel of Fig. 3.13. The pressure increase can be determined by the equation of state for an ideal gas mixture for an isochoric process

$$\overline{p} = \overline{p}^0 \frac{\overline{T}}{\overline{T}^0} \,, \tag{3.12}$$

with the superscript $\langle\cdot\rangle^0$ defining the initial state. Further, the pressure increase affects the thermo-chemical state throughout the whole domain, resulting in a rise of the local temperature T in regions with low heat release (e.g., fresh and burnt gases). In areas unaffected by heat losses, the effect of pressure on the local temperature is given by the equation of state of an ideal gas mixture during an adiabatic process

$$T = T^0 \left(\frac{p}{p^0} \right)^{\frac{\gamma-1}{\gamma}} \,, \tag{3.13}$$

with $\gamma = c_{\mathrm{p}}/c_{\mathrm{v}}$ and c_{p} and c_{v} being the specific heat capacity at constant pressure and constant volume, respectively. Until the flame experiences heat loss effects (grey area in Fig. 3.13), the correlation given in Eq. (3.13) matches the increase in the fresh gas temperature. Finally, the time-varying pressure and fresh gas temperature conditions significantly influence the flame characteristics. As an example, the maximum heat release rate $\mathrm{HRR}_{\mathrm{max}}$ is shown in the bottom panel of Fig. 3.13. During the isochoric flame propagation, the maximum heat release rate increases by a factor of six.

The characteristics found in the isochoric HOQ flame are consistent with findings reported in previous works. Yenerdag et al. [105–107] found an increase in local heat release rate and wall heat fluxes as well as a decrease in flame thickness in both laminar and turbulent isochoric HOQ flames. Similar trends are also reported by Jafargholi et al. [108] who investigated a premixed syngas-air flame in an enclosed two-dimensional domain. Generally, the isochoric flame propagation and the heat release rates are similar to one-dimensional, isobaric laminar flames when accounting for the increase in pressure and fresh gas temperature as long as the flame is unaffected by heat losses (grey area in Fig. 3.13). However, to capture the FWI phenomena and the pollutant formation in chemistry manifold models, it is necessary to include the effects of heat loss under varying pressure and fresh gas temperature conditions, which is the subject of ongoing research.

[7] Fuel composition: $X_{\mathrm{NH_3}} = 0.44$, $X_{\mathrm{H_2}} = 0.42$, $X_{\mathrm{N_2}} = 0.14$, $T_{\mathrm{wall}} = T_{\mathrm{u}}^0 = 750$ K, $p^0 = 1$ atm, $L_x = 0.01$ m

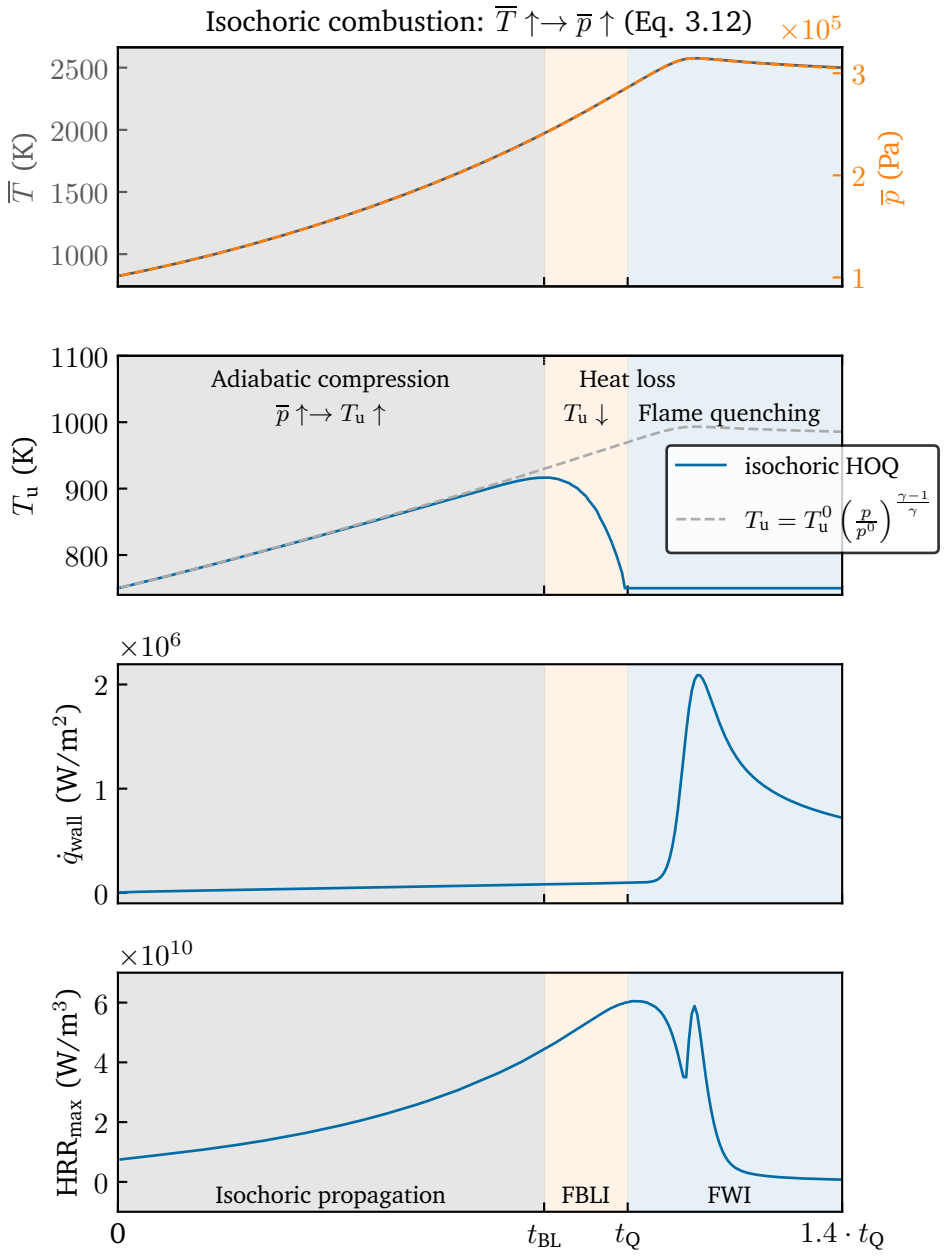

Fig. 3.13: Transient evolution of global flame properties for a laminar, isochoric HOQ of an ammonia-hydrogen flame. In the top panel, the spatially averaged temperature $\overline{T}$ and pressure $\overline{p}$ are depicted. The middle panels depict the fresh gas temperature T_u and the wall heat flux $\dot{q}_\mathrm{wall}$ and the bottom panel the maximum heat-release rate HRR$_\mathrm{max}$. The grey box indicates the time of isochoric flame propagation without heat loss effects. In the white area, the flame is influenced by heat losses from flame-boundary layer interaction (FBLI) and FWI. t_BL and t_Q mark the onset of FBLI and FWI, respectively.

In addition to Fig. 3.13, Fig. 3.14 shows a time series of the local temperature T (top) and H_2 mass fraction Y_{H_2} (bottom) profiles including a zoom into the near-wall region. In the top panel, the location of the flame tip at which the fresh gas temperature is extracted is indicated by circular markers. To gain a better understanding of the interplay of pressure and heat loss effects, the isochoric quenching process is subdivided into three stages based on the fresh gas temperature:[8]

- **Isochoric flame propagation:** ($t < t_{\mathrm{BL}}$; increasing T_{u}; grey)
  In the initial phase, the flame front remains unaffected by heat loss to the wall. As outlined above, the heat generated from combustion causes an elevation in pressure $\overline{p}$ that leads to an increase of the local temperatures, as governed by Eq. (3.13). The isochoric flame propagation and local heat release rates can be captured by an ensemble of isobaric freely propagating flames that consider the varying pressure and fresh gas temperature conditions [106, 108]. However, for a detailed description of the isochoric FWI, additional phenomena need to be incorporated into chemistry manifold closure models:
  - **Overheating of exhaust gases:** In the burnt area of the flame the exhaust gases overheat. This effect is strongest close to the domain center. Here, the burnt gas temperature T_{b} found in the isochoric flame exceeds the adiabatic flame temperature of a corresponding freely propagating flame $T_{\mathrm{b,\,fp}}$ by up to 200 K. For a detailed description of the isochoric FWI, these overheated states need to be considered in the chemistry manifold models.
  - **Temperature boundary layer:** In the near-wall region, a temperature boundary layer is formed due to the combined effect of increasing fresh gas temperatures and heat loss to the combustor walls, see top panel of Fig. 3.14. When thermal diffusion is considered, the temperature gradient at the wall also induces the development of a concentration boundary layer. This is shown exemplarly for the H_2 mass fraction in the bottom panel of Fig. 3.14. In most of the previous studies [105–108] thermal diffusion was neglected, hence, no concentration boundary layer was present.
- **Flame-boundary layer interaction (FBLI):** ($t_{\mathrm{BL}} < t < t_{\mathrm{Q}}$; decreasing T_{u}; orange)
  At a certain wall distance, the flame is affected by the changing flow field and thermodynamic conditions in the wall boundary layer. The interaction with the temperature boundary layer leads to a decrease in fresh gas temperature and mixture composition that affects the flame structure. During FBLI, the heat flux to the wall $\dot{q}_{\mathrm{wall}}$ is not affected by the reaction front of the flame, i.e., the decrease in flame temperature is caused by the interaction with the cold mixture in the vicinity of the wall and not directly by heat losses to the wall.
- **Flame-wall interaction (FWI):** ($t > t_{\mathrm{Q}}$, $T_{\mathrm{u}} = T_{\mathrm{wall}}$; blue)
  After traversing the temperature boundary layer, the flame tip finally reaches the wall. Here, the unburnt flame temperature is constant and similar to the wall temperature. The flame experiences heat loss from the wall, which leads to flame quenching. The FWI results in a significant rise in wall heat flux with the peak indicating the quenching time.

[8] The description in the brackets for each item read:

- the time interval where the state is found, i.e., $t < t_{\mathrm{BL}}$
- the condition based on which the time interval is defined, i.e., increasing T_{u}
- the color of the lines in Fig. 3.14, i.e., grey

In study [P6], the three phases of the quenching process will be investigated in the laminar, isochoric configuration with a focus on pollutant formation. Additionally, the isochoric HOQ will be compared to isobaric HOQ that is used for the creation of state-of-the-art chemistry manifolds for FWI to elaborate on how these manifolds need to be adapted for isochoric FWI. Further, given the insights of the laminar configuration, the influence of turbulence will be analyzed in an FRS of a turbulent, isochoric ammonia-air flame ignited in a box initialized with isotropic turbulence and initial conditions corresponding to the laminar counterpart.[9]

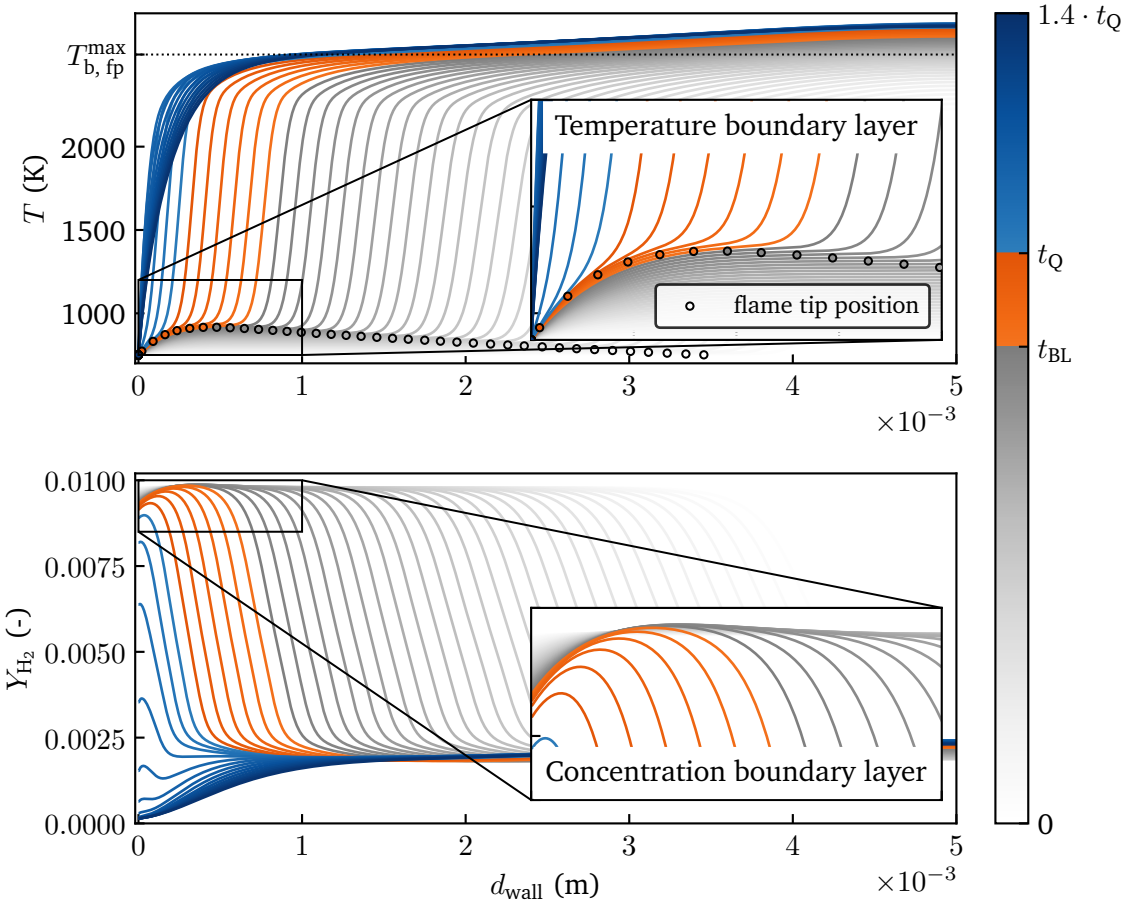

Fig. 3.14: Time series of a laminar, isochoric HOQ of an ammonia-hydrogen flame. The circular markers indicate the position of the flame tip defined by the isovalue of $Y_{\mathrm{H2O}} = 10^{-6}$. The variable $T^{\max}_{\mathrm{b,\,fp}}$ corresponds to the maximum adiabatic flame temperature over all time instances to indicate the overheating of exhaust gases.

[9]The FRS was already conducted, and the processing of the data is ongoing.

4 Conclusions and outlook

In this thesis, multiple aspects of FWI in combustion systems are comprehensively analyzed, namely the physical characteristics of alternative fuels, the effect of turbulence, the mixture stratification introduced by an active wall and pressure-rising conditions. The analyses are performed in four configurations specifically designed to highlight the effect under investigation. In each configuration, the determining physical phenomena are studied and the resulting modeling challenges for chemistry manifold closure models are identified. Based on the physical insights novel closure models are derived and validated before future challenges are outlined. The gained insights are:

- Configuration 1: **Laminar, premixed flame-wall interaction**
  The first configuration is used to investigate the specifics of FWI when alternative fuels are employed. More specifically, previous work of laminar, premixed SWQ methane-air flames is extended to oxygenated fuels.
  Publication [P1] comprises the first numerical investigation of such flames in the SWQ burner. FRC simulations were performed and a good agreement with measurements of the local heat release rate and the near-wall CO formation was found. Additionally, the prediction capabilities of three different chemistry manifolds, namely FGM, REDIM and QFM, were assessed using the FRC simulations as a reference. While the FGM is not able to capture the near-wall CO formation, the REDIM and the QFM show an improved prediction capability. These results are consistent with the previous investigations of methane-air flames, which show that the classical manifold approaches need to be adapted to capture the effects of FWI. Further, additional phenomena occurring in oxygenated fuels were investigated. While the role of low-temperature chemistry is neglectable [A2], differential diffusion [A2, A3] impacts the near-wall flame structure. Besides oxygenated fuels, differential diffusion is also relevant for hydrogen combustion systems. Chemistry manifold models need to be adapted to meet this future challenge. Therefore, a novel manifold approach was developed for hydrogen flames unaffected by walls [A6]. The integration of FWI effects in this approach leads to technical difficulties. In this context, the usage of a neural-network-based manifold, like the one employed in [A7], could be a promising alternative to the commonly used look-up tables.
- Configuration 2: **Turbulent, premixed flame-wall interaction**
  The second configuration is a turbulent, premixed SWQ flame stabilized in a fully developed turbulent channel flow. An FRS of a methane-air flame is performed and the complex interplay of the combustion chemistry with the turbulent flow is analyzed.
  Publications [P4, P5] cover FVI, a mixing phenomenon that is caused by the interaction of the flame tip with the near-wall vortical structures. FVI leads to a mixing-induced enthalpy loss that results in thermochemical states in the turbulent flame that are not present in the

laminar counterpart. To capture this effect a novel manifold that accounts for FVI by an additional manifold dimension is presented and validated *a-priori* and *a-posteriori*. Compared to FGM and QFM it shows an improved prediction capability of the near-wall flame dynamics and pollutant formation. In the turbulent SWQ configuration, the whole range of model development was covered from model derivation, application and validation. Now, the novel manifold approach can be applied to the simulation of more complex configurations and higher turbulence intensities.
In addition to chemistry manifold closure, the TCI closure based on statistical closure models was investigated in [P2]. In the FRS, complex two-dimensional joint PDFs of the progress variable and the enthalpy are found in the near-wall region that cannot be captured by the classical presumed PDF approaches reported in the literature. Therefore, a novel closure approach based on the CQMOM is derived and validated *a-priori* using the FRS as a reference. The CQMOM approach shows an improved prediction capability and can correctly capture the near-wall flame structure and pollutant formation. Future work should focus on the *a-posteriori* validation of the CQMOM closure in the context of RANS or LES.
While the above publications focus on methane as a fuel, the first investigation of oxygenated fuels in the turbulent configuration was performed in [A5]. Similar to the findings in the laminar configuration, for these alternative fuels, differential diffusion needs to be considered and incorporated into the chemistry manifolds in the future to improve the prediction of FWI characteristics in technical combustors.

- Configuration 3: **Partially premixed flame-wall interaction**
  In the third configuration, the effect of mixture stratification on FWI is studied. Therefore, the laminar SWQ burner is extended by a wall inlet, which mimics an active wall that releases additional gases.
  In [P3] the configuration is investigated in the context of fire safety by employing a methane inflow from the wall. The partially premixed SWQ flame is characterized both experimentally and numerically. The results exhibit the combined effect of flame stratification and heat loss to the wall. In the second step, the effect of flame retardants on the near-wall flame structure is analyzed. The gained insights serve as the starting point for the development of improved chemistry manifold models in the context of fire safety.
  These chemistry manifolds need to incorporate not only the effect of mixture stratification but also the amount of flame retardant compound in the burning mixture. Further, the configuration can be adapted to study the effect of flame-cooling-air interaction in the future.

- Configuration 4: **Pressurized flame-wall interaction**
  The fourth configuration is dedicated to IC engines where combustion takes place under pressure-rising conditions. The underlying physical processes are investigated in laminar, isochoric HOQ. The unique aspects of the configuration are described in Section 3.4. The analysis of the results is ongoing and will focus on pollutant formation. Further, isobaric and isochoric quenching will be compared to elaborate on how the existing chemistry manifolds can be adapted for isochoric FWI in IC engines.

The insights gained in this thesis present significant advancements in the modeling of various FWI scenarios using chemistry manifolds. They pave the path toward the simulation of partially premixed, turbulent FWI under pressurized conditions in technical combustors.

Scientific advancements of the main publications

In addition to the aforementioned conclusions, this section emphasizes the scientific progress made in the main publications of this thesis [P1–P5], illustrated in Fig. 4.1. In the plot, the horizontal position indicates the level of model maturity, ranging from the initial phase of gaining physical insight through model derivation to the ultimate stages of model validation and application.

The investigations of premixed FWI cover diverse physical aspects, including oxygenated fuels [P1], TCI [P2], and FVI [P4, P5]. Innovative closure models are introduced and validated, using FRS and experiments as references. The closure models show a high accuracy and can now be applied to more complex configurations. Publication [P3] expands upon premixed FWI and considers the mixture stratification by an active wall in the context of fire safety. The analysis deepens the understanding of the combined effects of heat loss and mixture stratification, laying the groundwork for the extension of the existing manifold models to partially premixed FWI. Overall, these publications significantly enhance the understanding of FWI, providing detailed physical insights. Furthermore, they present and validate novel closure approaches for FWI phenomena.

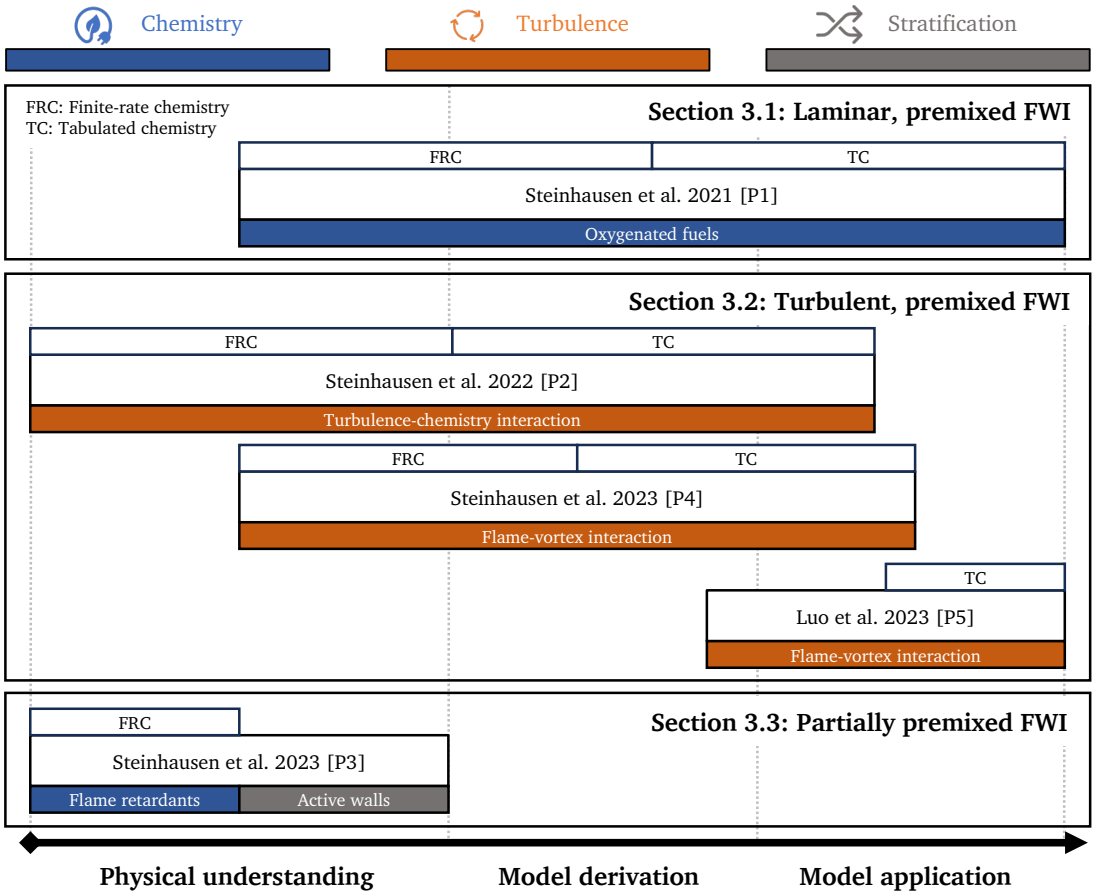

Fig. 4.1: Overview of the topics covered in the main publications of this dissertation. The publications are arranged according to the model maturity. The topics are given in the colored boxes below and the chemistry closure approach is in the boxes above the publication.

Bibliography

Publications included in the dissertation

[P1] **M. Steinhausen**, Y. Luo, S. Popp, C. Strassacker, T. Zirwes, H. Kosaka, F. Zentgraf, U. Maas, A. Sadiki, A. Dreizler, and C. Hasse. "Numerical Investigation of Local Heat-Release Rates and Thermo-Chemical States in Side-Wall Quenching of Laminar Methane and Dimethyl Ether Flames". In: *Flow Turbul. Combust.* 106 (2021), 681–700. DOI: 10.1007/s10494-020-00146-w.

[P2] **M. Steinhausen**, T. Zirwes, F. Ferraro, S. Popp, F. Zhang, H. Bockhorn, and C. Hasse. "Turbulent Flame-Wall Interaction of Premixed Flames Using Quadrature-based Moment Methods (QbMM) and Tabulated Chemistry: An a Priori Analysis". In: *Int. J. Heat Fluid Flow* 93 (2022), 108913. DOI: 10.1016/j.ijheatfluidflow.2021.108913.

[P3] **M. Steinhausen**, F. Ferraro, M. Schneider, F. Zentgraf, M. Greifenstein, A. Dreizler, C. Hasse, and A. Scholtissek. "Effect of Flame Retardants on Side-Wall Quenching of Partially Premixed Laminar Flames". In: *Proc. Combust. Inst.* 39 (2023), 3745–3754. DOI: 10.1016/j.proci.2022.07.207.

[P4] **M. Steinhausen**, T. Zirwes, F. Ferraro, A. Scholtissek, H. Bockhorn, and C. Hasse. "Flame-Vortex Interaction during Turbulent Side-Wall Quenching and Its Implications for Flamelet Manifolds". In: *Proc. Combust. Inst.* 39 (2023), 2149–2158. DOI: 10.1016/j.proci.2022.09.026.

[P5] Y. Luo, **M. Steinhausen**, D. Kaddar, C. Hasse, and F. Ferraro. "Assessment of Flamelet Manifolds for Turbulent Flame-Wall Interactions in Large-Eddy Simulations". In: *Combust. Flame* 255 (2023), 112923. DOI: 10.1016/j.combustflame.2023.112923.

[P6] **M. Steinhausen**, A. Scholtissek, C. Hasse, and A. Gruber. "Isochoric Flame-Wall Interaction of Ammonia-Hydrogen Flames". in preperation.

Additional publications as co-author

[A1] T. Zirwes, T. Häber, F. Zhang, H. Kosaka, A. Dreizler, **M. Steinhausen**, C. Hasse, A. Stagni, D. Trimis, R. Suntz, and H. Bockhorn. "Numerical Study of Quenching Distances for Side-Wall Quenching Using Detailed Diffusion and Chemistry". In: *Flow Turbul. Combust.* 106 (2021), 649–679. DOI: 10.1007/s10494-020-00215-0.

[A2] A. Stagni, Y. Luo, **M. Steinhausen**, A. Dreizler, and C. Hasse. "Chemistry Effects in the Wall Quenching of Laminar Premixed DME Flames". In: *Combust. Flame* 232 (2021), 111529. DOI: 10.1016/j.combustflame.2021.111529.

[A3] F. Zentgraf, P. Johe, **M. Steinhausen**, C. Hasse, M. Greifenstein, A. D. Cutler, R. S. Barlow, and A. Dreizler. "Detailed Assessment of the Thermochemistry in a Side-Wall Quenching Burner by Simultaneous Quantitative Measurement of CO_2, CO and Temperature Using Laser Diagnostics". In: *Combust. Flame* 235 (2022), 111707. DOI: 10.1016/j.combustflame.2021.111707.

[A4] P. Johe, F. Zentgraf, M. Greifenstein, **M. Steinhausen**, C. Hasse, and A. Dreizler. "Characterization of Flow Field and Combustion Dynamics in a Novel Pressurized Side-Wall Quenching Burner Using High-Speed PIV/OH-PLIF Measurements". In: *Int. J. Heat Fluid Flow* 94 (2022), 108921. DOI: 10.1016/J.IJHEATFLUIDFLOW.2021.108921.

[A5] D. Kaddar, **M. Steinhausen**, T. Zirwes, H. Bockhorn, C. Hasse, and F. Ferraro. "Combined Effects of Heat Loss and Curvature on Turbulent Flame-Wall Interaction in a Premixed Dimethyl Ether/Air Flame". In: *Proc. Combust. Inst.* 39 (2023), 2199–2208. DOI: 10.1016/j.proci.2022.08.060.

[A6] H. Böttler, H. Lulic, **M. Steinhausen**, X. Wen, C. Hasse, and A. Scholtissek. "Flamelet Modeling of Thermo-Diffusively Unstable Hydrogen-Air Flames". In: *Proc. Combust. Inst.* 39 (2023), 1567–1576. DOI: 10.1016/j.proci.2022.07.159.

[A7] J. Bissantz, J. Karpowski, **M. Steinhausen**, Y. Luo, F. Ferraro, A. Scholtissek, C. Hasse, and L. Vervisch. "Application of Dense Neural Networks for Manifold-Based Modeling of Flame-Wall Interactions". In: *Appl. Energy Combust. Sci.* 13 (2023), 100113. DOI: 10.1016/j.jaecs.2023.100113.

[A8] M. Greifenstein, F. Zentgraf, P. Johe, B. Boehm, **M. Steinhausen**, C. Hasse, and A. Dreizler. "Measurements of the Local Equivalence Ratio and Its Impact on the Thermochemical State in Laminar Partially Premixed Boundary Layer Flames". In: *Exp. Fluids* 65 (2023), 7. DOI: 10.1007/s00348-023-03747-z.

Other references

[1] IPCC. “Summary for Policymakers”. In: *Climate Change 2021: The Physical Science Basis. Contribution of Working Group I to the Sixth Assessment Report of the Intergovernmental Panel on Climate Change*. Ed. by V. Masson-Delmotte, P. Zhai, A. Pirani, S. Connors, C. Péan, S. Berger, N. Caud, Y. Chen, L. Goldfarb, M. Gomis, M. Huang, K. Leitzell, E. Lonnoy, J. Matthews, T. Maycock, T. Waterfield, O. Yelekçi, R. Yu, and B. Zhou. Cambridge, United Kingdom and New York, NY, USA: Cambridge University Press, 2021, pp. 3–32. DOI: 10.1017/9781009157896.001.

[2] *Net Zero by 2050 – Analysis*. IEA. URL: https://www.iea.org/reports/net-zero-by-2050 (visited on 08/18/2023).

[3] H. Wirth. *Aktuelle Fakten zur Photovoltaik in Deutschland*. Fraunhofer ISE, 2023. URL: www.pv-fakten.de (visited on 05/17/2023).

[4] A. M. Elbaz, S. Wang, T. F. Guiberti, and W. L. Roberts. “Review on the Recent Advances on Ammonia Combustion from the Fundamentals to the Applications”. In: *Fuel Commun.* 10 (2022), 100053. DOI: 10.1016/j.jfueco.2022.100053.

[5] E.-A. Tingas, ed. *Hydrogen for Future Thermal Engines*. Green Energy and Technology. Cham: Springer International Publishing, 2023. DOI: 10.1007/978-3-031-28412-0.

[6] D. Veynante and L. Vervisch. “Turbulent Combustion Modeling”. In: *Prog. Energy Combust. Sci.* 28 (2002), 193–266. DOI: 10.1016/S0360-1285(01)00017-X.

[7] A. Dreizler and B. Böhm. “Advanced Laser Diagnostics for an Improved Understanding of Premixed Flame-Wall Interactions”. In: *Proc. Combust. Inst.* 35 (2015), 37–64. DOI: 10.1016/j.proci.2014.08.014.

[8] W. Lazik, Th. Doerr, S. Bake, R. v. d. Bank, and L. Rackwitz. “Development of Lean-Burn Low-NOx Combustion Technology at Rolls-Royce Deutschland.” In: *Vol 3 Combust Fuels Emiss Parts B*. ASME, 2008, pp. 797–807. DOI: 10.1115/GT2008-51115.

[9] T. Poinsot and D. Veynante. *Theoretical and Numerical Combustion*. 2nd ed. Philadelphia, USA: R.T. Edwards, Inc., 2005.

[10] M. Luo and D. Liu. “Pollutants Emissions of CO and Soot from Flame-wall Interactions in Fundamental and Practical Energy Conversion Systems: A Review”. In: *ES Energy Environ.* 3 (2018), 4–24. DOI: 10.30919/esee8c218.

[11] C. Jainski, M. Rißmann, B. Böhm, J. Janicka, and A. Dreizler. “Sidewall Quenching of Atmospheric Laminar Premixed Flames Studied by Laser-Based Diagnostics”. In: *Combust. Flame* 183 (2017), 271–282. DOI: 10.1016/j.combustflame.2017.05.020.

[12] H. Kosaka, F. Zentgraf, A. Scholtissek, L. Bischoff, T. Häber, R. Suntz, B. Albert, C. Hasse, and A. Dreizler. “Wall Heat Fluxes and CO Formation/Oxidation during Laminar and Turbulent Side-Wall Quenching of Methane and DME Flames”. In: *Int. J. Heat Fluid Flow* 70 (2018), 181–192. DOI: 10.1016/j.ijheatfluidflow.2018.01.009.

[13] H. Kosaka, F. Zentgraf, A. Scholtissek, C. Hasse, and A. Dreizler. “Effect of Flame-Wall Interaction on Local Heat Release of Methane and DME Combustion in a Side-Wall Quenching Geometry”. In: *Flow Turbul. Combust.* 104 (2019), 1029–1046. DOI: 10.1007/s10494-019-00090-4.

[14] F. Zentgraf, P. Johe, A. D. Cutler, R. S. Barlow, B. Böhm, and A. Dreizler. “Classification of Flame Prehistory and Quenching Topology in a Side-Wall Quenching Burner at Low-Intensity Urbulence by Correlating Transport Effects with CO_2, CO and Temperature”. In: *Combust. Flame* 239 (2022), 111681. DOI: 10.1016/j.combustflame.2021.111681.

[15] O. Ezekoye, R. Greif, and R. F. Sawyer. “Increased Surface Temperature Effects on Wall Heat Transfer during Unsteady Flame Quenching”. In: *Symp. Int. Combust.* Twenty-Fourth Symposium on Combustion 24 (1992), 1465–1472. DOI: 10.1016/S0082-0784(06)80171-2.

[16] I. S. Wichman and G. Bruneaux. “Head-on Quenching of a Premixed Flame by a Cold Wall”. In: *Combust. Flame* 103 (1995), 296–310. DOI: 10.1016/0010-2180(95)00100-X.

[17] P. Popp, M. Smooke, and M. Baum. “Heterogeneous/Homogeneous Reaction and Transport Coupling during Flame-Wall Interaction”. In: *Symp. Int. Combust.* 26 (1996), 2693–2700. DOI: 10.1016/S0082-0784(96)80105-6.

[18] P. Popp and M. Baum. “Analysis of Wall Heat Fluxes, Reaction Mechanisms, and Unburnt Hydrocarbons during the Head-On Quenching of a Laminar Methane Flame”. In: *Combust. Flame* 108 (1997), 327–348. DOI: 10.1016/S0010-2180(96)00144-7.

[19] C. Hasse, M. Bollig, N. Peters, and H. A. Dwyer. “Quenching of Laminar Iso-Octane Flames at Cold Walls”. In: *Combust. Flame* 122 (2000), 117–129. DOI: 10.1016/S0010-2180(00)00107-3.

[20] J. Lai and N. Chakraborty. “Effects of Lewis Number on Head on Quenching of Turbulent Premixed Flames: A Direct Numerical Simulation Analysis”. In: *Flow Turbul. Combust.* 96 (2016), 279–308. DOI: 10.1007/s10494-015-9629-x.

[21] J. Sellmann, J. Lai, A. M. Kempf, and N. Chakraborty. “Flame Surface Density Based Modelling of Head-on Quenching of Turbulent Premixed Flames”. In: *Proc. Combust. Inst.* 36 (2017), 1817–1825. DOI: 10.1016/J.PROCI.2016.07.114.

[22] J. Lai, D. Alwazzan, and N. Chakraborty. “Turbulent Scalar Flux Transport in Head-on Quenching of Turbulent Premixed Flames: A Direct Numerical Simulations Approach to Assess Models for Reynolds Averaged Navier Stokes Simulations”. In: *J. Turbul.* 18 (2017), 1033–1066. DOI: 10.1080/14685248.2017.1353218.

[23] J. Lai, D. H. Wacks, and N. Chakraborty. “Flow Topology Distribution in Head-on Quenching of Turbulent Premixed Flame: A Direct Numerical Simulation Analysis”. In: *Fuel* 224 (2018), 186–209. DOI: 10.1016/j.fuel.2018.03.021.

[24] P. Zhao, L. Wang, and N. Chakraborty. “Analysis of the Flame-Wall Interaction in Premixed Turbulent Combustion”. In: *J. Fluid Mech.* 848 (2018), 193–218. DOI: 10.1017/jfm.2018.356.

[25] J. Lai, M. Klein, and N. Chakraborty. “Direct Numerical Simulation of Head-On Quenching of Statistically Planar Turbulent Premixed Methane-Air Flames Using a Detailed Chemical Mechanism”. In: *Flow Turbul. Combust.* 101 (2018), 1073–1091. DOI: 10.1007/S10494-018-9907-5/FIGURES/10.

[26] U. Ahmed, N. Chakraborty, and M. Klein. “Assessment of Bray Moss Libby Formulation for Premixed Flame-Wall Interaction within Turbulent Boundary Layers: Influence of Flow Configuration”. In: *Combust. Flame* 233 (2021), 111575. DOI: 10.1016/j.combustflame.2021.111575.

[27] P. Zhao, L. Wang, and N. Chakraborty. “Effects of the Cold Wall Boundary on the Flame Structure and Flame Speed in Premixed Turbulent Combustion”. In: *Proc. Combust. Inst.* 38 (2021), 2967–2976. DOI: 10.1016/j.proci.2020.06.214.

[28] J. Lai, U. Ahmed, M. Klein, and N. Chakraborty. “A Comparison between Head-on Quenching of Stoichiometric Methane-Air and Hydrogen-Air Premixed Flames Using Direct Numerical Simulations”. In: *Int. J. Heat Fluid Flow* 93 (2022), 108896. DOI: 10.1016/j.ijheatfluidflow.2021.108896.

[29] J. Andrae, P. Björnbom, L. Edsberg, and L.-E. Eriksson. “A Numerical Study of Side Wall Quenching with Propane/Air Flames”. In: *Proc. Combust. Inst.* 29 (2002), 789–795. DOI: 10.1016/S1540-7489(02)80101-8.

[30] S. Ganter, A. Heinrich, T. Meier, G. Kuenne, C. Jainski, M. C. Rißmann, A. Dreizler, and J. Janicka. “Numerical Analysis of Laminar Methane-Air Side-Wall-Quenching”. In: *Combust. Flame* 186 (2017), 299–310. DOI: 10.1016/j.combustflame.2017.08.017.

[31] R. Palulli, D. Brouzet, M. Talei, and R. Gordon. “A Comparative Study of Flame-Wall Interaction and Flame-Cooling Air Interaction”. In: *Int. J. Heat Fluid Flow* 92 (2021), 108888. DOI: 10.1016/j.ijheatfluidflow.2021.108888.

[32] R. Palulli, M. Talei, and R. L. Gordon. “Unsteady Flame-Wall Interaction: Impact on CO Emission and Wall Heat Flux”. In: *Combust. Flame* 207 (2019), 406–416. DOI: 10.1016/J.COMBUSTFLAME.2019.06.012.

[33] T. Alshaalan and C. J. Rutland. “Wall Heat Flux in Turbulent Premixed Reacting Flow”. In: *Combust. Sci. Technol.* 174 (2002), 135–165. DOI: 10.1080/713712913.

[34] A. Gruber, R. Sankaran, E. R. Hawkes, and J. H. Chen. “Turbulent Flame-Wall Interaction: A Direct Numerical Simulation Study”. In: *J. Fluid Mech.* 658 (2010), 5–32. DOI: 10.1017/S0022112010001278.

[35] B. Jiang, D. Brouzet, M. Talei, R. L. Gordon, Q. Cazeres, and B. Cuenot. “Turbulent Flame-Wall Interactions for Flames Diluted by Hot Combustion Products”. In: *Combust. Flame* 230 (2021), 111432. DOI: 10.1016/j.combustflame.2021.111432.

[36] U. Ahmed, N. Chakraborty, and M. Klein. “Influence of Thermal Wall Boundary Condition on Scalar Statistics during Flame-Wall Interaction of Premixed Combustion in Turbulent Boundary Layers”. In: *Int. J. Heat Fluid Flow* 92 (2021), 108881. DOI: 10.1016/j.ijheatfluidflow.2021.108881.

[37] U. Ahmed, N. Chakraborty, and M. Klein. “Scalar Gradient and Strain Rate Statistics in Oblique Premixed Flame-Wall Interaction Within Turbulent Channel Flows”. In: *Flow Turbul. Combust.* 106 (2021), 701–732. DOI: 10.1007/s10494-020-00169-3.

[38] U. Maas and S. B. Pope. “Simplifying Chemical Kinetics: Intrinsic Low-Dimensional Manifolds in Composition Space”. In: *Combust. Flame* 88 (1992), 239–264. DOI: 10.1073/pnas.1619819114.

[39] O. Gicquel, N. Darabiha, and D. Thévenin. “Laminar Premixed Hydrogen/Air Counterflow Flame Simulations Using Flame Prolongation of ILDM with Differential Diffusion”. In: *Proc. Combust. Inst.* 28 (2000), 1901–1908. DOI: 10.1016/s0082-0784(00)80594-9.

[40] V. Bykov and U. Maas. “The Extension of the ILDM Concept to Reaction-Diffusion Manifolds”. In: *Combust. Theory Model.* 11 (2007), 839–862. DOI: 10.1080/13647830701242531.

[41] J. A. van Oijen and L. P. H. de Goey. “Modelling of Premixed Laminar Flames Using Flamelet-Generated Manifolds”. In: *Combust. Sci. Technol.* 161 (2000), 113–137. DOI: 10.1080/00102200008935814.

[42] C. D. Pierce and P. Moin. “Progress-Variable Approach for Large-Eddy Simulation of Non-Premixed Turbulent Combustion”. In: *J. Fluid Mech.* 504 (2004), 73–97. DOI: 10.1017/S0022112004008213.

[43] S. Ganter, C. Straßacker, G. Kuenne, T. Meier, A. Heinrich, U. Maas, and J. Janicka. “Laminar Near-Wall Combustion: Analysis of Tabulated Chemistry Simulations by Means of Detailed Kinetics”. In: *Int. J. Heat Fluid Flow* 70 (2018), 259–270. DOI: 10.1016/j.ijheatfluidflow.2018.02.015.

[44] C. Strassacker, V. Bykov, and U. Maas. “Comparative Analysis of Reaction-Diffusion Manifold Based Reduced Models for Head-On- and Side-Wall-Quenching Flames”. In: *Proc. Combust. Inst.* 38 (2021), 1025–1032. DOI: 10.1016/j.proci.2020.06.130.

[45] D. V. Efimov, P. de Goey, and J. A. van Oijen. “QFM: Quenching Flamelet-Generated Manifold for Modelling of Flame-Wall Interactions”. In: *Combust. Theory Model.* 24 (2020), 72–104. DOI: 10.1080/13647830.2019.1658901.

[46] B. Fiorina, O. Gicquel, L. Vervisch, S. Carpentier, and N. Darabiha. “Premixed Turbulent Combustion Modeling Using Tabulated Detailed Chemistry and PDF”. In: *Proc. Combust. Inst.* 30 (2005), 867–874. DOI: 10.1016/j.proci.2004.08.062.

[47] P. Pantangi, A. Sadiki, J. Janicka, M. Mann, and A. Dreizler. “LES of Premixed Methane Flame Impinging on the Wall Using Non-adiabatic Flamelet Generated Manifold (FGM) Approach”. In: *Flow Turbul. Combust.* 92 (2014), 805–836. DOI: 10.1007/s10494-013-9526-0.

[48] A. Heinrich, G. Kuenne, S. Ganter, C. Hasse, and J. Janicka. “Investigation of the Turbulent Near Wall Flame Behavior for a Sidewall Quenching Burner by Means of a Large Eddy Simulation and Tabulated Chemistry”. In: *Fluids* 3 (2018), 65. DOI: 10.3390/fluids3030065.

[49] A. Heinrich, F. Ries, G. Kuenne, S. Ganter, C. Hasse, A. Sadiki, and J. Janicka. “Large Eddy Simulation with Tabulated Chemistry of an Experimental Sidewall Quenching Burner”. In: *Int. J. Heat Fluid Flow* 71 (March 2018), 95–110. DOI: 10.1016/j.ijheatfluidflow.2018.03.011.

[50] A. Heinrich, S. Ganter, G. Kuenne, C. Jainski, A. Dreizler, and J. Janicka. “3D Numerical Simulation of a Laminar Experimental SWQ Burner with Tabulated Chemistry”. In: *Flow Turbul. Combust.* 100 (2018), 535–559. DOI: 10.1007/s10494-017-9851-9.

[51] J. C. Cheng, R. D. Vigil, and R. O. Fox. “A Competitive Aggregation Model for Flash NanoPrecipitation”. In: *J. Colloid Interface Sci.* 351 (2010), 330–342. DOI: 10.1016/j.jcis.2010.07.066.

[52] **M. Steinhausen**. *Turbulent Flame-Wall Interaction Visualization*. DOI: 10.48328/tudatalib-674.

[53] D. L. Marchisio and R. O. Fox. *Computational Models for Polydisperse Particulate and Multiphase Systems*. Cambride: Cambridge University Press, 2013. DOI: 10.1176/pn.39.24.00390022b.

[54] R. J. Kee, M. E. Coltrin, P. Glarborg, and H. Zhu. *Chemically Reacting Flow: Theory, Modeling, and Simulation*. Wiley, 2017. DOI: 10.1002/9781119186304.

[55] A. Fick. “Ueber Diffusion”. In: *Ann. Phys.* 170 (1855), 59–86. DOI: 10.1002/andp.18551700105.

[56] C. F. Curtiss and J. O. Hirschfelder. “Transport Properties of Multicomponent Gas Mixtures”. In: *J. Chem. Phys.* 17 (1949), 550–555. DOI: 10.1063/1.1747319.

[57] D. G. Goodwin, H. K. Moffat, I. Schoegl, R. L. Speth, and B. W. Weber. *Cantera: An Object-Oriented Software Toolkit for Chemical Kinetics, Thermodynamics, and Transport Processes*. 2022. DOI: 10.5281/zenodo.6387882.

[58] A. Ern and V. Giovangigli. “EGLIB: A General-Purpose Fortran Library for Multicomponent Transport Property Evaluation”. In: *CERMICS Intern. Rep.* (1996), 96–51.

[59] J. A. van Oijen, F. A. Lammers, and L. P. H. de Goey. “Modeling of Complex Premixed Burner Systems by Using Flamelet-Generated Manifolds”. In: *Combust. Flame* 127 (2001), 2124–2134. DOI: 10.1016/S0010-2180(01)00316-9.

[60] B. Fiorina, R. Baron, O. Gicquel, D. Thevenin, S. Carpentier, and N. Darabiha. “Modelling Non-Adiabatic Partially Premixed Flames Using Flame-Prolongation of ILDM”. In: *Combust. Theory Model.* 7 (2003), 449–470. DOI: 10.1088/1364-7830/7/3/301.

[61] A. Ketelheun, G. Kuenne, and J. Janicka. “Heat Transfer Modeling in the Context of Large Eddy Simulation of Premixed Combustion with Tabulated Chemistry”. In: *Flow Turbul. Combust.* 91 (2013), 867–893. DOI: 10.1007/s10494-013-9492-6.

[62] S. B. Pope. *Turbulent Flows*. Cambridge University Press, 2000.

[63] H. Pitsch. “Large-Eddy Simulation of Turbulent Combustion”. In: *Annu. Rev. Fluid Mech.* 38 (2006), 453–482. DOI: 10.1146/annurev.fluid.38.050304.092133.

[64] J. Janicka and A. Sadiki. “Large Eddy Simulation of Turbulent Combustion Systems”. In: *Proc. Combust. Inst.* 30 (2005), 537–547. DOI: 10.1016/j.proci.2004.08.279.

[65] B. Fiorina, D. Veynante, and S. Candel. “Modeling Combustion Chemistry in Large Eddy Simulation of Turbulent Flames”. In: *Flow Turbul. Combust.* 94 (2015), 3–42. DOI: 10.1007/s10494-014-9579-8.

[66] O. Colin, F. Ducros, D. Veynante, and T. Poinsot. “A Thickened Flame Model for Large Eddy Simulations of Turbulent Premixed Combustion”. In: *Phys. Fluids* 12 (2000), 1843–1863. DOI: 10.1063/1.870436.

[67] A. Donini, R. J. M. Bastiaans, J. A. van Oijen, and L. P. H. de Goey. “A 5-D Implementation of FGM for the Large Eddy Simulation of a Stratified Swirled Flame with Heat Loss in a Gas Turbine Combustor”. In: *Flow Turbul. Combust.* 98 (2017), 887–922. DOI: 10.1007/s10494-016-9777-7.

[68] W. Zhang, S. Karaca, J. Wang, Z. Huang, and J. van Oijen. “Large Eddy Simulation of the Cambridge/Sandia Stratified Flame with Flamelet-Generated Manifolds: Effects of Non-Unity Lewis Numbers and Stretch”. In: *Combust. Flame* 227 (2021), 106–119. DOI: 10.1016/j.combustflame.2021.01.004.

[69] M. Muradoglu, P. Jenny, S. B. Pope, and D. A. Caughey. “A Consistent Hybrid Finite-Volume/Particle Method for the PDF Equations of Turbulent Reactive Flows”. In: *J. Comput. Phys.* 154 (1999), 342–371. DOI: 10.1006/jcph.1999.6316.

[70] S. B. Pope. “A Monte Carlo Method for the Pdf Equations of Turbulent Reactive Flow”. In: *Combust. Sci. Technol.* 25 (1981), 159–174. DOI: 10.1080/00102208108547500.

[71] L. Valiño. “Field Monte Carlo Formulation for Calculating the Probability Density Function of a Single Scalar in a Turbulent Flow”. In: *Flow Turbul. Combust.* 60 (1998), 157–172. DOI: 10.1023/A:1009968902446.

[72] R. McGraw. “Description of Aerosol Dynamics by the Quadrature Method of Moments”. In: *Aerosol Sci. Technol.* 27 (1997), 255–265. DOI: 10.1080/02786829708965471.

[73] M. Pollack, F. Ferraro, J. Janicka, and C. Hasse. “Evaluation of Quadrature-based Moment Methods in Turbulent Premixed Combustion”. In: *Proc. Combust. Inst.* 38 (2021), 2877–2884. DOI: 10.1016/j.proci.2020.06.127.

[74] S. B. Pope. “The Statistical Theory of Turbulent Flames”. In: *Philos Trans R Soc Lond. Ser A* 291 (1979), 529–568.

[75] J. Villermaux and J. C. Devillon. “Représentation de La Coalescence et de La Redispersion Des Domaines de Ségrégation Dans Un Fluide Par Un Modèle d’interaction Phénoménologique”. In: *Proc. 2nd Int. Symp. Chem. React. Eng.* Vol. 26. Elsevier New York, 1972, pp. 1–13.

[76] J. C. Wheeler. “Modified Moments and Gaussian Quadratures”. In: *Rocky Mt. J. Math.* 4 (1974), 287–296. DOI: 10.1216/RMJ-1974-4-2-287.

[77] R. O. Fox. *Quadrature-Based Moment Methods for Multiphase Chemically Reacting Flows*. Vol. 52. 1. Elsevier Inc., 2018. 1–50. DOI: 10.1016/bs.ache.2018.01.001.

[78] Y. Luo, C. Strassacker, C. Hasse, and U. Maas. “Simulation of Side-Wall Quenching of Laminar Premixed Flames with Manifold-Based Reduced Kinetic Models Implemented in Generalised Coordinates”. In: *Combust. Theory Model.* 25 (2021), 669–694. DOI: 10.1080/13647830.2021.1933603.

[79] Y. Luo, C. Strassacker, F. Ferraro, F. Zentgraf, A. Dreizler, U. Maas, and C. Hasse. “A Manifold-Based Reduction Method for Side-Wall Quenching Considering Differential Diffusion Effects and Its Application to a Laminar Lean Dimethyl Ether Flame”. In: *Int. J. Heat Fluid Flow* 97 (2022), 109042. DOI: 10.1016/j.ijheatfluidflow.2022.109042.

[80] T. Häber and R. Suntz. “Effect of Different Wall Materials and Thermal-Barrier Coatings on the Flame-Wall Interaction of Laminar Premixed Methane and Propane Flames”. In: *Int. J. Heat Fluid Flow* 69 (2018), 95–105. DOI: 10.1016/j.ijheatfluidflow.2017.12.004.

[81] J. Schlup and G. Blanquart. “Reproducing Curvature Effects Due to Differential Diffusion in Tabulated Chemistry for Premixed Flames”. In: *Proc. Combust. Inst.* 37 (2019), 2511–2518. DOI: 10.1016/j.proci.2018.06.211.

[82] N. Mukundakumar, D. Efimov, N. Beishuizen, and J. van Oijen. “A New Preferential Diffusion Model Applied to FGM Simulations of Hydrogen Flames”. In: *Combust. Theory Model.* 25 (2021), 1245–1267. DOI: 10.1080/13647830.2021.1970232.

[83] H. Böttler, X. Chen, S. Xie, A. Scholtissek, Z. Chen, and C. Hasse. “Flamelet Modeling of Forced Ignition and Flame Propagation in Hydrogen-Air Mixtures”. In: *Combust. Flame* 243 (2022), 112125. DOI: 10.1016/j.combustflame.2022.112125.

[84] L. L. C. Franke, A. K. Chatzopoulos, and S. Rigopoulos. “Tabulation of Combustion Chemistry via Artificial Neural Networks (ANNs): Methodology and Application to LES-PDF Simulation of Sydney Flame L”. In: *Combust. Flame* 185 (2017), 245–260. DOI: 10.1016/J.COMBUSTFLAME.2017.07.014.

[85] T. Readshaw, T. Ding, S. Rigopoulos, and W. P. Jones. “Modeling of Turbulent Flames with the Large Eddy Simulation-Probability Density Function (LES–PDF) Approach, Stochastic Fields, and Artificial Neural Networks”. In: *Phys. Fluids* 33 (2021), 035154. DOI: 10.1063/5.0041122.

[86] T. Ding, T. Readshaw, S. Rigopoulos, and W. P. Jones. “Machine Learning Tabulation of Thermochemistry in Turbulent Combustion: An Approach Based on Hybrid Flamelet/Random Data and Multiple Multilayer Perceptrons”. In: *Combust. Flame* 231 (2021), 111493. DOI: 10.1016/j.combustflame.2021.111493.

[87] O. Owoyele, P. Kundu, M. M. Ameen, T. Echekki, and S. Som. “Application of Deep Artificial Neural Networks to Multi-Dimensional Flamelet Libraries and Spray Flames”. In: *Int. J. Engine Res.* 21 (2020), 151–168. DOI: 10.1177/1468087419837770.

[88] R. Ranade, G. Li, S. Li, and T. Echekki. “An Efficient Machine-Learning Approach for PDF Tabulation in Turbulent Combustion Closure”. In: *Combust. Sci. Technol.* 193 (2021), 1258–1277. DOI: 10.1080/00102202.2019.1686702.

[89] M. Hansinger, Y. Ge, and M. Pfitzner. “Deep Residual Networks for Flamelet/Progress Variable Tabulation with Application to a Piloted Flame with Inhomogeneous Inlet”. In: *Combust. Sci. Technol.* 194 (2022), 1587–1613. DOI: 10.1080/00102202.2020.1822826.

[90] E. Ranzi, A. Frassoldati, R. Grana, A. Cuoci, T. Faravelli, A. P. Kelley, and C. K. Law. “Hierarchical and Comparative Kinetic Modeling of Laminar Flame Speeds of Hydrocarbon and Oxygenated Fuels”. In: *Prog. Energy Combust. Sci.* 38 (2012), 468–501. DOI: 10.1016/j.pecs.2012.03.004.

[91] S. Ganter. “Verbrennung in Wandnähe: Numerische Analyse von Phänomenen und Modellentwicklung”. Darmstadt: Technical University of Darmstadt, 2019.

[92] F. Zentgraf. “Investigation of Reaction and Transport Phenomena during Flame-Wall Interaction Using Laser Diagnostics”. PhD thesis. Technical University of Darmstadt, 2022. DOI: 10.26083/tuprints-00021314.

[93] J. Green. “Mechanisms for Flame Retardancy and Smoke Suppression – A Review”. In: *J. Fire Sci.* 14 (1996), 426–442. DOI: 10.1177/073490419601400602.

[94] R. Palulli, M. Talei, and R. L. Gordon. “Analysis of Near-Wall CO Due to Unsteady Flame-Cooling Air Interaction”. In: *Flow Turbul. Combust.* 107 (2021), 343–365. DOI: 10.1007/s10494-020-00233-y.

[95] M. Greifenstein, J. Hermann, B. Boehm, and A. Dreizler. “Flame-Cooling Air Interaction in an Effusion-Cooled Model Gas Turbine Combustor at Elevated Pressure”. In: *Exp. Fluids* 60 (2019), 10. DOI: 10.1007/s00348-018-2656-3.

[96] M. Greifenstein, J. Heinze, C. Willert, L. Voigt, M. Zedda, C. Richter, and A. Dreizler. “Time-Resolved Temperature Profile Measurements in the Exhaust of a Single Sector Gas Turbine Combustor at Realistic Operating Conditions”. In: *Exp. Fluids* 61 (2020), 177. DOI: 10.1007/s00348-020-03011-8.

[97] M. Greifenstein and A. Dreizler. “Investigation of Mixing Processes of Effusion Cooling Air and Main Flow in a Single Sector Model Gas Turbine Combustor at Elevated Pressure”. In: *Int. J. Heat Fluid Flow* 88 (2021), 108768. DOI: 10.1016/j.ijheatfluidflow.2020.108768.

[98] M. Greifenstein and A. Dreizler. “Influence of Effusion Cooling Air on the Thermochemical State of Combustion in a Pressurized Model Single Sector Gas Turbine Combustor”. In: *Combust. Flame* 226 (2021), 455–466. DOI: 10.1016/j.combustflame.2020.12.031.

[99] C. Hasse and N. Peters. “A Two Mixture Fraction Flamelet Model Applied to Split Injections in a DI Diesel Engine”. In: *Proc. Combust. Inst.* 30 (2005), 2755–2762. DOI: 10.1016/j.proci.2004.08.166.

[100] J. Watanabe and K. Yamamoto. “Flamelet Model for Pulverized Coal Combustion”. In: *Proc. Combust. Inst.* 35 (2015), 2315–2322. DOI: 10.1016/j.proci.2014.07.065.

[101] R. Knappstein, G. Kuenne, H. Nicolai, F. di Mare, A. Sadiki, and J. Janicka. “Description of the Char Conversion Process in Coal Combustion Based on Premixed FGM Chemistry”. In: *Fuel* 236 (2019), 124–134. DOI: 10.1016/j.fuel.2018.08.158.

[102] H. Nicolai, L. Dressler, J. Janicka, and C. Hasse. “Assessing the Importance of Differential Diffusion in Stratified Hydrogen-Methane Flames Using Extended Flamelet Tabulation Approaches”. In: *Phys. Fluids* 34 (2022), 085118. DOI: 10.1063/5.0102675.

[103] Y. Luo, F. Ferraro, A. Breicher, H. Böttler, A. Dreizler, D. Geyer, C. Hasse, and A. Scholtissek. “A Novel Flamelet Manifold Parametrization Approach for Lean CH_4-H_2-air Flames”. In: *Int. J. Hydrog. Energy* 48 (2023), 407–421. DOI: 10.1016/j.ijhydene.2022.09.233.

[104] P. Johe, F. Zentgraf, M. Greifenstein, R. S. Barlow, and A. Dreizler. “Laser-Based Investigation of Flame Surface Density and Mean Reaction Rate during Flame-Wall Interaction at Elevated Pressure”. In: *Proc. Combust. Inst.* 39 (2023), 2159–2168. DOI: 10.1016/j.proci.2022.09.016.

[105] B. Yenerdag, N. Fukushima, M. Shimura, M. Tanahashi, and T. Miyauchi. “Turbulence-Flame Interaction and Fractal Characteristics of H_2-Air Premixed Flame under Pressure Rising Condition”. In: *Proc. Combust. Inst.* 35 (2015), 1277–1285. DOI: 10.1016/j.proci.2014.05.153.

[106] B. Yenerdag, Y. Minamoto, Y. Naka, M. Shimura, and M. Tanahashi. “Flame Propagation and Heat Transfer Characteristics of a Hydrogen-Air Premixed Flame in a Constant Volume Vessel”. In: *Int. J. Hydrog. Energy* 41 (2016), 9679–9689. DOI: 10.1016/j.ijhydene.2016.04.006.

[107] B. Yenerdag, Y. Minamoto, K. Aoki, M. Shimura, Y. Nada, and M. Tanahashi. “Flame-Wall Interactions of Lean Premixed Flames under Elevated, Rising Pressure Conditions”. In: *Fuel* 189 (2017), 8–14. DOI: 10.1016/j.fuel.2016.10.096.

[108] M. Jafargholi, G. K. Giannakopoulos, C. E. Frouzakis, and K. Boulouchos. “Laminar Syngas-Air Premixed Flames in a Closed Rectangular Domain: DNS of Flame Propagation and Flame/Wall Interactions”. In: *Combust. Flame* 188 (2018), 453–468. DOI: 10.1016/j.combustflame.2017.09.029.

[109] C. Yu, L. Cai, C. Chi, S. Mashruk, A. Valera-Medina, and U. Maas. “Numerical Investigation on the Head-on Quenching (HoQ) of Laminar Premixed Lean to Stoichiometric Ammonia-Hydrogen-Air Flames”. In: *Flow Turbul. Combust.* (2023). DOI: 10.1007/s10494-023-00489-0.

[110] L. Allen, A. O’Connell, and V. Kiermer. “How Can We Ensure Visibility and Diversity in Research Contributions? How the Contributor Role Taxonomy (CRediT) Is Helping the Shift from Authorship to Contributorship”. In: *Learn. Publ.* 32 (2019), 71–74. DOI: 10.1002/leap.1210.

[111] Y. Luo. “Modeling and Simulation of Near-Wall Combustion of Renewable Fuels”. PhD thesis. Darmstadt: Technische Universität Darmstadt, 2023. DOI: 10.26083/tuprints-00023365.

Acknowledgements

First and foremost, I extend my gratitude to Prof. Christian Hasse for supervising my doctoral thesis. The trust you placed in me and the numerous scientific discussions have been instrumental in helping me realize my full potential. Additionally, I thank Prof. Andrea Gruber for the warm welcome to his institute in Norway. Our collaboration has opened up exciting new perspectives for me, and I thoroughly enjoyed my research visit to Trondheim.

I want to express my thanks to all my collaboration partners over the years. A special acknowledgment goes to my experimental partners at the Institute for Reactive Flows and Diagnostics (RSM), including Florian Zentgraf, Max Greifenstein, Pascal Johe, and Prof. Andreas Dreizler, for the consistently open and pleasant collaboration. In addition to the excellent experimental validation data, the numerous scientific discussions and joint publications have consistently provided me with new insights and expanded my horizons. Furthermore, special thanks to Thorsten Zirwes for numerous technical insights into OpenFOAM and for executing and providing the turbulent FRS.

I express my gratitude to the SFB 150 and all its members, especially my colleagues at STFS, Yujuan Lou, and Andrea Pati. The Collaborative Research Center provided me with an inspiring framework, allowing for numerous interdisciplinary exchanges.

Thanks to all my colleagues and friends at STFS who have accompanied me over the years. Foremost, I want to thank my post-doc mentors, Sebastian Popp, Federica Ferraro, Arne Scholtissek, and Hendrik Nicolai, for their guidance over the last five years. A special "thanks" goes to Sebastian Popp, who introduced me to the world of flamelet tabulation. Thank you for the many technical tips and tricks and your pragmatic perspective on our research problems. Many thanks to the STFS IT admins, especially Driss Kaddar, for always handling my various informal requests. May the quota be with you! I also want to express my gratitude to my students over the years, especially Max Schneider, who accompanied me for three years as a student and research assistant. I wish you much success in your future endeavors at STFS. Finally, I want to express my gratitude towards my dearest colleagues and friends, Hannes Böttler and Magnus Kircher. It was always a pleasure working with you. Thank you for many formal and informal discussions, many memes shared, numerous card games at Darmstadt's breweries with Julian Bissantz and Vinzenz Schuh and our deep friendship outside of work. I am confident that our friendship will endure beyond our times at STFS.

The final thanks go to my family for their support during my time at the Technical University of Darmstadt. Special thanks to my fiancée, Tabea, the best home-office buddy one could wish for. Thanks for the many walks and window breaks to clear the mind. With your loving and empathetic nature, you have made me a better person!

Publications

P1 Flow Turbul. Combust. 106 (2021), 681–700

M. Steinhausen, Y. Luo, S. Popp, C. Strassacker, T. Zirwes, H. Kosaka, F. Zentgraf, U. Maas, A. Sadiki, A. Dreizler, and C. Hasse. “Numerical Investigation of Local Heat-Release Rates and Thermo-Chemical States in Side-Wall Quenching of Laminar Methane and Dimethyl Ether Flames”. In: *Flow Turbul. Combust.* 106 (2021), 681–700. DOI: 10.1007/s10494-020-00146-w

Author contributions

Tab. P.1: Author contributions to publication [P1] following CRediT [110]

Matthias Steinhausen	Conceptualization of the numerical investigation (equal) Implementation and validation for manifold creation and coupling (lead) Conduction of the numerical investigation (lead) Interpretation and discussion of the numerical and experimental results (lead) Data analysis and visualization Writing – Original draft Main and corresponding author
Yujuan Luo	Generation, validation, and provision of the detailed chemistry simulation data
Sebastian Popp	Conceptualization of the numerical investigation (equal) Implementation and validation for manifold creation and coupling (supporting) Interpretation and discussion of the numerical results (supporting) Supervision (equal)
Christina Strassacker **Ulrich Maas**	Development, implementation, and validation of the REDIM creation Generation, validation, and provision of the data for the REDIM
Thorsten Zirwes	Support with the numerical setup in OpenFOAM
Hidemasa Kosaka **Florian Zentgraf** **Andreas Dreizler**	Design and conduction of the experiment Provision of the experimental data Interpretation and discussion of the experimental results (supporting)
Christian Hasse	Conceptualization of the numerical investigation (equal) Interpretation and discussion of the numerical results (supporting) Supervision (equal) Funding acquisition
All co-authors	Writing – Review & Editing

Use of publication contents in finalized and ongoing dissertations

This publication is part of the ongoing dissertation of Matthias Steinhausen at the Institute for Simulation of reactive Thermo-Fluid Systems at the Technical University of Darmstadt, Germany.

Flow, Turbulence and Combustion (2021) 106:681–700
https://doi.org/10.1007/s10494-020-00146-w

Numerical Investigation of Local Heat-Release Rates and Thermo-Chemical States in Side-Wall Quenching of Laminar Methane and Dimethyl Ether Flames

M. Steinhausen[1] · Y. Luo[1] · S. Popp[1] · C. Strassacker[2] · T. Zirwes[3,4] · H. Kosaka[5] · F. Zentgraf[5] · U. Maas[2] · A. Sadiki[5] · A. Dreizler[5] · C. Hasse[1]

Received: 9 December 2019 / Accepted: 14 April 2020 / Published online: 13 May 2020
© The Author(s) 2020

Abstract
The local heat-release rate and the thermo-chemical state of laminar methane and dimethyl ether flames in a side-wall quenching configuration are analyzed. Both, detailed chemistry simulations and reduced chemistry manifolds, namely Flamelet-Generated Manifolds (FGM), Quenching Flamelet-generated Manifolds (QFM) and Reaction-Diffusion Manifolds (REDIM), are compared to experimental data of local heat-release rate imaging of the lab-scale side-wall quenching burner at Technical University of Darmstadt. To enable a direct comparison between the measurements and the numerical simulations, the measurement signals are computed in all numerical approaches. Considering experimental uncertainties, the detailed chemistry simulations show a reasonable agreement with the experimental heat-release rate. The comparison of the FGM, QFM and REDIM with the detailed simulations shows the high prediction quality of the chemistry manifolds. For the first time, the thermo-chemical state during quenching of a dimethyl ether-air flame is examined numerically. Therefore, the carbon monoxide and temperature predictions are analyzed in the vicinity of the wall. The obtained results are consistent with previous studies for methane-air flames and extend these findings to more complex oxygenated fuels. Furthermore, this work presents the first comparison of the QFM and the REDIM in a side-wall quenching burner.

Keywords Flame-wall interaction · Side-wall quenching · REDIM · FGM · QFM · DME

✉ M. Steinhausen
steinhausen@stfs.tu-darmstadt.de

[1] Simulation of reactive Thermo-Fluid Systems, Technical University of Darmstadt, Otto-Berndt-Str. 2, 64287 Darmstadt, Germany

[2] Institute of Technical Thermodynamics, KIT, Engelbert-Arnold-Str. 4, 76131 Karlsruhe, Germany

[3] Steinbuch Centre for Computing, KIT, Hermann-von-Helmholtz-Platz 1, 76344 Eggenstein-Leopoldshafen, Germany

[4] Engler-Bunte-Institute, Division of Combustion Technology, KIT, Hermann-von-Helmholtz-Platz 1, 76344 Eggenstein-Leopoldshafen, Germany

[5] Reactive Flows and Diagnostics, Technical University of Darmstadt, Otto-Berndt-Str. 3, 64287 Darmstadt, Germany

1 Introduction

In the context of global warming and limited resources, the development of low-emission and high-efficiency combustion applications arises. Additionally, for the transformation to a CO_2-neutral energy system, it is essential to find replacements for fossil fuels like diesel or gasoline. These alternative fuels are produced from biomass or by using H_2 from renewable electricity and CO_2 from the atmosphere and thereby allow for a CO_2-neutral combustion process. Dimethyl ether (DME) is a promising low-emission and environmentally-friendly alternative fuel (Semelsberger et al. 2006) and possesses the potential to become an important fuel in the future since it can be produced from biomass (Fleisch et al. 2012) or H_2 (Matzen and Demirel 2016). Furthermore, for more complex flame configurations, like flame-wall interactions, DME can serve as a starting point for systematic studies of more complex oxygenated fuels.

To optimize current combustors for alternative fuels, a more profound understanding of the main combustion characteristics and especially flame-wall interactions is necessary. Thereby, numerical simulations play an important role. The description of a combustion process in a numerical simulation, however, requires the accurate modeling of the combustion chemistry. The detailed chemistry (DC) simulation solves the conservation equations of all combustion-related species directly. This, however, includes solving a large set of equations and requires a high spatial resolution which restricts the method to generic cases and simple geometries. To simulate technically relevant combustion configurations it is essential to reduce the combustion chemistry. Reduced chemistry approaches based on tabulated manifolds combine the high prediction accuracy of the chemical state of a DC simulation with low computational costs. Due to the numerous benefits of this method, several different approaches exist including FGM (van Oijen and de Goey 2000), FPI (Gicquel et al. 2000), ILDM (Maas and Pope 1992) and REDIM (Bykov and Maas 2007). The methods are based on the pre-calculation of a thermo-chemical state which is stored in a table that is accessed by control parameters. During the simulation, only the transport equations of these control parameters need to be solved to account for the chemical reaction.

Technical combustion systems are enclosed by (cold) walls, hence, the investigation of flame-wall interaction is a relevant research area. In the vicinity of the wall, the thermo-chemical reaction within the flame stagnates, leading to incomplete combustion which results in a lowered efficiency and the formation of pollutants (Poinsot and Veynante 2011). Therefore, flame-wall interaction effects have practical relevance for several thermo-chemical processes, e.g. in internal combustion engines and gas turbines (Dec and Tree 2001; Drake and Haworth 2007; Hyvönen et al. 2005). The importance of flame-wall interactions increases even further with the concept of downsizing in internal combustion engines (Dreizler and Böhm 2015) or lean-burn technologies in aero engines (Lazik et al. 2008).

Detailed investigations of flame-wall interaction are often carried out in generic configurations. Recently, flame-wall interactions in a side-wall quenching (SWQ) geometry were studied experimentally (Jainski et al. 2017a, b; Kosaka et al. 2019, 2018) and numerically (Ganter et al. 2017, 2018; Efimov et al. 2019) for methane-air flames. In the experimental studies of Kosaka et al. (2018, 2019) DME was considered for the first time. The first study (Kosaka et al. 2018) analyzed the near-wall thermo-chemical state of the flames using Coherent anti-Stokes Raman spectroscopy (CARS) for temperature and two-photon laser-induced fluorescence (LIF) of the CO molecule. In a second measurement campaign (Kosaka et al. 2019), the local heat-release rate (HRR) and its correlation with

the flame structure of laminar and turbulent methane-air and DME-air flames in a SWQ geometry were analyzed using HRR imaging with simultaneous OH-LIF and CH_2O-LIF measurements. This work is the first complementary numerical investigation based on these experiments using DC simulations, as well as chemistry manifolds, namely Flamelet-generated Manifolds (FGM), Quenching Flamelet-generated Manifolds (QFM) and Reaction-Diffusion Manifolds (REDIM).

This paper is structured as follows. Section 2 describes the table generation procedure and the computation of the measurement signals. In Sect. 3, the experimental and numerical setups are outlined. Section 4 analyzes the local HRR of a stoichiometric methane-air and DME-air flame. In the first step, the DC simulations are compared to the measurement data using computed signals. Afterwards, the reduced chemistry manifolds FGM, QFM and REDIM are investigated. Finally, the near-wall thermo-chemical state of the flames is discussed in Sect. 5 and conclusions are drawn in Sect. 6.

2 Numerical Methods and Modeling

In this work, DC simulations are compared with approaches using reduced chemistry manifolds, specifically FGM, QFM and REDIM. The DC implementation and the reduced chemistry approaches are described below.

2.1 Detailed Chemistry (DC)

In the DC simulation the laminar flow field is described by the conservation equation for mass and momentum. Neglecting body forces, the equations read

$$\frac{\partial \rho}{\partial t} + \frac{\partial \rho u_j}{\partial x_j} = 0 \,, \tag{1}$$

$$\frac{\partial \rho u_i}{\partial t} + \frac{\partial}{\partial x_j}\left(\rho u_i u_j\right) = \frac{\partial}{\partial x_j}\left(\rho\nu\left(\frac{\partial u_i}{\partial x_j} + \frac{\partial u_j}{\partial x_i}\right) - \frac{2}{3}\rho\nu\frac{\partial u_k}{\partial x_k}\delta_{ij}\right) - \frac{\partial p}{\partial x_i} \,, \tag{2}$$

where ρ is the density, u the flow velocity, p the pressure and ν the kinematic viscosity obtained through Sutherland's law (Saksena and Saxena 1963). The laminar flow is treated as incompressible using the low Mach number assumption. Besides these two equations, a transport equation for each species considered in the reaction mechanism has to be solved. Assuming unity Lewis number for all species, the balance equation reads

$$\frac{\partial \rho Y_k}{\partial t} + \frac{\partial}{\partial x_j}\left(\rho u_j Y_k\right) = \frac{\partial}{\partial x_j}\left(\rho D\frac{\partial Y_k}{\partial x_j}\right) + \dot{\omega}_k \,, \tag{3}$$

where Y_k and $\dot{\omega}_k$ are the mass fraction and the species source term for species k, and D is the diffusion coefficient, respectively. Finally, the transport equation of the enthalpy h as sum of sensible and enthalpy of formation reads

$$\frac{\partial \rho h}{\partial t} + \frac{\partial}{\partial x_j}\left(\rho u_j h\right) = \frac{\partial}{\partial x_j}\left(\rho D\frac{\partial h}{\partial x_j}\right) . \tag{4}$$

For the simulations, the GRI 3.0 mechanism (Smith et al. 1999) (53 species and 325 reactions) and the Zhao mechanism (Zhao et al. 2008) (55 species and 290 reactions) are used for the methane-air and the DME-air flame, respectively.

2.2 Chemistry Manifolds

Three models for the description of mixing-chemistry interaction, namely Flamelet-generated Manifolds (FGM), Quenching Flamelet-generated Manifolds (QFM) and Reaction-Diffusion Manifolds (REDIM), are considered. The manifolds are stored in so-called flamelet look-up tables (FLUTs) based on two control variables: the progress variable and the enthalpy. The latter is important since heat transfer to the wall must be accounted for. Thereby, the thermo-chemical quantities, the source term of the progress variable, and the computed signals are parameterized as a function of enthalpy h and progress variable Y_c

$$\Psi = \Psi\left(h, Y_c\right) . \tag{5}$$

The progress variable Y_c for methane and DME is chosen to be the mass fraction of CO_2, which is consistent with previous studies of flame-wall interactions (Ganter et al. 2017, 2018). The construction of FGM, QFM and REDIM is described in Sects. 2.2.1, 2.2.2 and 2.2.3, respectively.

In a coupled simulation using FLUTs the flow field is described by the mass and momentum transport, see Eqs. (1) and (2), respectively. To account for the chemical processes, additional transport equations for the control variables are solved: The equation for the enthalpy is given in Eq. (4), while for the progress variable the balance equation reads

$$\frac{\partial \rho Y_c}{\partial t} + \frac{\partial}{\partial x_j}\left(\rho u_j Y_c\right) = \frac{\partial}{\partial x_j}\left(\rho D \frac{\partial Y_c}{\partial x_j}\right) + \dot{\omega}_{Y_c} . \tag{6}$$

After solving the transport equations, the progress variables can be used to access the thermo-chemical state stored in the FLUT. All other thermo-chemical quantities, the reaction rate and computed signals (see Sect. 2.3) are retrieved from the tabulated manifold. Figure 1 shows the look-up procedure during a coupled simulation using chemistry manifolds.

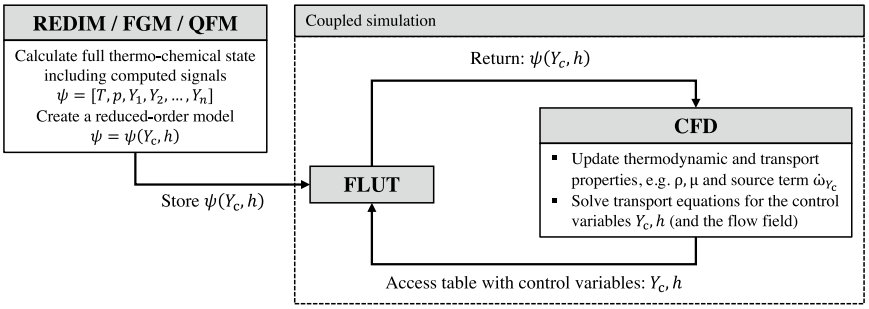

Fig. 1 Illustration of the look-up procedure of a coupled simulation using chemistry manifolds. The full thermo-chemical state is estimated by the chemistry manifold including computed signals and incorporated into a FLUT. During the coupled simulation, the transport equations of the control parameters are solved and the thermodynamic and transport properties are updated by a table look-up during runtime

2.2.1 Flamelet-Generated Manifolds (FGM)

The FGM table generation procedure is detailed in van Oijen and de Goey (2000) and Ketelheun et al. (2013, 2009). The FLUT is based on a series of 1D calculations of adiabatic freely propagating flames. The corresponding simulations are performed with the in-house DC solver ULF (Universal Laminar Flame Solver) (Zschutschke et al. 2017). The wall heat transfer leads to different local enthalpy levels in the flow field that need to be considered during the flamelet generation procedure. The enthalpy variation is realized using exhaust gas recirculation. This approach has been used previously (van Oijen et al. 2016). To change the enthalpy of the specific flamelet, exhaust gases at the temperature of the unburnt gases are mixed with the fresh gas mixture. The enthalpy of the flamelet can be controlled by the ratio between fresh and burned gases. Note that the particular method to generate the different enthalpy levels has only a small influence on the resulting chemistry manifold, mostly because the flame structures do not show significant differences (Fiorina et al. 2003).

2.2.2 Quenching Flamelet-Generated Manifolds (QFM)

QFM are an extension of FGM which account for effects of flame quenching during flame-wall interactions. In contrast to FGM, QFM are based on a transient Head-On Quenching (HOQ) flame, where the flame front of a premixed laminar flame (here methane-air or DME-air) propagates perpendicular to the wall and extinguishes due to heat losses. Thereby, the scalar diffusion due to the enthalpy gradient is incorporated into the chemistry manifold. In this study, a 2D QFM is used that consists of a single transient HOQ simulation performed with the in-house solver ULF. The resulting HOQ solution is a function of the spatial coordinate x and the time t and can be interpolated onto the progress variable/enthalpy space and stored in a two-dimensional FLUT. The tabulation approach is further described in Efimov et al. (2019).

2.2.3 Reaction-Diffusion Manifolds (REDIM)

REDIM are an approach for reduced kinetics that accounts for both chemical reaction and molecular diffusion (Bykov and Maas 2007). It is based on the invariance condition (Gorban and Karlin 2003), and the manifold is generated by solving the REDIM evolution equation

$$\begin{aligned}\frac{\partial \boldsymbol{\Psi}(\boldsymbol{\theta})}{\partial t} &= (I - \boldsymbol{\Psi}_{\theta}(\boldsymbol{\theta})\boldsymbol{\Psi}_{\theta}^{+}(\boldsymbol{\theta})) \cdot \{\boldsymbol{F}(\Psi(\boldsymbol{\theta})) \\ &\quad + \frac{1}{\rho}(\bar{\bar{\boldsymbol{D}}}\boldsymbol{\Psi}_{\theta}(\boldsymbol{\theta})\ \mathrm{grad}\boldsymbol{\theta})_{\theta}\ \mathrm{grad}\boldsymbol{\theta}\}\ ,\end{aligned} \tag{7}$$

to a stationary state (Bykov and Maas 2007). Here, $\boldsymbol{\Psi}$ is the state vector consisting of specific enthalpy, pressure and species, $\bar{\bar{\boldsymbol{D}}}$ is the transport matrix with thermal conductivity and diffusion coefficients, I is the identity matrix, $\boldsymbol{\Psi}_{\theta}(\boldsymbol{\theta})$ is the matrix of partial derivatives of $\boldsymbol{\Psi}$ with respect to $\boldsymbol{\theta}$ and $\boldsymbol{\Psi}_{\theta}^{+}(\boldsymbol{\theta})$ is the Moore-Penrose pseudo-inverse of $\boldsymbol{\Psi}_{\theta}(\boldsymbol{\theta})$, see e.g. Golub and van Loan (1989). $\boldsymbol{\Psi}_{\theta}(\boldsymbol{\theta})$ spans the tangential subspace to the manifold which means that the projection operator $(I - \boldsymbol{\Psi}_{\theta}(\boldsymbol{\theta})\boldsymbol{\Psi}_{\theta}^{+}(\boldsymbol{\theta}))$ projects the vector field consisting

of source term and diffusion term onto the normal subspace of the manifold. Due to this projection, the convective term of the evolution equation is canceled out in the REDIM evolution equation (Bykov and Maas 2007).

Before the REDIM evolution equation is solved, an initial guess and a gradient estimation need to be specified. Both are obtained from a detailed sample solution of a HOQ flame similar to the ones used for QFM. Due to the symmetry of this model system, the model configuration can be assumed to be one-dimensional and the system is described by one spatial coordinate. This means that a one-dimensional gradient estimation is obtained and all assessed states during the transient HOQ-phenomenon are used for the generation of the REDIM. Note that the gradient estimation has only a small influence on the REDIM for FWI. This has been shown in Steinhilber et al. (2017) and Strassacker et al. (2019) where the gradient estimation has been changed drastically while the results of the reduced computations only changed slightly. Therefore, even if the REDIM is generated with the gradient estimation of a HOQ flame, it can be used for computations of the SWQ configuration (Steinhilber et al. 2017; Ganter et al. 2018; Strassacker et al. 2019).

For the parametrization of the initial guess of the manifold, the specific enthalpy as well as the species CO_2 are used. Note that this specification is only important for the generation of the initial guess, not for the integration procedure of the REDIM, because it is scale invariant (Bykov and Maas 2007).

The molecular transport is modeled with equal diffusivities and unity Lewis number. It should be mentioned that this assumption is made for simplicity. The use of more detailed transport models is possible (Maas and Bykov 2011; Strassacker et al. 2018a).

At the boundaries of the REDIM, boundary conditions that allow the REDIM to evolve are applied (Neagos et al. 2017; Strassacker et al. 2018b).

The computed REDIM table contains the source terms and the transport properties that are both projected onto the tangential subspace of the manifold to solve the reduced computation in the generalized coordinates $\boldsymbol{\theta}$. To implement the reduced model equation in physical variables, the REDIM is reparametrized in physical variables and the source term as well as the diffusion coefficients are appropriately reformulated to use them in Eqs. (4) and (6). The progress variables for the look-up, in the following sections referred to as control variables to be consistent with the FGM approach, are chosen to be the progress variable Y_c and the enthalpy h.

2.3 Co-simulation of Computed Signals

For the DC simulations, as well as the reduced manifolds, the OH-LIF and CH_2O-LIF signals are computed based on the numerical thermo-chemical state. For the chemistry manifolds, the signals are incorporated in the FLUT as a function of progress variable and enthalpy. OH (Popp et al. 2015; Hunger et al. 2017) and CH_2O-LIF (Popp et al. 2015) computed signals were used previously. Within these studies a detailed description of the underlying method is given. In this section, the method is briefly introduced.

The OH-LIF signal for the $Q_1(6)$ transition of the $A^2\Sigma^+ \leftarrow X^2\prod^+$ band is calculated for the linear LIF regime with the excited-state decay rate that is dominated by collisional quenching (Kosaka et al. 2019),

$$S_{\text{OH-LIF}} \propto N_{\text{OH}} f_{\text{J}} \frac{A}{A+Q}\,, \tag{8}$$

with N_{OH} being the OH number density, f_J the Boltzmann fraction population of the absorbing state with rotational quantum number J. The spontaneous emission rate is described by A; Q is the total collisional quenching rate of the excited state, which is the sum of the quenching rates for each collisional partner and is dependent on the composition and the local temperature. The total collisional quenching rate is given by

$$Q = N_{\text{tot}} \sum_i X_i \sigma_i \left(\frac{8 k_B T}{\pi \mu_i} \right)^{0.5}, \tag{9}$$

with N_{tot} being the total number density. The parameters k_B, X_i, σ_i and μ_i are the Boltzmann constant, the mole fraction, the quenching cross-section and the reduced mass of the species i, respectively. The quenching cross sections are obtained from Tamura et al. (1998).

The calculation of the CH_2O-LIF signal is very challenging since it involves excitation of overlapping transitions and complex temperature and species-dependent cross sections. The CH_2O-LIF signal is calculated following the methodology described by Kosaka et al. (2019), which goes back to the procedure proposed in Coriton et al. (2015) and Popp et al. (2015). The CH_2O-LIF signal is obtained using Eqs. (8) and (9) with an additional term accounting for the temperature dependence of the quenching cross-sections and the populations of overlapping transitions. The temperature dependence is considered using the same polynomial fit as in the experiments by Kosaka et al. (2019) that is based on spectral simulations using the simulation code AsyrotWin (Birss and Ramsay 1985; Judge and Clouthier 2001). Within the simulations, the transitions near the 339 nm excitation of the $\widetilde{A}^1A_2 \leftarrow \widetilde{X}^1A_1$ system are considered.

3 Experimental and Numerical Setup

Figure 2 shows the setup used in the experimental studies by Kosaka et al. (2018, 2019) that are examined in this work and the numerical subdomain. A homogeneous mixture of dry air and fuel enters the experimental domain from the nozzle at ambient conditions. The Reynolds number is 5.000 based on nozzle exit conditions of the fuel-air jet. The flow passes a rod with a diameter of approximately 1 mm, where a V-flame stabilizes. The left branch of the flame approaches the wall, where the flame is quenched. The wall temperature in the experiments is controlled at the axial position $z = 48$ mm by a bath-thermostat with thermal oil. The wall temperature considered in this work is 330 K. The experimental setup is described in more detail in Kosaka et al. (2019) and Jainski et al. (2017).

In this work two experimental studies are considered. In the first one (Kosaka et al. 2018), Coherent anti-Stokes Raman spectroscopy (CARS) and two-photon laser-induced fluorescence (LIF) of the CO molecule are used to determine the thermo-chemical state of methane-air and DME-air flames with respect to the point-wise gas phase temperatures and CO concentrations. Wall-normal profiles of species concentrations are measured using this technique in order to validate CFD predictions. The second one (Kosaka et al. 2019) focuses on the characterization of the local HRR. Therefore, simultaneous formaldehyde and hydroxyl radical planar laser-induced fluorescence (PLIF) measurements are used. The calculation of the measured signals is described in Sect. 2.3 and incorporated into the numerical simulations.

Following the approach by Ganter et al. (2017, 2018), the simulation domain is reduced to a two-dimensional subdomain which covers approximately 80% of the left flame branch. Consistent with previous studies for the methane-air flame,

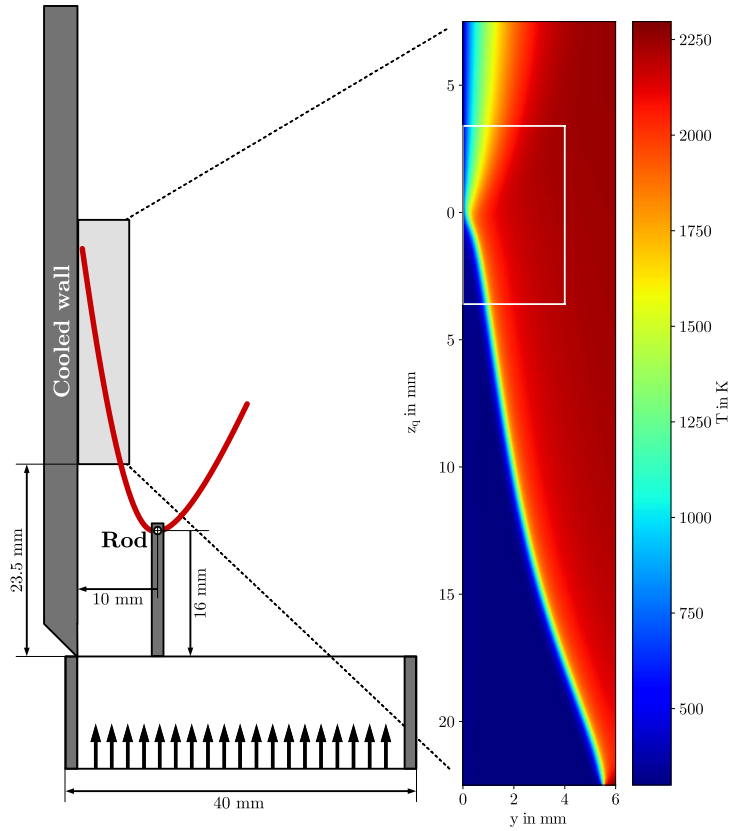

Fig. 2 Illustration of the SWQ burner geometry (left) and the numerical subdomain (right) showing the simulated temperature of the DME case. The coordinate system of the numerical domain is defined relative to the quenching height of the flame. The wall is located at $y = 0$. The area within the white lines in the numerical domain marks the region of the LIF-measurements by Kosaka et al. (2019)

the computational mesh consists of a rectilinear mesh with a uniform grid size of $\Delta = 50$ µm. Due to the reduced flame thickness of the DME-air flame, the grid resolution for the DME simulations is increased towards the wall using a uniform grading. The cell size at the wall is $\Delta = 24$ µm to ensure a sufficient resolution of the flame in the near-wall region. The computational domain is shown on the right in Fig. 2 where the DME case discussed below is displayed. The white lines depict the boundary of the domain of the LIF-measurements performed in Kosaka et al. (2019).

The numerical simulations are performed using a coupled solver using tabulated chemistry manifolds (Popp et al. 2015; Gierth et al. 2018) as well as a DC solver based on OpenFOAM. For the discretization of spatial gradients, an interpolation method from third-degree polynomials is used, while the time is discretized implicitly using the second-order backward Euler method. For all simulations, a Courant-Friedrich-Lewy number of CFL ≈ 0.1 is employed. Since laminar flames are analyzed, the simulation is conducted until a steady solution is obtained.

For all simulations, the wall is assumed to have a constant temperature of 330 K. For the velocity, a no-slip condition is applied, while for the species mass fractions a zero gradient boundary condition is chosen at the wall. At the top and right outlet, zero gradient boundary conditions are applied for enthalpy, species mass fractions, and velocity. Similar to Ganter et al. (2017, 2018), a generic parabolic inflow velocity profile is used. The flame is stabilized by injecting hot exhaust gases at equilibrium conditions in a 0.5 mm wide section of the inlet. The inflow velocity of the hot exhaust gases is set to 3.81 m/s for the methane-air flame to compensate partially for the density difference of the fresh and burned inlet gases. For the DME-air flame the velocity profile of the inlet gases is scaled according to the inflow Reynolds number. For the burned gases a constant velocity of 4.98 m/s is used. The inlet gas mixture temperature and pressure are set to ambient conditions ($T = 300$ K; $p = 1$ atm). The numerical results are analyzed in a relative coordinate system, that uses the quenching point as the origin of the wall-parallel direction. The quenching height is defined based on the OH gradient within the flame which is described in more detail in Ganter et al. (2017).

4 Analysis of the Local Heat-Release Rate

In the following, the DC simulations are compared to the experimental data from Kosaka et al. (2018, 2019) as well as the chemistry manifolds. In this section the local HRR is analyzed as a global flame property starting with a comparison of the DC simulations and the experimental findings. Afterwards, the results obtained using chemistry manifolds are compared to corresponding DC simulations. In Sect. 5, the thermo-chemical state of the flame is analyzed with particular emphasis on the near-wall processes.

4.1 Definition of Heat-Release Rate

In the study by Kosaka et al. (2019), a correlation based on the product of the normalized LIF signals of OH and CH_2O is used to predict the HRR. Based on the product of the measurement signals a normalized local HRR of the flame can be defined

$$\mathrm{HRR}_{\mathrm{exp}} = \frac{\langle S_{\mathrm{OH\text{-}LIF}} \rangle \cdot \langle S_{\mathrm{CH_2O\text{-}LIF}} \rangle}{\max\left(\langle S_{\mathrm{OH\text{-}LIF}} \rangle \cdot \langle S_{\mathrm{CH_2O\text{-}LIF}} \rangle \right)} \tag{10}$$

with $\langle S_{\mathrm{OH\text{-}LIF}} \rangle$ and $\langle S_{\mathrm{CH_2O\text{-}LIF}} \rangle$ being the normalized averaged measured signal intensity of OH and CH_2O, respectively. The product is normalized using the maximum value along the flame front in the lower part of the measurement domain ($z_q < -3$ mm) corresponding to an unstretched flame region. To allow a direct comparison between the DC simulations and the experiments, the above HRR definition is used in both. In the DC simulation the HRR is calculated using computed signals (see Sect. 2.3). The HRR definition was validated in Kosaka et al. (2019) using three different flame configurations (1) an unstretched planar flame (2) a curved and stretched flame and (3) a HOQ configuration. For the first two configurations, the results agree qualitatively with the normalized HRR defined as

$$\mathrm{HRR}_{\mathrm{num}} = \frac{\sum_{i=1}^{N} \dot{\omega}_i h_{f,i}}{\max\left(\sum_{i=1}^{N} \dot{\omega}_i h_{f,i} \right)}, \tag{11}$$

where $\dot{\omega}_i$ is the source term and $h_{f,i}$ is the enthalpy of formation of the species i. For the unsteady HOQ configuration, the HRR correlations agree reasonably well until the point where the flame is quenched at the wall. During the quenching process the radicals in the vicinity of the wall are consumed faster than the HRR declines and the correlation deteriorates (Kosaka et al. 2019). In this work, the validation is extended to the steady SWQ scenario, which will be discussed further for the methane-air flame next.

4.2 Comparison to Experimental Findings

In "Appendix" the flame structure and the specifics of the methane-air and DME-air flame are discussed. Thereby, the fundamental flame characteristics of the two fuels are outlined. In the following, we focus on the local HRR during SWQ. Figure 3 shows the local HRR over the wall-normal direction y and the relative quenching height z_q for the methane case. The experimental results are displayed in subfigure (a), while (b) and (c) correspond to the DC simulation with the HRR definition based on Eqs. (10) and (11), respectively. Additionally, the white line in the Fig. 3c displays the isoline of $\mathrm{HRR_{num}} = 0.05$. The HRR definition used in the experiments $\mathrm{HRR_{exp}}$ is in very good agreement with $\mathrm{HRR_{num}}$ considering HRR values greater than 5% (see Fig. 3b, c). At the edges of the reaction zone, however, the formaldehyde vanishes and the prediction based on $\mathrm{HRR_{exp}}$ deteriorates. These results are consistent with the HOQ scenario analyzed in Kosaka et al. (2019) and extend those findings to the more complex SWQ configuration. Similar results are obtained for the DME-air flame that are not shown here for brevity.

For a consistent comparison with the experimental data, $\mathrm{HRR_{exp}}$ is used. The HRR prediction of the DC simulation in Fig. 3b shows an overall good agreement with the measurements shown in Fig. 3a. Nevertheless, the experimental results show a broader reaction zone. This is particularly evident in the lower part of the flame where the flame structure should correspond to an unperturbed laminar flame. Potential reasons for these differences are (1) the measurement resolution, (2) the measurement uncertainties caused by the image intensifiers, and (3) fluctuations in the instantaneous flame position and flame angle of the laminar flame due to Helmholtz resonances originating from the plenum of the burner.

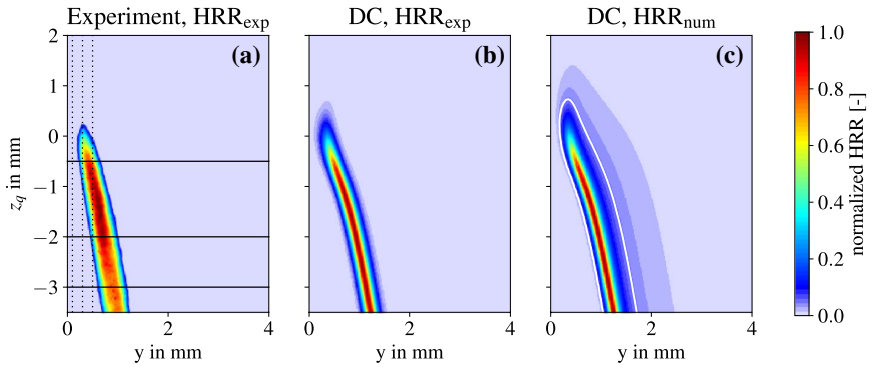

Fig. 3 Local HRR in the methane-air flame. The experimental results are taken from Kosaka et al. (2019). The HRR definitions $\mathrm{HRR_{exp}}$ and $\mathrm{HRR_{num}}$ correspond to Eqs. (10) and (11), respectively. The white isoline in **c** shows a HRR value of 5% of the maximum HRR. The black solid lines in **a** display the wall-normal lines along which the HRR profiles are extracted. The thermo-chemical state that is discussed in Sect. 5 is analyzed along the black dotted lines

Even though these fluctuations are accounted for in the post-processing of the measurements by shifting the individual images vertically on the average quenching point, uncertainties regarding the exact flame position and flame angle remain (Jainski et al. 2017a, b; Kosaka et al. 2018, 2019).

To further investigate potential reasons for the differences in the numerical simulation and the experimental findings, the HRR based on Eq. (10) is analyzed along wall-normal profiles that are shown as black solid lines in Fig. 3a. The obtained HRR profiles are normalized such that the integral of the numerical simulations and the experimental data match. This allows a comparison of the shape of the HRR distribution along the wall normal lines. Then, artificial measurement uncertainties are superimposed onto the simulation results using a box filter with a variable filter width Δ. Since the measurement uncertainties cannot be specified, the use of a box filter presents a worst-case estimation of errors originating from the measurement uncertainties. Figure 4 displays the corresponding profiles of the methane case in a coordinate system relative to the HRR peak. While in the undisturbed part of the flame the HRR peak position differs by over 200 µm, in the near-wall region the shift vanishes. Therefore, the thermo-chemical state during quenching is unaffected by this shift.

The filtering of the signals leads to a broadening of the HRR profile in the y-direction. In the unperturbed part of the flame ($z_q = -3$ mm), a filter width of $\Delta > 300$ µm is necessary to match the width of the experimental profile. With decreasing distance from the quenching height, however, the required filter width decreases. In the vicinity of the quenching height ($z_q = -0.5$ mm), a filter with of $\Delta = 200$ µm is sufficient. Assuming remaining uncertainties in the flame angle in the post-processed measurement results, the measurement uncertainty would increase with increasing distance from the quenching point, since the spatial distortion increases proportionally with the distance. This leads to an increasing filter width with increasing distance to the quenching height.

Figure 5 shows the corresponding HRR profiles of the DME case. In contrast to the methane-air flame, the DC simulation of the DME case predicts the thickness of the HRR profile in the undisturbed part of the flame satisfactorily using a filter width of $\Delta \approx 250$ µm. Additionally, the position of the HRR peak in the numerical simulations of the DME-air flame is shifted between 60 µm and 140 µm to larger wall distances over the whole flame

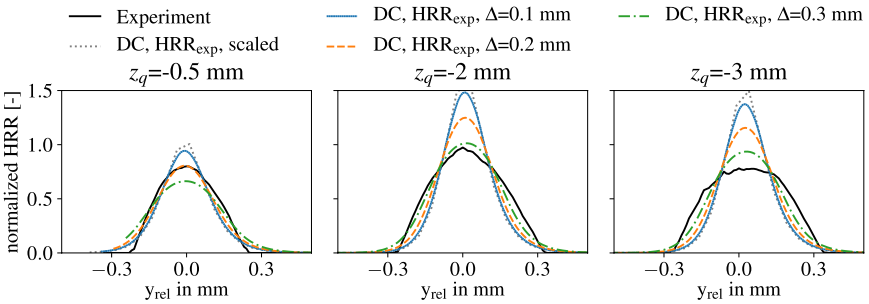

Fig. 4 Local HRR profiles of the methane-air flame based on HRR$_{exp}$ [see Eq. (10)]. The experimental results are taken from Kosaka et al. (2019). The profiles are extracted along wall-normal lines at different heights z_q that are displayed as black solid lines in Fig. 3a. The extracted profiles are scaled to match the integral of the experimental signal. The obtained signal is filtered using a box filter with variable filter widths Δ. The numerical profiles are shifted towards the wall by $\Delta_y = 50$ µm, 225 µm and 250 µm for $z_q = -0.5$ mm, −2 mm and −3 mm, respectively

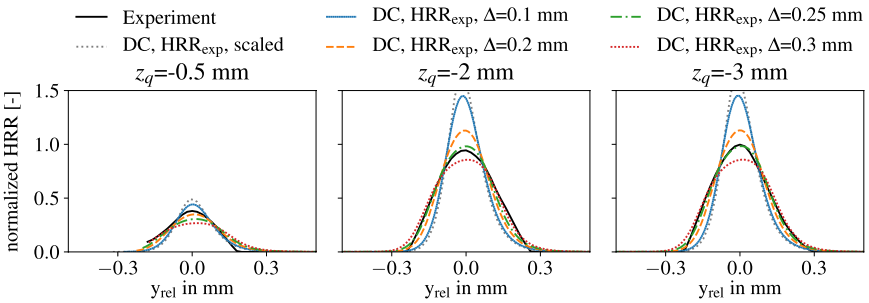

Fig. 5 Local HRR profiles of the DME-air flame based on HRR$_{exp}$ [see Eq. (10)]. The experimental results are taken from Kosaka et al. (2019). The profiles are extracted along wall-normal lines at different heights z_q that are displayed as black solid lines in Fig. 3a. The extracted profiles are scaled to match the integral of the experimental signal. The obtained signal is filtered using a box filter with variable filter widths Δ. The numerical profiles are shifted towards the wall by $\Delta_y = 140$ µm, 115 µm and 60 µm for $z_q = -0.5$ mm, −2 mm and −3 mm, respectively

front. Other than in the methane case, the shift does not decrease in the near-wall region ($\Delta_y = 140$ µm). The thermo-chemical state that is discussed in Sect. 5 shows a similar shift. Even though great care has been taken to determine the exact distance to the wall in the experiments, thermal disturbances and beam steering, that affect the determination of the horizontal position of the wall, cannot be avoided. The resulting uncertainties lie in the range of the deviations.

Compared to the methane-air flame (Fig. 4), the DME-air flame shows a thinner HRR zone in the undisturbed part of the flame. This is related to the flame thickness of a stochiometric DME-air flame compared to a methane-air flame and can already be observed in a simple freely propagating flame, see "Appendix" for further detail. During quenching, the HRR peak decreases, while the width of the HRR zone is unaffected by the quenching process. It is interesting to note that the different flame thickness of the methane-air and DME-air flame during quenching can be explained by fuel characteristics that can already be observed in very simple flame configurations, like a freely propagating flame.

Finally, Fig. 6a, b display the 2D profiles of the unfiltered and filtered HRR using a filter width of $\Delta = 300$ µm and $\Delta = 250$ µm for the methane-air and DME-air flame, respectively. The filtered and unfiltered signals agree reasonably well with the measurement data. Based on the discussion above, filtered signals result in a thickened HRR profile in the undisturbed part of the flame which better reflect the measurement results. This finding, however, does not imply that the measurement resolution is only Δ, rather we believe that the potential reasons (1)-(3) are responsible for the experimentally observed broadening. As mentioned above, the agreement between the experiment and simulation deteriorates with increasing distance from the quenching height for the methane case. This could be related to the fluctuations in the instantaneous flame position.

4.3 Prediction of the Heat-Release Rate Using Tabulated Manifold Approaches

While in the previous section DC simulations for the HRR were compared to experimental data, in the following the suitability of manifold-based approaches to predict the near-wall HRR, is investigated. Therefore, the manifold-based approaches are compared to their corresponding DC simulations. The HRR definition used for the comparison is based on Eq. (11).

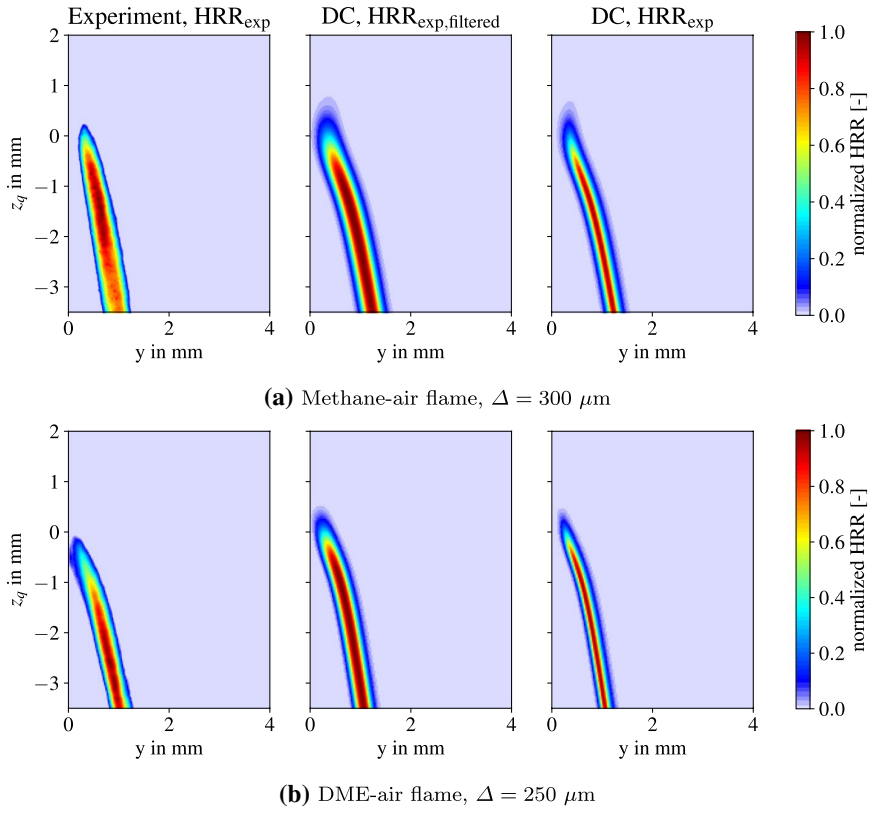

Fig. 6 2D plot of the local HRR based on HRR$_{exp}$ [see Eq. (10)]. In the figure, the experimental results (left) and two versions of the DC simulations, filtered (middle) using a box filter with the filter width Δ and unfiltered (right) are shown. The experimental results are taken from Kosaka et al. (2019)

Figure 7 displays the obtained results for the methane-air (top) and DME-air (bottom) flame along wall-normal lines. For both fuels, FGM, QFM and REDIM compare favorably with the DC results. This is not a trivial finding, since within the near-wall region the enthalpy level in the flame varies due to heat transfer to the wall. These different enthalpy levels in the flame are considered in the manifolds by using the enthalpy as a control variable of the FLUT. The agreement of the manifolds with the DC simulations reveals, that the manifolds, even though they use different approaches to obtain the thermo-chemical state, are suitable to predict the HRR in the near-wall region and thereby to account for the enthalpy losses to the wall. This is consistent with previous findings that showed a good prediction quality for the tabulation strategies regarding global flame properties in methane-air flames (Ganter et al. 2017, 2018; Efimov et al. 2019).

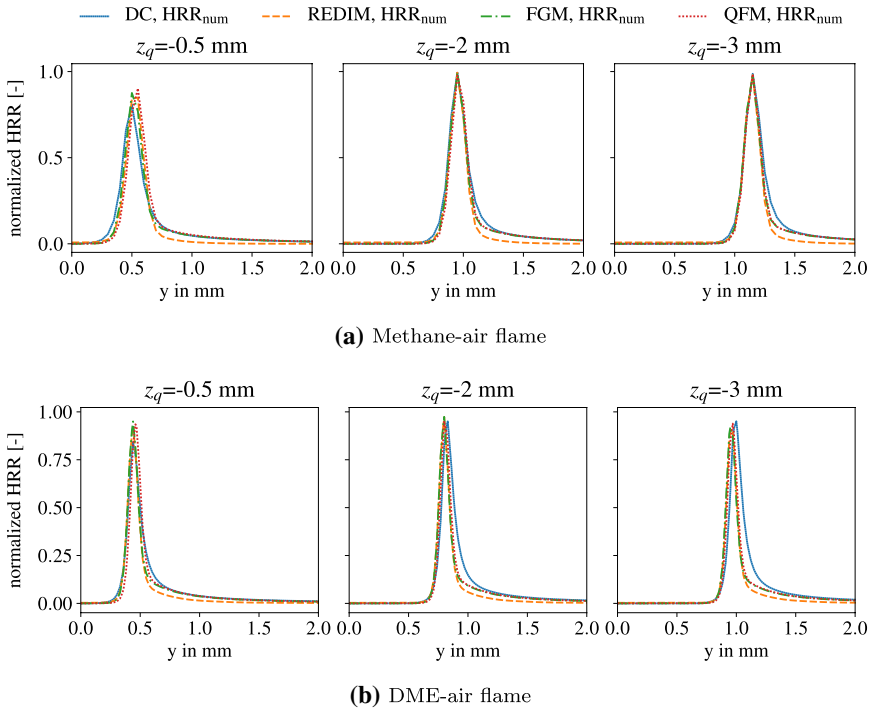

Fig. 7 Local HRR profiles based on the HRR definition HRR$_{num}$ [see Eq. (11)] for the DC, REDIM, FGM and QFM simulation. The profiles are extracted along wall-normal lines at different heights z_q that are displayed as black solid lines in Fig. 3a

5 Analysis of the Thermo-Chemical State

In this section, the thermo-chemical state of the flames is analyzed. The thermo-chemical state, specifically looking at CO and temperature, of methane-air flames in the SWQ burner was discussed previously in various studies (Ganter et al. 2017, 2018; Efimov et al. 2019). Thereby laminar flames and different tabulation strategies were considered. This is the first study for DME-air flames in the SWQ configuration.

5.1 Comparison to Experimental Findings

The numerical simulations of the methane-air flame conducted here, confirm the observations published in the previous studies and, therefore, are not shown for brevity. In the following we focus on the DC simulation of the DME-air flame by first comparing with the available experimental data. Afterwards, the suitability of the chemistry manifolds to describe the near-wall thermo-chemical state is analyzed. The analysis is performed using FGM, QFM, an extension of FGM, and REDIM. The latter two have been specifically designed to model the thermo-chemical state during flame-wall interactions (Strassacker et al. 2018a, b; Efimov et al. 2019). Note, as stated above, REDIM are not very sensitive with respect to the gradient estimation.

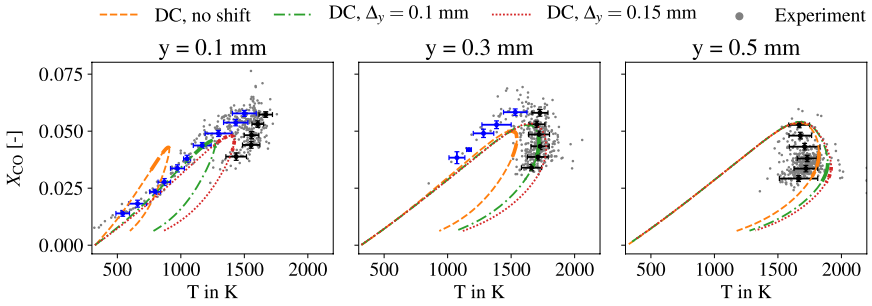

Fig. 8 Thermo-chemical state of the DME-air flame at different axial positions. The measurement data previously reported in Kosaka et al. (2018) is shown as scatter together with the conditional mean and the standard deviation separated into a CO formation (blue) and oxidation branch (black). In addition, the DC simulation results are plotted along wall-parallel lines for different axial shifts Δ_y. The thick part of the DC lines corresponds to an area ±200 µm around the quenching height. The wall-parallel lines are displayed as dotted black lines in Fig. 3a. Here, the shifted wall-parallel lines are not displayed

In the experimental study by Kosaka et al. (2018) (see also Sect. 3) the thermo-chemical state of the flame was characterized using the CO concentration from CO-LIF measurements and the temperature based on CARS. Figure 8 shows the thermo-chemical state for the DME-air flame at wall distances of $y = 0.1$ mm, $y = 0.3$ mm and $y = 0.5$ mm along a wall-normal line at quenching height. The experimental data is shown as scatter. The conditional mean as well as the standard deviation is included, separated into a CO formation (blue dots) and a CO oxidation (black dots) branch, based on the CO-T probe volume position. As mentioned previously, the flame tip is not stationary in the experiments, but it fluctuates around the quenching point reported to be in the range of ±200 µm (Kosaka et al. 2018). These flame tip fluctuations are not present in the DC simulations. To allow a comparison with the experimental data, the CO-T state of the DC simulation is plotted along wall-parallel lines. Thereby, the flame fluctuations are captured, since both, the CO formation, as well as the oxidation branch, are crossed. The thick solid part of the lines corresponds to the area ±200 µm around the quenching height. Even though the majority of the points lies within this range, it seems that the measurement uncertainty of the flame tip position is higher than anticipated in the near-wall region ($y = 0.1$ mm and $y = 0.3$ mm). Similar observations were made in a recent numerical study of the SWQ burner (Zirwes et al. 2019). Therefore, the numerical results are plotted also over the entire simulation domain.

Additionally, as discussed in the previous section, the analysis of the local HRR reveals a deviation between the measurement data and the simulations results regarding the wall-normal position of the HRR peak of around 140 µm. This difference in the flame position effects the thermo-chemical state of the flame. To asses the sensitivity of the wall-normal flame distance to the wall on the thermo-chemical state, the extraction lines of the DC simulations are shifted in wall-normal direction by 100 µm and 150 µm. While the region far away from the wall ($y = 0.5$ mm) shows a small sensitivity, the near-wall region is strongly affected by uncertainties in the wall position. This demonstrates the high complexity of the near-wall diagnostics, since on the one hand, the thermo-chemical state is very sensitive to the wall-normal position, on the other hand, the measurements very close to the wall are especially challenging. After correcting for

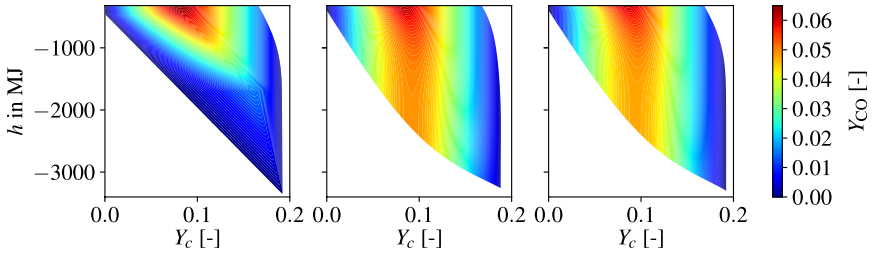

Fig. 9 Mass fraction of CO for FGM (left), QFM (middle) and REDIM (right) shown in the enthalpy progress variable space

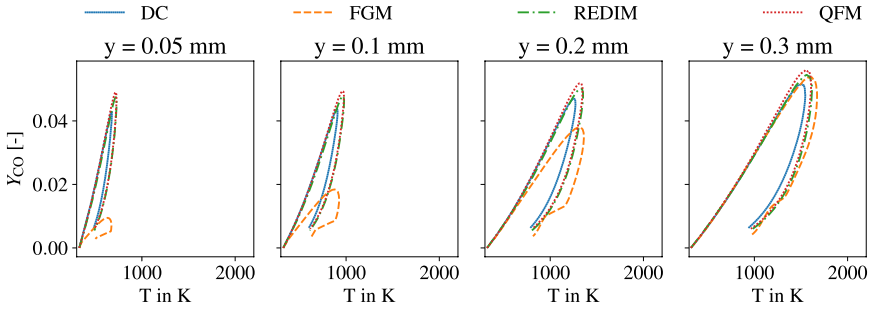

Fig. 10 Thermo-chemical state of the DME-air flame for the DC simulation, REDIM and FGM at different axial positions. The extracted lines are parallel to the black dotted lines displayed in Fig 3a

the observed shift, the DC results achieve good agreement with the experimental data in the near-wall region ($y = 0.1$ mm and $y = 0.3$ mm).

5.2 Prediction of the Thermo-Chemical State Using Tabulated Manifold Approaches

In the following, near-wall CO predictions for the reduced chemistry manifolds, namely FGM, QFM and REDIM, are compared and analyzed. Thereby, the DC simulations serve as a reference solution. While FGM are based on a series of freely propagating flames with different enthalpy levels, QFM and REDIM are based on a transient 1D HOQ simulation, see Sect. 2. Diffusive effects in enthalpy direction that are not captured in the FGM tabulation can be accounted for. Figure 9 shows the CO mass fraction in the enthalpy progress variable space for the chemistry manifolds. While QFM and REDIM do not show significant differences, FGM predict a lower CO concentration in the near-wall region (left boundary). It is interesting to note that QFM as well as REDIM lead to a similar thermo-chemical state, even though the table generation procedure differs between the two methods.

In Fig. 10, the tabulated chemistry simulations are compared with the DC simulation results for different wall distances. In the undisturbed region of the flame ($y > 0.3$ mm) the FGM prediction is of comparable accuracy to REDIM and QFM. All manifolds over-predict the CO concentration of the flame slightly. In the near-wall region, however, the FGM prediction, deteriorates with decreasing wall-normal distance. This is caused by diffusive

effects in enthalpy direction that are not captured by the FGM creation procedure described in Sect. 2.2.1. Similar observations were made for methane-air flames in previous studies (Strassacker et al. 2018b; Ganter et al. 2017, 2018; Efimov et al. 2019). As mentioned above, QFM and REDIM are able to capture these effects and, hence, show a significantly improved prediction of the CO concentration at the wall. While, the peak CO concentration is still over-predicted. This is evident in the near-wall region and the undisturbed part of the flame. Efimov et al. (2019) showed (for methane-air) that even though the species diffusion in the direction of the enthalpy gradient is included in an HOQ configuration, its rate might be over-predicted leading to an increased CO concentration in the vicinity of the wall. This is caused by the rate of heat loss to the wall which is up to a factor of two lower in the SWQ scenario compared to HOQ. To model these effects, a third control variable accounting for the varying heat transfer rate to the wall could be introduced in future REDIM tabulations or QFM (Efimov et al. 2019).

6 Conclusion

This work is the first comparison of experimental and numerical data of local HRR imaging in an SWQ configuration of methane-air and DME-air flames considering DC simulations and reduced chemistry simulations using FGM, QFM and REDIM. Additionally, the thermo-chemical state during quenching of a DME-air flame is analyzed with respect to the prediction of carbon monoxide and temperature in the near-wall region. Previously, this was only performed for other fuels, especially methane. The main conclusions are as follows:

1. The HRR definition based on the normalized product of OH-LIF and CH_2O-LIF signals used in the measurements shows very good agreement with a HRR definition based on the species source term and the enthalpy of formation for HRR>5% in the SWQ configuration.
2. The experimental HRR results are compared to DC simulations using computed signals. Measurement uncertainties are superimposed on the numerical simulation which results in a favorable comparison with the experiments.
3. The normalized HRR prediction using reduced chemistry manifolds, namely FGM, QFM and REDIM, are in very good agreement with the DC simulations.
4. The thermo-chemical state shows a high sensitivity towards the wall-normal position of the flame in the near-wall region.
5. In the numerical simulations, the DME-air flame burns further away from the wall. This shift is observed in the measurement of the HRR profiles, as well as in the thermo-chemical state of the flame. Correcting for the shift, the thermo-chemical states of the DC simulations show satisfactory agreement with the experimental results.
6. FGM show a systematic prediction deficiency of the near-wall CO concentration, while REDIM and QFM are able to capture the thermo-chemical state more accurately. REDIM and QFM do not show a significant difference regarding the CO prediction capability. This extends previous findings for methane-air flames. This is the first direct comparison of QFM and REDIM.

Overall, the combined analysis of experimental and numerical data for the HRR using computed signals allows for a direct comparison with the measurements, including

measurement uncertainties. The analysis of different chemistry manifolds shows consistent trends with previous studies using methane-air flames, however, these findings have now been extended to more complex oxygenated fuels such as DME.

Acknowledgements Open Access funding provided by Projekt DEAL. Funded by the Deutsche Forschungsgemeinschaft (DFG, German Research Foundation)—Projektnummer 237267381—TRR 150

Compliance with Ethical Standards

Conflicts of interest The authors declare that they have no conflict of interest.

Open Access This article is licensed under a Creative Commons Attribution 4.0 International License, which permits use, sharing, adaptation, distribution and reproduction in any medium or format, as long as you give appropriate credit to the original author(s) and the source, provide a link to the Creative Commons licence, and indicate if changes were made. The images or other third party material in this article are included in the article's Creative Commons licence, unless indicated otherwise in a credit line to the material. If material is not included in the article's Creative Commons licence and your intended use is not permitted by statutory regulation or exceeds the permitted use, you will need to obtain permission directly from the copyright holder. To view a copy of this licence, visit http://creativecommons.org/licenses/by/4.0/.

Appendix: Flame Structure of Freely Propagating Methane-Air and DME-Air Flames

Figure 11 displays the thermo-chemical structure of a freely propagating methane-air (left) and DME-air (right) flame under stoichiometric conditions calculated under unity Lewis number assumption. The DME-air flame has a higher burning velocity and a decreased flame thickness. Using the definition of the thermal flame thickness based on the temperature gradient in Poinsot and Veynante (2011), the flame thickness of the displayed methane-air and DME-air flame are 0.5 mm and 0.4 mm, respectively. The DME-air flame has an overall increased fuel and CO_2 mass fraction and shows steeper gradients. A similar observation can be made for CO and OH. As a result of the more complex fuel structure, the combustion of DME produces a higher amount of

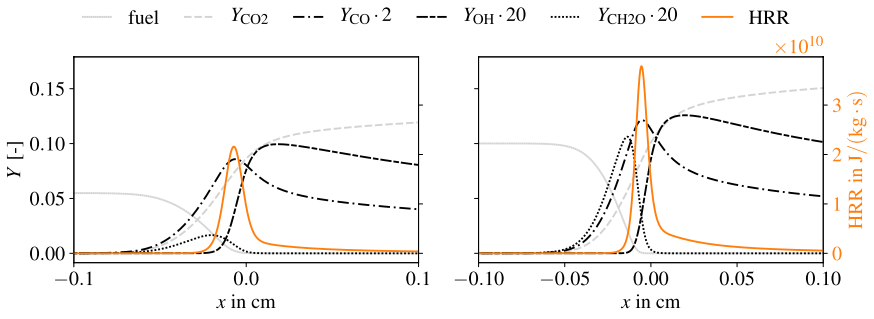

Fig. 11 Flame structure of a freely propagating methane-air (left) and DME-air (right) flame. The species mass fractions of major species are shown in grey, minor species in black and the local HRR of the flame is shown in orange. The mass fraction of CO is multiplied by a factor of 2, while CH_2O and OH are multiplied by 20

hydrocarbons, which is apparent in the amount of formaldehyde that is by a factor of 6 higher in the DME-air flame.

In addition to the species mass fractions, the local HRR defined as $\mathrm{HRR} = -\sum_{i=1}^{N} \dot{\omega}_i h_{f,i}$ is shown in Fig. 11. The DME-air flame shows a higher local HRR rate and steeper gradients compared to the methane-air flame. Similar observations can be made in the SWQ configuration, where the DME-air flame has a thinner and steeper HRR zone in the undisturbed part of the flame, see e.g. Figs. 4 and 5 on the right. The characteristics in the unperturbed part of the flame can also be observed in the near-wall region of the two flames.

References

Birss, F., Ramsay, D.: Computer assistance in the analysis of molecular spectra: I. Rotational structure of high resolution singlet–singlet bands. Comput. Phys. Commun. **38**(1), 83–112 (1985)

Bykov, V., Maas, U.: The extension of the ILDM concept to reaction–diffusion manifolds. Combust. Theor. Model. **11**(6), 839–862 (2007)

Coriton, B., Zendehdel, M., Ukai, S., Kronenburg, A., Stein, O.T., Im, S.K., Gamba, M., Frank, J.H.: Imaging measurements and LES-CMC modeling of a partially-premixed turbulent dimethyl ether/air jet flame. Proc. Combust. Inst. **35**, 1251–1258 (2015)

Dec, J.E., Tree, D.R.: Diffusion-flame/wall interactions in a heavy-duty DI diesel engine. SAE Trans. **110**, 1599–1617 (2001)

Drake, M.C., Haworth, D.C.: Advanced gasoline engine development using optical diagnostics and numerical modeling. Proc. Combust. Inst. **31**, 99–124 (2007)

Dreizler, A., Böhm, B.: Advanced laser diagnostics for an improved understanding of premixed flame–wall interactions. Proc. Combust. Inst. **35**, 37–64 (2015)

Efimov, D.V., de Goey, P., van Oijen, J.A.: QFM: quenching flamelet-generated manifold for modelling flame–wall interactions. Combust. Theory Model. **24**, 72–104 (2019)

Fiorina, B., Baron, R., Gicquel, O., Thevenin, D., Carpentier, S., Darabiha, N.: Modelling non-adiabatic partially premixed flames using flame-prolongation of ILDM. Combust. Theor. Model. **7**(3), 449–470 (2003)

Fleisch, T.H., Basu, A., Sills, R.A.: Introduction and advancement of a new clean global fuel: the status of DME developments in China and beyond. J. Nat. Gas Sci. Eng. **9**, 94–107 (2012)

Ganter, S., Heinrich, A., Meier, T., Kuenne, G., Jainski, C., Rißmann, M.C., Dreizler, A., Janicka, J.: Numerical analysis of laminar methane–air side-wall-quenching. Combust. Flame **186**, 299–310 (2017)

Ganter, S., Straßacker, C., Kuenne, G., Meier, T., Heinrich, A., Maas, U., Janicka, J.: Laminar near-wall combustion: analysis of tabulated chemistry simulations by means of detailed kinetics. Int. J. Heat Fluid Flow **70**, 259–270 (2018)

Gicquel, O., Darabiha, N., Thévenin, D.: Laminar premixed hydrogen/air counterflow flame simulations using flame prolongation of ILDM with differential diffusion. Proc. Combust. Inst. **28**(2), 1901–1908 (2000)

Gierth, S., Hunger, F., Popp, S., Wu, H., Ihme, M., Hasse, C.: Assessment of differential diffusion effects in flamelet modeling of oxy-fuel flames. Combust. Flame **197**, 134–144 (2018)

Golub, G.H., van Loan, C.F.: Matrix Computation. Technical report, Baltimore (1989)

Gorban, A.N., Karlin, I.V.: Method of invariant manifold for chemical kinetics. Chem. Eng. Sci. **58**(21), 4751–4768 (2003)

Hunger, F., Zulkifli, M.F., Williams, B.A., Beyrau, F., Hasse, C.: Comparative flame structure investigation of normal and inverse turbulent non-premixed oxy-fuel flames using experimentally recorded and numerically predicted Rayleigh and OH-PLIF signals. Proc. Combust. Inst. **36**(2), 1713–1720 (2017)

Hyvönen, J., Haraldsson, G., Johansson, B.: Operating Conditions Using Spark Assisted HCCI Combustion During Combustion Mode Transfer to SI in a Multi-cylinder VCR-HCCI Engine. SAE Technical Paper (2005)

Jainski, C., Rißmann, M., Böhm, B., Dreizler, A.: Experimental investigation of flame surface density and mean reaction rate during flame–wall interaction. Proc. Combust. Inst. **36**(2), 1827–1834 (2017a)

Jainski, C., Rißmann, M., Böhm, B., Janicka, J., Dreizler, A.: Sidewall quenching of atmospheric laminar premixed flames studied by laser-based diagnostics. Combust. Flame **183**, 271–282 (2017b)

Judge, R., Clouthier, D.J.: AsyrotWin: a 32-bit Windows version of Asyrot, A program for the analysis of high resolution singlet-singlet band spectra of asymmetric tops. Comput. Phys. Commun. **135**(3), 293–311 (2001)

Ketelheun, A., Kuenne, G., Janicka, J.: Heat transfer modeling in the context of large eddy simulation of premixed combustion with tabulated chemistry. Flow Turbul. Combust. **91**(4), 867–893 (2013)

Ketelheun, A., Olbricht, C., Hahn, F., Janicka, J.: Premixed Generated Manifolds for the Computation of Technical Combustion Systems. Volume 2: Combustion, Fuels and Emissions. Turbo Expo: Power for Land, Sea, and Air, pp. 695–705 (2009)

Kosaka, H., Zentgraf, F., Scholtissek, A., Bischoff, L., Häber, T., Suntz, R., Albert, B., Hasse, C., Dreizler, A.: Wall heat fluxes and CO formation/oxidation during laminar and turbulent side-wall quenching of methane and DME flames. Int. J. Heat Fluid Flow **70**(January), 181–192 (2018)

Kosaka, H., Zentgraf, F., Scholtissek, A., Hasse, C., Dreizler, A.: Effect of flame–wall interaction on local heat release of methane and DME combustion in a side-wall quenching geometry. Flow Turbul. Combust. **104**, 1029–1046 (2019)

Lazik, W., Doerr, T., Bake, S., v. d. Bank, R., Rackwitz, L.: Development of Lean-Burn Low-NOx Combustion Technology at Rolls-Royce Deutschland. Volume 3: Combustion, Fuels and Emissions, Parts A and B, pp. 797–807 (2008)

Maas, U., Bykov, V.: The extension of the reaction/diffusion manifold concept to systems with detailed transport models. Proc. Combust. Inst. **33**(1), 1253–1259 (2011)

Maas, U., Pope, S.B.: Simplifying chemical kinetics: intrinsic low-dimensional manifolds in composition space. Combust. Flame **88**, 239–264 (1992)

Matzen, M., Demirel, Y.: Methanol and dimethyl ether from renewable hydrogen and carbon dioxide: alternative fuels production and life-cycle assessment. J. Clean. Prod. **139**, 1068–1077 (2016)

Neagos, A., Bykov, V., Maas, U.: Adaptive hierarchical construction of reaction–diffusion manifolds for simplified chemical kinetics. Proc. Combust. Inst. **36**(1), 663–672 (2017)

Poinsot, T., Veynante, D.: Theoretical and Numerical Combustion, 3 edn. RT Edwards, Inc., (2011)

Popp, S., Hunger, F., Hartl, S., Messig, D., Coriton, B., Frank, J.H., Fuest, F., Hasse, C.: LES flamelet-progress variable modeling and measurements of a turbulent partially-premixed dimethyl ether jet flame. Combust. Flame **162**, 3016–3029 (2015)

Saksena, M.P., Saxena, S.: Viscosity of multicomponent gas mixtures. In: Proceedings of the 6th Symposium on Thermophysical Properties, vol. 31, pp. 100–110 (1963)

Semelsberger, T.A., Borup, R.L., Greene, H.L.: Dimethyl ether (DME) as an alternative fuel. J. Power Sources **156**, 497–511 (2006)

Smith, G.P., Golden, D.M., Frenklach, M., Moriarty, N.W., Eiteneer, B., Goldenberg, M., Bowman, C.T., Hanson, R.K., Song, S., Gardiner, W.C.J., Lissianski, V.V., Qin, Z.: GRI 3.0 reaction mechanism. http://www.me.berkeley.edu/grimech (1999). Accessed Oct 2019

Steinhilber, G., Bykov, V., Maas, U.: REDIM reduced modeling of flame–wall-interactions: quenching of a premixed methane/air flame at a cold inert wall. Proc. Combust. Inst. **36**(1), 655–661 (2017)

Strassacker, C., Bykov, V., Maas, U.: REDIM reduced modeling of flame quenching at a cold wall—the influence of detailed transport models and detailed mechanisms. Combust. Sci. Technol. **191**(2), 208–222 (2018)

Strassacker, C., Bykov, V., Maas, U.: REDIM reduced modeling of quenching at a cold wall including heterogeneous wall reactions. Int. J. Heat Fluid Flow **69**(January), 185–193 (2018)

Strassacker, C., Bykov, V., Maas, U.: Comparitive analysis of reaction–diffusion manifold based reduced models for head-on- and side-wall-quenching flames. In: Combustion Symposium (2019). Publication submitted

Tamura, M., Berg, P.A., Harrington, J.E., Luque, J., Jeffries, J.B., Smith, G.P., Crosley, D.R.: Collisional quenching of CH(A), OH(A), and NO(A) in low pressure hydrocarbon flames. Combust. Flame **114**, 502–514 (1998)

van Oijen, J.A., Donini, A., Bastiaans, R.J., ten Thije Boonkkamp, J.H., de Goey, L.P.: State-of-the-art in premixed combustion modeling using flamelet generated manifolds. Prog. Energy Combust. Sci. **57**, 30–74 (2016)

van Oijen, J.A., de Goey, L.P.: Modelling of premixed laminar flames using flamelet-generated manifolds. Combust. Sci. Technol. **161**(1), 113–137 (2000)

Zhao, Z., Chaos, M., Kazakov, A., Dryer, F.L.: Thermal decomposition reaction and a comprehensive kinetic model of dimethyl ether. Int. J. Chem. Kinet. **40**, 1–18 (2008)

Zirwes, T., Häber, T., Zhang, F., Kosaka, H., Dreizler, A., Steinhausen, M., Hasse, C., Suntz, R., Bockhorn, H., Trimis, D.: Numerical and Experimental Investigation of Chemiluminescent Radical Concentrations During Side-Wall Quenching. Flow, Turbulence and Combustion (2019). Publication submitted

Zschutschke, A., Messig, D., Scholtissek, A., Hasse, C.: Universal Laminar Flame Solver (ULF). figshare (2017). https://figshare.com/articles/ULF_code_pdf/5119855/2

P2 Int. J. Heat Fluid Flow 93 (2022), 108913

M. Steinhausen, T. Zirwes, F. Ferraro, S. Popp, F. Zhang, H. Bockhorn, and C. Hasse. “Turbulent Flame-Wall Interaction of Premixed Flames Using Quadrature-based Moment Methods (QbMM) and Tabulated Chemistry: An a Priori Analysis”. In: *Int. J. Heat Fluid Flow* 93 (2022), 108913. DOI: 10.1016/j.ijheatfluidflow.2021.108913

Author contributions

Tab. P.2: Author contributions to publication [P2] following CRediT [110]

Matthias Steinhausen	Conceptualization of the numerical setup and investigation (equal) Development of the Conditional Quadrature Method of Moments (CQMOM) closure for turbulence-chemistry interaction in near-wall flows (lead) Implementation of the CQMOM closure Interpretation and discussion of the numerical results (lead) Data analysis and visualization Data curation Writing – Original draft Main and corresponding author
Thorsten Zirwes	Conduction of the detailed numerical simulation (lead) Provision of the detailed numerical simulation data
Federica Ferraro **Sebastian Popp**	Development of the CQMOM closure (supporting) Interpretation and discussion of the numerical results (supporting) Supervision (equal)
Feichi Zhang	Conduction the detailed numerical simulation (support) Provision of the computational resources
Henning Bockhorn	Supervision (T. Zirwes, F. Zhang) Interpretation and discussion of the numerical results (supporting)
Christian Hasse	Conceptualization of the numerical setup and investigation (equal) Supervision (equal) Funding acquisition
All co-authors	Writing – Review & Editing

Use of publication contents in finalized and ongoing dissertations

This publication is part of the ongoing dissertation of Matthias Steinhausen at the Institute for Simulation of reactive Thermo-Fluid Systems at the Technical University of Darmstadt, Germany.

International Journal of Heat and Fluid Flow 93 (2022) 108913

Contents lists available at ScienceDirect

International Journal of Heat and Fluid Flow

journal homepage: www.elsevier.com/locate/ijhff

Turbulent flame-wall interaction of premixed flames using Quadrature-based Moment Methods (QbMM) and tabulated chemistry: An *a priori* analysis

M. Steinhausen [a,*], T. Zirwes [b,c], F. Ferraro [a], S. Popp [a], F. Zhang [c], H. Bockhorn [c], C. Hasse [a]

[a] Simulation of Reactive Thermo-Fluid Systems, Technical University of Darmstadt, Otto-Berndt-Str. 2, 64287 Darmstadt, Germany
[b] Steinbuch Centre for Computing, Karlsruhe Institute of Technology, Hermann-von-Helmholtz-Platz 1, 76344 Eggenstein-Leopoldshafen, Germany
[c] Engler-Bunte-Institute, Karlsruhe Institute of Technology, Engler-Bunte-Ring 7, 76131 Karlsruhe, Germany

ARTICLE INFO

Keywords:
Quadrature-based Moment Methods
Flame-wall interaction
Turbulent premixed flame
Direct Numerical Simulation (DNS)
Turbulent side-wall quenching

ABSTRACT

Presumed probability density function (PDF) and transported PDF methods are commonly applied to model the turbulence chemistry interaction in turbulent reacting flows. However, little focus has been given to the turbulence chemistry interaction PDF closure for flame-wall interaction. In this study, a quasi-DNS of a turbulent premixed, stoichiometric methane-air flame ignited in a fully developed turbulent channel flow undergoing side-wall quenching is investigated. The objective of this study is twofold. First, the joint PDF of the progress variable and enthalpy that needs to be accounted for in turbulence chemistry interaction closure models is analyzed in the quasi-DNS configuration, both in the core flow and the near-wall region. Secondly, a transported PDF closure model, based on a Conditional Quadrature Method of Moments approach, and a presumed PDF approach are examined in an *a priori* analysis using the quasi-DNS as a reference both in the context of Reynolds-Averaged Navier Stokes (RANS) and Large-Eddy Simulations (LESs). The analysis of the joint PDF demonstrates the high complexity of the reactive scalar distribution in the near-wall region. Here, a high correlation between the progress variable and enthalpy is found, where the flame propagation and quenching are present simultaneously. The transported PDF approach presented in this work, based on the Conditional Quadrature Method of Moments, accounts for the moments of the joint PDF of progress variable and enthalpy coupled to a Quenching-Flamelet Generated Manifold. In the *a priori* analysis both turbulence chemistry interaction PDF closure models show a high accuracy in the core flow. In the near-wall region, however, only the Conditional Quadrature Method of Moments approach is suitable to predict the flame structures.

1. Introduction

In most industrial systems the combustion takes place in a vessel to allow the generation of power. In the vessel, flames develop in the vicinity of walls and interact with them, leading to flame-wall interactions (FWIs) that lower the overall combustion efficiency, impact the pollutant formation (Poinsot and Denis, 2005) and can also lead to undesired flame behavior, such as flame flashback (Fritz et al., 2001). In turbulent FWIs, turbulence increases the complexity even further.

Numerical simulations of turbulent flames in the close vicinity of walls pose two major challenges. First, the thermochemical reactions inside the flame that are influenced by heat losses to the (cold) walls need to be considered and, secondly, it is necessary to account for the fluctuations of the reactive scalars caused by the turbulence. In direct numerical simulations (DNSs) of turbulent FWI (Gruber et al., 2010; Ahmed et al., 2021), typically, finite-rate chemistry is used to model the reactions in the flame, while the fluctuations of the reactive scalars are resolved by the simulation. This, however, leads to high computational costs and is not suitable for real combustion applications. Here, Reynolds-Averaged Navier Stokes (RANS) or Large-Eddy Simulations (LESs) are employed that use reduced or tabulated chemistry approaches and require turbulence chemistry interaction (TCI) closure models to account for the unresolved fluctuations of the reactive scalars. In the context of tabulated chemistry approaches, chemistry manifolds for FWI have been studied extensively (van Oijen and de Goey, 2000; Ganter et al., 2017, 2018; Strassacker et al., 2019; Efimov et al., 2019;

* Corresponding author.
E-mail address: steinhausen@stfs.tu-darmstadt.de (M. Steinhausen).

https://doi.org/10.1016/j.ijheatfluidflow.2021.108913
Received 31 July 2021; Received in revised form 2 December 2021; Accepted 2 December 2021
Available online 29 December 2021
0142-727X/© 2021 Elsevier Inc. All rights reserved.

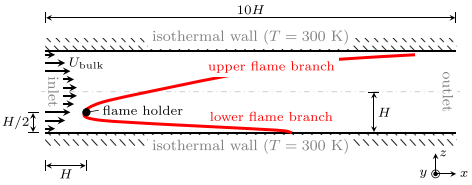

Fig. 1. 2D sketch of the reactive quasi-DNS. The flame is depicted in red and the boundaries of the domain are labeled in gray. In the lateral direction (y) the channel width is $3H$ and the flow is assumed to be statistically independent, hence, periodic boundary conditions are applied. (For interpretation of the references to color in this figure legend, the reader is referred to the web version of this article.)

Steinhausen et al., 2021) using mostly experiments of premixed, laminar methane-air flames (Jainski et al., 2017a; Jainski et al., 2017b; Kosaka et al., 2018, 2019) as a reference. These manifolds have also been applied for the simulation of turbulent flames using RANS (Fiorina et al., 2005) and LES (Heinrich et al., 2018a,b; Wu and Ihme, 2015).

For the TCI closure, multiple approaches are reported in the literature. In the context of this work, TCI closure models for the joint probability density function (PDF) are discussed. In these PDF based methods the unresolved fluctuations of the reactive scalars are modeled by their statistical behavior that is captured in a PDF in the context of RANS and a filtered density function (FDF) in the context of LES. In presumed PDF (pPDF) approaches, the PDF shape is assumed and parameterized by low order moments, e.g. the mean and the variance. They have been applied in multiple studies of turbulent premixed flames (Fiorina et al., 2005; Bray et al., 2006; Jin et al., 2008; Fiorina et al., 2010; Salehi et al., 2013; Donini et al., 2017; Zhang et al., 2021) also considering enthalpy losses in the flame using a β-PDF for the progress variable and a δ-peak for the enthalpy (Fiorina et al., 2005; Donini et al., 2017; Zhang et al., 2021). However, it is only in (Fiorina et al., 2005) that the focus is particularly on FWI. In transported PDF (tPDF) models the whole (joint) PDF is solved for during runtime and the statistical behavior of the unresolved fluctuations is represented by a one-point, one-time joint PDF of relevant flow variables (Muradoglu et al., 1999). Different Monte-Carlo methods were established to solve the high-dimensional PDF efficiently. The Lagrangian approach (Pope, 1981) models the PDF transport equation by the evolution of a large set of stochastic particles, while the Eulerian stochastic fields (SF) approach (Valiño, 1998) solves for a set of stochastic fields. Both Lagrangian and Eulerian PDF methods are constructed such that their one-point one-time joint PDF corresponds to that of a real turbulent reacting system (Haworth, 2010). Using these methods, non-premixed (Jones and Prasad, 2010; Cao and Pope, 2005; Ferraro et al., 2019), partially premixed (Jones and Navarro-Martinez, 2009) and premixed flames (Avdić et al., 2016; Tirunagari and Pope, 2016) have been simulated.

A computationally more efficient approach to solve PDF-based systems is the Method of Moments. In contrast to the Monte-Carlo methods, a set of integral PDF properties, i.e., its moments, are solved. The Method of Moments has been successfully applied to various applications, including nano-particles and aerosols (McGraw, 1997), sprays (Pollack et al., 2016) and combustion-related problems, such as soot formation (Salenbauch et al., 2019; Wick et al., 2017; Ferraro et al., 2021). For the closure of the joint PDF, similarly to Monte-Carlo transported PDF methods, the Method of Moments was primarily applied to turbulent non-premixed flames (Raman et al., 2006; Tang et al., 2007; Koo et al., 2011; Jaishree and Haworth, 2012; Donde et al., 2012; Madadi Kandjani, 2017). In (Pollack et al., 2021), the Quadrature Method of Moments (QMOM) (McGraw, 1997) was applied to premixed turbulent flames. In the study, the thermochemical state ϕ is reconstructed from a chemistry manifold f as a function of the progress variable Y_c, i.e. $\phi = f(Y_c)$. Closure of the joint PDF reduces to a univariate representation of the PDF, in this case for the progress variable Y_c. The QMOM approach showed similar accuracy to previous Monte-Carlo simulations while reducing the computational costs.

As outlined above, TCI in premixed flames has been studied extensively, however, the closure of the joint PDF for FWI has received little attention. This work focuses on the analysis and modeling of the joint PDF of the progress variable and enthalpy in the context of turbulent FWI. A quasi-DNS of a stoichiometric methane-air flame ignited in a fully developed turbulent channel flow is performed. Note that the term quasi-DNS (Zirwes et al., 2020) indicates that all scales in the region of interest are resolved (Kolmogorov length, flame thickness, y^+), but the convergence-order of the numerical schemes are limited to fourth-order for spatial schemes and second-order for the time discretization. The setup is inspired by the DNS of a hydrogen-air flame by Gruber et al. (2010). Using the quasi-DNS data, both the marginal PDFs/FDFs of the progress variable and enthalpy and their joint PDF/FDF are analyzed in the context of RANS/LES and the unresolved fluctuations in the near-wall region are taken into particular consideration. The open question posed in (Fiorina et al., 2005) of the statistical independence of the progress variable and enthalpy in the close vicinity of the wall is addressed, giving useful insights for closure models of the joint PDF in the context of FWI. Based on these insights, a novel tPDF approach is presented and compared to a pPDF approach from the literature (Fiorina et al., 2005; Donini et al., 2017; Zhang et al., 2021). The tPDF closure model is an extension of the work of Pollack et al. (2021). It couples the joint PDF of the progress variable and enthalpy using a Conditional QMOM (CQMOM) approach (Cheng et al., 2010) with a Quenching-Flamelet Generated Manifold (QFM) (Efimov et al., 2019). The suitability of the CQMOM closure is assessed by means of an *a priori* analysis (Bray et al., 2006; Jin et al., 2008).

In the first part of this work, the quasi-DNS of the generic side-wall quenching configuration is introduced. Then, the chemistry manifold employed in this work is presented together with the novel CQMOM approach for the closure of the joint PDF. Using the quasi-DNS data the PDFs/FDFs of the progress variable and enthalpy are analyzed in the context of RANS/LES. In the second part, the CQMOM approach is evaluated in an *a priori* analysis with a special focus on the near-wall region and how it differs from the core region with unconstrained flame propagation.

2. Quasi-DNS of a turbulent side-wall quenching configuration

The generic side-wall quenching case analyzed in this work is inspired by Gruber et al. (2010). A V-shaped, premixed stoichiometric methane-air flame anchored in a fully developed turbulent channel flow is simulated. Fig. 1 shows a sketch of the quasi-DNS setup. At the inlet the unburnt stoichiometric methane-air mixture at $T = 300$ K enters the channel with an inflow velocity corresponding to a fully developed channel flow at a flow Reynolds number of $\mathrm{Re} = (U_{\mathrm{bulk}} H)/\nu \approx 2770$, with U_{bulk} being the mean flow velocity, H the channel half-width and ν the dynamic viscosity. This corresponds to $\mathrm{Re}_\tau = H/\delta_\nu = 180$, with $\delta_\nu = \nu \cdot \sqrt{\rho/\tau_w}$ being the viscous length scale, ρ the density of the unburnt methane-air mixture and τ_w the wall shear stress. The mean inflow velocity is chosen to be $U_{\mathrm{bulk}} = 4.4\ \mathrm{ms}^{-1}$, leading to a channel half-width of $H = 10$ mm. The flame is anchored at $H/2$ above the bottom wall inside the core flow of the channel. The flame holder is not modeled as a physical object (i.e. a wall-boundary in the simulation), but instead simply as a cylindrical region ($r = 0.09 \cdot H$) of burnt gas temperature. Because of this, the influence of the numerical flame holder on the flow field is given by thermal expansion and thus acceleration of the flow. A similar flame anchor has also been used in previous studies (Gruber et al., 2010). At the flame holder a V-shaped flame is formed that propagates through the turbulent boundary layer to the isothermal channel walls ($T_{\mathrm{wall}} = 300$ K), where it finally quenches.

The quasi-DNS consists of two parts: a non-reactive simulation of the

Table 1
Numerical setup of the reactive case.

Parameter	Property
Gas mixture	Stoichiometric methane-air flame
Reaction mechanism	Reduced CRECK (Ranzi et al., 2012)
Species diffusion model	Unity Lewis number transport
Dimensions ($x \times y \times z$)	100 mm × 30 mm × 20 mm
Flame anchor position (axial, wall-normal)	(10 mm, 5 mm)
Flame anchor radius	0.9 mm
Mean inflow velocity	4.4 ms^{-1}
Gas inlet temperature	300 K
Wall temperature	300 K
Reynolds number	2770

turbulent channel flow to generate appropriate turbulent inflow conditions and a reactive simulation of the V-shaped flame. The simulation domain of the non-reactive case is a channel with a length of $14H$, $3H$ and $2H$ in stream-wise (x), lateral (y) and wall-normal (z) direction, respectively. The flow is periodic in stream-wise and lateral direction, with a no-slip boundary condition applied at the walls. The computational mesh consists of 60 million hexahedral cells and is refined towards the walls, with a minimum grid size of 25 µm or $y^+ = 0.24$. The inflow velocity fields at the boundary are stored at an interval corresponding to the simulation time step of 3 µs and serve as an inflow condition for the reactive case. In the reactive simulation, the channel dimensions match the non-reactive counterpart, except for the channel length, which is reduced to $10H$. The computational mesh consists of 200 million cells (purely hexahedral, orthogonal mesh) refined towards the bottom wall with a minimum grid size of 12 µm at the wall in the wall-normal direction or $y^+ = 0.14$. In this region, the Kolmogorov length scale η has a minimum value of 45 µm and the laminar flame thickness of the methane-air flame is

$$\delta_L = \frac{T_{\text{burnt}} - T_{\text{unburnt}}}{\max\left(\frac{\delta T}{\delta x}\right)} \approx 0.5 \text{ mm}, \tag{1}$$

ensuring a sufficient grid resolution. The fine resolution near the bottom wall is not motivated by the resolution of the Kolmogorov length or the flame thickness, but by the sufficient resolution of the FWI zone, because the flame can move as close as 100 µm toward the cold wall (Zirwes et al., 2021a). In the center of the domain (height of 1 cm), the wall-normal resolution is 100 µm and the Kolmogorov length at that position is 150 µm. The velocity fields at the inlet boundary generated by the inert channel flow simulation are spatially and temporally interpolated to the inlet boundary face at every time step of the reactive simulation, which is about $\Delta t = 0.3$ µs or CFL $= 0.15$. In the lateral direction, periodic boundary conditions are applied. At the outlet a zero-gradient boundary condition is used for the velocity and the reactive scalars, while a Dirichlet boundary condition is employed for the pressure. The molecular diffusion coefficients for all species are assumed to be equal using a unity Lewis number assumption. The employed reaction mechanism is a reduced version of the CRECK mechanism (Ranzi et al., 2012) consisting of 24 species and 165 chemical reactions. The most important parameters of the numerical setup of the reactive simulation are summarized in Table 1. Fig. 2 shows the instantaneous flame front of the reactive simulation, depicted by the $Y_{CO_2} = 0.1$ isoline.

The quasi-DNS are performed with an in-house solver (Zirwes et al., 2017, 2018) implemented in the open-source CFD code OpenFOAM (Weller et al., 2017), Version v1712. The solver uses finite-rate chemistry and was validated to be suitable for quasi-DNS in (Zirwes et al., 2017) using multiple DNS reference cases from the literature. The spatial discretization is based on a fourth-order interpolation scheme, and a second-order fully implicit backward scheme is used for the temporal discretization. The solver was used successfully for quasi-DNS of turbulent flames, examples are reported in (Zirwes et al., 2020; Hansinger et al., 2020; Zirwes et al., 2021b). The reactive quasi-DNS was averaged over the duration of 20 flow trough times $20 \cdot (10H)/U_{\text{bulk}} \approx 20 \cdot 0.02$ s. The simulations were performed on approximately 32,000 cores and more than 18 million core-h were consumed.

3. Modeling of turbulent flames using chemistry manifolds

In the context of turbulent combustion modeling using chemistry manifolds two major challenges need to be tackled; (i) a suitable chemistry manifold needs to be found that is able to reproduce the flame structure, and (ii) a TCI closure model is necessary that accounts for the unresolved contributions of the reactive scalars, which in this particular context is the closure of the joint PDF. While the generation of a suitable manifold for FWI has been addressed in multiple studies of laminar (Ganter et al., 2017, 2018; Strassacker et al., 2019; Efimov et al., 2019) and turbulent (Heinrich et al., 2018a,b; Wu and Ihme, 2015) flames, the TCI closure in the close vicinity of the wall has received less attention. This work focuses primarily on the closure of the joint PDF, hence, a state-of-the-art manifold is used. Its suitability is demonstrated in Appendix B.

The remainder of this section first introduces the manifold used in this work. Then, the modeling approaches for unresolved contributions of the reactive scalars are discussed in the context of both RANS and LES. Finally, the coupled CQMOM closure model employed in this work is presented.

3.1. Chemistry manifolds for FWI

Chemistry manifolds for FWI have been validated in multiple studies of laminar side-wall quenching flames (Ganter et al., 2018; Steinhausen et al., 2021; Strassacker et al., 2019) using detailed chemistry simulations and experiments. However, a comparison of the tabulated thermochemical states of the manifolds with a (quasi-)DNS of a turbulent side-wall quenching flame has not been investigated, yet. In this work,

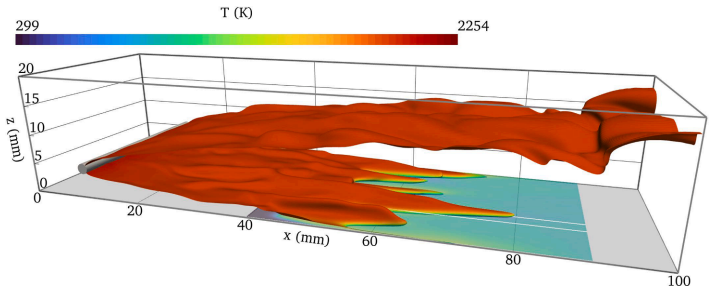

Fig. 2. Snapshot of the reactive flow simulation. The flame surface is visualized by the iso-contour of $Y_{CO_2} = 0.1$ and colored by temperature. The flame holder is indicated by the gray cylinder. At $z = 0$ mm the wall is shown in gray. The simulation domain is shown as a gray bounding box. The slice close to the bottom wall corresponds to the area depicted in Fig. 6 and is colored by temperature. (For interpretation of the references to color in this figure legend, the reader is referred to the web version of this article.)

a two-dimensional Quenching Flamelet-Generated Manifold (QFM) (Efimov et al., 2019) is used, a state-of-the-art manifold for FWI. It consists of a single, transient head-on quenching simulation and a series of preheated, one-dimensional freely propagating flames that extend the manifold at the upper enthalpy range. The simulation results are mapped on the normalized progress variable-enthalpy space $\phi = \phi(C,H)$, with the normalized enthalpy H and progress variable C given by

$$H = \frac{h - h_{\min}}{h_{\max} - h_{\min}}, \tag{2}$$

$$C = \frac{Y_c - Y_{c,\min}(H)}{Y_{c,\max}(H) - Y_{c,\min}(H)}. \tag{3}$$

In the equation above, $h_{\min}$ and $h_{\max}$ are the minimum and maximum enthalpy in the chemistry manifold, respectively, while $Y_{c,\min}(H)$ and $Y_{c,\max}(H)$ are the minimum and maximum progress variable for a given enthalpy level. The progress variable Y_c is defined as the mass fraction of CO_2. Further details regarding the thermochemical manifold and the table generation can be found in (Steinhausen et al., 2021; Efimov et al., 2019). The suitability of the manifold for turbulent side-wall quenching flames is studied in Appendix B.

3.2. Closure of the joint PDF in the context of RANS and LES

In the context of RANS/LES averaged/filtered balance equations are solved. Thereby, the local fluctuations and turbulent structures are integrated into mean/filtered quantities and do not need to be resolved in the simulation (Vervisch and Veynante, 2002). In the simulation of turbulent reacting flows instead of the commonly used Reynolds-average usually a Favre-average (mass-weighted) is used. In this work, the notation from Vervisch and Veynante (2002) is employed, with $\overline{Q}$ and Q' denoting the Reynolds mean and fluctuations of a quantity Q, respectively, while $\widetilde{Q}$ and Q'' correspond to the Favre-averaged counterparts. In the context of RANS, the averaging corresponds to a temporal average. Note that in the investigated channel flow, the temporal averaging is additionally performed in the statistical independent lateral direction. In the context of LES, a spatial filter operation is performed using a box filter. A detailed description of the operations performed in the context of RANS and LES can be found in Appendix A.

To capture the correct behavior of the turbulent flame, the unresolved fluctuations of the reactive scalars can be described by their joint probability density function (PDF) that accounts for the temporal statistic in the flow in the context of RANS and the filtered density function (FDF) that considers the spatial fluctuations in the context of LES. For the two-dimensional QFM employed in this work the bivariate PDF/FDF of the progress variable and enthalpy needs to be accounted for. In the following, both PDF and FDF are denoted by $\widetilde{P}$. Given the PDF/FDF $\widetilde{P}(Y_c, H)$ of the progress variable Y_c and normalized enthalpy H a mean/filtered quantity $\widetilde{Q}$ can be calculated in the context of RANS/LES

$$\widetilde{Q} = \int_{Y_c}\int_{H} f_Q(Y_c,H)\widetilde{P}(Y_c,H)dY_c dH. \tag{4}$$

Here f_Q is a function that describes the dependency of Q on the progress variable and normalized enthalpy (i.e. the thermochemical manifold) and $\widetilde{P}$ denotes the Favre-weighted PDF/FDF, which can be determined from the non-density weighted PDF/FDF P as

$$\widetilde{P}(Y_c,H) = \frac{\rho}{\overline{\rho}} P(Y_c,H). \tag{5}$$

3.3. Closure of the joint PDF with CQMOM

The Quadrature Method of Moments (QMOM) (McGraw, 1997) is based on Gaussian quadrature and approximates the unclosed integrals in the moment transport equations containing the unknown PDF/FDF. The approximation is accurate up to the order $2N-1$ with N being the number of integration nodes employed. In this work, a Conditional Quadrature Method of Moments (CQMOM) (Cheng et al., 2010) is employed to model the moments of the bivariate PDF/FDF $\widetilde{P}(Y_c,H)$; this represents an extension of the standard (univariate) QMOM approach (McGraw, 1997) to multivariate PDFs/FDFs based on the concept of a conditional PDF/FDF (Yuan and Fox, 2011), i.e. the bivariate PDF/FDF is given as

$$\widetilde{P}(Y_c,H) = \widetilde{P}(Y_c)P(H|Y_c), \tag{6}$$

where $\widetilde{P}(Y_c)$ is the marginal PDF/FDF of the progress variable and $P(H|Y_c)$ indicates the conditional PDF/FDF of the normalized enthalpy for a given value of the progress variable. The CQMOM uses a set of primary ϕ_α and secondary (conditional) $\phi_{\alpha;\beta}$ nodes to approximate the joint PDF. The subscript α hereby describes the index of the primary direction, while $(\alpha;\beta)$ reads as index β of the secondary direction for a given index in the primary direction α. In the approximation, for each N_α nodes in the primary direction, N_β nodes in the secondary direction are defined that model the conditional PDF/FDF $P(H|Y_c)$. Thus, a single node in secondary direction implies that for every integration node in primary direction a single integration node in secondary direction is used. In this work, the primary and secondary (conditional) direction correspond to the progress variable Y_c and normalized enthalpy H, respectively. The integral approximation can be written as

$$\int_{\mathscr{R}_\psi} q(\phi_\alpha,\phi_{\alpha;\beta})\widetilde{P}(\phi_\alpha,\phi_{\alpha;\beta})d\phi_\alpha d\phi_{\alpha;\beta} \approx \sum_{\alpha=1}^{N_\alpha}\sum_{\beta=1}^{N_\beta} w_\alpha w_{\alpha;\beta} q(\phi_\alpha,\phi_{\alpha;\beta}), \tag{7}$$

with w_α and $w_{\alpha;\beta}$ being the primary and conditional weights of the bivariate PDF/FDF and $q(\phi_\alpha,\phi_{\alpha;\beta})$ containing all terms except the PDF/FDF itself. Using $q(\phi_\alpha,\phi_{\alpha;\beta}) = \phi_\alpha^k \phi_{\alpha;\beta}^l$ yields the moment definition

$$\widetilde{m}_{k,l} = \int_{\mathscr{R}_\psi} \phi_\alpha^k \phi_{\alpha;\beta}^l \widetilde{P}(\phi_\alpha,\phi_{\alpha;\beta})d\phi_\alpha d\phi_{\alpha;\beta} \approx \sum_{\alpha=1}^{N_\alpha}\sum_{\beta=1}^{N_\beta} w_\alpha w_{\alpha;\beta}\phi_\alpha^k \phi_{\alpha;\beta}^l. \tag{8}$$

To perform the moment conversion (calculation of integration nodes and weights) a system of moments is used that is solved for in a coupled CFD simulation. To reach a fully determined system of moments for the bivariate PDF/FDF, a minimum of $2{\cdot}N_\alpha$ primary moments and $N_\alpha{\cdot}(2{\cdot}N_\beta - 1)$ conditional moments are necessary. For additional information on the system of moments, the reader is referred to (Marchisio and Fox, 2013). The nodes and weights of the PDF/FDF are computed using a two-stage Wheeler algorithm that is described in (Wheeler, 1974; Marchisio and Fox, 2013). First, the primary nodes ϕ_α are computed corresponding to the progress variable direction. The results are then used to calculate the nodes of the conditional moments in the enthalpy direction $\phi_{\alpha;\beta}$. Finally, the PDF/FDF is represented as a weighted sum of Dirac delta functions

$$\widetilde{P}(Y_c,H) \approx \sum_{\alpha=1}^{N_\alpha}\sum_{\beta=1}^{N_\beta} w_\alpha w_{\alpha;\beta}\delta(Y_c - \phi_\alpha)\delta(H - \phi_{\alpha;\beta}). \tag{9}$$

Note that in the equation above, the PDF/FDF is modeled using a conditional PDF/FDF in the secondary direction, since the nodes in the secondary (conditional) direction are defined for every primary node separately, indicated by the subscript $(\alpha;\beta)$. An integral quantity $\widetilde{Q}$, can then be approximated by

$$\widetilde{Q} \approx \sum_{\alpha=1}^{N_\alpha}\sum_{\beta=1}^{N_\beta} w_\alpha w_{\alpha;\beta} f_Q(\phi_\alpha,\phi_{\alpha;\beta}). \tag{10}$$

In a coupled simulation, the algorithm presented in (Madadi Kandjani, 2017; Fox, 2018; Pollack et al., 2021) can be used to solve the moment transport equations.

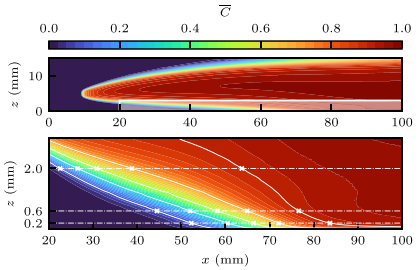

Fig. 3. Contour plot of the time-averaged normalized progress variable $\overline{C}$ (top) and a zoomed image of the near-wall region (bottom). The white rectangle in the top plot shows the magnified region in the bottom. In the zoomed image, the iso-contours of $\overline{C} = [0.1, 0.3, 0.5, 0.7, 0.9]$ are shown as solid lines. The dash-dotted lines correspond to $z = [0.2, 0.6, 2]$ mm. The markers indicate the extraction points for the PDFs that are shown in Fig. 4. (For interpretation of the references to color in this figure legend, the reader is referred to the web version of this article.)

4. PDFs and FDFs in the context of flame-wall interaction

In the following, the particular challenges of the closure of the joint PDF in the context of FWI are examined. First, the joint PDF of the progress variable and enthalpy to be modeled in the context of RANS is examined for various wall distances. Secondly, selected FDFs at specific flame positions are discussed in the context of LES.

4.1. Analysis of the joint PDF in the context of RANS

To calculate the joint PDF the quasi-DNS is sampled with a time-step of $\Delta t = 2.5{\cdot}10^{-4}$ s over the duration of two flow-through times (0.04 s). Additionally, the data is averaged over the statistically independent lateral channel dimension. The PDF is extracted at different positions (x_i, z_i) defined by the wall-normal distance and a stream-wise location:

- **Wall-normal distance (z):** Different wall-normal distances are examined to investigate the impact of wall-heat losses on the joint PDF.
- **Stream-wise location (x):** Different stream-wise locations are extracted to analyze the influence of the reaction progress on the PDF. The stream-wise location is defined for every wall-normal position, separately, and is based on the time-averaged normalized progress variable $\overline{C}$.

Fig. 3 shows a contour plot of the time-averaged normalized progress variable $\overline{C}$ (top) and a zoomed image of the near-wall region (bottom). In the zoomed image the sample positions for data extraction are indicated by the markers and the wall-normal extraction heights are shown as dash-dotted lines. Note that for the methane-air flame ($\delta_L \approx 0.5$ mm) investigated in this work the wall distance normalized by the laminar flame thickness z/δ_L is equivalent to approximately twice the wall distance z.

Fig. 4 shows the extracted temporal joint PDFs of the progress variable and normalized enthalpy and their respective marginal PDFs at the figure borders for the progress variable (top) and normalized enthalpy (right). First, the joint PDFs are discussed with respect to the wall distance. Therefore, the isoline $\overline{C} = 0.5$ is considered and the plots are analyzed from the core flow (top) to the close vicinity of the wall (bottom). In the core flow ($z = 2.0$ mm, top row), the flame is unaffected by enthalpy losses to the wall and a univariate PDF solely dependent on the progress variable can be observed, i.e. the enthalpy is constant as expected for a unity Lewis number case. With decreasing wall distance, the PDF shape changes. Due to enthalpy losses to the wall the PDF becomes bivariate varying with both progress variable and enthalpy. At $z = 0.6$ mm (middle row), only high values of the progress variable ($Y_c > 0.1$) are significantly affected by the wall heat losses, showing a decrease in normalized enthalpy. In these regions, the PDF broadens in enthalpy direction. For lower progress variables ($Y_c < 0.1$), however,

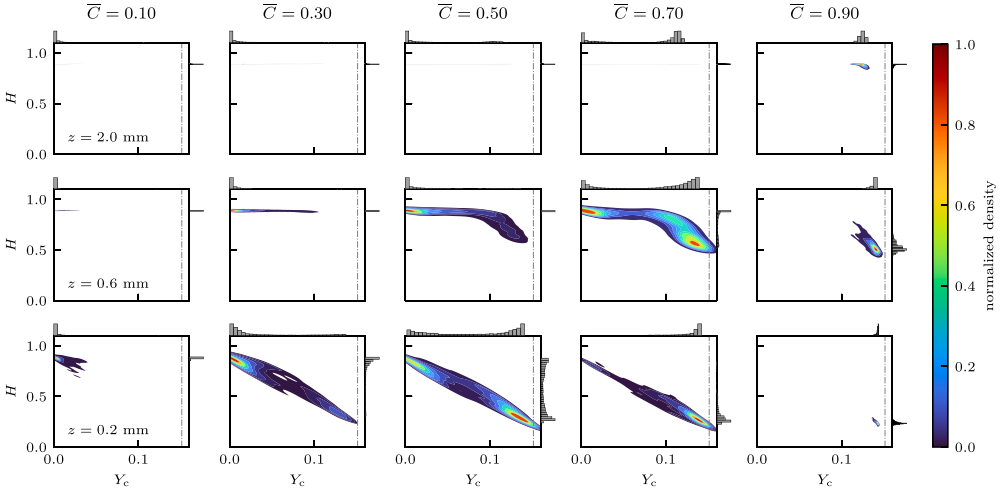

Fig. 4. PDFs at a wall distance of $z = 2.0$ mm (top) $z = 0.6$ mm (middle) and $z = 0.2$ mm (bottom). Each subplot shows the joint PDF of the progress variable Y_c and normalized enthalpy H as a contour colored according to the probability normalized by its maximum. The marginal PDF of the progress variable (top) and normalized enthalpy (right) are shown at the figure borders as bar plots with a bin size of 20. The mean reaction progress increases from left to right. The dash-dotted line corresponds to the global maximum value of Y_c and the minimum is 0. (For interpretation of the references to color in this figure legend, the reader is referred to the web version of this article.)

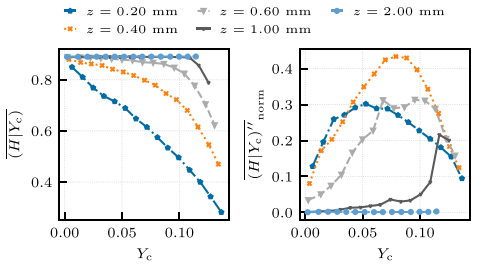

Fig. 5. Conditional mean and normalized standard deviation of the normalized enthalpy for a given progress variable at different wall distances z and $\widetilde{C} = 0.5$.

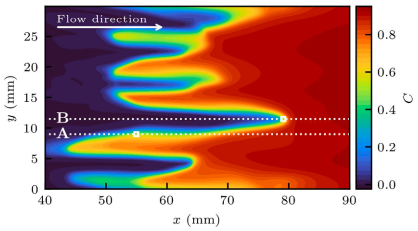

Fig. 6. Snapshot of a wall-parallel cut through the domain at $z = 0.2$ mm colored by the normalized progress variable. Two representative flame positions are indicated by the dotted lines: flame flank (A), flame tip (B). The markers depict the center points of the box-samples used to calculate the FDFs. The slice is also shown in the 3D view of the flame in Fig. 2. (For interpretation of the references to color in this figure legend, the reader is referred to the web version of this article.)

the PDF retains its univariate character of the core flow. Finally, in the close vicinity to the wall ($z = 0.2$ mm, bottom row), a bivariate PDF can be observed for all values of the mean progress variable.

Secondly, the influence of mean reaction progress on the PDF is discussed at different stream-wise locations shown in Fig. 4 from left to right. At the unburnt ($\widetilde{C} = 0.1$) edges of the flame the fluctuations in both the progress variable and enthalpy direction vanish and the PDF can be approximated by a single point in the progress variable-enthalpy space. With increasing reaction progress, first the PDF widens in progress variable direction, still showing mainly low progress variable values ($\widetilde{C} = 0.3$). Then, a typical double peak PDF of the progress variable can be observed ($\widetilde{C} = 0.5/0.7$), showing a high probability of low and high values of the progress variable and few occurrences of intermediate values. This shape of the distribution is a direct effect of the thin reaction zones in premixed flames. With further increasing reaction progress, the PDF shows mainly high values of progress variable, before it approaches a single peak PDF with a small variance towards the burnt state.

In summary, the influence of enthalpy losses at the wall increases with both, increasing reaction progress and decreasing wall distance due to higher temperature gradients in the flow. These enthalpy losses in the near-wall region yield a complex bivariate PDF in the reaction zone of the flame that need to be accounted for in TCI closure. The trends of the joint PDFs are also reflected in their marginal counterparts leading to a broadening of the univariate distributions of the progress variable and enthalpy. However, the correlation of the progress variable and enthalpy, as e.g. observed for $z = 0.2$ mm, is not captured by the marginal PDFs. In particular, statistical independence (Fiorina et al., 2005; Donini et al., 2017; Zhang et al., 2021) as often used in presumed PDF methods, is not applicable for FWI. In this context, the CQMOM approach that models the joint PDF as a marginal PDF of the progress variable and a conditional PDF of the enthalpy, see Eq. (6) is advantageous. Fig. 5 shows the conditional mean and normalized standard deviation of the normalized enthalpy for a given progress variable at different wall distances. The conditional quantities clearly reflect the correlation of progress variable and enthalpy in the joint PDFs, indicating the benefit of the CQMOM method over the pPDF approach. Additionally, the wall normal distance affected by enthalpy losses to the wall can be deduced from the left plot in Fig. 5. While for laminar flames (Zhang et al., 2021) an influence of the wall on the flame can be observed for $z/\delta_L < 1$, in the turbulent flame investigated here $z/\delta_L < 2$.

4.2. Analysis of the joint FDF in the context of LES

In the context of LES, the flame is filtered locally for instantaneous fields using a box filter operation (Eq. (A.4)). Therefore, transient processes in the flame affect the FDF and need to be considered in the analysis. In Fig. 2 a snapshot of the DNS is shown and distinctive flame tongues can be observed at different lateral positions. Over time, these flame tongues emerge at different lateral locations in the flame, slowly propagate forward and are finally rapidly pushed back to the position of the main reaction front. This results in a locally high-intensity wall heat flux. A similar behavior is also described in (Gruber et al., 2010) for a hydrogen-air flame and in (Heinrich et al., 2018a) for a methane-air flame and can be explained by the interaction of the flame with the near-wall vortices. Fig. 6 shows a wall-parallel cut at $z = 0.2$ mm of the flame snapshot in Fig. 2. In the figure, two representative flame zones are depicted as dotted lines: a flame flank (A) and a flame tip (B). The flame flank (A) is characterized by a position in the flame with a high progress variable gradient in the lateral direction, while the flame tip (B) corresponds to the maximum of the flame front in the stream-wise direction. Furthermore, similar to Fig. 3, the box filter's center points of the FDFs analyzed in the following are shown. The center points ($x_{l,\mathrm{center}}$, $y_{l,\mathrm{center}}$, $z_{l,\mathrm{center}}$) are determined as follows:

- **Wall-normal distance (z_{center}):** Different wall-normal distances are examined to investigate the impact of wall-heat losses on the joint FDF.
- **Lateral location (y_{center}):** Other than in the context of RANS, in LES the lateral direction is relevant for the flame, since the data is not averaged over time, but resolved locally (3D). Two respective lateral positions are chosen corresponding to a flame tip and a flame flank.
- **Stream-wise location (x_{center}):** Different stream-wise locations are extracted to analyze the influence of the reaction progress on the FDF. The stream-wise location is defined for every wall-normal and lateral position, separately, and is based on the instantaneous normalized progress variable C. Different stream-wise locations were analyzed that showed the highest challenges for the closure of the joint PDF in the reaction zone of the flame. In the following, only a representative position is discussed with $C = 0.5$. At the other stream-wise locations similar observation can be made.

In the following analysis different exemplary filter kernels are employed to show the influence of the LES resolution on the FDF closure. The filter kernel size is given by

$$(\Delta_x, \Delta_y, \Delta_z) = (\mathrm{AR}\cdot\delta_z, \mathrm{AR}\cdot\delta_z, \delta_z), \tag{11}$$

with δ_z being the filter width in wall-normal direction and AR the aspect ratio of the filter kernel, indicating the influence of a grid refinement at the wall in an LES simulation. Note that even though the mesh is (formally) unstructured, due to its purely hexahedral and orthogonal structure the application of a box filter is a straight forward operation. In the following, first the FDF is discussed for different lateral positions and wall normal filter width δ_z. Then, the influence of the apect ratio is analyzed.

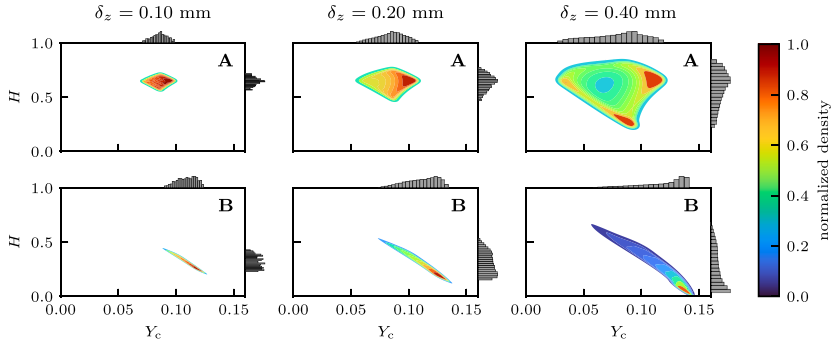

Fig. 7. FDFs in the context of LES at a wall distance of $z = 0.2$ mm and a normalized progress variable of $C = 0.5$. At the top the FDFs at the flame flank (A) are shown, while at the bottom the FDFs at the flame tip (B) are depicted. From left to right the box-size (LES filter width) increases. The aspect ratio of the box filter is AR = 2.5. Each subplot shows the joint FDF of the progress variable Y_c and normalized enthalpy H as a contour (middle) colored according to the probability normalized by its maximum. The marginal FDF of the progress variable (top) and normalized enthalpy (right) are shown at the figure borders as bar plots with a bin size of 20. (For interpretation of the references to color in this figure legend, the reader is referred to the web version of this article.)

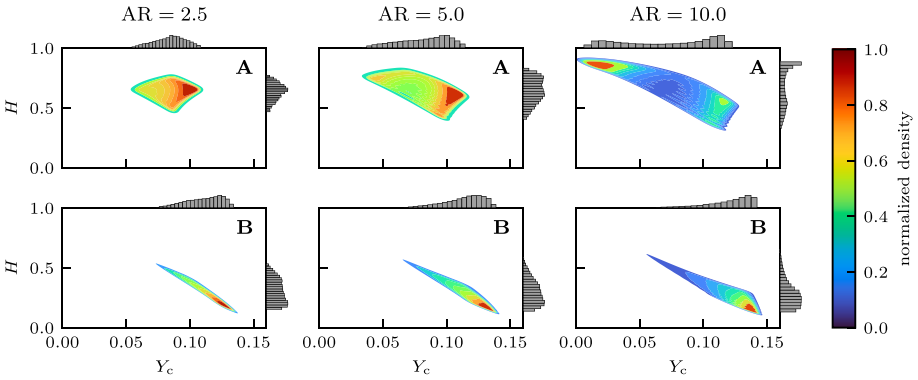

Fig. 8. FDFs in the context of LES at a wall distance of $z = 0.2$ mm and a normalized progress variable of $C = 0.5$. At the top the FDFs at the flame flank (A) are shown, while at the bottom the FDFs at the flame tip (B) are depicted. From left to right the aspect ratio increases. The wall-normal filter width is $\delta_z = 0.2$ mm. Each subplot shows the joint FDF of the progress variable Y_c and normalized enthalpy H as a contour (middle) colored according to the probability normalized by its maximum. The marginal FDF of the progress variable (top) and normalized enthalpy (right) are shown at the figure borders as bar plots with a bin size of 20. (For interpretation of the references to color in this figure legend, the reader is referred to the web version of this article.)

The marginal and joint Favre-weighted FDFs of the progress variable and enthalpy are shown in Fig. 7 for different δ_z and AR = 2.5. The flame flank (A) shows a wide distribution for the progress variable and enthalpy and no significant correlation between the two variables can be observed. The flame tip (B), on the other hand, shows a line-like distribution that indicates a strong correlation between the progress variable and enthalpy in this area of the flame. These two completely different FDF shapes show the challenge for any TCI closure model for FWI, which must be able to describe both FDF shapes. Note that the marginal FDFs (subfigure borders) that are used in pPDF approaches, do not reflect the correlations of progress variable and enthalpy in the joint FDFs. In the context of CQMOM, the FDFs at the flame tip (B) are straightforward due to the use of a conditional FDF for the enthalpy. For classical pPDF approaches from literature (Fiorina et al., 2005; Donini et al., 2017; Zhang et al., 2021), however, the high correlation between progress variable and enthalpy is in contradiction to the modeling assumptions of independence of the progress variable and enthalpy. The flame flank (A), on the other hand, features a more challenging FDF for the CQMOM approach due to the low correlation between the progress variable and enthalpy and this is investigated in the following section.

Secondly, the impact of wall-normal filter width δ_z on the FDF complexity is discussed. In Fig. 7 the filter width is increased from left to right by a factor of two for each subplot. While the FDF shape is mostly dependent on the specific flame area (flame flank/flame tip), the FDF widens with increasing filter width and shows increasing variance in the progress variable and enthalpy direction leading to a more complex FDF that needs to be accounted for by the TCI closure model. This aspect of TCI closure is also discussed in Section 5.3.

Finally, the influence of the aspect ratio AR is discussed. Fig. 8 shows the FDFs corresponding to $\delta_z = 0.2$ mm and varying aspect ratio. At the flame flank (A) the FDF is significantly influenced by the aspect ratio. While for small aspect ratios, a relatively uniform distribution is present, with increasing aspect ratio the FDF approaches a double peak FDF, similar to the ones observed in the context of RANS with a high probability of fresh and burnt gas states. The flame tip (B) on the other hand is not significantly influenced by the aspect ratio remaining its general

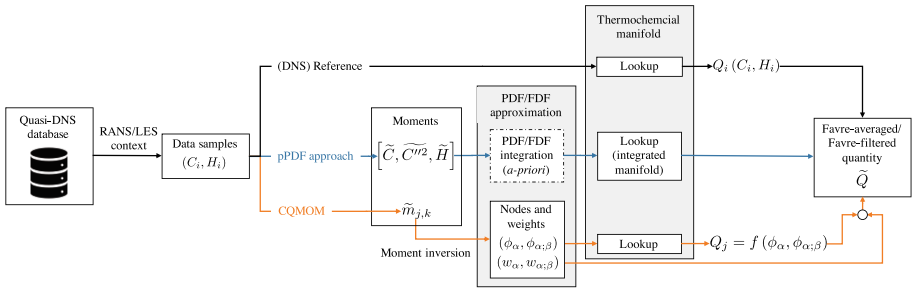

Fig. 9. Schematic view of the *a priori* analysis for a flow quantity Q. The steps of the analysis are illustrated from left to right, starting from the quasi-DNS database and resulting in an approximation of a Favre-averaged/Favre-filtered quantity $\widetilde{Q}$. In the context of RANS, a temporal average is performed, while in the context of LES, Favre-filtered quantities are considered. Note that the PDF/FDF approximation step of the pPDF approach can be performed prior to a simulation, while the CQMOM calculations of nodes and weights are performed during runtime.

shape, showing only a broadening of the FDF with increasing aspect ratio.

Note that the filter widths discussed above have a maximum value of 2 mm (four time the laminar flame thickness δ_L) in the stream-wise and lateral direction and 0.4 mm in the wall-normal direction. Dependent on the configuration considered the LES filter widths can be even larger in a coupled simulation.

5. *A priori* validation of the CQMOM closure of the joint PDF

In this section, the suitability of the CQMOM approach to model the unresolved PDFs/FDFs is assessed in an *a priori* analysis and compared to a pPDF approach from the literature (Fiorina et al., 2005) that uses a β-PDF for the progress variable and a δ-peak for the enthalpy. The analysis focuses on the PDFs/FDFs in the reaction zone. Here, the modeling challenges for the closure of the joint PDF are the highest due the very complex PDF/FDF shapes as discussed in the previous section.

It is important to note that this *a priori* analysis differs from other analyses performed in the literature (Bray et al., 2006; Jin et al., 2008) that directly compare the PDF/FDF shapes of the DNS reference with the presumed PDF/FDF counterpart. The CQMOM approach does not predict the PDF/FDF itself but instead estimates integrals based on the unknown PDF/FDF. Hence, the shape of the PDF/FDF cannot be directly analyzed (or compared) in the context of the QMOM method used here. Thus, the *a priori* analysis examines the prediction accuracy of Favre-averaged/Favre-filtered quantities originating from the respective PDFs/FDFs. Such an approach is particularly advantageous for the latter use in LES or RANS. Fig. 9 illustrates the workflow of the *a priori* analysis performed in this work.

To ensure a fully consistent comparison of the closure models of the joint PDF/FDF, all thermochemical quantities are taken directly from the QFM manifold, i.e. we also perform a lookup using the DNS values of progress variable and enthalpy. This effectively decouples the error in the manifold from the TCI analysis. Starting from the quasi-DNS database, the data is sampled according to the respective context. In the context of RANS the Favre-averaged quantities are calculated on the same samples that are used to calculate a temporal PDF as described in Section 4.1, while in the context of LES the filtered quantites are based on the FDF data extraction, described in Section 4.2. From these samples, the Favre-averaged/Favre-filtered quantities can be calculated as follows for the quasi-DNS, the pPDF approach and the CQMOM closure:

- **(DNS) Reference:** The quasi-DNS reference values are calculated from the N samples that estimate the unresolved PDFs/FDFs, see Section 4:

$$\widetilde{Q}_{\text{ref}} = \frac{1}{\widetilde{\rho}} \sum_{i=0}^{N} \underbrace{f_\rho(C_i, H_i)}_{\text{from QFM}} \underbrace{f_Q(C_i, H_i)}_{\text{from QFM}}. \tag{12}$$

Note that both the density and the quantity Q are estimated from the thermochemical manifold indicated by f_ρ and f_Q, respectively.

- **pPDF approach:** The approach by Fiorina et al. (Fiorina et al., 2005) using a β-PDF for the normalized progress variable and a δ-peak for the normalized enthalpy results in:

$$\widetilde{Q} = f\left(\widetilde{C}, \widetilde{C''^2}, \widetilde{H}\right) = \int\int f_Q(C,H) \cdot \widetilde{P}(C) \widetilde{P}(H) dC dH, \tag{13}$$

where the β-PDF $\widetilde{P}(C)$ is defined by the first and second moment $\left(\widetilde{C}, \widetilde{C''^2}\right)$, and $\widetilde{P}(H) \approx \delta(H - \widetilde{H})$ is a δ-PDF centered at $\widetilde{H}$.

- **CQMOM:** In the *a priori* CQMOM closure, only part of the algorithm described in (Madadi Kandjani, 2017; Fox, 2018; Pollack et al., 2021) needs to be used. In particular, instead of solving transport equations for the moments, they are directly calculated from the quasi-DNS samples (step i. below) and used as input parameters for the CQMOM algorithm. The CQMOM approximation, for a Favre-averaged/Favre-filtered quantity $\widetilde{Q}$, is calculated in a multi-step process:
  - i. **Moment calculation:** The Favre-averaged/Favre-filted moments $\widetilde{m}_{k,j}$ are calculated directly from N sample points acquired from the quasi-DNS result:

$$\widetilde{m}_{k,j} = \frac{\sum_{i=0}^{N} f_\rho(C_i, H_i) Y_{c,i}^k H_i^j}{\sum_{i=0}^{N} \underbrace{f_\rho(C_i, H_i)}_{\text{from QFM}}}. \tag{14}$$

  - ii. **Moment inversion:** The nodes $(\phi_\alpha; \phi_{\alpha;\beta})$ and weights $(w_\alpha; w_{\alpha;\beta})$ corresponding to the given moment set $\widetilde{m}_{k,j}$ are calculated.
  - iii. **Table lookup:** For each node, the flow quantity can be extracted from the chemistry manifold $f_Q(\phi_\alpha, \phi_{\alpha;\beta})$. Note here that the PDF/FDF nodes correspond to a point in the progress variable-enthalpy state.
  - iv. **Calculate the means:** Finally, the Favre-averaged/Favre-filtered quantity $\widetilde{Q}$ can be calculated using the interpolation weights and nodes corresponding to the Favre-averaged moments using Eq. (10).

For the analysis two flow quantities are examined that show a strong

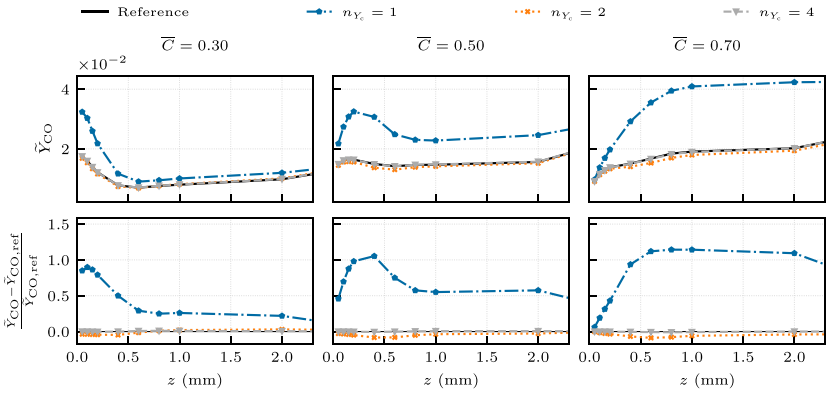

Fig. 10. Prediction of the Favre-averaged CO mass fraction $\widetilde{Y}_{CO}$ as a function of the wall distance in the context of RANS. The CQMOM approximation is performed using a different number of nodes in the progress variable direction n_{Y_c}, while in the enthalpy direction only a single node is used ($n_H = 1$). The different columns show different stream-wise locations in the flame defined by $\overline{C}$ at the respective wall distance, see Section 4. At the top the absolute value is shown, while at the bottom the relative deviation from the quasi-DNS reference is depicted.

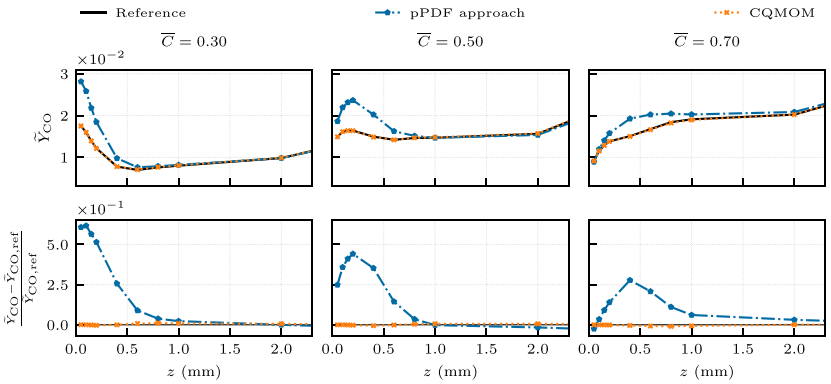

Fig. 11. Prediction of the Favre-averaged CO mass fraction $\widetilde{Y}_{CO}$ as a function of the wall distance in the context of RANS. Next to the CQMOM a pPDF approach from the literature (Fiorina et al., 2005) is shown. The different columns show different stream-wise locations in the flame defined by $\overline{C}$ at the respective wall distance, see Section 4. At the top the absolute value is shown, while at the bottom the relative deviation from the quasi-DNS reference is depicted.

sensitivity to wall heat losses, namely the temperature and the mass fraction of CO. These two quantities have also been of central interest in multiple studies of laminar (Ganter et al., 2017, 2018; Kosaka et al., 2018; Jainski et al., 2017a,b) and turbulent (Jainski et al., 2018; Kosaka et al., 2018) side-wall quenching. Even though the source term of the progress variable is a central quantity for the closure of the joint PDF it is not used for the analysis performed in the following, since (i) the suitability of the QMOM approach to predict the source term of the progress variable are discussed in a previous study of laminar freely propagating flames (Pollack et al., 2021) and (ii) due to flame quenching the reaction in the flame stagnates in the close vicinity to the wall leading to a vanishing source term in the FWI area. In the following, after a convergence study in Section 5.1, the CQMOM closure is discussed in the context of RANS (Section 5.2) and and LES (Section 5.3).

5.1. CQMOM moment convergence study

Before the CQMOM approach is compared to the pPDF approach from the literature the necessary number of integration nodes in the progress variable n_{Y_c} and normalized enthalpy n_H direction needs to be assessed. Therefore, the prediction of the Favre-averaged/Favre-filtered CO mass fraction is analyzed in the context of RANS/LES.

Fig. 10 shows the convergence for the Favre-averaged CO mass fraction for an increasing number of nodes in the direction of the progress variable n_{Y_c} and with one node in the direction of the enthalpy ($n_H = 1$). When only a single node in the progress variable direction is employed, the CQMOM approach shows a high model deviation compared to the reference DNS results. In this particular case, only the Favre-averaged mean of the progress variable $\widetilde{Y}_c$ and normalized enthalpy $\widetilde{H}$ are used for the determination of the Favre-averaged CO mass fraction. Using two integration nodes, the CQMOM approach already shows a high prediction accuracy both in the core flow and in the proximity to the wall. With four integration nodes in the progress variable direction and a single node in the enthalpy direction, a nearly perfect agreement between the CQMOM estimate and the quasi-DNS reference can be observed. For the context of LES a corresponding

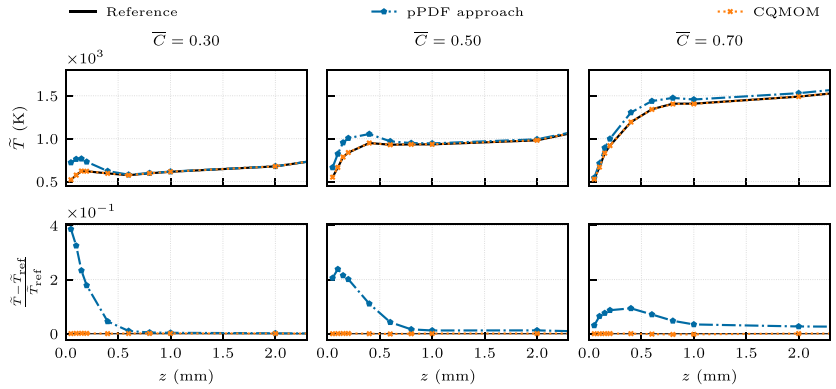

Fig. 12. Prediction of the Favre-averaged temperature $\widetilde{T}$ as a function of the wall distance in the context of RANS. Next to the CQMOM a pPDF approach from the literature (Fiorina et al., 2005) is shown. The different columns show different stream-wise locations in the flame defined by $\overline{C}$ at the respective wall distance, see Section 4. At the top the absolute value is shown, while at the bottom the relative deviation from the quasi-DNS reference is depicted.

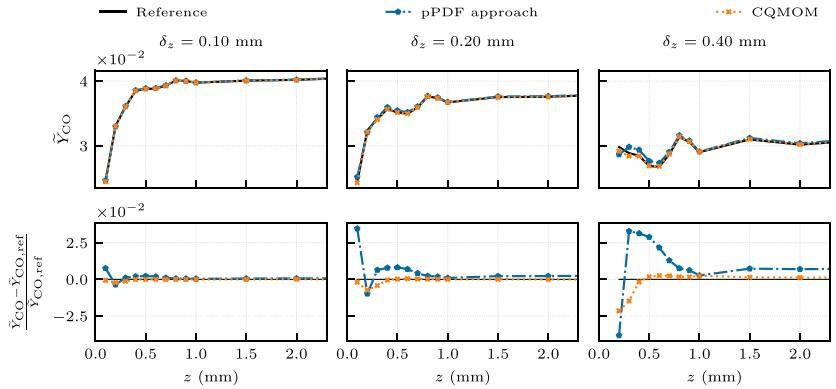

Fig. 13. Prediction of the instantaneous Favre-filtered CO mass fraction as a function of the wall distance in the context of LES. The data is extracted at the flame flank (A) at a stream-wise direction corresponding to $C = 0.5$, see Section 4.2. The different columns show different box filter width, see Eq. (11), with varying wall-normal filter width δ_z and AR $= 2.5$. At the top the absolute value is shown, while at the bottom the relative deviation from the quasi-DNS reference is depicted.

study was performed, using the respective spatially filtered values, leading to similar results that are not shown here for brevity. In the following analysis, all RANS and LES CQMOM results are shown for four nodes in the progress variable direction and a single node in the enthalpy direction.

5.2. *A priori assessment of the CQMOM approach in the context of RANS*

Figs. 11 and 12 show the CQMOM prediction of the Favre-averaged CO mass fraction and temperature in comparison to the pPDF approach from the literature (Fiorina et al., 2005). At the top row, the Favre-averaged quantity is shown, while the relative deviation from the quasi-DNS reference is depicted at the bottom.

Different stream-wise locations in the reaction zone of the flame are displayed, with increasing reaction progress from left to right. The free flow region ($z > 1$ mm) that is unaffected by enthalpy losses to the wall confirms that in this region both models are in excellent agreement with the reference, both for the CO mass fraction and the temperature. Due to negligible enthalpy losses, the PDFs reduce to a univariate distribution solely dependent on the progress variable, see Section 4.1. With decreasing distance to the wall ($z < 1$ mm), the flame is affected by increasing enthalpy losses leading to a bivariate PDF of the progress variable and enthalpy. In this close proximity to the wall, the prediction accuracy of the pPDF approach deteriorates substantially with deviations up to 50% from the quasi-DNS reference. Here, the pPDF approach suffers from two drawbacks: (i) the enthalpy PDF cannot be modeled by a simple δ-peak and (ii) the modeling assumption of independence of the normalized progress variable and normalized enthalpy (Fiorina et al., 2005) is no longer valid in the close vicinity of the wall. Contrary, the CQMOM approach can capture the near-wall behavior accurately by accounting for the conditional PDF of the enthalpy for a given progress variable $P(Y_c|H)$ using only a single node in the enthalpy direction. In the close vicinity to the wall the CQMOM approach makes use of the additional moment information compared to the pPDF approach and is able to approximate the complex bivariate PDF of the progress variable and enthalpy leading to an excellent agreement with the quasi-DNS reference.

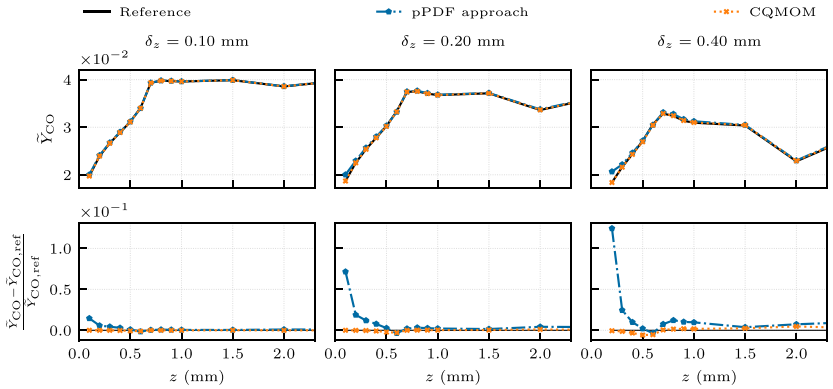

Fig. 14. Prediction of the instantaneous Favre-filtered CO mass fraction as a function of the wall distance in the context of LES. The data is extracted at the flame tip (B) at a stream-wise direction corresponding to $C = 0.5$, see Section 4.2. The different columns show different box filter width, see Eq. (11), with varying wall-normal filter width δ_z and AR = 2.5. At the top the absolute value is shown, while at the bottom the relative deviation from the quasi-DNS reference is depicted.

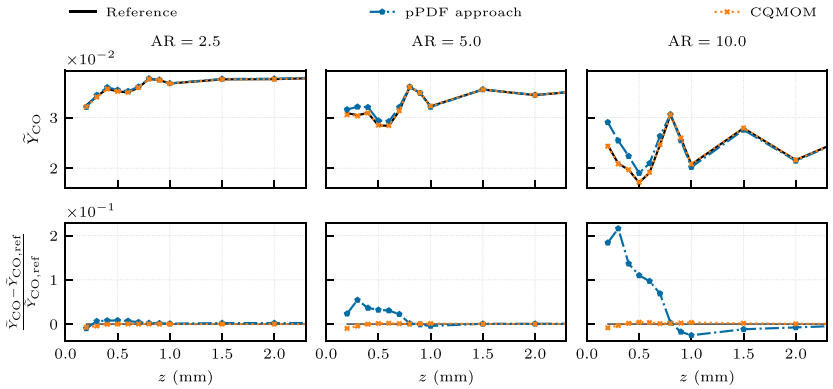

Fig. 15. Prediction of the instantaneous Favre-filtered CO mass fraction as a function of the wall distance in the context of LES. The data is extracted at the flame flank (A) at a stream-wise direction corresponding to $C = 0.5$, see Section 4.2. The different columns show different box filter aspect ratios, see Eq. (11), for $\delta_z = 0.2$ mm. At the top the absolute value is shown, while at the bottom the relative deviation from the quasi-DNS reference is depicted.

5.3. *A priori assessment of the CQMOM approach in the context of LES*

Finally, the suitability of the CQMOM approach to model the different FDF shapes presented in Section 4.2 is discussed. The prediction accuracy of the Favre-filtered CO mass fraction is assessed, since it showed the highest deviations in the context of RANS and, hence, is most challenging to model. Two scenarios are studied, the flame flank (A) and the flame tip (B) for different wall distances and wall-normal filter width δ_z. Furthermore, the influence of the filter kernel's aspect ratio AR is discussed for $\delta_z = 0.2$ mm. The stream-wise location of the box filer's center point corresponds to a value of $C = 0.5$.

Figs. 13 and 14 show the results for varying wall-normal filter width and an aspect ratio of AR = 2.5 for the flame flank and the flame tip, respectively. Again, both closure models show a high prediction accuracy in the free flow ($z > 1.0$ mm). However, closer to the wall ($z < 0.5$ mm) the prediction accuracy deteriorates particularly for the pPDF approach. At the flame flank in Fig. 13, the CQMOM predictions show a relative difference of up to 2.5% from the DNS reference for the highest wall-normal filter width $\delta_z = 0.4$ mm, while still remaining a higher prediction accuracy compared to the pPDF approach. With decreasing filter width the prediction of the PDF models improves significantly. As discussed in the previous section, the flame flank has a wide FDF of the progress variable and enthalpy and, therefore, it is particularly challenging to model with the CQMOM approach. This can be overcome in two ways: (i) the number of nodes in the enthalpy direction can be increased and (ii) the filter width at the wall can be decreased (e.g. the grid resolution is increased), leading to less complex FDFs. At the flame tip in Fig. 14 the progress variable and enthalpy show a very high correlation. In this area, the CQMOM modeling assumption of a conditional FDF of enthalpy for a given progress variable is especially advantageous. Here, the CQMOM shows a nearly perfect agreement with the reference. The pPDF approach, on the other hand, assuming the independence of progress variable and enthalpy is not able to predict the correct Favre-filtered CO mass fraction in the close vicinity of the wall.

Finally, the influence of the box filter's aspect ratio is discussed. As discussed in Section 4.2, the FDF shape at the flame flank is significantly influenced by the aspect ratio. In Fig. 15 the results for the flame flank

are shown. While the prediction accuracy of the pPDF approach deteriorates with increasing aspect ratio, the CQMOM is able to correctly model the FDF showing a high accuracy for all aspect ratios. This emphasises the importance of a suitable FDF closure model with decreasing LES resolution. For the flame tip the aspect ratio has only a small influence on the prediction accuracy of both PDF closure models. The corresponding results are therefore not shown.

6. Conclusion

Turbulent FWI in a generic turbulent side-wall quenching configuration is investigated in this work. A quasi-DNS of a stoichiometric methane-air flame was performed. From the quasi-DNS data the joint PDFs/FDFs of the progress variable and normalized enthalpy were extracted and analyzed in the context of RANS/LES. The influence of enthalpy losses at the wall on the joint PDFs/FDFs was assessed for different wall distances and mean reaction progress in the flame. Analyzing the PDFs in the context of RANS clearly showed that the wall distance has a strong influence on the PDF shape and dimension. While in the core flow a univariate PDF solely dependent on the progress variable is observed, the PDF shape becomes increasingly complex and bivariate closer to the wall. In the context of LES, the FDF has a high dependency on the spatial position in the flow and two representative flame positions were discussed: a flame flank (A) and a flame tip (B). At the flame flank a wide FDF was present that showed a high dependency on the box filter's aspect ratio and size (e.g. LES grid resolution). At the flame tip the FDF is less affected by the box filter's shape, however, a strong correlation was observed between the progress variable and normalized enthalpy close to the wall. This finding is in contradiction to the often used modeling assumption of statistical independence, i.e. in pPDF approaches (Fiorina et al., 2005; Donini et al., 2017; Zhang et al., 2021).

In the second part of this work, a novel CQMOM approach, coupled to a Quenching-Flamelet Generated manifold is assessed in an *a priori* analysis in the context of RANS and LES. The results are compared to the quasi-DNS data and a pPDF approach from the literature using a β-PDF for the progress variable and a δ-peak for enthalpy. First, a moment convergence study was performed, showing very good agreement with the quasi-DNS reference for four nodes in the progress variable direction and a single node in the enthalpy direction. In the core flow region unaffected by wall heat losses, both models are in good agreement with the quasi-DNS reference. In close proximity to the wall, however, the pPDF approach is not able to capture the correct flame behavior in the context of RANS and for coarse LES (large box filter sizes). The CQMOM approach, on the other hand, shows excellent agreement with the quasi-DNS reference both in the near-wall region and in the core flow. These results are very promising for future fully coupled LES or RANS simulations and provide an alternative approach to pPDF to account for TCI.

Data availability statement

The data presented in this study is available as supplementary material under https://doi.org/10.48328/tudatalib-673.

CRediT authorship contribution statement

M. Steinhausen: Conceptualization, Methodology, Software, Validation, Formal analysis, Data curation, Writing - original draft, Visualization. **T. Zirwes:** Formal analysis, Software, Writing - review & editing. **F. Ferraro:** Conceptualization, Methodology, Writing - review & editing. **S. Popp:** Conceptualization, Writing - review & editing. **F. Zhang:** Formal analysis, Resources, Writing - review & editing. **H. Bockhorn:** Writing - review & editing, Supervision. **C. Hasse:** Conceptualization, Funding acquisition, Writing - review & editing, Supervision.

Declaration of Competing Interest

The authors declare that they have no known competing financial interests or personal relationships that could have appeared to influence the work reported in this paper.

Acknowledgments

This work has been funded by the Deutsche Forschungsgemeinschaft (DFG, German Research Foundation) – Projektnummer 237267381 – TRR 150. Calculations for this research were conducted on the Lichtenberg high performance computer of the TU Darmstadt. The DNS simulation was performed on the national supercomputer HAWK at the High Performance Computing Center Stuttgart (HLRS) under the Grant No. DNSbomb/xbifezh and on the HoreKa supercomputer funded by the Ministry of Science, Research and the Arts Baden-Württemberg and by the Federal Ministry of Education and Research. Finally, we would like to thank Dr. Martin Pollack for his contribution and discussion about QbMM closure.

Appendix A. Favre-averaging in the context of RANS and LES

To calculate a Favre-averaged quantity in the context of RANS a temporal average is performed and the Favre-averaged quantity $\widetilde{Q}(\mathbf{x},t)$ is given by

$$\widetilde{Q}_{\mathrm{RANS}}(\mathbf{x}) = \frac{\int_{-T/2}^{T/2} \rho(\mathbf{x},t) Q(\mathbf{x},t) dt}{\int_{-T/2}^{T/2} \rho(\mathbf{x},t) dt}, \tag{A.1}$$

where t corresponds to the time, T is the temporal integration interval and ρ the density. In the investigated channel flow in this work, the averaging is additionally performed in the statistical independent lateral direction, leading to

$$\widetilde{Q}_{\mathrm{RANS}}(\mathbf{x}) = \frac{\int_{y_{\min}}^{y_{\max}} \int_{-T/2}^{T/2} \rho(\mathbf{x},t) Q(\mathbf{x},t) dt dy}{\int_{y_{\min}}^{y_{\max}} \int_{-T/2}^{T/2} \rho(\mathbf{x},t) dt dy}, \tag{A.2}$$

with $y_{\min}$ and $y_{\max}$ being the minimum and maximum lateral coordinate, respectively. In LES a spatial filter operation is performed and $\widetilde{Q}(\mathbf{x},t)$ is given by

$$\widetilde{Q}_{\mathrm{LES}}(\mathbf{x},t) = \frac{\int \rho(\mathbf{x}^*,t) Q(\mathbf{x}^*,t) F(\mathbf{x}-\mathbf{x}^*) d\mathbf{x}^*}{\int \rho(\mathbf{x}^*,t) F(\mathbf{x}-\mathbf{x}^*) d\mathbf{x}^*}, \tag{A.3}$$

where $\mathbf{x} = (x_1, x_2, x_3)$ is the spatial coordinate and $F(\mathbf{x} - \mathbf{x}^*)$ is a normalized spatial filter function. In the following analysis a box filter is applied given by

$$F(x_1, x_2, x_3) = \begin{cases} \left(\Delta_{x_1} \cdot \Delta_{x_2} \cdot \Delta_{x_3}\right)^{-1} & \text{if } |x_i| \leqslant \Delta_{x_i}/2,\ i = 1, 2, 3 \\ 0 & \text{otherwise} \end{cases}. \tag{A.4}$$

Appendix B. QFM validation in turbulent side-wall quenching

In this section, the QFM manifold is validated for the turbulent side-wall quenching. Therefore, Figs. B.16 and B.17 show the Favre-filtered temperature and CO mass fraction calculated directly from the quasi-DNS and estimated with the QFM through a table lookup. The data is extracted with a wall normal filter width of $\delta_z = 0.2$ mm and AR = 2.5 at different stream-wise locations defined by the normalized progress variable, see Eq. (2). The quasi-DNS reference quantity $\widetilde{Q}$ is calculated as

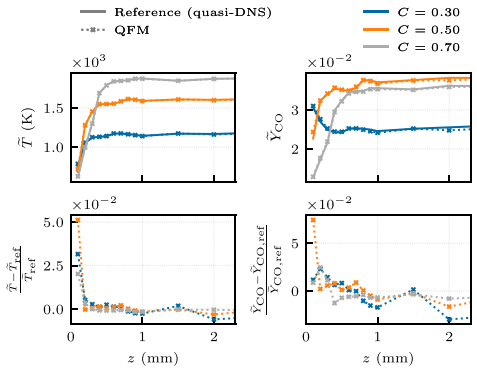

Fig. B.16. Instantaneous Favre-filtered temperature (left) and CO mass fraction (right) calculated directly from the quasi-DNS and using a lookup with the QFM (top) and the relative error of the means (bottom). The plot shown corresponds to the flame flank (A), see Fig. 6.

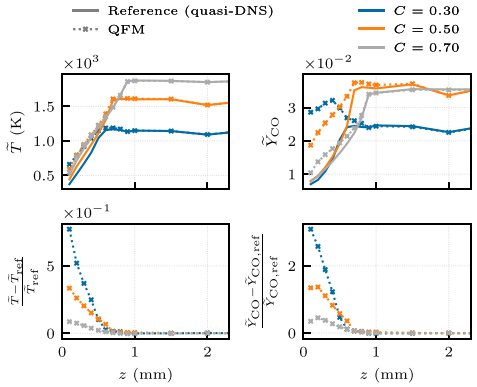

Fig. B.17. Instantaneous Favre-filtered temperature (left) and CO mass fraction (right) calculated directly from the quasi-DNS and using a lookup with the QFM (top) and the relative error of the means (bottom). The plot shown corresponds to the flame tip (B), see Fig. 6.

$$\widetilde{Q} = \frac{\sum_{i=0}^{N} \rho_i Q_i}{\sum_{i=0}^{N} \rho_i}, \tag{B.1}$$

while, for the QFM value, both the density and the quantity are estimated from the chemistry manifold:

$$\widetilde{Q}_{\mathrm{QFM}} = \frac{\sum_{i=0}^{N} f_\rho(C_i, H_i) f_Q(C_i, H_i)}{\sum_{i=0}^{N} f_\rho(C_i, H_i)}. \tag{B.2}$$

While the manifold shows very good agreement with the quasi-DNS in the free flow and at the flame flank (A), at the flame tip (B) the manifold shows a deviation from the quasi-DNS reference in the near-wall region. These deviations in the manifold are due to turbulent mixing processes that do not occur in the laminar flames and are subject to future investigations.

References

Ahmed, U., Chakraborty, N., Klein, M., 2021. Scalar gradient and strain rate statistics in oblique premixed flame-wall interaction within turbulent channel flows. Flow Turbul. Combust. 106, 701–732.

Avdić, A., Kuenne, G., Janicka, J., 2016. Flow Physics of a Bluff-Body Swirl Stabilized Flame and their Prediction by Means of a Joint Eulerian Stochastic Field and Tabulated Chemistry Approach. Flow Turbul. Combust. 97, 1185–1210.

Bray, K.N., Champion, M., Libby, P.A., Swaminathan, N., 2006. Finite rate chemistry and presumed PDF models for premixed turbulent combustion. Combust. Flame 146, 665–673.

Cao, R.R., Pope, S.B., 2005. The influence of chemical mechanisms on PDF calculations of nonpremixed piloted jet flames. Combust. Flame 143, 450–470.

Cheng, J.C., Vigil, R.D., Fox, R.O., 2010. A competitive aggregation model for Flash NanoPrecipitation. J. Colloid Interface Sci. 351, 330–342.

Donde, P., Koo, H., Raman, V., 2012. A multivariate quadrature based moment method for LES based modeling of supersonic combustion. J. Comput. Phys. 231, 5805–5821.

Donini, A., Bastiaans, R.J.M., van Oijen, J.A., de Goey, L.P.H., 2017. A 5-D Implementation of FGM for the Large Eddy Simulation of a Stratified Swirled Flame with Heat Loss in a Gas Turbine Combustor. Flow Turbul. Combust. 98, 887–922.

Efimov, D.V., de Goey, P., van Oijen, J.A., 2019. QFM: quenching flamelet-generated manifold for modelling of flame–wall interactions. Combust. Theory Model. 1–33.

Ferraro, F., Ge, Y., Pfitzner, M., Cleary, M.J., 2019. A Fully Consistent Hybrid Les/Rans Conditional Transported Pdf Method for Non-premixed Reacting Flows. Combust. Sci. Technol. 193, 379–418.

Ferraro, F., Russo, C., Schmitz, R., Hasse, C., Sirignano, M., 2021. Experimental and numerical study on the effect of oxymethylene ether-3 (OME3) on soot particle formation. Fuel 286.

Fiorina, B., Gicquel, O., Vervisch, L., Carpentier, S., Darabiha, N., 2005. Premixed turbulent combustion modeling using tabulated detailed chemistry and PDF. Proc. Combust. Inst. 30, 867–874.

Fiorina, B., Vicquelin, R., Auzillon, P., Darabiha, N., Gicquel, O., Veynante, D., 2010. A filtered tabulated chemistry model for LES of premixed combustion. Combust. Flame 157, 465–475.

Fox, R.O., 2018. Quadrature-Based Moment Methods for Multiphase Chemically Reacting Flows, vol. 52, 1st ed., Elsevier Inc. doi:10.1016/bs.ache.2018.01.001.

Fritz, J., Kröner, M., Sattelmayer, T., 2001. Flashback in a Swirl Burner With Cylindrical Premixing Zone Volume 2: Coal, Biomass and Alternative Fuels; Combustion and Fuels; Oil and Gas Applications; Cycle Innovations (2001). V002T02A021.

Ganter, S., Heinrich, A., Meier, T., Kuenne, G., Jainski, C., Rißmann, M.C., Dreizler, A., Janicka, J., 2017. Numerical analysis of laminar methane–air side-wall-quenching. Combust. Flame 186, 299–310.

Ganter, S., Straßacker, C., Kuenne, G., Meier, T., Heinrich, A., Maas, U., Janicka, J., 2018. Laminar near-wall combustion: Analysis of tabulated chemistry simulations by means of detailed kinetics. Int. J. Heat Fluid Flow 70, 259–270.

Gruber, A., Sankaran, R., Hawkes, E.R., Chen, J.H., 2010. Turbulent flame-wall interaction: A direct numerical simulation study. J. Fluid Mech. 658, 5–32.

Hansinger, M., Zirwes, T., Zips, J., Pfitzner, M., Zhang, F., Habisreuther, P., Bockhorn, H., 2020. The Eulerian Stochastic Fields Method Applied to Large Eddy Simulations of a Piloted Flame with Inhomogeneous Inlet. Flow Turbul. Combust. 105, 837–867.

Haworth, D.C., 2010. Progress in probability density function methods for turbulent reacting flows. Prog. Energy Combust. Sci. 36, 168–259.

Heinrich, A., Ries, F., Kuenne, G., Ganter, S., Hasse, C., Sadiki, A., Janicka, J., 2018a. Large Eddy Simulation with tabulated chemistry of an experimental sidewall quenching burner. Int. J. Heat Fluid Flow 71, 95–110.

Heinrich, A., Kuenne, G., Ganter, S., Hasse, C., Janicka, J., 2018b. Investigation of the Turbulent Near Wall Flame Behavior for a Sidewall Quenching Burner by Means of a Large Eddy Simulation and Tabulated Chemistry. Fluids 3, 65.

Jainski, C., Rißmann, M., Böhm, B., Janicka, J., Dreizler, A., 2017a. Sidewall quenching of atmospheric laminar premixed flames studied by laser-based diagnostics. Combust. Flame 183, 271–282.

Jainski, C., Rißmann, M., Böhm, B., Dreizler, A., 2017b. Experimental investigation of flame surface density and mean reaction rate during flame-wall interaction. Proc. Combust. Inst. 36, 1827–1834.

Jainski, C., Rißmann, M., Jakirlic, S., Böhm, B., Dreizler, A., 2018. Quenching of Premixed Flames at Cold Walls: Effects on the Local Flow Field. Flow Turbul. Combust. 100, 177–196.

Jaishree, J., Haworth, D.C., 2012. Comparisons of Lagrangian and Eulerian PDF methods in simulations of non-premixed turbulent jet flames with moderate-to-strong turbulence-chemistry interactions. Combust. Theory Model. 16, 435–463.

Jin, B., Grout, R., Bushe, W.K., 2008. Conditional Source-Term Estimation as a Method for Chemical Closure in Premixed Turbulent Reacting Flow. Flow Turbul. Combust 81, 563–582.

Jones, W.P., Navarro-Martinez, S., 2009. Numerical study of n-heptane auto-ignition using LES-PDF methods. Flow Turbul. Combust. 83, 407–423.

Jones, W.P., Prasad, V.N., 2010. Large Eddy Simulation of the Sandia Flame Series (D-F) using the Eulerian stochastic field method. Combust. Flame 157, 1621–1636.

Koo, H., Donde, P., Raman, V., 2011. A quadrature-based LES/transported probability density function approach for modeling supersonic combustion. Proc. Combust. Inst. 33, 2203–2210.

Kosaka, H., Zentgraf, F., Scholtissek, A., Bischoff, L., Häber, T., Suntz, R., Albert, B., Hasse, C., Dreizler, A., 2018. Wall heat fluxes and CO formation/oxidation during laminar and turbulent side-wall quenching of methane and DME flames. Int. J. Heat Fluid Flow 70, 181–192.

Kosaka, H., Zentgraf, F., Scholtissek, A., Hasse, C., Dreizler, A., 2019. Effect of Flame-Wall Interaction on Local Heat Release of Methane and DME Combustion in a Side-Wall Quenching Geometry. Flow Turbul. Combust. 104, 1029–1046.

Madadi Kandjani, E., 2017. Quadrature-based models for multiphase and turbulent reacting flows, Ph.D. thesis, Iowa State University, Digital Repository, Ames. doi: 10.31274/etd-180810-5801.

Marchisio, D.L., Fox, R.O., 2013. Computational Models for Polydesperse Particulate and Multiphase Systems, Cambridge University Press, Cambride. doi:10.1176/pn.39.24.00390022b.

McGraw, R., 1997. Description of aerosol dynamics by the quadrature method of moments. Aerosol Sci. Technol. 27, 255–265.

Muradoglu, M., Jenny, P., Pope, S.B., Caughey, D.A., 1999. A Consistent Hybrid Finite-Volume/Particle Method for the PDF Equations of Turbulent Reactive Flows. J. Comput. Phys. 154, 342–371.

Poinsot, T., Denis, V., 2005. Theoretical and Numerical Combustion, 2nd ed. R.T. Edwards, Inc., Philadelphia, USA.

Pollack, M., Salenbauch, S., Marchisio, D.L., Hasse, C., 2016. Bivariate extensions of the Extended Quadrature Method of Moments (EQMOM) to describe coupled droplet evaporation and heat-up. J. Aerosol Sci. 92, 53–69.

Pollack, M., Ferraro, F., Janicka, J., Hasse, C., 2021. Evaluation of Quadrature-based Moment Methods in turbulent premixed combustion. Proc. Combust. Inst. 38, 2877–2884.

Pope, S.B., 1981. A monte carlo method for the pdf equations of turbulent reactive flow. Combust. Sci. Technol. 25, 159–174.

Raman, V., Pitsch, H., Fox, R.O., 2006. Eulerian transported probability density function sub-filter model for large-eddy simulations of turbulent combustion. Combust. Theory Model. 10, 439–458.

Ranzi, E., Frassoldati, A., Grana, R., Cuoci, A., Faravelli, T., Kelley, A.P., Law, C.K., 2012. Hierarchical and comparative kinetic modeling of laminar flame speeds of hydrocarbon and oxygenated fuels. https://doi.org/10.1016/j.pecs.2012.03.004.

Salehi, M.M., Bushe, W.K., Shahbazian, N., Groth, C.P., 2013. Modified laminar flamelet presumed probability density function for LES of premixed turbulent combustion. Proc. Combust. Inst. 34, 1203–1211.

Salenbauch, S., Hasse, C., Vanni, M., Marchisio, D.L., 2019. A numerically robust method of moments with number density function reconstruction and its application to soot formation, growth and oxidation. J. Aerosol Sci. 128, 34–49.

Steinhausen, M., Luo, Y., Popp, S., Strassacker, C., Zirwes, T., Kosaka, H., Zentgraf, F., Maas, U., Sadiki, A., Dreizler, A., Hasse, C., 2021. Numerical Investigation of Local Heat-Release Rates and Thermo-Chemical States in Side-Wall Quenching of Laminar Methane and Dimethyl Ether Flames. Flow Turbul. Combust. 106, 681–700.

Strassacker, C., Bykov, V., Maas, U., 2019. Comparitive analysis of Reaction-Diffusion Manifold based reduced models for Head-On- and Side-Wall-Quenching flames. Combust. Symp.

Tang, Q., Zhao, W., Bockelie, M., Fox, R.O., 2007. Multi-environment probability density function method for modelling turbulent combustion using realistic chemical kinetics. Combust. Theory Model. 11, 889–907.

Tirunagari, R.R., Pope, S.B., 2016. An investigation of turbulent premixed counterflow flames using large-eddy simulations and probability density function methods. Combust. Flame 166, 229–242.

Valiño, L., 1998. Field Monte Carlo formulation for calculating the probability density function of a single scalar in a turbulent flow. Flow Turbul. Combust. 60, 157–172.

van Oijen, J.A., de Goey, L.P., 2000. Modelling of premixed laminar flames using flamelet-generated manifolds. Combust. Sci. Technol. 161, 113–137.

Vervisch, L., Veynante, D., 2002. Turbulent combustion modeling. Prog. Energy Combust. Sci. 28, 193–266.
Weller, H., Tabor, G., Jasak, H., Fureby, C., 2017. OpenFOAM, openCFD ltd. (2017). URL: https://openfoam.org/.
Wheeler, J.C., 1974. Modified moments and gaussian quadratures. Rocky Mt. J. Math. 4, 287–296.
Wick, A., Nguyen, T.-T., Laurent, F., Fox, R.O., Pitsch, H., 2017. Modeling soot oxidation with the extended quadrature method of moments. Proceedings of the Combustion Institute 36, 789–797.
Wu, H., Ihme, M., 2015. Modeling of Wall Heat Transfer and Flame/ Wall Interaction A Flamelet Model with Heat-Loss Effects. In: 9th U.S. Natl. Combust. Meet., pp. 1–10.
Yuan, C., Fox, R.O., 2011. Conditional quadrature method of moments for kinetic equations. J. Comput. Phys. 230, 8216–8246.
Zhang, W., Karaca, S., Wang, J., Huang, Z., van Oijen, J., 2021. Large eddy simulation of the Cambridge/Sandia stratified flame with flamelet-generated manifolds: Effects of non-unity Lewis numbers and stretch. Combust. Flame 227, 106–119.
Zirwes, T., Zhang, F., Denev, J.A., Habisreuther, P., Bockhorn, H., 2018. Automated code generation for maximizing performance of detailed chemistry calculations in OpenFOAM, in: High Perform. Comput. Sci. Eng. 17 Trans. High Perform. Comput. Center, Stuttgart 2017, Springer International Publishing, 2018, pp. 189–204. doi: 10.1007/978-3-319-68394-2_11.
Zirwes, T., Zhang, F., Denev, J., Habisreuther, P., Bockhorn, H., Trimis, D., 2018. Improved Vectorization for Efficient Chemistry Computations in OpenFOAM for Large Scale Combustion Simulations. In: Nagel, W., Kröner, D., Resch, M. (Eds.), High Performance Computing in Science and Engineering '18. Springer, pp. 209–224. https://doi.org/10.1007/978-3-030-13325-2_13.
Zirwes, T., Zhang, F., Habisreuther, P., Hansinger, M., Bockhorn, H., Pfitzner, M., Trimis, D., 2020. Quasi-DNS Dataset of a Piloted Flame with Inhomogeneous Inlet Conditions. Flow Turbul. Combust. 104, 997–1027.
Zirwes, T., Häber, T., Zhang, F., Kosaka, H., Dreizler, A., Steinhausen, M., Hasse, C., Stagni, A., Trimis, D., Suntz, R., et al., 2021a. Numerical study of quenching distances for side-wall quenching using detailed diffusion and chemistry. Flow Turbul. Combust. 106, 649–679.
Zirwes, T., Zhang, F., Habisreuther, P., Hansinger, M., Bockhorn, H., Pfitzner, M., Trimis, D., 2021b. Identification of Flame Regimes in Partially Premixed Combustion from a Quasi-DNS Dataset. Flow Turbul. Combust. 106, 373–404.

P3 Proc. Combust. Inst. 39 (2023), 3745–3754

M. Steinhausen, F. Ferraro, M. Schneider, F. Zentgraf, M. Greifenstein, A. Dreizler, C. Hasse, and A. Scholtissek. “Effect of Flame Retardants on Side-Wall Quenching of Partially Premixed Laminar Flames”. In: *Proc. Combust. Inst.* 39 (2023), 3745–3754. DOI: 10.1016/j.proci.2022.07.207

Author contributions

Tab. P.3: Author contributions to publication [P3] following CRediT [110]

Matthias Steinhausen	Conceptualization of the numerical investigation (equal) Implementation and validation of the numerical setup (lead) Conduction of the numerical investigation (lead) Interpretation and discussion of the numerical and experimental results (lead) Data analysis and visualization Data curation Writing – Original draft Main and corresponding author
Max Schneider	Bachelor’s thesis and working student supervised by Matthias Steinhausen Implementation and validation of the numerical setup (supporting) Conduction of the numerical investigation (supporting)
Federica Ferraro **Arne Scholtissek**	Conceptualization of the numerical investigation (equal) Interpretation and discussion of the numerical results (supporting) Supervision (equal)
Florian Zentgraf **Max Greifenstein** **Andreas Dreizler**	Design and conduction of the experiment Provision of the experimental data Interpretation and discussion of the experimental results (supporting)
Christian Hasse	Conceptualization of the numerical investigation (equal) Supervision (equal) Funding acquisition
All co-authors	Writing – Review & Editing

Use of publication contents in finalized and ongoing dissertations

This publication is part of the ongoing dissertation of Matthias Steinhausen at the Institute for Simulation of reactive Thermo-Fluid Systems at the Technical University of Darmstadt, Germany.

Available online at www.sciencedirect.com

ScienceDirect

Proceedings of the Combustion Institute 39 (2023) 3745–3754

Proceedings of the Combustion Institute

www.elsevier.com/locate/proci

Effect of flame retardants on side-wall quenching of partially premixed laminar flames

Matthias Steinhausen [a,*], Federica Ferraro [a], Max Schneider [a], Florian Zentgraf [b], Max Greifenstein [b], Andreas Dreizler [b], Christian Hasse [a], Arne Scholtissek [a]

[a] *Technical University of Darmstadt, Department of Mechanical Engineering, Simulation of reactive Thermo-Fluid Systems, Otto-Berndt-Straße 2, 64287 Darmstadt, Germany*

[b] *Technical University of Darmstadt, Department of Mechanical Engineering, Reactive Flows and Diagnostics, Otto-Berndt-Straße 3, 64287 Darmstadt, Germany*

Received 5 January 2022; accepted 23 July 2022
Available online 20 September 2022

Abstract

A combined experimental and numerical investigation of partially premixed laminar methane-air flames undergoing side-wall quenching (SWQ) is performed. A well-established SWQ burner is adapted to allow the seeding of the main flow with additional gaseous products issued from a (secondary) wall inlet close to the flame's quenching point. First, the characteristics of the partially premixed flame that quenches at the wall are assessed using planar laser-induced fluorescence measurements of the OH radical, and a corresponding numerical simulation with fully-resolved transport and chemistry is conducted. A boundary layer of enriched mixture is formed at the wall, leading to a reaction zone parallel to the wall for high injection rates from the wall inlet. Subsequently, in a numerical study, the wall inflow is mixed with dimethylmethylphosphonat (DMMP), a phosphor-based flame retardant. The DMMP addition allows the assessment of the combined effects of heat loss and flame retardants on the flame structure during flame-wall interaction. With an increasing amount of DMMP in the injected mixture, the flame stabilizes further away from the wall and shows a decrease in the local heat-release rate. Thereby, the maximum wall heat flux is significantly reduced. That results in a lower thermal load on the quenching wall. The flame structure analysis shows an accumulation of the intermediate species HOPO at the wall similar to the CO accumulation during the quenching of premixed flames without flame retardant addition. The study shows how the structure of a partially premixed flame is influenced by a wall that releases either additional fuel or a mixture of fuel and flame retardant. The insights gained from the canonical configuration can lead to a better understanding of the combined effects of flame retardants and heat losses in near-wall flames.
© 2022 The Combustion Institute. Published by Elsevier Inc. All rights reserved.

Keywords: Flame retardants; DMMP; Side-Wall quenching (SWQ); Detailed chemistry (DC); Partially premixed flames

* Corresponding author.
E-mail address: steinhausen@stfs.tu-darmstadt.de (M. Steinhausen).

https://doi.org/10.1016/j.proci.2022.07.207
1540-7489 © 2022 The Combustion Institute. Published by Elsevier Inc. All rights reserved.

1. Introduction

Chemical inhibition of combustion processes is of considerable scientific and practical relevance for the prevention and suppression of fire hazards [1]. Fire retardant compounds are commonly used as additives to polymers to enhance their resistance to ignition and to reduce the flame spread without significantly affecting their properties [2]. They contribute to the gas phase decomposition products with flame extinguishing effects but may also promote the char formation on the polymer surface, which acts as a protective coating [3]. The flame retardant (FR) addition reduces the ignition probability of the material and slows the fire spread, providing more time to escape or for fire suppression activities. Due to their advantageous properties, polymer materials with FR are largely used in construction, furniture, technical equipment, and transportation.

Previous scientific investigations of FRs were mostly related to the search for suitable chemical substances that meet certain criteria, such as flame inhibition, non-hazardousness, and climate friendliness. For example, CF_3Br, also known as Halon 1301, one of the most used FR, has been phased out after the Montreal Protocol in 1987 for its ozone-depleting potential. Several agents have been investigated to identify suitable Halon substitutes with a similar fire suppression efficiency. Phosphorous-containing compounds (PCCs) are one of the most prominent groups of FRs, especially due to their low toxicity and high efficiency [4]. The inhibition mechanism and effectiveness of gaseous FRs are usually investigated in canonical flames. Spherically expanding flames [5], co-flow diffusion flames [6,7], counterflow flames [8,9] and premixed flames [10–12] doped with PCCs have been experimentally investigated to analyze the combustion suppression capability of different PCCs. The ignition delay time has been also investigated in a heated shock tube by Mathieu et al. [13]. Numerical simulations of one-dimensional laminar flames have often been reported in these works to analyze the effects of FR on the flame structure and to validate kinetic mechanisms [11,14–16] for phosphorous-containing mixtures. It has been observed that the effectiveness of PCCs as gas-phase combustion inhibitors varies widely with the flame type [7].

In a fire scenario, the onset of the fire is usually at the surface of a burnable compound and, hence, in proximity to cold walls. In these configurations, the flames are additionally influenced by heat losses to the walls that affect the combustion chemistry. In recent years, detailed experimental and numerical investigations of the combustion chemistry during flame-wall interactions (FWIs) have been carried out in generic configurations. Experimental studies of head-on quenching and side-wall quenching (SWQ) flames were recently reviewed in [17]. Jainski et al. [18] introduced an atmospheric SWQ burner that was extended and used in multiple experimental investigations [19–22] of the thermochemical state and local heat-release rate (HRR) in laminar and turbulent flames. In the most recent studies, Zentgraf et al. measured the thermochemical state, represented by the temperature and the mole fractions of CO and CO_2 (measured simultaneously), in laminar [22] and turbulent [21] flames. In addition to the experiments, corresponding numerical investigations with fully-resolved chemistry and transport were conducted. Ganter et al. [23] investigated the CO production mechanism close to the wall in a two-dimensional subdomain of the SWQ burner, and the authors were able to achieve very good agreement with the measurement results [18]. In a similar numerical configuration, Steinhausen et al. [24] assessed the local HRR in a dimethyl ether-air flame using the measurements performed in [20] as validation data. Palulli et al. [25] assessed the CO formation in laminar SWQ flames prone to velocity fluctuations using a similar setup. Further, the thermochemical state during turbulent FWI has been investigated in multiple direct numerical simulations in a fully developed channel flow [26–28].

Even though FWI and FR have been independently investigated in generic configurations in detailed numerical and experimental studies, only a few combined investigations of the effects of FR and heat losses on the near-wall flame structure are reported in the literature. This study aims to narrow this gap by investigating a partially premixed methane-air flame mixed with dimethylmethylphosphonat (DMMP) undergoing SWQ in a combined numerical and experimental study. First, the SWQ configuration investigated in [22] is extended by a secondary inlet at the wall that allows seeding of the main flow with gaseous products close to the flame's quenching point. This adaption of the burner results in a partially-premixed flame structure that is significantly different from the premixed flames investigated previously [18–22] and enables the assessment of the effect of an active wall releasing fuel or flame retardants towards the flame. With a pure methane inflow at the wall, the behavior of the partially premixed flame during SWQ is assessed with planar laser-induced fluorescence (PLIF) measurements of the OH radical and a corresponding numerical simulation. In a numerical study, the methane inflow from the wall is mixed with DMMP, a PCC, and the combined effects of FR and heat losses on the combustion chemistry are investigated.

2. Experimental and numerical setup

In the following, first, the experimental SWQ burner and the measurement setup are outlined. Secondly, the numerical setup is described. Figure 1

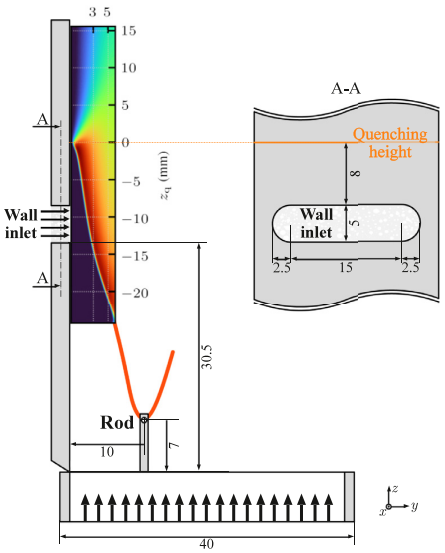

Fig. 1. Schematic view of the SWQ burner and the numerical subdomain used for simulation. In section A-A (right), a slice through the wall is shown. The wall inlet is a porous media through which the methane(-DMMP) mixture is seeded to the main flow. The simulation and measurements are performed in a 2D subdomain that is located in the middle of the wall, i.e., in the middle of the porous media. All scales are given in mm.

shows a schematic view of the SWQ burner and the numerical subdomain investigated in this work. The burner configuration and measurement setup are similar to the one investigated in [22] with a modification of the quenching wall for additional fuel seeding. The burner is operated at ambient conditions (around 293.15 K, 1 atm) and with laminar inflow. At the nozzle exit a fully premixed stoichiometric methane-air flow enters the domain at a Reynolds-number of $\mathrm{Re} = u_{\mathrm{bulk}} d_{\mathrm{h}} / \nu \approx 5900$, with u_{bulk} being the bulk velocity, d_{h} the hydraulic diameter of the nozzle and ν the kinematic viscosity of the mixture. A V-flame is stabilized at a ceramic rod with a diameter of 1 mm. One flame branch is then quenched at the wall with a temperature stabilized at around 333 K. A porous media (sintered structure inlay) is placed inside the wall to allow a secondary inflow close to the flame's quenching point. The wall inlet is located 30.5 mm downstream of the nozzle exit and has a height of 5 mm. The detailed geometry is shown in the sectional drawing A-A in Fig. 1. Through the porous media, methane at around 293.15 K is seeded to the premixed main flow, resulting in a partially premixed methane-air flame in the vicinity of the wall. The volume flow of methane at the wall is controlled by a mass flow controller. In the experimental campaign, the flame is visualized using PLIF measurements of the OH radical, shown in Fig. 2. For the PLIF measurements, the $Q_1(9)+Q_2(8)$ line pair of OH was excited by pulsed UV-radiation around 284 nm using a frequency-doubled dye laser (pumped by a Nd:YAG at 532 nm, 10 Hz). The UV beam was formed to a light sheet with approximately 220 µm thickness. The emission was collected by a UV lens (Sodern, Cerco 2073, 100 mm) equipped with a bandpass filter, and detected by an intensified relay optic (LaVision GmbH) coupled to a CCD camera (LaVision GmbH, Imager E-Lite 1.4M). For more details on the burner geometry and the measurement setup, the reader is referred to the partially premixed investigations performed in [29].

Following previous numerical investigations of the SWQ burner [23,24], the numerical setup consists of a two-dimensional subdomain of the quenching flame branch. The computational mesh is a rectilinear grid with a uniform grid size of 50 µm. The computational domain has a length of 6 mm in the wall-normal direction and a height of 40 mm in the wall-parallel direction as shown in Fig. 1. Similar to Ganter et al. [23] and Steinhausen et al. [24], the inlet is modeled using a generic parabolic velocity profile. Hot exhaust gases are injected in a 0.5 mm wide section to stabilize the flame. In this area, the inflow velocity is increased by a factor of 2.244 to compensate for the density difference of the fresh and burnt gases. The top and right outlets are modeled using zero gradient boundary conditions for enthalpy, species, and velocity. For the pressure, a Dirichlet boundary condition is employed. The wall is modeled using a constant temperature of 333 K, a no-slip boundary condition for the velocity and for the species, a zero gradient boundary condition is employed. At the wall inlet (WI), a zero gradient boundary condition for the pressure is used, while the inflow velocity is assumed to be uniform over the inlet and therefore given by

$$u_{\mathrm{WI}} = \frac{\dot{V}}{A_{\mathrm{WI}}}, \tag{1}$$

with A_{WI} being the total area of the wall inlet and $\dot{V}$ the volume flow through the wall inlet. The species are modeled with a Robin boundary condition that accounts for both diffusive and convective fluxes at the wall

$$\dot{m}_i'' = \dot{m}_{\mathrm{tot}}'' Y_i - \rho D_i \frac{\partial Y_i}{\partial y}, \tag{2}$$

with $\dot{m}_{\mathrm{tot}}''$ being the total mass flux per area, ρ the density of the injected gas and $\dot{m}_i''$, D_i and Y_i being the mass flux per area, the diffusion coefficient and the mass fraction of the species i in the injected gas, respectively. The simulations are performed using an in-house solver with fully-resolved transport and chemistry (FTC) based on OpenFOAM (v2006). The species diffusion coefficients

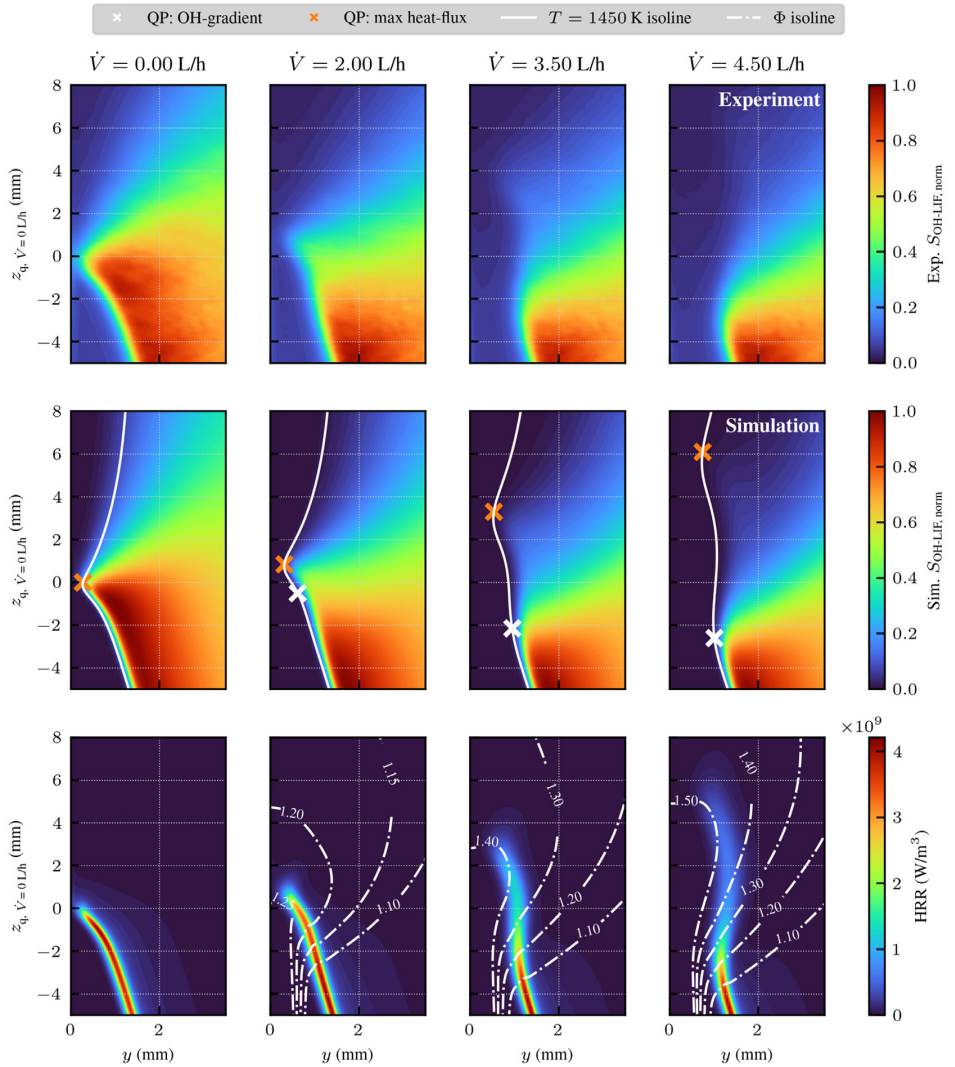

Fig. 2. Normalized OH-PLIF measurements (top), computed OH-PLIF signals (middle) and local HRR (bottom) based on the numerical simulations. Different methane wall inflow rates (left to right) are shown, given in norm liter per hour. In the middle row, the 1450 K temperature isoline is shown together with two quenching point (QP) definitions, based on the OH-gradient and the maximum heat flux to the wall. In the bottom row, isolines of the local equivalence ratio are shown as dashed-dotted lines.

are modeled using a mixture-averaged transport approach [30,31], and the reaction mechanism of Babushok et al. [16] is employed. Due to the minor effect on the results, radiative heat transfer is neglected in the simulations shown in the main part of the paper. For the interested reader, the radiation effects are discussed in the appendix. The results are plotted in a coordinate system relative to the quenching height. Two definitions of the quenching height are used:

- **OH-gradient:** The quenching height is based on the OH-gradient as used in [22–24]. This definition has been mainly used in experi-

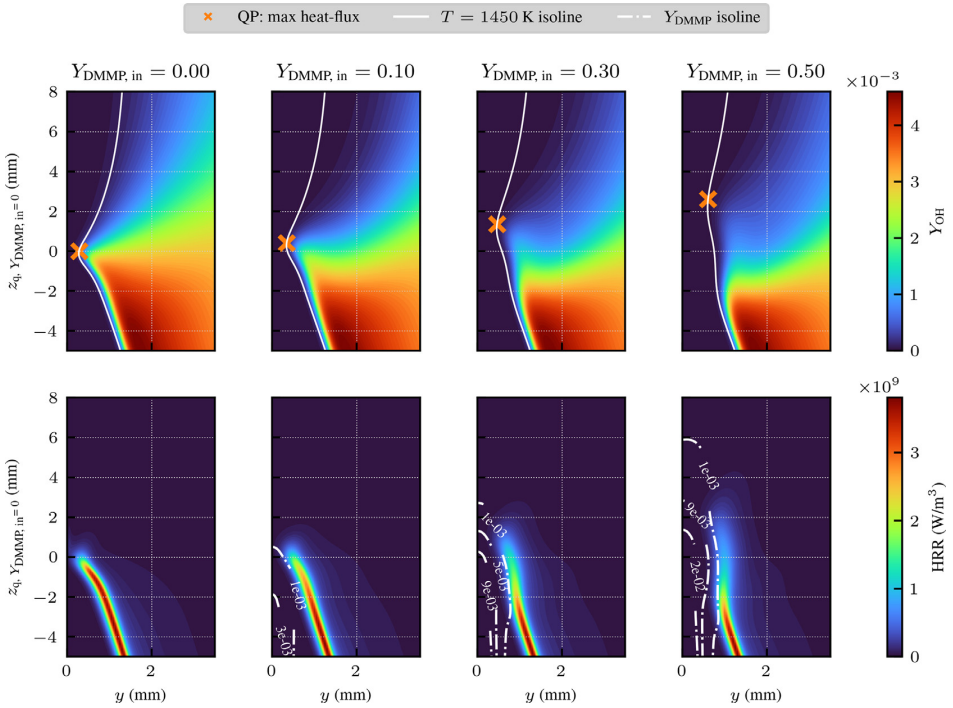

Fig. 3. Mass fraction of OH (top) and local heat-relase rate (bottom). From left to right the amount of DMMP in the injected mixture was increased. In the top row, the 1450 K temperature isoline is shown together with the quenching point based on the maximum heat flux to the wall. In the bottom row, isolines of the DMMP mass fraction are shown as dashed-dotted lines.

mental investigations, where the flame position was determined by qualitative OH-PLIF measurements.

- **Wall heat flux:** The quenching height is located at the maximum heat flux at the wall

$$\dot{q}_{\text{wall}} = -\lambda \left| \frac{\partial T}{\partial y} \right|_{\text{wall}}, \tag{3}$$

with λ being the thermal conductivity and y the wall normal direction. This has also been used in [19].

For both quenching height definitions, the quenching distance y_q is then defined by the wall distance of the 1450 K temperature isoline at the respective quenching height [19].

3. Laminar side-wall quenching with methane addition

Before the effect of flame retardants is discussed, the numerical setup for laminar SWQ with an additional CH_4 wall inflow is validated utilizing OH-PLIF measurements. Furthermore, the characteristics of the partially premixed flame are discussed. Figure 2 shows the measured normalized OH-PLIF signal (top, ensemble-average based on 400 samples) and its numerical counterpart (middle) that is calculated from the thermochemical state of the simulation, following [24]. At the bottom of the plot, the local HRR of the flame is shown together with isolines of the local equivalence ratio (dashed-dotted lines) taken from the numerical simulations. From left to right different injection rates of CH_4 are shown. Note that the wall inflow is very small in comparison to the inflow at the nozzle. For the maximum volume flow shown in Fig. 2 the ratio of the inlet velocities is

$$\frac{u_{\text{WI}}}{u_{\text{bulk}}} = \frac{0.014\ \text{ms}^{-1}}{2.12\ \text{ms}^{-1}} \approx 0.6\,\%. \tag{4}$$

The data are plotted relative to the quenching height based on the OH-gradient of the case without CH_4 addition at the wall ($\dot{V} = 0$ L/h). The experimental (top) and numerical (middle) data are in excellent agreement for all investigated inflow rates. The two quenching point definitions intro-

duced above are shown as white (OH-gradient) and orange (maximum heat flux) markers in the middle row of Fig. 2. While for the flame without an additional wall inflow, the quenching point definitions lead to similar quenching heights, they deviate with increasing methane inflow at the wall (left to right). That is a result of the enrichment of the flame close to the wall. The richer flames produce less OH compared to the stoichiometric flame, resulting in a lowered OH-PLIF signal in the reaction zone of the flame. For these partially premixed flames, the quenching point definition based on the OH-gradient fails to predict the correct quenching location, since the flame is not only affected by heat losses to the wall, but also by the change in the local equivalence ratio. For low inflow rates ($\dot{V} = 2.0$ L/h), the flame is only slightly affected, showing a slight increase in quenching height and distance. At higher inflow rates ($\dot{V} \geq 3.5$ L/h), however, a concentration boundary layer of enriched mixture is formed, leading to a reaction front parallel to the wall at increased quenching height and distance.

4. Effect of flame retardants on side-wall quenching flames

In the following, the effect of FR on the partially premixed methane-air flame is investigated. The case with a wall inflow of 2.0 L/h is chosen as the base case for the analysis since it already shows an influence of the concentration boundary layer on the flame. However, compared to higher inflow rates, the flame shape and quenching distance of the flame are only slightly affected (see Fig. 2), allowing the investigation of the combined effect of heat loss and FR at the wall. In this study, the methane inflow is gradually mixed with the flame retardant DMMP ($Y_{\mathrm{CH_4,\,in}} = 1 - Y_{\mathrm{DMMP,\,in}}$) while keeping the volume flow through the wall inlet constant. The inflow temperature is increased to 373.15 K to prevent condensation of DMMP. Figure 3 shows the simulation results for different compositions of the gas mixture injected at the wall inlet with an increasing amount of DMMP from left to right. Note that the amount of DMMP in the inlet mixture at the wall ($Y_{\mathrm{DMMP,\,in}}$) is much larger than the amount of DMMP in the concentration boundary layer due to the low inflow velocity at the wall inlet ($u_{\mathrm{WI}}/u_{\mathrm{bulk}} < 0.3\,\%$). For $Y_{\mathrm{DMMP,\,in}} = 0.5$ the maximum mass fraction of DMMP in the simulation domain is smaller than 0.1, which is further reduced when approaching the reaction zone of the flame (see the isolines in Fig. 3). The data are plotted relative to the quenching height based on the maximum heat flux of the case without DMMP addition. At the top of the figure, the mass fraction of OH is shown together with the 1450 K temperature isoline and the quenching point based on the maximum wall heat flux for each case. At the bottom, the local HRR of the flame is shown together with isocontours of the DMMP mass fraction. Similar to the pure methane case, a boundary layer of DMMP develops at the wall, which changes the chemical composition of the burning mixture near the wall. This variation in mixture composition is decreasing the local HRR at the flame tip, which also affects the quenching at the wall.

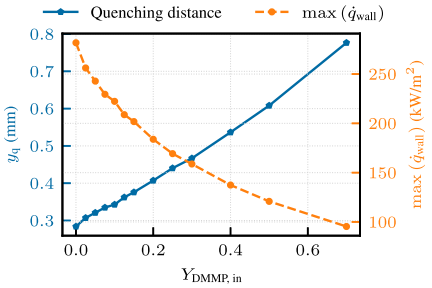

Fig. 4. Quenching distance to the wall based on the maximum wall heat flux and the 1450 K temperature isoline. Additionally, the peak wall heat flux is shown.

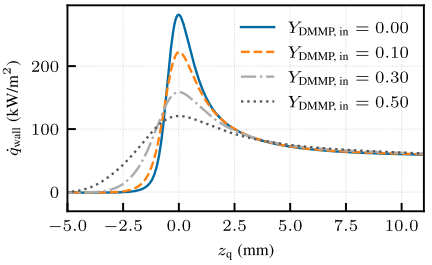

Fig. 5. Wall heat flux over the wall-parallel coordinate for different inflow mixtures injected at the wall inlet.

Figure 4 shows the quenching distance and the maximum wall heat flux as a function of the mass fraction of DMMP in the gas mixture injected at the wall inlet. With an increasing amount of DMMP the quenching point moves downstream (see Fig. 3) and further away from the wall. At the same time, the maximum wall heat flux is decreased. This decrease can be explained by two phenomena: (i) close to the wall a non-flammable mixture is present due to the high amount of FR in the mixture; (ii) the enrichment of FR leads to a lower HRR and subsequently lower temperatures of the mixture with FR. In addition to the maximum wall heat flux, Fig. 5 shows the heat flux profile over the wall-parallel coordinate relative to the quenching height. The addition of FR to the flame results in a significantly lowered peak heat flux at the wall, while the integral heat flux in the quenching region is approximately constant. The lowered peak heat

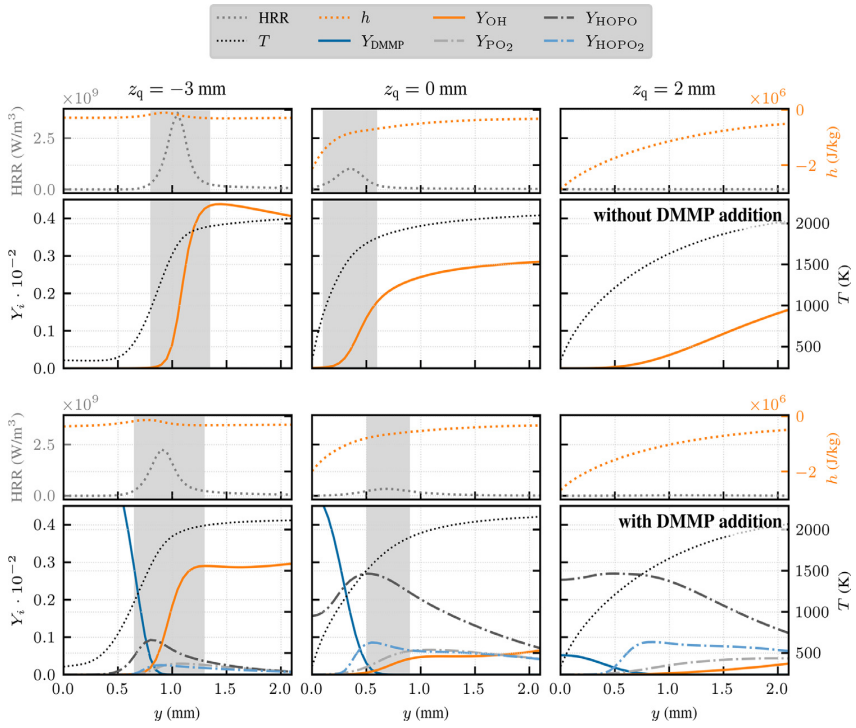

Fig. 6. Flame structure at different stream-wise positions relative to the quenching point based on the maximum heat flux to the wall (orange marker in Fig. 3). The top panel corresponds to the case without DMMP addition at the inlet, while the lower panel corresponds to $Y_{DMMP,\,in} = 0.3$. In the top subplots, the local HRR and the enthalpy are shown, while in the bottom the mass fractions of OH and the most important phosphorous species are depicted. The grey box in the plots depicts the reaction zone of the flame (HRR $> 2 \cdot 10^8$ W/m^3).

flux to the wall reduces the thermal load on the wall and thereby the risk of fire outbreaks.

Figure 6 shows the flame structure at different stream-wise locations for a reference case without the addition of FR (top) and with DMMP addition (bottom), where a mixture of methane and DMMP is injected at the wall inlet. In the individual subplots, the local HRR and total enthalpy h are shown in the top subplot, while at the bottom, the mass fractions of OH, DMMP, PO_2, HOPO and $HOPO_2$ are depicted. Note that the H radical shows a similar trend to the OH radical and is therefore not shown for clarity in the figures. The species were chosen following Babushok et al. [16], who identified these species as those involved in the most relevant reaction pathways of methane-air freely propagating flames diluted with PCCs. In their work, they also provided an illustrative pathway analysis for the reaction pathway of the phosphorous species. First, the local HRR and the enthalpy loss to the wall (top subplots) are discussed for both flames. Then, the flame structure with DMMP addition is assessed in more detail using the mass fraction of OH and the temperature profile of the flame without DMMP addition as a reference. In the region upstream the quenching point ($z_q = -3$ mm) both flames are not yet affected by enthalpy losses to the wall, showing an approximately constant enthalpy profile in the wall-normal direction y. In the flame with DMMP addition, the HRR already shows a lowered peak due to the enrichment of FR in the reaction zone. Once entering the reaction zone, the DMMP is consumed, HOPO is formed and further converted to $HOPO_2$ and PO_2, resulting in a lowered mass fraction of OH and thereby inhibition of the flame. Note, however, that the phosphorous products are only present inside the reaction zone and the burnt part of the flame at higher temperatures and not in the near-wall region. At the quenching point ($z_q = 0$ mm) both flames are affected by enthalpy losses to the wall, resulting in a lowered enthalpy in the near-wall region and a lowered HRR in both flames. Again, the flame with DMMP addition shows a

significantly reduced HRR and mass fraction of OH. It burns further away from the wall, resulting in a decreased temperature gradient and thereby a reduced heat flux to the wall (see Fig. 5). A high amount of the DMMP is already consumed by the flame. In the reaction zone, the amount of the phosphorous species is increased compared to the upstream location. Similar to the upstream direction, PO_2 and $HOPO_2$ are only present in the high-temperature part of the flame. In contrast to that the intermediate phosphorous species HOPO is built up at the wall. Finally, downstream the quenching point ($z_q = 2$ mm) both flames are fully quenched. In this region, DMMP is almost entirely consumed, while HOPO is (still) accumulated at the wall. A similar accumulation can also be observed for CO during laminar SWQ of fully premixed flames [23].

5. Conclusion

In this study, the effect of a (cold) wall, which either releases additional fuel or a mixture of fuel and flame retardant, on a partially premixed flame is assessed in a canonical side-wall quenching configuration. First, the effect of pure fuel addition is considered. Therefore, an established experimental SWQ burner [22] has been adapted to allow seeding of the main flow with gaseous components at the wall near the quenching point. The OH-PLIF measurements are compared to corresponding numerical simulations, which show a very good agreement. The local enrichment at the wall leads to complex partially premixed flames. These flames show an increased quenching distance with increasing inflow rates from the wall inlet and build up a wide reaction zone parallel to the wall at high injection rates. Subsequently, the combined effect of flame retardant and heat loss to the wall is assessed by adding the phosphor-based flame retardant DMMP to the mixture injected at the wall inlet. The addition of DMMP leads to lower local heat-release rates in the flame, which result in higher quenching distances and reduced maximum wall heat fluxes, i.e., a reduced thermal load. Further, the analysis of the structure of the flame with DMMP addition at the wall inlet shows an accumulation of intermediate phosphorous product species (HOPO) in the near-wall region. A similar observation has been made for CO in laminar flames undergoing SWQ without flame retardant addition. The insights gained from this canonical configuration lead to a better understanding of the effect of flame retardants on near-wall combustion, which is of relevance to fire safety and prevention. Future work should address the influence of flame retardants on turbulent boundary layer flames, which could be realized by an extension of the present active wall configuration. Together with suitable experiments, numerical simulations of such configurations could lead to important insights in the field of fire safety.

Declaration of Competing Interest

The authors declare that they have no known competing financial interests or personal relationships that could have appeared to influence the work reported in this paper.

Acknowledgments

This work has been funded by the Deutsche Forschungsgemeinschaft (DFG, German Research Foundation) – Project Number 237267381 – TRR 150. Calculations were conducted on the Lichtenberg high-performance computer of the TU Darmstadt. We thank P. Johe from RSM for his support during the measurements.

Appendix A. Impact of radiative heat transfer

To assess the role of radiation, the case without the additional wall inlet ($\dot{V} = 0.0$ L/h) is simulated with and without modeling radiative heat transfer. The radiation model employed is described in [32]. For the optically thin model (OTM), the radiative heat loss between a given fluid element in the flame and the cold surroundings is given by

$$\dot{Q} = 4\sigma \cdot \left(T^4 - T_b^4\right) \sum_i \left(p_i a_{p,i}\right), \tag{A.1}$$

with $\sigma = 5.669e^{-8}$ W/m^{2}K^4, T and T_b being the local flame temperature and the background temperature, and p_i and $a_{p,i}$ being the partial pressure and the Planck mean absorption coefficient of species i, respectively. The most important radiating species for hydrocarbon flames, i.e. H_2O, CO_2, CO and CH_4, are accounted for and their mean Planck absorption coefficients are calculated using RADCAL [33]. Figure A.1 shows the wall heat flux with and without radiative heat transfer. The inclusion of radiative heat transfer has only a minor effect on the results, which is also confirmed in the maximum heat flux, quenching distance, quenching height, and overall flame structure (not shown here). These findings are in accordance with the typical modeling assumption in flame-wall interactions that "radiative fluxes are neglected [...] because they are small compared to the maximum heat flux obtained when the flame touches the wall" [34]. In the flames diluted with DMMP, the amount of phosphorous species is very small, i.e. the elemental mass fraction is smaller than 1% in the reaction zone of the flame. For this reason, the radiation of the phosphorous species is not expected to be of high relevance due to the low amount of phosphor in the flame. However, the information on the radiative

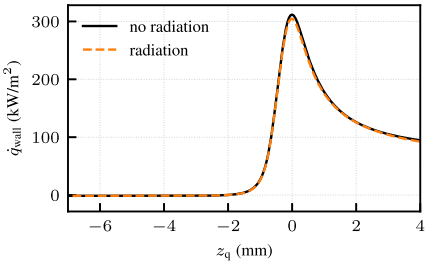

Fig. A.1. Wall heat flux over the wall-parallel coordinate with and without accounting for radiative heat transfer for the case without additional wall inlet ($\dot{V} = 0.0$ L/h).

properties of the phosphorous species is very sparse and their role in radiative heat transfer could be explored in future experimental studies.

References

[1] A.R. Masri, Chemical inhibition of nonpremixed flames of hydrocarbon fuels with CF_3Br, Combust. Sci. Technol. 96 (4–6) (1994) 189–212, doi:10.1080/00102209408935355.

[2] J. Green, Mechanisms for flame retardancy and smoke suppression - a review, J. Fire Sci. 14 (6) (1996) 426–442, doi:10.1177/073490419601400602.

[3] E. Schmitt, Phosphorus-based flame retardants for thermoplastics, Plast. Addit. Compd. 9 (3) (2007) 26–30, doi:10.1016/S1464-391X(07)70067-3.

[4] L. Wang, Y. Jiang, R. Qiu, Experimental study of combustion inhibition by trimethyl phosphate in turbulent premixed methane/air flames using OH-PLIF, Fuel 294 (2021) 120324, doi:10.1016/J.FUEL.2021.120324.

[5] T. Sikes, O. Mathieu, W.D. Kulatilaka, M.S. Mannan, E.L. Petersen, Laminar flame speeds of DEMP, DMMP, and TEP added to H_2- and CH_4-air mixtures, Proc. Combust. Inst. 37 (3) (2019) 3775–3781, doi:10.1016/j.proci.2018.05.042.

[6] N. Bouvet, G.T. Linteris, V.I. Babushok, F. Takahashi, V.R. Katta, R. Krämer, A comparison of the gas-phase fire retardant action of DMMP and Br_2 in co-flow diffusion flame extinguishment, Combust. Flame 169 (2016) 340–348, doi:10.1016/J.COMBUSTFLAME.2016.04.023.

[7] N. Bouvet, G. Linteris, V. Babushok, F. Takahashi, V. Katta, R. Krämer, Experimental and numerical investigation of the gas-phase effectiveness of phosphorus compounds, Fire Mater. 40 (5) (2016) 683–696, doi:10.1002/FAM.2319.

[8] M.A. MacDonald, T.M. Jayaweera, E.M. Fisher, F.C. Gouldin, Inhibition of nonpremixed flames by phosphorus-containing compounds, Combust. Flame 116 (1–2) (1999) 166–176, doi:10.1016/S0010-2180(98)00034-0.

[9] M.A. MacDonald, F.C. Gouldin, E.M. Fisher, Temperature dependence of phosphorus-based flame inhibition, Combust. Flame 125 (4) (2001) 668–683, doi:10.1016/S0010-2180(00)00236-4.

[10] O.P. Korobeinichev, V.M. Shvartsberg, T.A. Bol'shova, A.G. Shmakov, D.A. Knyaz'kov, Inhibition of methane-oxygen flames by organophosphorus compounds, Combust. Explos. Shock Waves 38 (2) (2002) 127–133, doi:10.1023/A:1014937428678.

[11] O.P. Korobeinichev, V.M. Shvartsberg, A.G. Shmakov, T.A. Bolshova, T.M. Jayaweera, C.F. Melius, W.J. Pitz, C.K. Westbrook, H. Curran, Flame inhibition by phosphorus-containing compounds in lean and rich propane flames, Proc. Combust. Inst. 30 (2) (2005) 2353–2360, doi:10.1016/J.PROCI.2004.08.095.

[12] I.V. Rybitskaya, A.G. Shmakov, V.M. Shvartsberg, O.P. Korobeinichev, Effect of the equivalence ratio on the effectiveness of inhibition of laminar premixed hydrogen-air and hydrocarbon-air flames by trimethylphosphate, Combust. Explos. Shock Waves 44 (2) (2008) 133–140, doi:10.1007/S10573-008-0019-8.

[13] O. Mathieu, W.D. Kulatilaka, E.L. Petersen, Experimental and modeling study on the effects of dimethyl methylphosphonate (DMMP) addition on H_2, CH_4, and C_2H_4 ignition, Combust. Flame 191 (2018) 320–334, doi:10.1016/J.COMBUSTFLAME.2018.01.020.

[14] F. Takahashi, V.R. Katta, G.T. Linteris, V.I. Babushok, Numerical study of gas-phase interactions of phosphorus-containing compounds with co-flow diffusion flames, Proc. Combust. Inst. 37 (3) (2019) 4145–4153, doi:10.1016/j.proci.2018.06.140.

[15] T.M. Jayaweera, C.F. Melius, W.J. Pitz, C.K. Westbrook, O.P. Korobeinichev, V.M. Shvartsberg, A.G. Shmakov, I.V. Rybitskaya, H.J. Curran, Flame inhibition by phosphorus-containing compounds over a range of equivalence ratios, Combust. Flame 140 (1–2) (2005) 103–115, doi:10.1016/j.combustflame.2004.11.001.

[16] V.I. Babushok, G.T. Linteris, V.R. Katta, F. Takahashi, Influence of hydrocarbon moiety of DMMP on flame propagation in lean mixtures, Combust. Flame 171 (2016) 168–172, doi:10.1016/J.COMBUSTFLAME.2016.06.019.

[17] A. Dreizler, B. Böhm, Advanced laser diagnostics for an improved understanding of premixed flame-wall interactions, Proc. Combust. Inst. 35 (2015) 37–64, doi:10.1016/j.proci.2014.08.014.

[18] C. Jainski, M. Rißmann, B. Böhm, J. Janicka, A. Dreizler, Sidewall quenching of atmospheric laminar premixed flames studied by laser-based diagnostics, Combust. Flame 183 (2017) 271–282, doi:10.1016/j.combustflame.2017.05.020.

[19] H. Kosaka, F. Zentgraf, A. Scholtissek, L. Bischoff, T. Häber, R. Suntz, B. Albert, C. Hasse, A. Dreizler, Wall heat fluxes and CO formation/oxidation during laminar and turbulent side-wall quenching of methane and DME flames, Int. J. Heat Fluid Flow 70 (2018) 181–192, doi:10.1016/j.ijheatfluidflow.2018.01.009.

[20] H. Kosaka, F. Zentgraf, A. Scholtissek, C. Hasse, A. Dreizler, Effect of flame-Wall interaction on local heat release of methane and DME combustion in a side-Wall quenching geometry, Flow, Turbul. Combust. 104 (4) (2019) 1029–1046, doi:10.1007/s10494-019-00090-4.

[21] F. Zentgraf, P. Johe, A.D. Cutler, R.S. Barlow, B. Böhm, A. Dreizler, Classification of flame prehis-

tory and quenching topology in a side-wall quenching burner at low-intensity turbulence by correlating transport effects with CO_2, CO and temperature, Combust. Flame 239 (2022) 111681, doi:10.1016/j.combustflame.2021.111681.

[22] F. Zentgraf, P. Johe, M. Steinhausen, C. Hasse, M. Greifenstein, A.D. Cutler, R.S. Barlow, A. Dreizler, Detailed assessment of the thermochemistry in a side-wall quenching burner by simultaneous quantitative measurement of CO_2, CO and temperature using laser diagnostics, Combust. Flame 235 (1) (2022) 111707, doi:10.1016/j.combustflame.2021.111707.

[23] S. Ganter, A. Heinrich, T. Meier, G. Kuenne, C. Jainski, M.C. Rißmann, A. Dreizler, J. Janicka, Numerical analysis of laminar methane–air side-wall-quenching, Combust. Flame 186 (2017) 299–310, doi:10.1016/j.combustflame.2017.08.017.

[24] M. Steinhausen, Y. Luo, S. Popp, C. Strassacker, T. Zirwes, H. Kosaka, F. Zentgraf, U. Maas, A. Sadiki, A. Dreizler, C. Hasse, Numerical investigation of local heat-release rates and thermochemical states in side-wall quenching of laminar methane and dimethyl ether flames, Flow, Turbul. Combust. 106 (2) (2021) 681–700, doi:10.1007/s10494-020-00146-w.

[25] R. Palulli, M. Talei, R.L. Gordon, Unsteady flame–wall interaction: impact on CO emission and wall heat flux, Combust. Flame 207 (2019) 406–416, doi:10.1016/J.COMBUSTFLAME.2019.06.012.

[26] A. Gruber, R. Sankaran, E.R. Hawkes, J.H. Chen, Turbulent flame-wall interaction: a direct numerical simulation study, J. Fluid Mech. 658 (2010) 5–32, doi:10.1017/S0022112010001278.

[27] U. Ahmed, N. Chakraborty, M. Klein, Scalar gradient and strain rate statistics in oblique premixed flame-wall interaction within turbulent channel flows, Flow, Turbul. Combust. 106 (2) (2021) 701–732, doi:10.1007/s10494-020-00169-3.

[28] M. Steinhausen, T. Zirwes, F. Ferraro, S. Popp, F. Zhang, H. Bockhorn, C. Hasse, Turbulent flame-wall interaction of premixed flames using quadrature-based moment methods (QbMM) and tabulated chemistry: an a priori analysis, Int. J. Heat Fluid Flow 93 (2) (2022) 108913, doi:10.1016/j.ijheatfluidflow.2021.108913.

[29] F. Zentgraf, Investigation of reaction and transport phenomena during flame-wall interaction using laser diagnostics, Technical University of Darmstadt, 2022 Ph.D. thesis, doi:10.26083/tuprints-00021314.

[30] C.F. Curtiss, J.O. Hirschfelder, Transport properties of multicomponent gas mixtures, J. Chem. Phys. 17 (6) (1949) 550–555, doi:10.1063/1.1747319.

[31] T.P. Coffee, J.M. Heimerl, Transport algorithms for premixed, laminar steady state flames, Combust. Flame 43 (1981) 273–289, doi:10.1016/0010-2180(81)90027-4.

[32] R.S. Barlow, A.N. Karpetis, J.H. Frank, J.-Y. Chen, Scalar profiles and no formation in laminar opposed-flow partially premixed methane/air flames, Combust. Flame 127 (3) (2001) 2102–2118, doi:10.1016/S0010-2180(01)00313-3.

[33] W.L. Grosshandler, RADCAL: A Narrow-Band Model for Radiation Calculations in a Combustion Environment, Technical Report, NIST, 1993.

[34] T. Poinsot, D. Veynante, Theoretical and Numerical Combustion, second ed., R.T. Edwards, Inc., Philadelphia, USA, 2005.

P4 Proc. Combust. Inst. 39 (2023), 2149–2158

M. Steinhausen, T. Zirwes, F. Ferraro, A. Scholtissek, H. Bockhorn, and C. Hasse. “Flame-Vortex Interaction during Turbulent Side-Wall Quenching and Its Implications for Flamelet Manifolds”. In: *Proc. Combust. Inst.* 39 (2023), 2149–2158. DOI: 10.1016/j.proci.2022.09.026

Author contributions

Tab. P.4: Author contributions to publication [P4] following CRediT [110]

Matthias Steinhausen	Conceptualization of the numerical setup and investigation (equal) Detailed analysis and visualization of the flame-vortex interaction phenomena Implementation and validation of the flamelet-based chemistry manifolds Interpretation and discussion of the numerical results (lead) Data analysis and visualization Data curation Writing – Original draft Main and corresponding author
Federica Ferraro **Arne Scholtissek**	Interpretation and discussion of the numerical results (supporting) Supervision (equal)
Thorsten Zirwes	Conduction of the detailed numerical simulation Provision of the detailed numerical simulation data Interpretation and discussion of the DNS results (supporting)
Henning Bockhorn	Supervision (T. Zirwes) Interpretation and discussion of the DNS results (supporting)
Christian Hasse	Conceptualization of the numerical setup and investigation (equal) Supervision (equal) Funding acquisition
All co-authors	Writing – Review & Editing

Use of publication contents in finalized and ongoing dissertations

This publication is part of the ongoing dissertation of Matthias Steinhausen at the Institute for Simulation of reactive Thermo-Fluid Systems at the Technical University of Darmstadt, Germany.

Available online at www.sciencedirect.com

ScienceDirect

Proceedings of the Combustion Institute 39 (2023) 2149–2158

Proceedings of the Combustion Institute

www.elsevier.com/locate/proci

Flame-vortex interaction during turbulent side-wall quenching and its implications for flamelet manifolds

Matthias Steinhausen [a,*], Thorsten Zirwes [b,c], Federica Ferraro [a], Arne Scholtissek [a], Henning Bockhorn [b], Christian Hasse [a]

[a] *Technical University of Darmstadt, Department of Mechanical Engineering, Simulation of reactive Thermo-Fluid Systems, Otto-Berndt-Straße 2, 64287 Darmstadt, Germany*

[b] *Engler-Bunte-Institute, Karlsruhe Institute of Technology, Engler-Bunte-Ring 7, 76131 Karlsruhe, Germany*

[c] *Steinbuch Centre for Computing, Karlsruhe Institute of Technology, Hermann-von-Helmholtz-Platz 1, 76344 Eggenstein-Leopoldshafen, Germany*

Received 22 December 2021; accepted 22 September 2022
Available online 21 October 2022

Abstract

In this study, the thermochemical state during turbulent flame-wall interaction of a stoichiometric methane-air flame is investigated using a fully resolved simulation with detailed chemistry. The turbulent side-wall quenching flame shows both head-on quenching and side-wall quenching-like behavior that significantly affects the CO formation in the near-wall region. The detailed insights from the simulation are used to evaluate a recently proposed flame (tip) vortex interaction mechanism identified from experiments on turbulent side-wall quenching. It describes the entrainment of burnt gases into the fresh gas mixture near the flame's quenching point. The flame behavior and thermochemical states observed in the simulation are similar to the phenomena observed in the experiments. A novel chemistry manifold is presented that accounts for both the effects of flame dilution due to exhaust gas recirculation in the flame vortex interaction area and enthalpy losses to the wall. The manifold is validated in an *a-priori* analysis using the simulation results as a reference. The incorporation of exhaust gas recirculation effects in the manifold leads to a significantly increased prediction accuracy in the near-wall regions of flame-vortex interactions.
© 2022 The Combustion Institute. Published by Elsevier Inc. All rights reserved.

Keywords: Flame-wall interaction; Side-wall quenching (SWQ); Flame-vortex interaction; Chemistry manifold; Turbulence

1. Introduction

Technical combustors for power generation, such as internal combustion engines or gas turbines, are typically operated under turbulent flow conditions and enclosed by walls. The turbulent combustion process in the combustion chamber is a complex multi-scale, multi-physics phenomenon

* Corresponding author.
E-mail address: steinhausen@stfs.tu-darmstadt.de (M. Steinhausen).

https://doi.org/10.1016/j.proci.2022.09.026
1540-7489 © 2022 The Combustion Institute. Published by Elsevier Inc. All rights reserved.

that still poses a challenge for numerical simulations. During turbulent flame-wall interactions (FWIs), the complexity increases even further. In technical systems, the temperature of the combustor walls is often lower than the gas temperature. In these cases, the flame is affected by enthalpy losses at the walls, leading to incomplete combustion, which lowers the overall efficiency and enhances pollutant formation [1]. Additionally, FWI can lead to undesired flame behavior, such as flame flashback [2].

Two major effects need to be considered to simulate turbulent FWI processes: (i) the fluctuations of the reactive scalars and (ii) the influence of the cold walls on the combustion chemistry. In Direct Numerical Simulations (DNS) of FWIs [3–6], all relevant scales of transport and finite-rate chemistry are resolved, resulting in high computational costs that render this approach unfeasible for the simulation of real combustion applications. In the simulation of practical systems, Reynolds-Averaged Navier-Stokes (RANS) and Large Eddy Simulations (LESs) are typically used, which require a suitable turbulence chemistry interaction (TCI) closure model and a reduction of the combustion chemistry. While TCI closure approaches for FWI have been addressed recently [5], this study focuses on the latter using chemistry manifolds [7–10] that combine the high prediction accuracy of the thermochemical state of a finite-rate chemistry simulation with low computational costs.

Chemistry manifolds for FWI have been developed and validated in multiple studies of laminar flames [11–14] against fully resolved finite-rate chemistry simulations and measurements of the near-wall thermochemical states [15,16]. These studies showed that the near-wall flame structure cannot be fully captured by 1D laminar flamelets based on burner-stabilized flames. However, transient head-on quenching (HOQ) flames are suitable to describe the flame structure during FWI. It was validated in quenching laminar flames [11–14] and is extended to turbulent flames in the present work. Recent numerical [6,17] and experimental [18] studies also show a high dependency of the thermochemical state in transient and turbulent FWIs caused by velocity perturbations interacting with the quenching flame. Palulli et al. [17] investigated the influence of velocity perturbations on the near-wall thermochemical state, more specific the local heat-release rate and the CO formation. In that work, a 2D finite-rate chemistry simulation of a side-wall quenching (SWQ) flame was performed that is prone to velocity perturbations of varying frequencies. While at low and high forcing frequency, only SWQ-like behavior was observed, at an intermediate frequency, the flame showed both head-on quenching (HOQ) and SWQ-like behavior that significantly affects the CO formation at the wall. In [6] a 3D DNS of a diluted methane-air flame undergoing SWQ was performed and the CO formation in the flame was analyzed. In the study, the thermochemical state of the DNS was compared to 1D freely propagating flames with different amounts of exhaust gas added to the fresh gas mixture and opposed-flow flames with different strain rates. In the core flow, a good agreement of the thermochemical states was observed. In close vicinity to the wall, however, the thermochemical state was not captured by the adiabatic flame configurations. Finally, Zentgraf et al. [18] investigated the thermochemical state during turbulent atmospheric SWQ using simultaneous quantitative measurements of CO, CO_2 and temperature. They demonstrated that the observed thermochemical states in the turbulent SWQ scenario differ significantly from the laminar configuration investigated in [16]. In accordance to Palulli et al. [17] HOQ and SWQ-like behavior was observed in the turbulent flames. Furthermore, the authors proposed a possible flame-vortex interaction (FVI) mechanism that explains the differences between the observed laminar and turbulent states as originating from the recirculation of burnt exhaust gases into the unburnt part of the flame.

In the present study a three-dimensional fully-resolved simulation with detailed chemistry of the FWI of a stoichiometric methane-air flame in a fully developed turbulent channel flow is performed. The objective of this work is threefold:

(i) to investigate the FVI mechanism proposed in [18] for a turbulent SWQ with a focus on the observed thermochemical states. In this context, the FVI mechanism is numerically verified and analyzed based on a time series of the performed simulation;
(ii) to model the effects of FVI using a novel chemistry manifold that accounts for the effects of exhaust gas recirculation (EGR) and enthalpy losses at the wall;
(iii) to validate the manifold in an *a-priori* manner using the detailed simulation results as a reference.

2. Numerical setup

2.1. Turbulent side-wall quenching flame

In the following, the numerical setup of the turbulent SWQ flame analyzed in this work is outlined. The setup is inspired by Gruber et al. [3] and was used for the analysis of TCI closure in [5]. Figure 1 shows a schematic view of the numerical setup. In a fully developed turbulent channel flow, a V-shaped premixed stoichiometric methane-air flame is stabilized at a flame holder and undergoes side-wall quenching at the (cold) channel walls. The wall temperature is fixed and equal to the inflow temperature $T_{\text{in}} = T_{\text{wall}} = 300$ K. The channel flow has a Reynolds number of $Re = (U_{\text{bulk}} H)/\nu \approx$

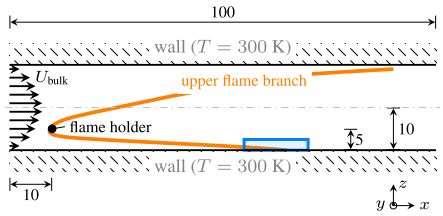

Fig. 1. Schematic of the numerical setup. In the (statistically independent) lateral direction (y) the channel width is 3 cm. The region of interest analyzed in Figs. 3 and 8 is shown as a blue rectangle. All measurements are given in mm. (For interpretation of the references to colour in this figure legend, the reader is referred to the web version of this article.)

2770, with U_{bulk} being the mean flow velocity, H the channel half-width and ν the kinematic viscosity. The mean inflow velocity is $U_{bulk} = 4.4$ ms^{-1}. The flame holder is modeled as a cylindrical region of burnt gas temperature with the center at $H/2$ above the bottom wall. Note that the equivalence ratio and wall temperatures are chosen to allow a comparison of the physical phenomena with recent experimental investigations [18,19]. While the work of Zentgraf et al. [18] focuses on dimethyl ether flames, a methane-air flame was also investigated in the experimental campaign. In their study, the equivalence ratio of the dimethyl ether flame was chosen to match the flame speed of a stoichiometric methane-air flame, which is investigated in this study.

A *non-reactive simulation* of the turbulent channel flow is performed to generate appropriate inflow conditions for the reactive case. The channel dimensions of the non-reactive case are $x \times y \times z = 14H \times 3H \times 2H$, with x being the stream-wise, y the lateral, and z the wall-normal direction. In the stream-wise and lateral direction, periodic boundary conditions are applied, while the wall is modeled with a no-slip boundary condition. The computational grid is refined towards the walls with a wall resolution of 25 μm ($y^+ = 0.24$), resulting in a total of 60 million hexahedral cells. The inflow velocity fields at the boundary serve as inflow conditions for the reactive case and are stored with a time-step of $\Delta t = 3$ μs.

The *reactive simulation* has a reduced channel dimension in stream-wise direction of $10H$. The purely hexahedral, orthogonal mesh is refined towards the bottom wall with a wall resolution of 12 μm ($y^+ = 0.14$) and a total of 200 million cells is used, ensuring a sufficient grid resolution (Kolmogorov length scale $\eta > 45$ μm, laminar flame thickness $\delta_L = (T_{burnt} - T_{unburnt})/|\delta T/\delta x|_{max} \approx 0.5$ mm). Note that the resolution at the bottom wall is motivated by the flame-wall interaction zone, where the flame can move as close as 100μm towards the cold wall [20]. The boundary conditions of the domain are set as follows: At the inlet, the inflow velocity fields from the non-reactive simulation are employed. Therefore, the velocity fields are spatially and temporally interpolated to the inlet boundary face at every time step of the reacting simulation. In the lateral direction, periodic boundary conditions are applied, while the walls are modeled using a no-slip boundary condition for the velocity, a zero-gradient boundary condition for the species, and a fixed temperature boundary condition ($T_{wall} = 300$ K). Finally, at the outlet, a Dirichlet boundary condition is employed for the pressure, while a zero-gradient boundary condition is used for the reactive scalars and the velocity. The source terms are described using a reduced version of the CRECK mechanism [21] that consists of 24 species and 165 reactions and a unity Lewis number assumption for the molecular diffusion coefficients. Table 1 summarises the most important setup parameters.

Table 1
Numerical setup of the reactive case.

Parameter	Property
Gas mixture	Methane-air ($\Phi = 1$)
Reaction mechanism	Reduced CRECK [21]
Diffusion model	Le=1 transport
($x \times y \times z$)	($100 \times 30 \times 20$) mm
Anchor position (x, z)	(10 mm, 5 mm)
Anchor radius	0.9 mm
Bulk velocity	4.4 ms^{-1}
Inlet temperature	300 K
Wall temperature	300 K
Reynolds number	2770

The simulations are performed with an in-house solver [22,23] that uses finite-rate chemistry. In [22] the solver was validated to be suitable for DNS-like simulations using multiple DNS reference cases from the literature. The spatial discretization is of fourth-order, and a second-order fully implicit backward scheme is used for the temporal discretization. The reactive simulation was performed on 32,678 CPU cores (AMD EPYC 7742), and more than 18 million core-h have been consumed.

2.2. Laminar side-wall quenching flame

In addition to the turbulent case, a corresponding laminar SWQ simulation is performed. The setup of the laminar case is similar to the one presented in [5,11]. The simulation is performed in a two-dimensional domain, where a flame is stabilized at the inlet away from the wall by injecting hot exhaust gases at equilibrium conditions. The flame approaches the wall with a wall temperature of 300 K, where it undergoes SWQ. The numerical solver employed is similar to the turbulent simulation described above. The boundary conditions

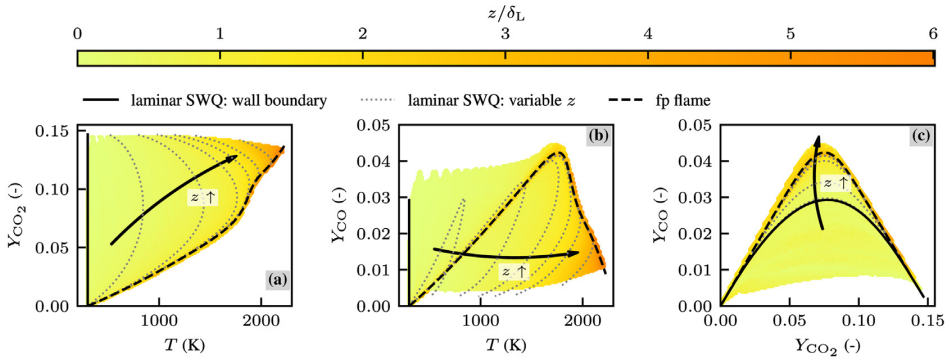

Fig. 2. Thermochemical states in the turbulent SWQ simulation colored by wall distance z. For reference, a 1D freely propagating (fp) flame and lines extracted parallel to the wall from a laminar SWQ are shown.

and the numerical grid of the simulations are equal to the one described in [5] except for the wall temperature.

3. Thermochemical state in turbulent SWQ

In this section, the thermochemical state of the turbulent SWQ simulation is analyzed in the near-wall region up to a normalized wall distance of $z/\delta_L = 6$ and compared to the thermochemical states of laminar SWQ and a freely propagating (fp) flame for reference.

Figures 2(a-c) show the thermochemical states from the turbulent SWQ represented by temperature T and CO_2 and CO mass fractions. The data is colored by the normalized wall distance z/δ_L. In addition to the turbulent SWQ, a corresponding laminar SWQ is shown. The spanned thermochemical state is bounded by the cold wall boundary (solid black line) and a freely propagating flame (dashed black line). Furthermore, different lines extracted parallel to the wall are shown to visualize the influence of the wall distance on the thermochemical state (gray dotted lines).

In the T-Y_{CO_2} plane (Fig. 2(a)), the state space spanned by the turbulent SWQ is also fully covered by its laminar counterpart. Similar observations can be made for T-Y_{CO} in Fig. 2(b). Only for low temperatures, the turbulent case shows states with higher Y_{CO} compared with its laminar counterpart. Finally, the Y_{CO_2}-Y_{CO} plane (Fig. 2(c)) is addressed. In the laminar SWQ, Y_{CO} shows a conditional maximum and minimum for a given value of Y_{CO_2}

$$\max\left(Y_{CO}|Y_{CO_2}\right) = \left(Y_{CO}|Y_{CO_2}\right)_{\text{fp-flame}} \tag{1}$$

$$\min\left(Y_{CO}|Y_{CO_2}\right) = \left(Y_{CO}|Y_{CO_2}\right)_{z=0\text{ mm}} \tag{2}$$

with $\left(Y_{CO}|Y_{CO_2}\right)$ being the value of Y_{CO} for a given value of Y_{CO_2}. While the highest $\left(Y_{CO}|Y_{CO_2}\right)$ is present in the undisturbed part of the flame (freely propagating flame / high wall distance), $\left(Y_{CO}|Y_{CO_2}\right)$ decreases with the wall distance and reaches a minimum at the wall ($z = 0$ mm), where the flame is quenched and cooled down to wall temperature. In the turbulent SWQ, the minimum value of $\left(Y_{CO}|Y_{CO_2}\right)$ is lower compared to the laminar counterpart, showing values comparable to the unburnt and burnt gas state over the whole range of Y_{CO_2}. A flame-vortex interaction (FVI) mechanism was proposed in [18] that explains the differences in the observed states of the laminar and turbulent SWQ originating from the mixing of (cold) burnt products with unburnt gases in the close vicinity of the quenching point.

To assess this hypothesis, Fig. 3 shows a time series for a slice of the flame in the lateral direction that displays a representative time series found in the turbulent SWQ flame. The area shown in the slice is marked by the blue box in Fig. 1. On the left, the flame is visualized by the reaction rate of CO_2, together with vortical structures indicated by the Q-criterion [24] (white lines). On the right, Y_{CO_2} is shown, as well as the reaction zone of the flame (black isoline of $\dot{\omega}_{CO_2} = 400$ 1/s). Furthermore, the area where Y_{CO} falls below the conditional minimum of the laminar SWQ flame (Fig. 2(c)) is indicated by a white isoline. In the following, this area is referred to as the area of FVI. In Fig. 4, a schematic representation of the FVI mechanism is shown for the same area and time steps that are depicted in Fig. 3. At $t = 0$ ms the flame is in a SWQ-like state, and no areas of FVI are observed. A vortical structure is present downstream of the flame tip. The flame tip propagates into the vortical structure, pushing the vortex in the stream-wise direction. This forwards motion, together with the entrainment of hot exhaust gases at the wall, leads to the mixing of cold, burnt products and fresh gases below the reaction zone and thus between the flame branch and the cold wall (see $t = [0.55, 1.1]$ ms).

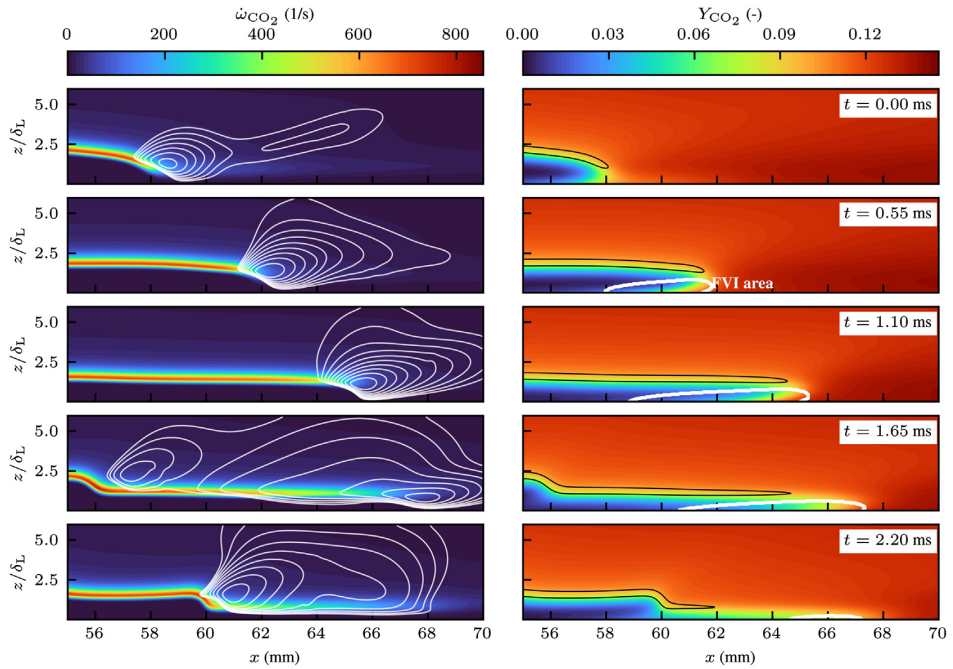

Fig. 3. Time series of a slice in lateral direction through the turbulent flame. On the left, the reaction rate of CO_2 is shown together with vortical structures visualized by the Q-criterion (white lines). On the right, Y_{CO_2} is shown and the flame front is visualized by a contour of $\dot{\omega}_{CO_2}$ (black). Additionally, the white isocontour represents the area of FVI. The area shown in the slices is also depicted Fig. 1 as a blue rectangle. (For interpretation of the references to colour in this figure legend, the reader is referred to the web version of this article.)

The mixing changes the flame velocity at the flame tip, leading to decreased heat release at the flame tip ($t = 1.65$ ms). At the same time, the vortex above the flame front spreads over a wide area and pushes the flame against the wall, resulting in a HOQ-like quenching region parallel to the wall ($t = 2.2$ ms). After the flame has been pushed back, it spreads out again, and the FVI mechanism described is repeated. The observed flame behavior is in agreement with the experimental hypothesis by Zentgraf et al. [18] and is mainly driven by the interaction of the flame with the near-wall vortical structures. It is not restricted to the equivalence ratio or even fuel. A video of the temporal evolution of the flame can be found in the supplementary material, including two additional lateral positions.

To assess the importance of the FVI mechanism, Fig. 5 shows a wall-parallel cut through the simulation domain at $z/\delta_L = 0.2$ and $t = 1.1$ ms. The investigated flow configuration is statistically independent in the lateral direction. Therefore, the lateral direction can be understood as multiple realizations of the temporal flame evolution, and the wall-normal cut is a reasonable indication for the likelihood of the exhaust gas recirculation events caused by FVI at a given wall distance. In the figure, the area of FVI, indicated by the white isoline, is distributed over most of the reaction zone of the flame. A similar picture can also be observed at other time instances of the flame. With increasing distance from the wall, the area affected by FVI decreases, see also Fig. 9. This shows the importance of FVI events in turbulent FWI, since in the near-wall region most of the reaction zone of the flame is prone to exhaust gas recirculation effects. Twenty simulation time steps throughout 5 ms have been analyzed concerning the probability of a FVI event to emphasize this aspect even further. Thereby, a FVI event was counted for every time step and lateral direction, if $\left(Y_{CO}|Y_{CO_2}\right)$ falls below the laminar SWQ simulation counterpart for more than one stream-wise location. In the analysis more than 80 % of the lateral locations are prone to exhaust gas recirculation, confirming the observations made in the single time step shown in Fig. 5. In the supplementary material the temporal evolution of three wall-normal slices at different wall distances are provided, additionally.

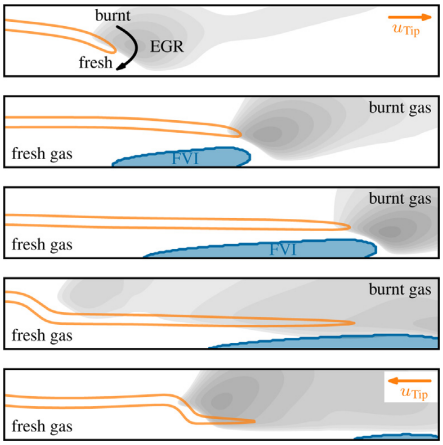

Fig. 4. Annotated visualization of the FVI mechanism shown in Fig. 3. In orange, the flame front visualized by a contour of $\dot{\omega}_{CO_2}$ is shown, while the area of FVI is colored in blue. The vertical structures are shown in grey. (For interpretation of the references to colour in this figure legend, the reader is referred to the web version of this article.)

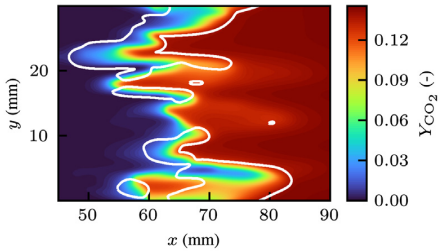

Fig. 5. Wall-parallel cut through the simulation domain at $z/\delta_L = 0.2$ and $t = 1.1$ ms. The FVI area is indicated by the white isoline. The statistically independent lateral direction (y) can be understood as multiple realizations of the temporal flame evolution.

4. Flamelet manifolds for turbulent SWQ

Based on the above discussion, a novel manifold is proposed for turbulent SWQ as an extension of Quenching Flamelet-Generated Manifolds (QFMs) [13,14]. In particular, an additional dimension is introduced to include the effects of exhaust gas recirculation (EGR) on the thermochemical state. The manifold consists of an ensemble of 1D HOQ flames. Starting from a freely propagating flame with fresh mixture on the unburnt side, the flame is gradually diluted with cold exhaust gases at inflow temperature. Each of the diluted flames is then used as the initial condition for a transient HOQ simulation with a wall temperature of 300 K. The numerical setup for the HOQ flames is described in detail in [13]. In total, 63 HOQ flames are calculated with varying EGR levels from 0 to 0.3. Further, the upper boundary of the manifold is extended using preheated HOQ flames ranging from 300 K to 750 K. The ensemble of HOQ flames spans a 3D manifold in (x, t, Y_{EGR}) space, with x being the spatial coordinate, t the time, and Y_{EGR} the amount of (cold) burnt gases mixed into the fresh gases. Figure 6 shows the thermochemical state from the HOQ manifold with and without EGR compared against the turbulent SWQ. The diluted flamelets exhibit a lowered limit of $(Y_{CO}|Y_{CO_2})$ and can cover the complete thermochemical state of the turbulent SWQ configuration.

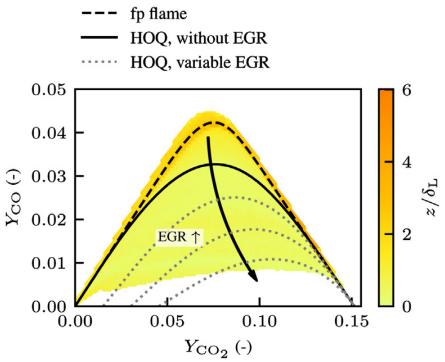

Fig. 6. Thermochemical states in the SWQ simulation colored by normalized wall distance z/δ_L. Additionally, reference data from 1D Head-On Quenching (HOQ) simulations and a freely propagating (fp) flame is shown.

The newly developed manifold is mapped in a three-step procedure onto a (c, c_2, h_{norm}) state with a resolution of ($150 \times 201 \times 101$). The variables c and c_2 are normalized progress variables and h_{norm} is the normalized enthalpy based on the total enthalpy h as sum of sensible and enthalpy of formation

$$c = \frac{Y_c - Y_{c,min}}{Y_{c,max} - Y_{c,min}} \tag{3}$$

$$c_2 = \frac{Y_{c,2} - Y_{c,2,min}(c)}{Y_{c,2,max}(c) - Y_{c,2,min}(c)} \tag{4}$$

$$h_{norm} = \frac{h - h_{min}(c, c_2)}{h_{max}(c, c_2) - h_{min}(c, c_2)} \tag{5}$$

The mapped manifold can then be accessed in a three-step look-up with c being the first, c_2 the second, and h_{norm} the third look-up parameter. The first and second progress variable Y_c and $Y_{c,2}$ are chosen to be the mass fraction of CO_2 and CO, respectively. The final manifold is referred to as QFM-EGR (Quenching Flamelet-Generated Manifold with Exhaust Gas Recirculation).

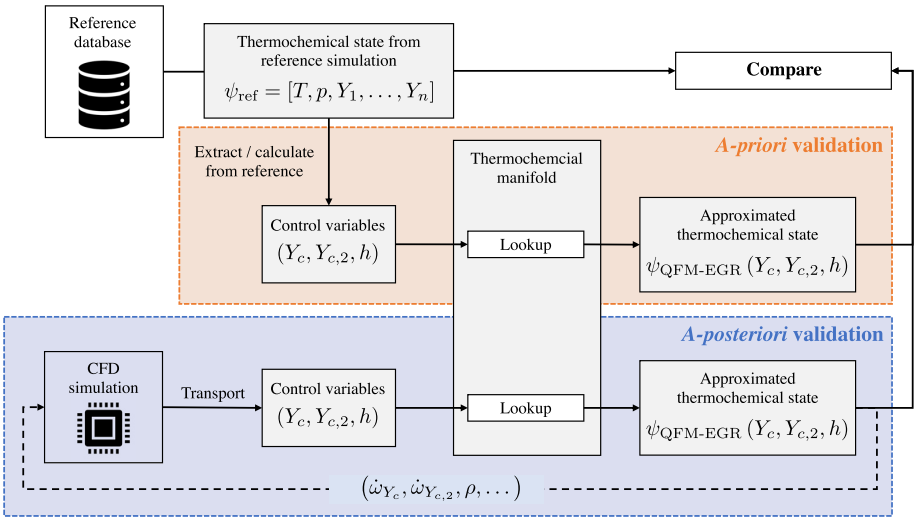

Fig. 7. Schematic representation of an *a-priori* analysis in comparison to an *a-posteriori* assessment in a fully coupled simulation. The approximated thermochemical states are compared to the reference data (here: turbulent SWQ simulation). The control variables shown in the figures correspond to the 3D QFM-EGR. For other manifolds the choice of control variables may differ. Note that in the CFD, the non-normalized progress variables are solved for. The normalized progress variables as shown in Eqs. (3)-(5) are calculated during the lookup on the manifold.

5. *A-priori* validation of the extended manifold

The extended 3D QFM-EGR is validated in an *a-priori* analysis using the turbulent SWQ simulation data as a reference. Figure 7 shows the procedure of the *a-priori* manifold assessment in comparison to a fully coupled (*a-posteriori*) validation. While in the fully coupled simulation transport equations for the control variables of the manifold are solved, in the *a-priori* validation, the control variables are taken directly from the reference data. This allows a detailed validation of the tabulated thermochemical state without the interference of errors caused by the inaccuracies in the solution of the transport equations in a coupled simulation.

Figure 8 shows the results of the *a-priori* validation for a QFM with two table dimensions and the extended three-dimensional QFM-EGR on the slice shown in Fig. 3 at $t = 1.10$ ms. The QFM consists of a single HOQ simulation of a freely propagating flame without EGR and, therefore, represents a subset of the QFM-EGR. The manifold generation of the QFM is described in more detail in [13,14]. The color code shows the relative deviation of the approximated quantity q from the reference data (turbulent SWQ simulation).

$$\Delta q = \frac{q_{\text{ref}} - q_{\text{Manifold}}}{q_{\text{ref}}} \tag{6}$$

In accordance with Fig. 3, the flame front is visualized (orange contour), and the area of FVI is shown

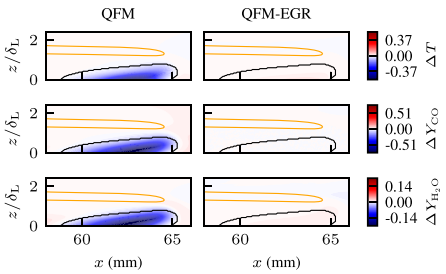

Fig. 8. Normalized difference between *a-priori* lookup quantities and the validation state at $t = 1.10$ ms. The plot shows results from 2D QFM (left) and the novel QFM-EGR (right) derived in this work. Note that the figure shows a zoom of the relevant area depicted in Fig. 3.

(black isoline). On the left, the lookup result for a QFM is shown, while on the right the QFM-EGR is depicted. Both manifolds show good agreement outside the area of FVI. Inside that area, however, the QFM shows discrepancies of up to 70 % for all species studied, indicating that not only the mass fraction of CO is incorrectly predicted, but the mixture at the wall in the reference data is not consistent with the tabulated states in the QFM. This results in an incorrect prediction of the composition space as a whole. The new tabulation approach ac-

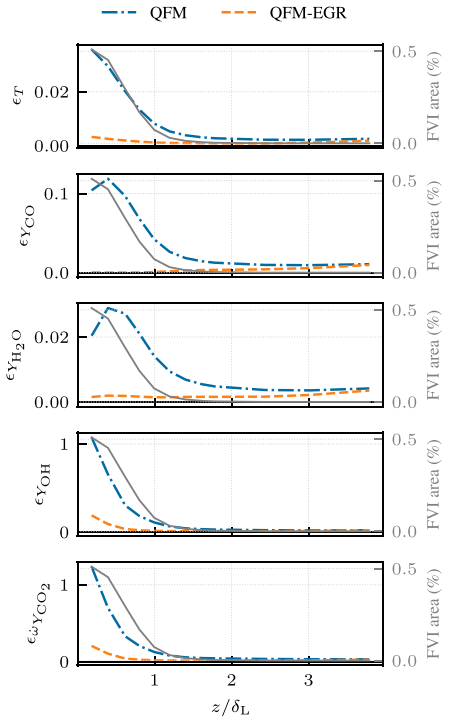

Fig. 9. Mean relative error of the *a-priori* lookup quantities and the reference simulation as a function of the normalized wall distance z/δ_L.

counts for this shift in mixture caused by the EGR by introducing the additional table dimension c_2, leading to a very good agreement with the reference simulation. In addition to the data shown, further time series of the *a-priori* validation are provided in the supplementary material for different lateral and wall-normal slices. The data also includes radicals and reaction rate predictions. The supplementary videos show the reference simulation and the prediction by the manifolds on the left, while the manifold deviations from the reference are depicted on the right.

Finally, Fig. 9 shows the mean relative error for a quantity q

$$\epsilon_q(z) = \frac{1}{N} \frac{\sum_{\Omega(z)} \left| q_{i,\mathrm{ref}} - q_{i,\mathrm{Manifold}} \right|}{\sum_{\Omega(z)} \left| q_{i,\mathrm{ref}} \right|}, \tag{7}$$

with N being the number of samples in Ω (reaction zone of the flame) and

$$\Omega(z) = \{(t, x, y, z) | c^* \in [0.3, 0.7] \wedge z = z\} \tag{8}$$

with

$$c^* = \frac{Y_{CO_2} - Y_{CO_2,min}(h)}{Y_{CO_2,max}(h) - Y_{CO_2,min}(h)} \tag{9}$$

being the normalized progress variable based on a given enthalpy. This definition was also used in [5] to track the reaction zone of the flame. The time average is calculated using twenty simulation time steps throughout 5 ms. In addition to the quantities discussed above, the mass fraction of the OH-radical Y_{OH} and the reaction rate of CO_2 are depicted. Again, the QFM prediction capability worsens in the areas of FVI close to the wall. Outside the FVI area ($z/\delta_L > 2$), the prediction accuracy of the QFM is very good, only slight deviations are found for the CO and H_2O mass fraction. The QFM-EGR shows an excellent agreement with the reference solution. Note that the observed increase in prediction error of the radicals and reaction rates in the near-wall region is not due to an increase in the absolute prediction error, but due to the fact, that the value of both the OH-radical mass fraction and reaction rate approach zero due to the high enthalpy losses at the wall.

6. Conclusion

In the present study, the thermochemical state of a turbulent methane-air flame interacting with a cold wall is investigated using a fully resolved simulation with detailed chemistry. The detailed insights from the simulation are used to confirm a recently proposed flame-vortex interaction mechanism, which describes the entrainment of burnt gases into the fresh gas mixture near the flame's quenching point. Based on these findings, an extended flamelet manifold generated from an ensemble of 1D HOQ flames is presented, accounting for this particular mixing process. In the manifold, the effects of flame-vortex interaction on the thermochemical state are accounted for by introducing a new dimension to the manifold, which accounts for the shift in mixture caused by exhaust gas recirculation. The new manifold is validated in an *a-priori* analysis. Without the additional dimension, large deviations between the previous manifold prediction (QFM) and the detailed reference simulation are observed in the flame-vortex interaction area near the cold wall. Accounting for exhaust gas recirculation in the manifold leads to significant improvements in the prediction of the thermochemical states. The improved manifold (QFM-EGR) constitutes a significant advance for the modeling of turbulent SWQ and will be further evaluated in coupled LES in future work.

Declaration of Competing Interest

The authors declare that they have no known competing financial interests or personal relationships that could have appeared to influence the work reported in this paper.

Acknowledgments

This work has been funded by the Deutsche Forschungsgemeinschaft (DFG, German Research Foundation) – Project Number 237267381 – TRR 150 and the Center of Excellence in Combustion project, grant agreement No. 952181 (F. Ferraro). The simulations were performed on the national supercomputer HAWK at the High Performance Computing Center Stuttgart (HLRS).

Supplementary material

Supplementary material associated with this article can be found, in the online version, at doi:10.1016/j.proci.2022.09.026.

References

[1] T. Poinsot, D. Veynante, Theoretical and numerical combustion, 2nd, R.T. Edwards, Inc., Philadelphia, USA, 2005.
[2] J. Fritz, M. Kröner, T. Sattelmayer, Flashback in a Swirl Burner With Cylindrical Premixing Zone, J. Eng. Gas Turbines Power 126 (2) (2004) 276–283, doi:10.1115/1.1473155.
[3] A. Gruber, R. Sankaran, E.R. Hawkes, J.H. Chen, Turbulent flame-wall interaction: a direct numerical simulation study, J. Fluid Mech. 658 (2010) 5–32, doi:10.1017/S0022112010001278.
[4] U. Ahmed, N. Chakraborty, M. Klein, Scalar Gradient and Strain Rate Statistics in Oblique Premixed Flame-Wall Interaction Within Turbulent Channel Flows, Flow, Turbul. Combust. 106 (2) (2021) 701–732, doi:10.1007/s10494-020-00169-3.
[5] M. Steinhausen, T. Zirwes, F. Ferraro, S. Popp, F. Zhang, H. Bockhorn, C. Hasse, Turbulent flame-wall interaction of premixed flames using Quadrature-based Moment Methods (QbMM) and tabulated chemistry: An a priori analysis, Int. J. Heat Fluid Flow 93 (2) (2022) 108913, doi:10.1016/j.ijheatfluidflow.2021.108913.
[6] B. Jiang, D. Brouzet, M. Talei, R.L. Gordon, Q. Cazeres, B. Cuenot, Turbulent flame-wall interactions for flames diluted by hot combustion products, Combust. Flame 230 (8) (2021) 111432, doi:10.1016/j.combustflame.2021.111432.
[7] J.A. van Oijen, L.P.H. de Goey, Modelling of Premixed Laminar Flames using Flamelet-Generated Manifolds, Combust. Sci. Technol. 161 (1) (2000) 113–137, doi:10.1080/00102200008935814.
[8] O. Gicquel, N. Darabiha, D. Thévenin, Laminar premixed hydrogen/air counterflow flame simulations using flame prolongation of ILDM with differential diffusion, Proc. Combust. Inst. 28 (2) (2000) 1901–1908, doi:10.1016/s0082-0784(00)80594-9.
[9] U. Maas, S.B. Pope, Simplifying chemical kinetics: Intrinsic low-dimensional manifolds in composition space, Combust. Flame 88 (1992) 239–264, doi:10.1016/0010-2180(92)90034-M.
[10] V. Bykov, U. Maas, The extension of the ILDM concept to reaction-diffusion manifolds, Combust. Theory Model. 11 (6) (2007) 839–862, doi:10.1080/13647830701242531.
[11] S. Ganter, C. Straßacker, G. Kuenne, T. Meier, A. Heinrich, U. Maas, J. Janicka, Laminar near-wall combustion: Analysis of tabulated chemistry simulations by means of detailed kinetics, Int. J. Heat Fluid Flow 70 (2018) 259–270, doi:10.1016/j.ijheatfluidflow.2018.02.015.
[12] C. Strassacker, V. Bykov, U. Maas, Comparative analysis of Reaction-Diffusion Manifold based reduced models for Head-On- and Side-Wall-Quenching flames, Proc. Combust. Inst. 38 (1) (2021) 1025–1032, doi:10.1016/J.PROCI.2020.06.130.
[13] M. Steinhausen, Y. Luo, S. Popp, C. Strassacker, T. Zirwes, H. Kosaka, F. Zentgraf, U. Maas, A. Sadiki, A. Dreizler, C. Hasse, Numerical Investigation of Local Heat-Release Rates and Thermo-Chemical States in Side-Wall Quenching of Laminar Methane and Dimethyl Ether Flames, Flow Turbul. Combust. 106 (2) (2021) 681–700, doi:10.1007/s10494-020-00146-w.
[14] D.V. Efimov, P. de Goey, J.A. van Oijen, QFM: quenching flamelet-generated manifold for modelling of flame–wall interactions, Combust. Theory Model. 24 (1) (2020) 72–104, doi:10.1080/13647830.2019.1658901.
[15] H. Kosaka, F. Zentgraf, A. Scholtissek, L. Bischoff, T. Häber, R. Suntz, B. Albert, C. Hasse, A. Dreizler, Wall heat fluxes and CO formation/oxidation during laminar and turbulent side-wall quenching of methane and DME flames, Int. J. Heat Fluid Flow 70 (1) (2018) 181–192, doi:10.1016/j.ijheatfluidflow.2018.01.009.
[16] F. Zentgraf, P. Johe, M. Steinhausen, C. Hasse, M. Greifenstein, A.D. Cutler, R.S. Barlow, A. Dreizler, Detailed assessment of the thermochemistry in a side-wall quenching burner by simultaneous quantitative measurement of CO2, CO and temperature using laser diagnostics, Combust. Flame 235 (1) (2022) 111707, doi:10.1016/j.combustflame.2021.111707.
[17] R. Palulli, M. Talei, R.L. Gordon, Unsteady flame–wall interaction: Impact on CO emission and wall heat flux, Combust. Flame 207 (2019) 406–416, doi:10.1016/J.COMBUSTFLAME.2019.06.012.
[18] F. Zentgraf, P. Johe, A.D. Cutler, R.S. Barlow, B. Böhm, A. Dreizler, Classification of flame prehistory and quenching topology in a side-wall quenching burner at low-intensity turbulence by correlating transport effects with CO2, CO and temperature, Combust. Flame (2021) 111681, doi:10.1016/j.combustflame.2021.111681.
[19] C. Jainski, M. Rißmann, B. Böhm, A. Dreizler, Experimental investigation of flame surface density and mean reaction rate during flame-wall interaction, Proc. Combust. Inst. 36 (2) (2017) 1827–1834, doi:10.1016/j.proci.2016.07.113.
[20] T. Zirwes, T. Häber, F. Zhang, H. Kosaka, A. Dreizler, M. Steinhausen, C. Hasse, A. Stagni, D. Trimis, R. Suntz, H. Bockhorn, Numerical Study of Quenching Distances for Side-Wall Quenching Using Detailed Diffusion and Chemistry, Flow Turbul. Combust. 106 (2) (2021) 649–679, doi:10.1007/s10494-020-00215-0.
[21] E. Ranzi, A. Frassoldati, R. Grana, A. Cuoci, T. Faravelli, A.P. Kelley, C.K. Law, Hierarchical and comparative kinetic modeling of laminar flame speeds of hydrocarbon and oxygenated fuels, (2012). doi:10.1016/j.pecs.2012.03.004.
[22] T. Zirwes, F. Zhang, J.A. Denev, P. Habisreuther, H. Bockhorn, Automated Code Generation for Max-

imizing Performance of Detailed Chemistry Calculations in OpenFOAM, in: High Perform. Comput. Sci. Eng. 17 Trans. High Perform. Comput. Center, Stuttgart 2017, Springer International Publishing, 2018, pp. 189–204, doi:10.1007/978-3-319-68394-2_11.

[23] T. Zirwes, F. Zhang, J.A. Denev, P. Habisreuther, H. Bockhorn, D. Trimis, Improved Vectorization for Efficient Chemistry Computations in OpenFOAM for Large Scale Combustion Simulations, in: W.E. Nagel, D.H. Kröner, M.M. Resch (Eds.), High Perform. Comput. Sci. Eng. '18, Springer, 2018, pp. 209–224, doi:10.1007/978-3-030-13325-2_13.

[24] J. Hunt, A. Wray, P. Moin, Eddies, Steams, and Convergence Zones in Turbulent Flows, in: Cent. Turbul. Res. Proc. Summer Progr., 1988, pp. 193–208.

P5 Combust. Flame 255 (2023), 112923

Y. Luo, **M. Steinhausen**, D. Kaddar, C. Hasse, and F. Ferraro. “Assessment of Flamelet Manifolds for Turbulent Flame-Wall Interactions in Large-Eddy Simulations”. In: *Combust. Flame* 255 (2023), 112923. DOI: 10.1016/j.combustflame.2023.112923

Author contributions

Tab. P.5: Author contributions to publication [P5] following CRediT [110]

Yujuan Luo	Implementation and validation of the numerical setup (lead) Implementation and validation of the Lagrangian particle tracking Conduction of the numerical simulations Interpretation and discussion of the numerical results (equal) Data analysis and visualization Data curation Writing – Original draft Main and corresponding author
Matthias Steinhausen	Conceptualization of the numerical setup and investigation (equal) Implementation and validation of the numerical setup (supporting) Implementation, validation, and provision of the flamelet-based manifolds Implementation and validation of the flamelet coupling in OpenFOAM (lead) Interpretation and discussion of the numerical results (equal) Writing – Review & Editing (equal)
Driss Kaddar	Implementation and validation of the numerical setup (supporting) Interpretation and discussion of the numerical results (equal) Writing – Review & Editing (equal)
Federica Ferraro	Interpretation and discussion of the numerical results (equal) Supervision (equal) Writing – Review & Editing (equal)
Christian Hasse	Conceptualization of the numerical setup and investigation (equal) Supervision (equal) Funding acquisition Writing – Review & Editing (equal)

Use of publication contents in finalized and ongoing dissertations

Parts of this publication are used in the dissertation of Yujuan Luo [111] who conducted the numerical study and was the corresponding and main author of the publication. This publication is part of the ongoing dissertation of Matthias Steinhausen at the Institute for Simulation of reactive Thermo-Fluid Systems at the Technical University of Darmstadt, Germany. Other than the dissertation of Yujuan Luo and the ongoing dissertation of Matthias Steinhausen, this publication is not the subject of any further ongoing or completed dissertation.

Combustion and Flame 255 (2023) 112923

Contents lists available at ScienceDirect

Combustion and Flame

journal homepage: www.elsevier.com/locate/combustflame

Assessment of flamelet manifolds for turbulent flame-wall interactions in large-eddy simulations

Yujuan Luo*, Matthias Steinhausen, Driss Kaddar, Christian Hasse, Federica Ferraro

Technical University of Darmstadt, Department of Mechanical Engineering, Simulation of Reactive Thermo-Fluid Systems, Otto-Berndt-Str. 2, Darmstadt 64287, Germany

ARTICLE INFO

Article history:
Received 6 March 2023
Revised 23 June 2023
Accepted 23 June 2023
Available online 1 July 2023

Keywords:
Flame-wall interaction
Turbulence
Flame-vortex interaction
FGM
QFM
QFM-EGR

ABSTRACT

A turbulent side-wall quenching (SWQ) flame in a fully developed channel flow is studied using Large-Eddy Simulation (LES) with a tabulated chemistry approach. Three different flamelet manifolds with increasing levels of complexity are applied: the Flamelet-Generated Manifold (FGM) considering varying enthalpy levels, the Quenching Flamelet-Generated Manifold (QFM), and the recently proposed Quenching Flamelet-Generated Manifold with Exhaust Gas Recirculation (QFM-EGR), with the purpose being to assess their capability to predict turbulent flame-wall interactions (FWIs), which are highly relevant to numerical simulations of real devices such as gas turbines and internal combustion engines.

The accuracy of the three manifolds is evaluated and compared a posteriori, using the data from a previously published flame-resolved simulation with detailed chemistry for reference. For LES with the FGM, the main characteristics such as the mean flow field, temperature, and major species can be captured well, while notable deviations from the reference results are observed for the near-wall region, especially for pollutant species such as CO. In accordance with the findings from laminar FWI, improvement is also observed in the simulation with QFM under turbulent flow conditions. Although LES with the QFM-EGR shows a similar performance in the prediction of mean quantities as LES with QFM, it presents significantly better agreement with the reference data regarding instantaneous thermo-chemical states near the quenching point. This indicates the necessity to take into account the mixing effects in the flamelet manifold to correctly capture the flame-vortex interaction near the flame tip in turbulent configurations. Based on the findings from this study, suitable flamelet manifolds can be chosen depending on the aspects of interest in practical applications.

© 2023 The Combustion Institute. Published by Elsevier Inc. All rights reserved.

1. Introduction

Combustion is a major way to generate power in modern society. Practical applications are usually operated in turbulent conditions. This results in a multi-physics phenomenon covering a wide range of length and time scales. When the combustion occurs in a confined space, the process becomes even more complicated due to flame-wall interactions (FWIs) [1]. Strong heat losses occur at the combustor wall, which can alter the flame structure and lead to flame quenching. This results in a lowered combustion efficiency and increased pollutant formation.

Turbulent FWI has a practical relevance for internal combustion devices such as power plant burners, gas turbines, and internal combustion engines. Therefore, extensive numerical investigations have been conducted to understand and model the underlying processes based on generic configurations, including both head-on quenching (HOQ) [2–8] and side-wall quenching (SWQ) [9–16] flames. Among them, studies using direct numerical simulations (DNS) can be found in Lai and Chakraborty [3], Lai et al. [4,5], Zhao et al. [6,7], Lai et al. [8], Alshaalan and Rutland [9], Gruber et al. [10], Steinhausen et al. [13], Jiang et al. [14], Ahmed et al. [15,16]. However, it must be noted that the current application of DNS mainly focuses on simple fuels such as H_2 [10], or simplified chemical mechanisms such as single-step Arrhenius type reaction mechanisms [3–7,9], or simple geometries [8,13–17]. Their application in real devices is usually prohibited due to the large computational cost. In this context, models based on chemistry manifolds can be a good alternative since they help to reduce the number of transport equations to be solved while maintaining a detailed chemistry representation. Such methods include the Flamelet/Progress Variable (FPV) model [18], Flamelet-Generated Manifolds (FGMs) [19], Intrinsic Low-Dimensional Manifolds (ILDMs) [20], flame prolongation of ILDM (FPI) [21], and

* Corresponding author.
E-mail address: luo@stfs.tu-darmstadt.de (Y. Luo).

https://doi.org/10.1016/j.combustflame.2023.112923
0010-2180/© 2023 The Combustion Institute. Published by Elsevier Inc. All rights reserved.

Reaction-Diffusion Manifolds (REDIMs) [22]. With these methods, thermo-chemical states are pre-calculated and stored in look-up tables that are accessed by the control variables during the CFD simulation. Since FWI presents unique characteristics compared to unconfined combustion, these models need to be extended and validated before they can be applied to the simulation of near-wall combustion processes in real devices. For example, complex physics such as the substantial heat losses and the transient effects in turbulent flows needs to be additionally accounted for.

The earliest attempts to describe the heat loss in FWI employed FGM, with the lower limit of the enthalpy level extended by burner stablized flamelets. Heinrich et al. [23] performed both two-dimensional and three-dimensional simulations of the SWQ of a laminar premixed CH_4-air flame, which was experimentally measured by Jainski et al. [24]. The results show that FGM can reproduce the flame structure correctly and capture major characteristics such as CO_2 and temperature. However, the near-wall CO is significantly underpredicted. The unsuitability of FGM in CO prediction was also found by Ganter et al. [25], who performed simulations on a two-dimensional subdomain of the configuration in Heinrich et al. [23] with a finer grid resolution. They also concluded that the near-wall CO accumulation results from transport originating from CO produced in regions away from the wall. To explore the root cause of the deficiencies of FGM, SWQ processes were taken into account in the composition space in Ganter et al. [26] to quantify the deviations from exact solutions employing scalar dissipation rates. It was found that the discrepancies in CO predicted by FGM are due to improper considerations of species diffusion in the enthalpy direction. To remedy this drawback, an improved chemistry manifold was developed: a REDIM based on one-dimensional detailed chemistry head-on quenching (HOQ) solutions. Similarly, Efimov et al. [27] proposed a Quenching Flamelet-Generated Manifold (QFM) to improve the accuracy of CO prediction in FWI. Based on HOQ flamelets, the effects of scalar dissipation in the direction of enthalpy can be included in the manifold. The method was validated against a detailed chemistry simulation of the SWQ of a two-dimensional premixed laminar CH_4-air flame. A comparison of the performance of REDIM and QFM was conducted by Steinhausen et al. [28], based on the SWQ of laminar CH_4-air and DME-air flames that were experimentally investigated by Kosaka et al. [29,30]. It was observed that REDIM and QFM do not exhibit a significant difference in CO prediction, and both are more accurate than FGM. Luo et al. [31–33] proposed the REDIM method formulated and constructed in generalized coordinates for FWI processes. The method performs well in predicting the SWQ of the laminar CH_4-air flame experimentally studied in Jainski et al. [24], and the SWQ of the laminar DME-air flame measured by Zentgraf et al. [34]. Note that the advantages of REDIM and QFM compared with FGM have mostly been proven in laminar SWQ flames. However, to the best of the authors' knowledge, these improved manifolds have not yet been validated and assessed in coupled simulations of turbulent FWI. For the Large-Eddy Simulation (LES) of turbulent FWI, FGM is the only method reported in the literature. For example, Heinrich et al. [11,12] performed LESs on an experimental SWQ burner [35] using FGM, coupled with the artificial thickened flame (ATF) approach [36,37]. Donini et al. [38], Proch et al. [39], and Tang et al. [40] simulated a generic lab scale burner [41] for high-velocity preheated jets with FGM considering heat losses. These studies only investigated velocities and global quenching quantities; information related to pollutant formation was not reported. Pantangi et al. [2] conducted simulations on an experimental HOQ burner [42] using similar methods, and found that the near-wall CO prediction shows discrepancies from the experimental data. This is consistent with the findings from the laminar studies [25,27,28].

In turbulent FWI, besides heat loss, the effects of turbulent mixing have to be considered. Jiang et al. [14] performed a three-dimensional DNS of FWI in the case of CH_4-air flames diluted by hot burned products. It was shown that solutions of one-dimensional freely propagating flames cannot describe the variation of CO in the region close to the wall. This was attributed to turbulent mixing and diffusion effects. The effect of turbulent mixing was also reported in a recent experimental study conducted by Zentgraf et al. [43]. Similarly to the findings in [12,44], both SWQ-like and HOQ-like behaviors were observed. Focusing on the SWQ-like scenarios, thermo-chemical states that have not been encountered in laminar conditions were observed in the near-wall region. To explain the phenomenon, a flame-vortex interaction (FVI) mechanism was proposed. According to this explanation, the flame interacts with the near-wall vortical structures, entraining the burned gases into the fresh gas mixture near the flame's quenching point. More recently, this mechanism was confirmed in a numerical study based on a three-dimensional flame-resolved simulation (FRS) with detailed chemistry of the turbulent FWI of a stoichiometric CH_4-air flame in a fully developed channel flow [45]. To take into account the effects of flame dilution due to exhaust gas recirculation in the FVI area, as well as substantial heat losses to the wall, a novel flamelet manifold, the QFM with Exhaust Gas Recirculation (QFM-EGR) was proposed. Moreover, the QFM and QFM-EGR were validated in an *a-priori* manner.

Although there are plenty of studies focusing on the validation of manifold-based models in turbulent combustion [46–48], the investigation of chemistry manifolds for turbulent FWI is rather rare. It has been shown for laminar FWI that the choice and the suitability of the manifold are crucial to capturing physical processes such as pollutant formation near the wall in fully coupled simulations, however this has not been investigated in turbulent FWI yet. To fill this gap, the performance of chemistry manifolds for FWI: FGM, QFM [27], and QFM-EGR [45] are evaluated in the LES of a turbulent CH_4-air SWQ, using the FRS performed by Steinhausen et al. [13] as a reference. The two main objectives of the paper are:

1. to assess the predictive capabilities of the existing flamelet manifolds for FWI in the context of LES. To our knowledge, this is the first attempt to apply both the QFM and QFM-EGR in a coupled LES, and compare the performance of FGM, QFM, and QFM-EGR following an *a-posteriori* approach;
2. to evaluate the relevance and statistical importance of the FVI mechanism in turbulent FWI, based on comparison between QFM and QFM-EGR, with the latter taking into account the effects of burned gas recirculation.

In the following, the numerical methods adopted are introduced in Section 2, including descriptions of the FGM, QFM, QFM-EGR, and the governing equations for the coupled simulations. The numerical configuration is outlined in Section 3. Section 4 contains results and discussions. Firstly, LES results for FGM, QFM, and QFM-EGR are presented and compared with data from the FRS. Afterwards, the influences of the FVI mechanism are discussed. Finally, conclusions are drawn in Section 5.

2. Numerical methods

In this study, a turbulent, premixed CH_4-air flame ignited in a fully developed channel flow undergoing SWQ at the channel wall is simulated using LES. The computations are performed with a reduced version of the CRECK mechanism [49], which was reduced ad hoc for FWI conditions using the approach described in Stagni et al. [50] and consists of 24 species and 165 chemical reactions. The mechanism was designed to capture all relevant combustion

Table 1
Characteristics of FGM, QFM, and QFM-EGR.

Tabulation strategy	Flamelet types	Physics included
FGM	(1) 1D freely propagating flames with $T_{\text{inflow}} \geqslant 300$ K, (2) 1D freely propagating flames with different EGR levels and $T_{\text{inflow}} = 300$ K	Mixing-induced enthalpy variations
QFM	(1) 1D freely propagating flames with $T_{\text{inflow}} > 300$ K, (2) 1D HOQ flame with $T_{\text{inflow}} = 300$ K	Quenching-induced heat losses
QFM-EGR	(1) 1D HOQ of 1D freely propagating flames with $T_{\text{inflow}} \geqslant 300$ K, (2) 1D HOQ of 1D freely propagating flames with different EGR levels and $T_{\text{inflow}} = 300$ K	Quenching-induced heat losses and mixing with cooled exhaust gas

physics in the investigated configuration. The unity Lewis number assumption is adopted for the calculation of molecular diffusion. To enable comparison between different models, the choice of the chemical mechanism and the transport model is consistent with the FRS studies [13,45]. Note that the chemistry manifold is not restricted to the choice of the reaction mechanism.

Turbulent combustion is modeled with flamelet manifolds in combination with the ATF approach. Specifically, three flamelet manifolds are assessed: (1) FGM [19,51], (2) QFM [27], and (3) QFM-EGR [45], an extension of QFM. The table generation procedure of the FGM and QFM follows the work of Steinhausen et al. [28], while the QFM-EGR table is generated similarly to Steinhausen et al. [45], as shown in Table 1. Note that the *a-priori* results based on QFM-EGR already showed a very good agreement with the FRS [45], therefore additional effects such as the flame stretch are not included in the manifolds. More details will be discussed in the following.

2.1. Generation of flamelet manifolds

To generate the FGM, a series of independent one-dimensional freely propagating flames with varying enthalpy levels are computed. Enthalpy reduction is achieved by exhaust gas recirculation, i.e., different amounts of cooled burned gases are added to the inflow mixture of the flame. The amount of burned gases is given by $\text{EGR} = m_{\text{bg}}/(m_{\text{fg}} + m_{\text{bg}})$, where m_{bg} denotes the mass flux of the cooled burned gas and m_{fg} the mass flux of the fresh gases. Additionally, the upper enthalpy limit is expanded using one-dimensional freely propagating flames with EGR = 0 and increased inflow temperatures. Finally, the spanned manifold $\psi = \psi(x, \text{EGR})$ is parameterized by a progress variable (Y_{PV}) and the enthalpy (h), with the former one characterizing the progress of the chemical reaction and the latter the heat loss to the wall. Here x is the spatial coordinate. Therefore, the enthalpy variation is decoupled from the reaction progress variable variation for FGM. Note that the choice of enthalpy-reduction method has only small influences on the resulting chemistry manifold [52], indicating that other methods, such as one-dimensional burner stablized flames [53], can also be used here. When generating the QFM, in order to take into account the substantial heat loss to the wall, a single transient HOQ flame is tabulated, resulting in a thermo-chemical state $\psi = \psi(x, t)$, where t is the time. The wall and the fresh gas temperature are set to 300 K, while the fresh gas composition is set according to the inflow conditions of the reference simulation. Similarly to the FGM, this two-dimensional manifold is mapped to a progress variable-enthalpy state, i.e., $\psi = \psi(Y_{\text{PV}}, h)$, with the upper enthalpy limit extended by one-dimensional freely propagating flames with increased inflow temperatures. However, in this case, the enthlapy dimension and the reaction progress dimension are closely related by the quenching process. For efficient access to the manifold, the control variables of both the FGM and the QFM are normalized, namely

$$h^* = \frac{h - h_{\text{min}}}{h_{\text{max}} - h_{\text{min}}} \tag{1}$$

$$Y^*_{\text{PV}} = \frac{Y_{\text{PV}} - Y_{\text{PV, min}}(h^*)}{Y_{\text{PV, max}}(h^*) - Y_{\text{PV, min}}(h^*)}\,. \tag{2}$$

The thermo-chemical states are stored in a table as $\psi = \psi\left(Y^*_{\text{PV}}, h^*\right)$ with a resolution of 101 × 101 for $Y^*_{\text{PV}} \times h^*$.

To generate the QFM-EGR, a series of transient, one-dimensional HOQ flames are calculated. The transient HOQ flames are initialized with one-dimensional freely propagating flames with different fresh gas compositions, leading to different thermo-chemical states. The initial freely propagating flames consist of (1) 61 flames with varying EGR levels from 0 to 0.3 and the same inflow temperature, with the fresh gas mixture gradually diluted with cold exhaust gases, similarly to FGM, and (2) 19 preheated one-dimensional flames with increased inflow temperatures. Note that the temperature of the cooled exhaust gas is set to be similar to the fresh gas temperature since it is reported in Zentgraf et al. [43] that the burned gas cools down significantly by heat transfer to the wall and mixes with fresh gas upstream the quenching point during its passage in the gap between the flame tip and the wall. The 80 individual HOQ simulations result in a three-dimensional manifold $\psi = \psi(x, t, \text{EGR})$, which is then mapped to $\psi = \psi(Y_{\text{PV}}, Y_{\text{PV2}}, h)$. Consistent with [45], CO is chosen as the second progress variable, i.e., $Y_{\text{PV2}} = Y_{\text{CO}}$, to account for the amount of exhaust gases added to the flame. Note that the choice of the second progress variable is not restricted to the CO value, and theoretically any other variables that fulfill the condition of unique parametrization of the EGR dimension can be used. Similarly to before, normalization is applied to all control variables, which reads

$$Y^*_{\text{PV}} = \frac{Y_{\text{PV}} - Y_{\text{PV, min}}}{Y_{\text{PV, max}} - Y_{\text{PV, min}}} \tag{3}$$

$$Y^*_{\text{PV2}} = \frac{Y_{\text{PV2}} - Y_{\text{PV2, min}}\left(Y^*_{\text{PV}}\right)}{Y_{\text{PV2, max}}\left(Y^*_{\text{PV}}\right) - Y_{\text{PV2, min}}\left(Y^*_{\text{PV}}\right)} \tag{4}$$

$$h^* = \frac{h - h_{\text{min}}\left(Y^*_{\text{PV}}, Y^*_{\text{PV2}}\right)}{h_{\text{max}}\left(Y^*_{\text{PV}}, Y^*_{\text{PV2}}\right) - h_{\text{min}}\left(Y^*_{\text{PV}}, Y^*_{\text{PV2}}\right)}\,. \tag{5}$$

In this case, the thermo-chemical states stored in the flamelet table can be expressed as $\psi = \psi\left(Y^*_{\text{PV}}, Y^*_{\text{PV2}}, h^*\right)$. The manifold dimensions are 150 × 201 × 101 for $Y^*_{\text{PV}} \times Y^*_{\text{PV2}} \times h^*$.

2.1.1. Governing equations for coupled simulations

Within the LES framework, the conservation equations for mass and momentum read

$$\frac{\partial \overline{\rho}}{\partial t} + \frac{\partial \overline{\rho}\widetilde{u}_i}{\partial x_i} = 0 \tag{6}$$

$$\frac{\partial \overline{\rho}\widetilde{u}_i}{\partial t} + \frac{\partial \overline{\rho}\widetilde{u}_i\widetilde{u}_j}{\partial x_j} = \frac{\partial}{\partial x_j}\left(\overline{\tau}_{ij} - \overline{\rho}\widetilde{u''_i u''_j}\right) - \frac{\partial \overline{p}}{\partial x_i} \tag{7}$$

where ρ is the density, u_i the ith component of the velocity, u''_i the ith subgrid component of the velocity, p the pressure, and τ_{ij} the component of the shear stress tensor. The operators $\bar{\cdot}$ and $\widetilde{\cdot}$ represent the filtering and the Favre filtering, respectively. The subgrid stresses $\widetilde{u''_i u''_j}$ are closed using the σ model [54,55].

The ATF approach [36,37] is adopted to correctly capture the turbulence-chemistry interaction. For the coupled simulations, the governing equations for the control variables read

$$\frac{\partial \overline{\rho}\widetilde{Y}_{\mathrm{PV}}}{\partial t}+\frac{\partial \overline{\rho}\widetilde{u}_i\widetilde{Y}_{\mathrm{PV}}}{\partial x_i}=\frac{\partial}{\partial x_i}\left(FE\overline{\rho}D\frac{\partial \widetilde{Y}_{\mathrm{PV}}}{\partial x_i}\right)+\frac{\partial}{\partial x_i}\left[(1-\Omega)\overline{\rho}D_t\frac{\partial \widetilde{Y}_{\mathrm{PV}}}{\partial x_i}\right]+\frac{E}{F}\overline{\dot{\omega}}_{\mathrm{PV}} \quad (8)$$

$$\frac{\partial \overline{\rho}\widetilde{h}}{\partial t}+\frac{\partial \overline{\rho}\widetilde{u}_i\widetilde{h}}{\partial x_i}=\frac{\partial}{\partial x_i}\left(FE\overline{\rho}D\frac{\partial \widetilde{h}}{\partial x_i}\right)+\frac{\partial}{\partial x_i}\left[(1-\Omega)\overline{\rho}D_t\frac{\partial \widetilde{h}}{\partial x_i}\right] \quad (9)$$

$$\frac{\partial \overline{\rho}\widetilde{Y}_{\mathrm{PV2}}}{\partial t}+\frac{\partial \overline{\rho}\widetilde{u}_i\widetilde{Y}_{\mathrm{PV2}}}{\partial x_i}=\frac{\partial}{\partial x_i}\left(FE\overline{\rho}D\frac{\partial \widetilde{Y}_{\mathrm{PV2}}}{\partial x_i}\right)+\frac{\partial}{\partial x_i}\left[(1-\Omega)\overline{\rho}D_t\frac{\partial \widetilde{Y}_{\mathrm{PV2}}}{\partial x_i}\right]+\frac{E}{F}\overline{\dot{\omega}}_{\mathrm{PV2}}\,. \quad (10)$$

Here, Ω denotes the flame sensor, which is used to avoid non-physical thickening outside the flame. The flame sensor employed here is an adaptation of the one in Heinrich et al. [11], using a second-order polynomial with the maximum located at the maximum reaction rate of the progress variable for each enthalpy level. In the non-reactive regions of the flame, the flame sensor is blended to zero to avoid thickening. F is the thickening factor, and it is dynamically evaluated based on Ω and the grid-dependent maximum thickening factor $F_{\max}$ [2]. E is the efficiency function, which is defined as the ratio between the total flame surface and its resolved part in the filtered volume. It is introduced to compensate for the flame surface loss due to the thickening, and the value is calculated using the analytical model developed by Charlette et al. [56]. D is the molecular diffusivity of the scalar. D_t is the subgrid diffusivity calculated as $D_t=\mu_t/Sc_t$, where μ_t is the turbulent viscosity and the turbulent Schmidt number Sc_t is chosen as 0.4. For the first progress variable ($Y_{\mathrm{PV}}=Y_{\mathrm{CO_2}}$), the reaction rate $\dot{\omega}_{\mathrm{PV}}$ is directly obtained from the flamelet manifold. For the second progress variable ($Y_{\mathrm{PV2}}=Y_{\mathrm{CO}}$), the reaction rate is calculated based on the production rate $\dot{\omega}^+$ and the consumption rate $\dot{\omega}^-$ taken from the flamelet manifold, namely $\dot{\omega}_{\mathrm{PV2}}=\dot{\omega}^+_{\mathrm{CO}}+Y_{\mathrm{PV2}}(\dot{\omega}^-_{\mathrm{CO}}/Y^{\mathrm{FLT}}_{\mathrm{CO}})$, allowing CO to evolve based on its own time scale [57]. Note that for FGM and QFM, equations only need to be solved for the first progress variable (Eq. (8)) and the enthalpy (Eq. (9)). For QFM-EGR, all three control variables need to be transported, i.e., Eqs. (8)–(10) need to be solved.

3. Numerical setup

The configuration has been studied by Steinhausen et al. [13,45] with an FRS. A V-shaped premixed flame stabilized by a flame holder in a fully developed turbulent channel undergoes FWI at the channel walls, as shown in Fig. 1. The coordinates are defined as follows: x, y, and z correspond to streamwise, lateral, and wall-normal directions, respectively. The inflow is a stoichiometric CH_4-air mixture at 300 K. The Reynolds number of the inert channel flow is $Re=(U_{\mathrm{bulk}}H)/\nu\approx 5540$, where U_{bulk} is the mean axial flow velocity (4.4 m/s), H the channel height (20 mm), and ν the kinematic viscosity of the inflow. Similarly to Gruber et al. [10], the flame holder is modeled as a cylindrical region ($r=0.9$ mm) filled with burned gases. It is placed at a distance of $H/4$ from the bottom wall. Both the upper and lower walls are assumed to be inert and have a fixed temperature that is equal to the inflow temperature, namely $T_{\mathrm{wall}}=300$ K.

An inert turbulent channel flow is simulated in a pre-processing step to provide proper inflow boundary conditions for the reactive case. For the inert case, the dimensions of the computational domain are $7H$, $1.5H$, and H in x, y, and z directions, respectively. A stretched structured grid is adopted, which is uniform in x and y directions and refined towards the wall in z direction. In the core flow, the non-dimensional grid resolution in x, y, and z directions is $\Delta x^+=\Delta y^+=\Delta z^+=5.14$, where the superscript $^+$ denotes non-dimensionalization with the viscous length scale. The finest grid spacing in the z direction is $\Delta z^+=1$. The total number of cells is 7.4 million. A no-slip boundary condition is applied to the channel walls, and a periodic boundary condition is used for lateral and streamwise boundaries. The inflow velocity field is used as the inflow boundary condition for the reactive case, and it is stored with a time interval of 17 µs.

Regarding the reactive case, the computational domain is similar to the inert case, except that the length is reduced from $7H$ to $5H$. With the same grid resolution as the inert case, the resulting total number of cells is 5.3 million. The boundary conditions employed are as follows: at the inlet, the inflow velocity field obtained from the inert case is spatially and temporally interpolated at every time step, which is about $\Delta t\approx 2.5$ µs. At the outlet, a zero gradient boundary condition is applied for the velocity, progress variables, and enthalpy. At the channel walls, a no-slip boundary condition is employed for the velocity, a zero-gradient boundary condition for the progress variables, and a fixed value of 300 K for the temperature. In the lateral direction, periodic boundary conditions are adopted.

The numerical simulations are performed using an in-house solver [58] based on OpenFOAM [59] with second-order discretizations in time and space.

4. Results and discussion

In the following, the performances of FGM, QFM, and QFM-EGR are assessed by comparison with the FRS results from Steinhausen et al. [13,45]. Firstly, profiles of mean flow field quantities are analyzed. Afterwards, instantaneous results are presented to further show the capability of the models. Specifically, probability density functions (PDFs) of CO are evaluated first. Then, the importance of FVI is studied based on cross-comparison of the simulation results.

Since the thermo-chemical states within the quenching region strongly depend on the streamwise position, a flame-fixed coordinate system is introduced, following previous studies [23,25,28]. The coordinates of the quenching point are defined as (x_Q, y_Q, z_Q). Similarly to previous works [10,23], the quenching point for each wall-normal plane is determined based on the maximum wall heat flux, which is evaluated at a near-wall horizontal plane $z=50$ µm for consistency. The instantaneous wall heat flux is calculated according to

$$\lambda\left.\frac{\partial T}{\partial z}\right|_{z=50\,\mu\mathrm{m}}, \quad (11)$$

where λ corresponds to the gas phase thermal conductivity at $z=50$ µm. With the variation of the wall heat flux, the streamwise position of the quenching point x_Q can be found. To further determine its lateral and wall-normal coordinates, position of the flame front is used. Similarly to Mann et al. [42], the flame front is defined based on an isothermal contour, i.e., $T=1500$ K. Based on the quenching point, a relative coordinate system is defined. Within these coordinates, y and z remain unchanged and x_q denotes the coordinate parallel with the wall determined by $x_q=x-x_Q$.

4.1. Reactive scalars and mean flow field

The major flame characteristics are assessed based on several mean flame quantities, which are obtained based on both time and

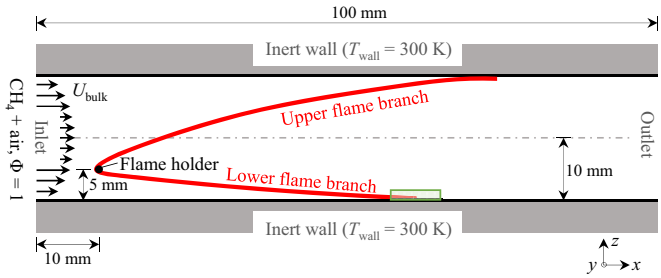

Fig. 1. Schematic of the configuration investigated. The x, y, and z coordinates are the streamwise, lateral, and wall-normal directions, respectively. The dimension in the lateral direction is 30 mm. The region of interest analyzed in Fig. 9 is denoted by the green rectangle. (For interpretation of the references to color in this figure legend, the reader is referred to the web version of this article.)

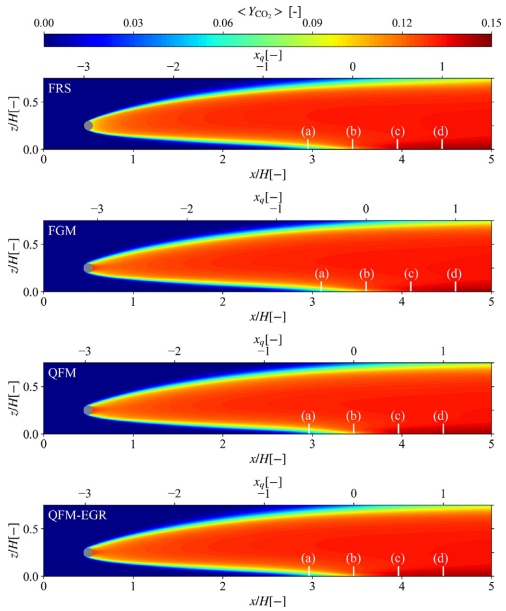

Fig. 2. Contour of mean Y_{CO_2}, which is averaged both temporally and spatially in the lateral (y) direction. White lines denote positions where mean values of velocity and thermo-chemical quantities are extracted: (a) $x_q = -0.5H$, (b) $x_q = 0$, (c) $x_q = 0.5H$, and (d) $x_q = H$. Here, (b) $x_q = 0$ corresponds to the streamwise position of the mean quenching point.

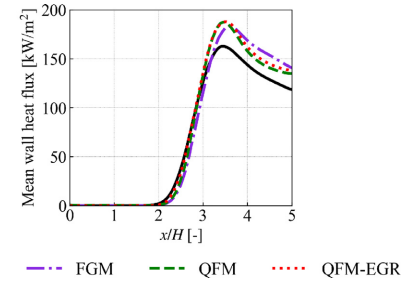

Fig. 3. Distributions of the mean wall heat flux along the normalized streamwise coordinate x/H. The reference FRS result is denoted by the black solid line. The violet, the green, and the red dashed lines correspond to FGM, QFM, and QFM-EGR results, respectively. (For interpretation of the references to color in this figure legend, the reader is referred to the web version of this article.)

space averaging of the instantaneous fields. Firstly, the instantaneous results are averaged over a sufficiently long time, i.e., more than 10 flow-through times, to ensure time independence. Afterwards, the time-averaged quantities are further averaged along the y direction. These are referred to as mean quantities in the following, as denoted by $< \cdot >$.

The mean CO_2 mass fraction is displayed in Fig. 2. It is observed that the overall flame appears similar comparing all the simulations. To enable a quantitative comparison between FRS, FGM, QFM, and QFM-EGR, the mean quenching points are first determined based on the profiles of the mean wall heat fluxes. As shown in Fig. 3, the general trend observed for all simulations is that there is no heat transfer to the wall from the inlet until $x/H = 2$, which is due to that the wall is assumed to be isothermal and its temperature is the same as the unburned gas. Afterwards, the mean wall heat flux gradually rises to reach a peak where the mean quenching point is defined, following which it decreases to a non-zero value until the outlet. Overall, FGM, QFM, and QFM-EGR show greater heat transfer to the wall than the FRS. FGM, QFM, and QFM-EGR give similar predictions of the peak value, at 183.0 kW/m^2, 187.2 kW/m^2, and 187.7 kW/m^2, respectively. However, they are all higher than the reference value 162.7 kW/m^2, and the overprediction remains in the downstream region. This may be attributed to the deviations in λ and the temperature gradient in the z direction, according to the definition of the wall heat flux. Regarding the position where the wall heat flux reaches a maximum, it is quite close when comparing different simulations, at $x/H = 3.45$, 3.6, 3.4625, 3.4625 for FRS, FGM, QFM, and QFM-EGR, respectively. The small differences are mainly originated from the quenching area, since the performances of FGM, QFM, and QFM-EGR are similar for the region away from the wall, see Figs. 4, 5, and 6 below.

For a more detailed investigation, mean quantities of the velocity, temperature, enthalpy and progress variables are analyzed for four representative streamwise positions (white lines (a)–(d) in Fig. 2):

- (a) upstream of the quenching point ($x_q = -0.5H$)
- (b) at the quenching point ($x_q = 0$)
- (c) downstream of the quenching point ($x_q = 0.5H$)

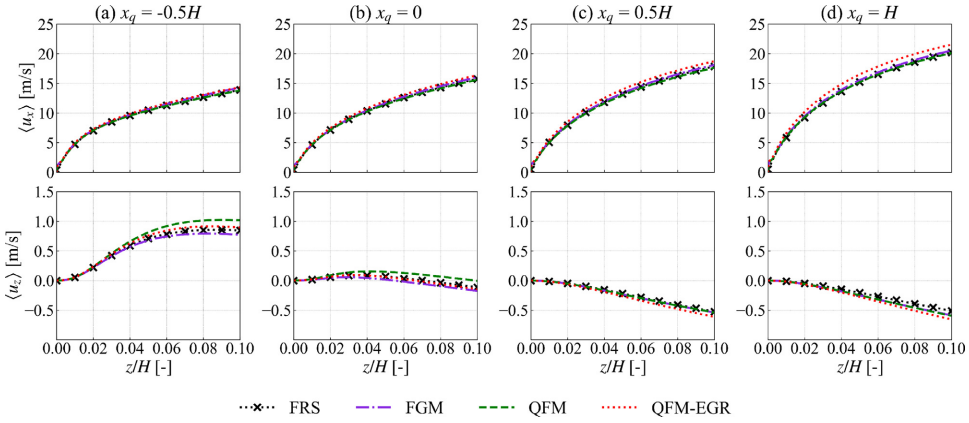

Fig. 4. Distributions of the mean streamwise velocity (top) and wall-normal velocity (bottom) from the bottom wall to the height of 0.1H at different streamwise positions: (a) $x_q = -0.5H$, (b) $x_q = 0$, (c) $x_q = 0.5H$, and (d) $x_q = H$. The reference FRS results are denoted by black dashed lines marked with cross symbols. The violet, the green, and the red dashed lines correspond to FGM, QFM, and QFM-EGR results, respectively. (For interpretation of the references to color in this figure legend, the reader is referred to the web version of this article.)

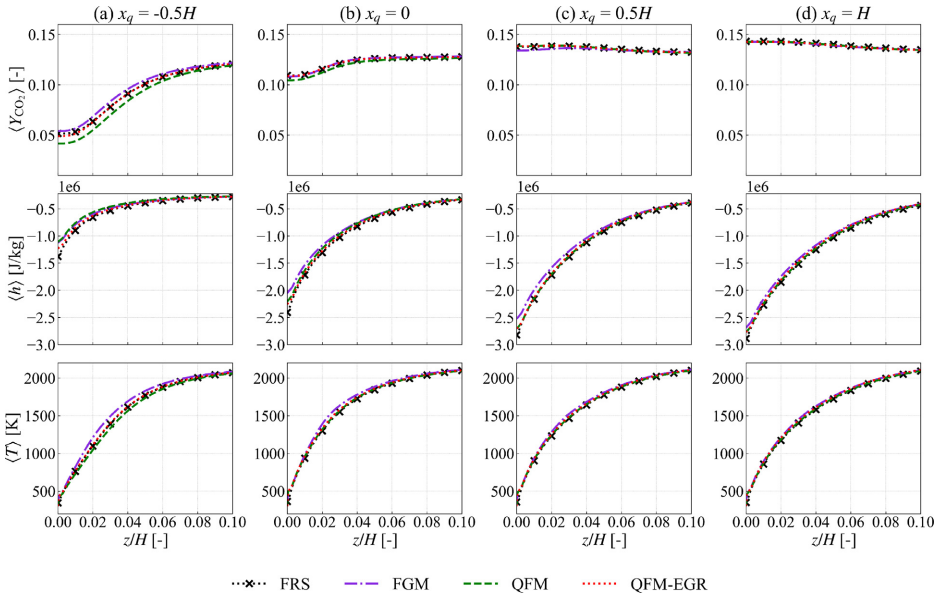

Fig. 5. Distributions of mean progress variable Y_{CO_2} (top), enthalpy h (middle), and temperature T (bottom) from the bottom wall to the height of 0.1H at different streamwise positions: (a) $x_q = -0.5H$, (b) $x_q = 0$, (c) $x_q = 0.5H$, and (d) $x_q = H$. The reference FRS results are denoted by black dashed lines marked with cross symbols. The violet, the green, and the red dashed lines correspond to FGM, QFM, and QFM-EGR results, respectively. (For interpretation of the references to color in this figure legend, the reader is referred to the web version of this article.)

- (d) close to the outlet ($x_q = H$).

Figure 4 shows the streamwise velocity u_x and the wall-normal velocity u_z plotted along the wall-normal lines. For each position, the streamwise velocity is zero at the wall, which fulfills the no-slip boundary condition, and increases monotonically with increasing wall distance. The gradient of the streamwise velocity reaches a maximum at the wall, and gradually decreases along the wall-normal direction. Different trends are observed for the gradient of the wall-normal velocity, which remains at a low level close to the wall. In addition, the variation in the wall-normal velocity is different for the four positions considered. For position (a), the wall-normal velocity is positive and increases with the wall distance. For position (b), the wall-normal velocity remains almost zero from the wall until $z/H = 0.1$. In contrast, a mainly negative wall-normal velocity is observed for positions (c) and (d), which is due to the

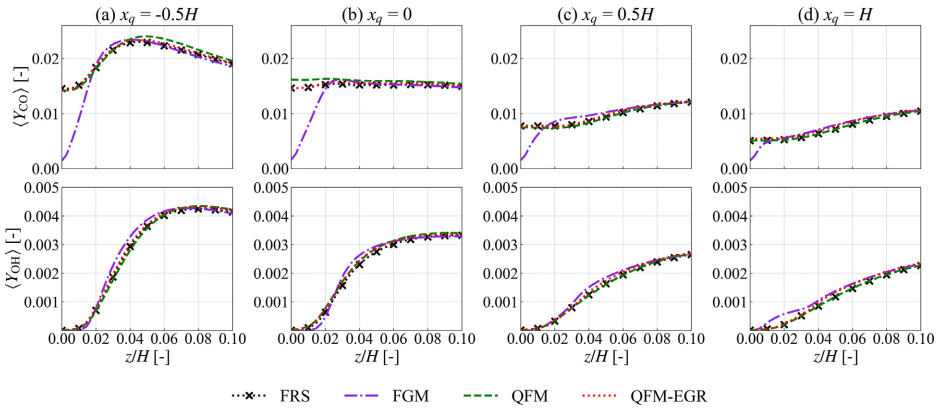

Fig. 6. Distributions of mean mass fractions of CO (top) and OH (bottom) from the bottom wall to the height of 0.1H at different streamwise positions: (a) $x_q = -0.5H$, (b) $x_q = 0$, (c) $x_q = 0.5H$, and (d) $x_q = H$. The reference FRS results are denoted by black dashed lines marked with cross symbols. The violet, the green, and the red dashed lines correspond to FGM, QFM, and QFM-EGR results, respectively. (For interpretation of the references to color in this figure legend, the reader is referred to the web version of this article.)

thermal expansion of the burned gases, and the magnitude increases when moving away from the wall. This phenomenon is also observed in Heinrich et al. [23]. These major characteristics are well captured by all manifolds. The absolute value of the wall-normal velocity is generally much smaller than that of the streamwise velocity, and the wall-normal velocity shows slightly larger discrepancies than the streamwise velocity at positions (a) and (b). However, overall, for both the streamwise and the wall-normal velocity, FGM, QFM, and QFM-EGR show good agreement with the reference data for all four streamwise positions considered.

Figure 5 presents the results for the first progress variable, Y_{CO_2}, enthalpy, and the temperature. All flamelet manifolds yield profiles for the progress variable and temperature that are comparable to the reference. Small discrepancies are found in enthalpy distributions. The results from QFM-EGR are closest to the FRS for all positions. Meanwhile, QFM shows a slight overprediction in the near-wall region at position (a), and FGM leads to overprediction for all positions considered. The differences in the enthalpy profiles can be explained by the model limitations of the manifolds employed. The enthalpy boundary condition at the wall is set based on the species composition and the temperature, i.e., $h = h(Y_1, Y_2, \ldots, Y_k, T, p)$ [51], and the species composition is retrieved from the tabulated manifolds. Therefore, any deviations in the tabulated thermo-chemical states will result in differences in the enthalpy boundary condition that are then reflected in the near-wall enthalpy profiles at the wall. Note that, however, the enthalpy set at the wall needs to be consistent with the manifold-based model employed to correctly capture the wall temperature. Nevertheless, in summary, the results from the three flamelet manifolds do not show much difference.

To assess the capability of the flamelet manifolds to predict the pollutants and radicals, distributions of mean CO and OH for the same four positions shown in Fig. 2 are plotted in Fig. 6. Accurate predictions can still be observed for QFM and QFM-EGR, with QFM-EGR performing slightly better, which is similar to the findings for major species. In contrast, deviations from the reference results are shown for FGM, regarding both CO and OH. In the case of CO especially, even different variation trends are presented. For FRS, QFM, and QFM-EGR, the CO distribution does not change much near the wall, while FGM presents a notable decrease towards the wall. Consequently, the near-wall CO is significantly underpredicted by FGM, especially at positions (a) and (b), meaning that FGM is unable to reproduce the CO accumulation here. Even at position (d), which is close to the outlet, FGM still underestimates the CO at the wall. The deficiency of the FGM in capturing the near-wall CO is consistent with previous laminar studies [26,27], and it is originated from the improper CO diffusion in the enthalpy direction included in the FGM table.

Further, the CO mass fraction profiles in the streamwise direction for different wall distances are plotted in Fig. 7 to gain deeper insights into the CO prediction. The minimum wall distance considered in Fig. 7 corresponds to the unstretched laminar flame thickness δ. It is calculated using $\delta = \lambda_u / \left(\rho_u c_{p,u} s_L\right)$, where λ_u, ρ_u, and $c_{p,u}$ are the thermal conductivity, density, and heat capacity of the unburned gas, respectively, and s_L denotes the laminar burning velocity. CO is always underpredicted by FGM in the vicinity of the wall, e.g., position (a), which is consistent with previous studies [25]. With increasing wall distance, the deviations in CO prediction can still be found before the outlet, while the computed values at the outlet are close to reference results, such as positions (b), (c), and (d). Compared with FGM, results from QFM show evident improvement. This is similar to the findings in laminar SWQ cases [27,28]. However, slight overprediction exists near the peak value. Compared to QFM, QFM-EGR provides an even better prediction, which shows excellent agreement with the FRS reference.

Based on the above discussions, it can be concluded that all three flamelet manifolds considered are capable of capturing the major global characteristics of the turbulent FWI. However, FGM shows significant deficiencies in the prediction of pollutants and radicals. These findings apply to both turbulent and laminar flames. Different from laminar cases, FVI exists in turbulent conditions. Therefore, the performance of the QFM and the recently introduced QFM-EGR specifically designed for turbulent FWI is further compared. It is observed that the latter shows a slight improvement in the prediction of the mean quantities. In the following chapter, results from these two approaches will be comprehensively compared.

4.2. Probability density functions of the CO mass fraction

In addition to the mean quantities, the PDFs of the CO mass fraction are analyzed in this section, as shown in Fig. 8. The PDFs

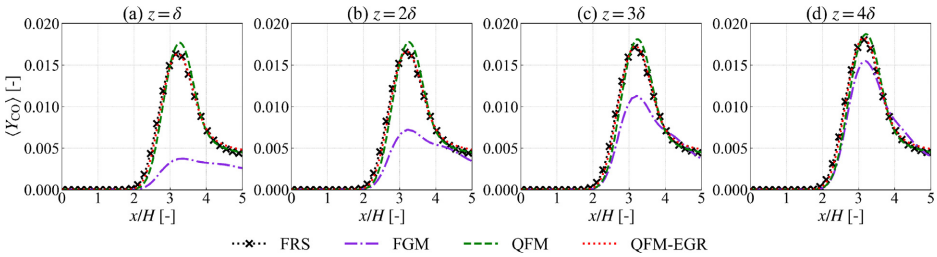

Fig. 7. Distributions of the mean CO mass fraction from the inlet to the outlet at different vertical positions: (a) $z = \delta$, (b) $z = 2\delta$, (c) $z = 3\delta$, and (d) $z = 4\delta$. The reference FRS results are denoted by black dashed lines marked with cross symbols. The violet, the green, and the red dashed lines correspond to FGM, QFM, and QFM-EGR results, respectively. (For interpretation of the references to color in this figure legend, the reader is referred to the web version of this article.)

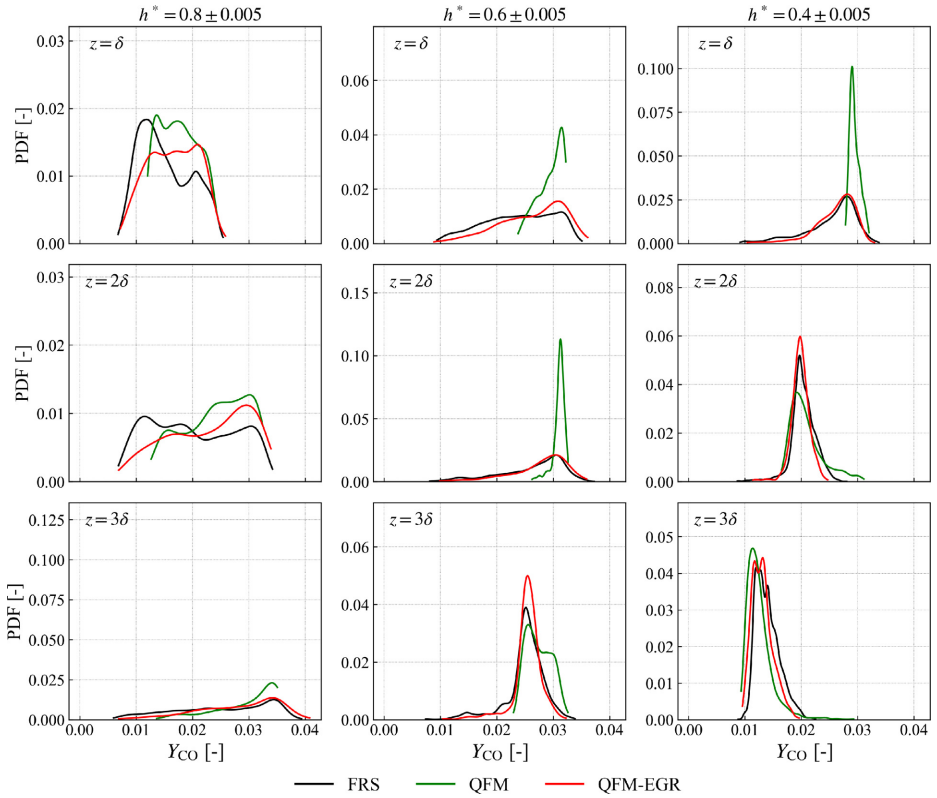

Fig. 8. PDFs of CO conditioned on wall distance and enthalpy level. (For interpretation of the references to color in this figure legend, the reader is referred to the web version of this article.)

are computed based on the resolved quantities and extracted at different wall distances ($z = \delta$, 2δ, 3δ) for a given enthalpy interval ($h^* = 0.8 \pm 0.005$, 0.6 ± 0.005, 0.4 ± 0.005). Here, h^* denotes the normalized enthalpy $h^* = (h - h_{min})/(h_{max} - h_{min})$, with $h^* = 1$ corresponding to an undisturbed flame and $h^* = 0$ to a fully quenched state. The data are sampled from 10 time instants.

Unlike the observations regarding the mean quantities, which reveal only small differences between QFM and QFM-EGR, significant and non-negligible differences are found in the PDFs of CO, especially for positions very close to the wall. At the plane closest to the wall, i.e., $z = \delta$, the distribution of CO predicted by QFM-EGR agrees quite well with the FRS. The variation range of CO is almost the same when comparing QFM-EGR and FRS. However, the PDF of QFM is much narrower, and concentrates at higher CO values. This corresponds to the overprediction of the peak of the mean CO shown in Fig. 7. The deviation between QFM and QFM-EGR

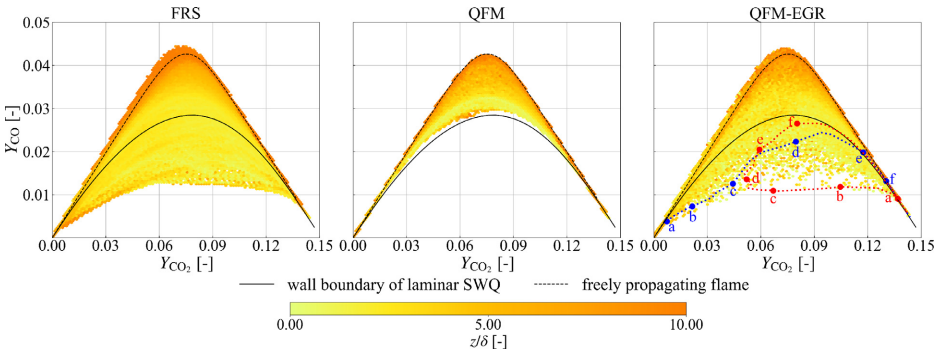

Fig. 9. Thermo-chemical states near the quenching point for different lateral positions and time instants: (left) FRS, (middle) QFM, and (right) QFM-EGR. The scatters are colored by the normalized wall distance z/δ. For reference, the states of a 1D freely propagating flame and on the wall boundary of a laminar SWQ are denoted by black dashed lines and black solid lines, respectively. (For interpretation of the references to color in this figure legend, the reader is referred to the web version of this article.)

increases with increasing heat loss. For low enthalpy levels such as $h^* = 0.6$ and $h^* = 0.4$, a distinct peak can be observed in the PDF of QFM, while the PDF distribution is much wider in QFM-EGR and FRS. Moving further away from the wall to $z = 2\delta$, the discrepancies between QFM and QFM-EGR still exist, especially for $h^* = 0.6$. However, for high enthalpy losses, e.g., $h^* = 0.4$, the PDF of CO narrows, leading to a better agreement between QFM and QFM-EGR. This means that the enthalpy range where QFM and QFM-EGR differ significantly becomes smaller with increasing wall distance. At $z = 3\delta$, the PDFs from QFM and QFM-EGR are quite similar. Therefore, it is reasonable to deduce that there would be almost no differences between QFM and QFM-EGR in the case of positions far away from the wall. Based on the above findings, it can be concluded that the significant differences in the PDFs of CO between QFM and QFM-EGR mainly exist in the region near the flame tip, which is located close to the wall at an intermediate level of enthalpy losses. According to Zentgraf et al. [43], Steinhausen et al. [45], this is also the area where the FVI mechanism plays a role. Therefore, it is assumed that the characteristics of the PDFs shown above are related to this mechanism. To verify this, the FVI mechanism will be studied in the following sections.

4.3. Prediction of flame-vortex interaction

Firstly, the instantaneous thermo-chemical states that are directly influenced by the FVI mechanism are compared for FRS, QFM, and QFM-EGR, so that the importance of the mechanism can be illustrated. Afterwards, the flame dynamics of an FVI event using QFM-EGR is compared to the FRS based on a time-series analysis to further evaluate the performance of QFM-EGR in capturing the FVI mechanism.

4.3.1. Comparison of thermo-chemical states

To investigate the instantaneous local thermo-chemical states, quantities are evaluated over 10 time steps. For each time instant, data are collected from 31 independent slices parallel to the xz plane. For each slice, the region of interest covers a range of $(x_Q - 50\delta, x_Q + 50\delta)$ in x direction and $(0, z_Q + 10\delta)$ in z direction, as denoted by the green rectangle in Fig. 1.

Figure 9 shows the thermo-chemical states in CO_2-CO space for the region of interest at different lateral positions and times instants, with results from FRS on the left, QFM in the middle, and QFM-EGR on the right. The data are colored by the normalized wall distance (z/δ). Additionally, the thermo-chemical states on the wall boundary of a corresponding laminar SWQ are shown as black solid lines. Here, the laminar SWQ simulation is performed on a two-dimensional domain, similarly to Steinhausen et al. [28]. The thermo-chemical states of a freely propagating flame are denoted by black dashed lines, where the composition and the temperature of the fresh gas remain the same as the current turbulent SWQ configuration. From the FRS results, it is observed that the state space spanned by the turbulent SWQ can not be fully covered by its laminar counterpart, as shown by the area surrounded by the black solid and dashed lines in Fig. 9. Especially for the region very close to the wall, i.e., the low-temperature region, the minimum value of the conditional CO mass fraction is significantly below the limit of the wall boundary of the laminar SWQ, namely $\min\left(Y_{CO}|Y_{CO_2}\right) < \left(Y_{CO}|Y_{CO_2}\right)_{\text{laminar},z=0}$. According to Zentgraf et al. [43], Steinhausen et al. [45], this is due to cooled burned products mixing with fresh gases in the vicinity of the quenching point. In the study by Steinhausen et al. [45], the QFM-EGR was introduced to incorporate the mixing effect in the thermo-chemical state and validated a priori. As a result, the LES with the QFM-EGR is able to correctly capture the local mixing processes caused by FVI in the turbulent flame, showing a large portion of the scatters below the limit of the wall boundary of the laminar SWQ. To further illustrate the mixing process, the evidence of FVI in the physical space is additionally shown for better understanding. Here, Lagrangian massless particles are placed in the flow field. Note that more details about the flow field, e.g., Q-criteria, can be found in the supplementary material and also previous studies [43,45].As an example, the trajectories of two Lagrangian particles in CO_2-CO space are additionally highlighted in the scatters of QFM-EGR in Fig. 9. Initially, the two particles locate on the same xz plane. Their corresponding trajectories in the physical space projected onto the initial xz plane for 6 representative time instants are indicated in Fig. 10, where a slice of the flame in the lateral direction is shown for QFM-EGR. Note that the movement in the lateral direction is minor during these 1.375 ms in the case of both particles. A relative time t' is introduced and $t' = 0$ refers to the first time instant considered. Initially, the blue particle is located in the unburned part of the flame, while the red one is in the burned region. In the following, the particles move closer to each other until they almost collide at $t' = 0.55$ ms, consistent with the mixing process proposed in Zentgraf et al. [43], Steinhausen et al. [45]. Note that the movement of the red particle is against the main flow direction due to the interaction with the turbulent vortices, which can be observed from its location relative to the flame tip. This is also re-

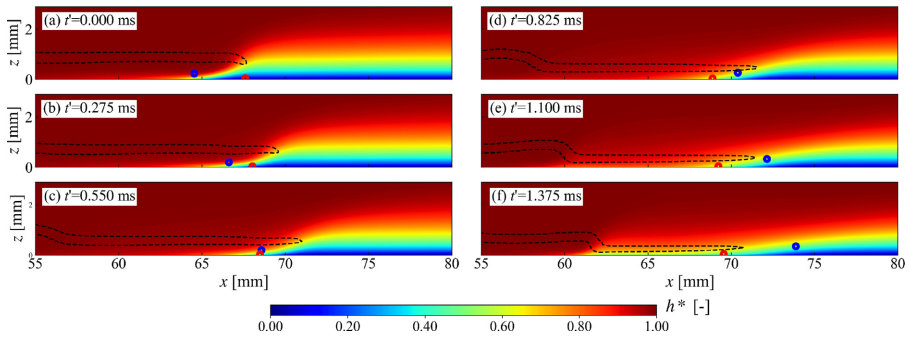

Fig. 10. Time series of a slice in the lateral direction through the turbulent flame for QFM-EGR. Contours of the normalized enthalpy (h^*) are shown. Isocontours of heat release rate ($0.1 \times \mathrm{HRR}_{\mathrm{max}}$) are denoted by black dashed lines. The blue and red points correspond to the positions of the Lagrangian particles projected to the xz plane where the two particles initially locate. (For interpretation of the references to color in this figure legend, the reader is referred to the web version of this article.)

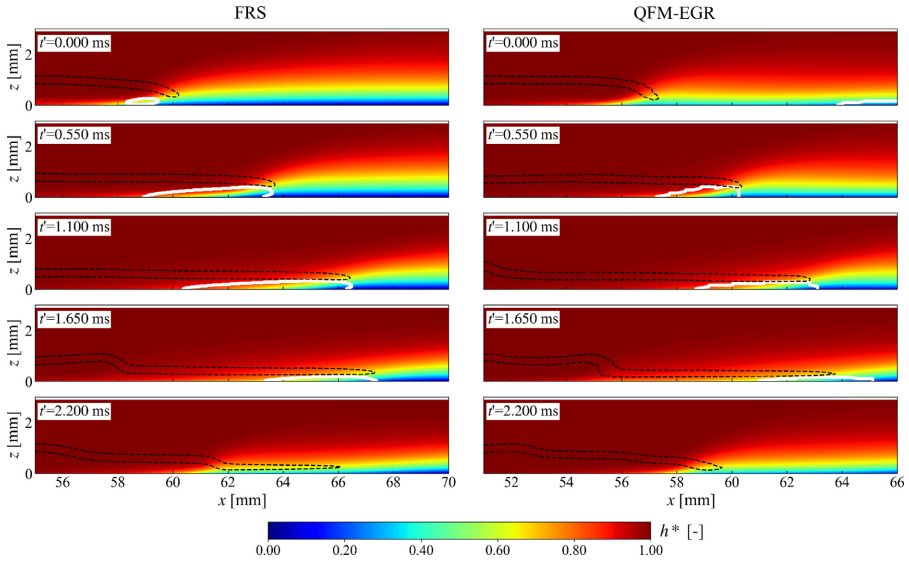

Fig. 11. Time series of a slice in the lateral direction through the turbulent flame: (left) FRS, (right) QFM-EGR. Contours of the normalized enthalpy (h^*) are shown. Isocontours of heat release rate ($0.1 \times \mathrm{HRR}_{\mathrm{max}}$) are denoted by black dashed lines. The white isocontour represents the area of FVI.

flected in the thermo-chemical states shown in Fig. 9, where both particles exhibit CO values far below the laminar limit that is also the lower bound of the QFM accessible range. After $t' = 0.825$ ms, the thermo-chemical states of both particles move in the direction of the burned gas. Based on the above observations, it can be concluded that FVI leads to a mixing process of burned and fresh gases in the near-wall region, which results in thermo-chemical states that are not present in the laminar cases. This has been found both in simulations [45] and experiments [43]. Therefore, the capability of QFM-EGR to correctly predict FVI in the turbulent FWI is demonstrated. The QFM, on the other hand, only accounts for the strong heat losses due to the flame quenching at the wall. This is the reason for the much narrower state space spanned by the LES with QFM and the narrower PDF distributions in Fig. 8, since the states originating by the turbulent mixing are not included in the manifold. This means that QFM can not capture the mixing process in the near-wall region, because there is no variation in the composition of the unburned gas in the flamelets used for the manifold generation. This model limitation is overcome by the QFM-EGR. Considering the notable difference between QFM and QFM-EGR in Fig. 9, the importance of the FVI mechanism is verified. Therefore, in the prediction of transient thermo-chemical states in the near-wall region for turbulent conditions, the benefit of the QFM-EGR becomes evident.

4.3.2. Evolution of the FVI area

To further demonstrate the capability of QFM-EGR to correctly capture the FVI mechanism, the time evolution of the FVI area is investigated in this section. A time series for a slice of the flame in the lateral direction for both FRS and QFM-EGR are depicted in Fig. 11. Here, isolines of the heat release rate ($0.1 \times \mathrm{HRR}_{\mathrm{max}}$) are denoted by black dashed lines.

The white isolines corresponds to $\left(Y_{CO}|Y_{CO_2}\right) = \left(Y_{CO}|Y_{CO_2}\right)_{laminar.z=0}$. The states of the region surrounded by the white isolines fulfill the condition that $\left(Y_{CO}|Y_{CO_2}\right) < \left(Y_{CO}|Y_{CO_2}\right)_{laminar.z=0}$. According to Section 4.3.1 and [43,45], this is caused by the FVI. Therefore, this region is called FVI region, which is related to the turbulent flow structures. The time series from the FRS is chosen to display the typical behavior found in the turbulent SWQ flame, similarly to Steinhausen et al. [45]. For QFM-EGR, results from different time instants are used, so that they present similar flame movements to FRS. For each simulation, the time interval of the neighboring two slices stays at 0.55 ms. Similarly to the last section, the relative time t' is also introduced here; $t' = 0$ refers to the first time instant considered for each simulation in Fig. 11. Following [11], all flame angles less than 2° are categorized as HOQ-like events, while other cases are classified as SWQ-like scenarios. Based on FRS results, it is observed that the flame is in an SWQ-like state at $t' = 0$, and FVI takes place in only a very small area. Afterwards, the angle between the flame and wall decreases and the FVI area begins to grow, e.g., at $t' = 0.55$ ms and 1.1 ms. As the flame-wall impact angle decreases further, the FVI region begins to shrink. Consequently, an HOQ-like event occurs at $t' = 1.65$ ms, with the FVI mechanism only playing a role in a very small region close to the wall. In the following, the quenching scenario transfers to SWQ-like again, as can be observed for $t' = 2.2$ ms. At this time instant, no FVI region is detected. A repeated flame behavior between the HOQ-like scenario and the SWQ-like scenario is observed, so the evolution after $t' = 2.2$ ms is not shown for brevity. Readers interested in additional time instants may refer to the supplementary materials of [45]. For all time instants when FVI occurs, it is observed that the FVI area decreases with increasing wall distance, both in physical space and enthalpy space. This helps to explain the findings from Fig. 8 that significant differences between QFM and QFM-EGR are mainly seen in the vicinity of the wall, and the enthalpy range involved becomes smaller when moving further away from the wall. These major characteristics of the flame dynamics can also be found in QFM-EGR, as shown in the right-hand column of Fig. 11. According to Steinhausen et al. [45], the repeated flame behavior is caused by the interaction between the flame and the vortex. Therefore, it indicates that QFM-EGR is able to correctly capture the dynamic evolution of the FVI mechanism.

5. Conclusions

In the current study, three flamelet manifolds with different levels of complexity are applied to the LES of a turbulent SWQ flame with the purpose of comprehensively evaluating their predictive capability in *a-posteriori* calculations. These help to provide guidance for practical applications. In FGM, heat losses are considered without the inclusion of species gradients in the enthalpy direction. This drawback is remedied by QFM, where heat losses to the wall are taken into account based on HOQ flamelets. QFM-EGR combines QFM with EGR to further consider the flame dilution, following our previous work [45]. Models are assessed with the results from an FRS as a reference, and the following conclusions can be drawn:

- Regarding the mean quantities, all three flamelet manifolds are good at predicting general flame characteristics, such as the mean flow and temperature fields, as well as major species. However, the flamelet manifolds perform differently in the prediction of pollutants and radicals. FGM presents significant deviations from the reference results in the near-wall region. In contrast, results from QFM and QFM-EGR show great improvement, with QFM-EGR performing slightly better.
- In the case of the PDFs of CO, significant differences are observed between QFM and QFM-EGR. Compared to QFM, the distribution of CO covers a wider range in QFM-EGR, which shows better agreement with the reference.
- Looking into the local thermo-chemical states, scatters of the QFM results are found to be restricted within the laminar counterpart, while QFM-EGR results span a much wider space, including a large portion of scatters below the limit of the wall boundary of the laminar SWQ. The results from QFM-EGR are more consistent with the FRS, indicating the importance of the FVI mechanism in the transient near-wall behavior. Moreover, the FVI mechanism is also illustrated in physical space with injected Lagrangian massless particles.
- To further verify the capability of QFM-EGR to capture the FVI mechanism, the time evolution of the FVI is investigated. It is found that a flame dynamic similar to that shown in FRS also exists in QFM-EGR.

In conclusion, the FGM considering varying enthalpy levels, is the simplest manifold to build and accurately predicts general flame quantities, such as the flow field, temperature, and major species. However, it fails in the prediction of pollutants and radicals. For this purpose, the QFM shows an improved prediction accuracy at the cost of more complex manifold generation, while the manifold dimensions remain unchanged and the computational cost thus stays at a similar level. The QFM-EGR shows the overall best prediction accuracy by capturing the influence of FVI at the cost of an additional table dimension and thus increased computational cost and memory requirements. When these manifolds are applied in real combustors, the benefits and drawbacks of each model should be considered when choosing the manifold.

Declaration of Competing Interest

Authors declare that they have no conflict of interest.

Acknowledgments

The authors thank Dr. Thorsten Zirwes from the group of Prof. Henning Bockhorn (Karlsruhe Institute of Technology) for supplying the data on the flame-resolved simulation with detailed chemistry. This research is supported by Deutsche Forschungsgemeinschaft (DFG, German Research Foundation) within SFB/Transregio 150 (project number 237267381), the Darmstadt Graduate School of Excellence Energy Science and Engineering (GSESE), and the European Union's Horizon 2020 research and innovation programme under the Center of Excellence in Combustion project, grant agreement no. 952181. Calculations for this research were conducted on the Lichtenberg high-performance computer at TU Darmstadt.

Supplementary material

Supplementary material associated with this article can be found, in the online version, at doi:10.1016/j.combustflame.2023.112923.

References

[1] A. Dreizler, B. Böhm, Advanced laser diagnostics for an improved understanding of premixed flame-wall interactions, Proc. Combust. Inst. 35 (2015) 37–64.
[2] P. Pantangi, A. Sadiki, J. Janicka, M. Mann, A. Dreizler, LES of premixed methane flame impinging on the wall using non-adiabatic flamelet generated manifold (FGM) approach, Flow, Turbul. Combust. 92 (2014) 805–836.
[3] J. Lai, N. Chakraborty, Effects of lewis number on head on quenching of turbulent premixed flames: a direct numerical simulation analysis, Flow, Turbul. Combust. 96 (2016) 279–308.
[4] J. Lai, D. Alwazzan, N. Chakraborty, Turbulent scalar flux transport in head-on quenching of turbulent premixed flames: a direct numerical simulations approach to assess models for reynolds averaged navier stokes simulations, J. Turbul. 18 (2017) 1033–1066.

[5] J. Lai, D.H. Wacks, N. Chakraborty, Flow topology distribution in head-on quenching of turbulent premixed flame: a direct numerical simulation analysis, Fuel 224 (2018) 186–209.
[6] P. Zhao, L. Wang, N. Chakraborty, Analysis of the flame-wall interaction in premixed turbulent combustion, J. Fluid Mech. 848 (2018) 193–218.
[7] P. Zhao, L. Wang, N. Chakraborty, Effects of the cold wall boundary on the flame structure and flame speed in premixed turbulent combustion, Proc. Combust. Inst. 38 (2021) 2967–2976.
[8] J. Lai, U. Ahmed, M. Klein, N. Chakraborty, A comparison between head-on quenching of stoichiometric methane-air and hydrogen-air premixed flames using direct numerical simulations, Int. J. Heat Fluid Flow 93 (2022) 108896.
[9] T. Alshaalan, C.J. Rutland, Wall heat flux in turbulent premixed reacting flow, Combust. Sci. Technol. 174 (2002) 135–165.
[10] A. Gruber, R. Sankaran, E.R. Hawkes, J.H. Chen, Turbulent flame-wall interaction: a direct numerical simulation study, J. Fluid Mech. 658 (2010) 5–32.
[11] A. Heinrich, F. Ries, G. Kuenne, S. Ganter, C. Hasse, A. Sadiki, J. Janicka, Large eddy simulation with tabulated chemistry of an experimental sidewall quenching burner, Int. J. Heat Fluid Flow 71 (2018) 95–110.
[12] A. Heinrich, G. Kuenne, S. Ganter, C. Hasse, J. Janicka, Investigation of the turbulent near wall flame behavior for a sidewall quenching burner by means of a large eddy simulation and tabulated chemistry, Fluids 3 (2018) 65.
[13] M. Steinhausen, T. Zirwes, F. Ferraro, S. Popp, F. Zhang, H. Bockhorn, C. Hasse, Turbulent flame-wall interaction of premixed flames using quadrature-based moment methods (QbMM) and tabulated chemistry: an a priori analysis, Int. J. Heat Fluid Flow 93 (2022) 108913.
[14] B. Jiang, D. Brouzet, M. Talei, R.L. Gordon, Q. Cazeres, B. Cuenot, Turbulent flame-wall interactions for flames diluted by hot combustion products, Combust. Flame 230 (2021) 111432.
[15] U. Ahmed, N. Chakraborty, M. Klein, Scalar gradient and strain rate statistics in oblique premixed flame-wall interaction within turbulent channel flows, Flow, Turbul. Combust. 106 (2021) 701–732.
[16] U. Ahmed, N. Chakraborty, M. Klein, Influence of thermal wall boundary condition on scalar statistics during flame-wall interaction of premixed combustion in turbulent boundary layers, Int. J. Heat Fluid Flow 92 (2021) 108881.
[17] D. Kaddar, M. Steinhausen, T. Zirwes, H. Bockhorn, C. Hasse, F. Ferraro, Combined effects of heat loss and curvature on turbulent flame-wall interaction in a premixed dimethyl ether/air flame, Proc. Combust. Inst. 39 (2) (2023) 2199–2208.
[18] P.J. Coelho, N. Peters, Unsteady modelling of a piloted methane/air jet flame based on the Eulerian particle flamelet model, Combust. Flame 124 (2001) 444–465.
[19] J.A. van Oijen, P. de Goey, Modelling of premixed laminar flames using flamelet-generated manifolds, Combust. Sci. Technol. 161 (2000) 113–137.
[20] U. Maas, S.B. Pope, Simplifying chemical kinetics: intrinsic low-dimensional manifolds in composition space, Combust. Flame 88 (1992) 239–264.
[21] O. Gicquel, N. Darabiha, D. Thévenin, Laminar premixed hydrogen/air counterflow flame simulations using flame prolongation of ILDM with differential diffusion, Proc. Combust. Inst. 28 (2000) 1901–1908.
[22] V. Bykov, U. Maas, The extension of the ILDM concept to reaction-diffusion manifolds, Combust. Theory Model. 11 (2007) 839–862.
[23] A. Heinrich, S. Ganter, G. Kuenne, C. Jainski, A. Dreizler, J. Janicka, 3D numerical simulation of a laminar experimental SWQ burner with tabulated chemistry, Flow, Turbul. Combust. 100 (2018) 535–559.
[24] C. Jainski, M. Rißmann, B. Böhm, J. Janicka, A. Dreizler, Sidewall quenching of atmospheric laminar premixed flames studied by laser-based diagnostics, Combust. Flame 183 (2017) 271–282.
[25] S. Ganter, A. Heinrich, T. Meier, G. Kuenne, C. Jainski, M.C. Rißmann, A. Dreizler, J. Janicka, Numerical analysis of laminar methane-air side-wall-quenching, Combust. Flame 186 (2017) 299–310.
[26] S. Ganter, C. Straßacker, G. Kuenne, T. Meier, A. Heinrich, U. Maas, J. Janicka, Laminar near-wall combustion: analysis of tabulated chemistry simulations by means of detailed kinetics, Int. J. Heat Fluid Flow 70 (2018) 259–270.
[27] D.V. Efimov, P. de Goey, J.A. van Oijen, QFM: quenching flamelet-generated manifold for modelling of flame-wall interactions, Combust. Theory Model. 24 (2020) 72–104.
[28] M. Steinhausen, Y. Luo, S. Popp, C. Strassacker, T. Zirwes, H. Kosaka, F. Zentgraf, U. Maas, A. Sadiki, A. Dreizler, et al., Numerical investigation of local heat-release rates and thermo-chemical states in side-wall quenching of laminar methane and dimethyl ether flames, Flow, Turbul. Combust. 106 (2021) 681–700.
[29] H. Kosaka, F. Zentgraf, A. Scholtissek, L. Bischoff, T. Häber, R. Suntz, B. Albert, C. Hasse, A. Dreizler, Wall heat fluxes and CO formation/oxidation during laminar and turbulent side-wall quenching of methane and DME flames, Int. J. Heat Fluid Flow 70 (2018) 181–192.
[30] H. Kosaka, F. Zentgraf, A. Scholtissek, C. Hasse, A. Dreizler, Effect of flame-wall interaction on local heat release of methane and DME combustion in a side-wall quenching geometry, Flow, Turbul. Combust. 104 (2020) 1029–1046.
[31] Y. Luo, C. Strassacker, C. Hasse, U. Maas, Simulation of side-wall quenching of laminar premixed flames with manifold-based reduced kinetic models implemented in generalised coordinates, Combust. Theory Model. 25 (2021) 669–694.
[32] Y. Luo, C. Strassacker, F. Ferraro, F. Zentgraf, A. Dreizler, U. Maas, C. Hasse, A manifold-based reduction method for side-wall quenching considering differential diffusion effects and its application to a laminar lean dimethyl ether flame, Int. J. Heat Fluid Flow 97 (2022) 109042.
[33] Y. Luo, C. Strassacker, U. Maas, C. Hasse, Model reduction on the fly: simultaneous identification and application of reduced kinetics for the example of flame-wall interactions, Proc. Combust. Inst. 39 (4) (2023) 5239–5248.
[34] F. Zentgraf, P. Johe, M. Steinhausen, C. Hasse, M. Greifenstein, A.D. Cutler, R.S. Barlow, A. Dreizler, Detailed assessment of the thermochemistry in a side-wall quenching burner by simultaneous quantitative measurement of CO_2, CO and temperature using laser diagnostics, Combust. Flame 235 (2022) 111707.
[35] C. Jainski, M. Rißmann, B. Böhm, A. Dreizler, Experimental investigation of flame surface density and mean reaction rate during flame-wall interaction, Proc. Combust. Inst. 36 (2017) 1827–1834.
[36] O. Colin, F. Ducros, D. Veynante, T. Poinsot, A thickened flame model for large eddy simulations of turbulent premixed combustion, Phys. fluids 12 (2000) 1843–1863.
[37] G. Kuenne, A. Ketelheun, J. Janicka, LES modeling of premixed combustion using a thickened flame approach coupled with FGM tabulated chemistry, Combust. Flame 158 (2011) 1750–1767.
[38] A. Donini, S.M. Martin, R.J.M. Bastiaans, J.A. van Oijen, L.P.H. de Goey, Numerical simulations of a premixed turbulent confined jet flame using the flamelet generated manifold approach with heat loss inclusion, Proceedings of ASME Turbo Expo, Paper (2013), doi:10.1115/GT2013-94363.
[39] F. Proch, A.M. Kempf, Modeling heat loss effects in the large eddy simulation of a model gas turbine combustor with premixed flamelet generated manifolds, Proc. Combust. Inst. 35 (3) (2015) 3337–3345.
[40] Y. Tang, V. Raman, Large eddy simulation of premixed turbulent combustion using a non-adiabatic, strain-sensitive flamelet approach, Combust. Flame 234 (2021) 111655.
[41] O. Lammel, M. Stöhr, P. Kutne, C. Dem, W. Meier, M. Aigner, Experimental analysis of confined jet flames by laser measurement techniques, J. Eng. Gas Turbine Power 134 (4) (2012) 041506.
[42] M. Mann, C. Jainski, M. Euler, B. Böhm, A. Dreizler, Transient flame-wall interactions: experimental analysis using spectroscopic temperature and CO concentration measurements, Combust. Flame 161 (2014) 2371–2386.
[43] F. Zentgraf, P. Johe, A.D. Cutler, R.S. Barlow, B. Böhm, A. Dreizler, Classification of flame prehistory and quenching topology in a side-wall quenching burner at low-intensity turbulence by correlating transport effects with CO_2, CO and temperature, Combust. Flame 239 (2022) 111681.
[44] R. Palulli, M. Talei, R.L. Gordon, Unsteady flame–wall interaction: impact on CO emission and wall heat flux, Combust. Flame 207 (2019) 406–416.
[45] M. Steinhausen, T. Zirwes, F. Ferraro, A. Scholtissek, H. Bockhorn, C. Hasse, Flame-vortex interaction during turbulent side-wall quenching and its implications for flamelet manifolds, Proc. Combust. Inst. 39 (2) (2023) 2149–2158.
[46] P.-D. Nguyen, L. Vervisch, V. Subramanian, P. Domingo, Multidimensional flamelet-generated manifolds for partially premixed combustion, Combust. Flame 157 (1) (2010) 43–61.
[47] S. Popp, F. Hunger, S. Hartl, D. Messig, B. Coriton, J.H. Frank, F. Fuest, C. Hasse, LES flamelet-progress variable modeling and measurements of a turbulent partially-premixed dimethyl ether jet flame, Combust. Flame 162 (8) (2015) 3016–3029.
[48] J.A. van Oijen, A. Donini, R.J.M. Bastiaans, J.H.M. ten Thije Boonkkamp, L.P.H. de Goey, State-of-the-art in premixed combustion modeling using flamelet generated manifolds, Prog. Energy Combust. Sci. 57 (2016) 30–74.
[49] E. Ranzi, A. Frassoldati, R. Grana, A. Cuoci, T. Faravelli, A.P. Kelley, C.K. Law, Hierarchical and comparative kinetic modeling of laminar flame speeds of hydrocarbon and oxygenated fuels, Prog. Energy Combust. Sci. 38 (2012) 468–501.
[50] A. Stagni, A. Frassoldati, A. Cuoci, T. Faravelli, E. Ranzi, Skeletal mechanism reduction through species-targeted sensitivity analysis, Combust. Flame 163 (2016) 382–393.
[51] A. Ketelheun, G. Kuenne, J. Janicka, Heat transfer modeling in the context of large eddy simulation of premixed combustion with tabulated chemistry, Flow, Turbul. Combust. 91 (2013) 867–893.
[52] J.A. van Oijen, L.P.H. de Goey, Modelling of premixed laminar flames using flamelet-generated manifolds, Combust. Sci. Technol. 161 (2000) 113–137.
[53] B. Fiorina, R. Baron, O. Gicquel, D. Thevenin, S. Carpentier, N. Darabiha, Modelling non-adiabatic partially premixed flames using flame-prolongation of ILDM, Combust. Theory Model. 7 (2003) 449.
[54] F. Nicoud, H.B. Toda, O. Cabrit, S. Bose, J. Lee, Using singular values to build a subgrid-scale model for large eddy simulations, Phys. Fluids 23 (2011) 085106.
[55] B.T. Hubert, O. Cabrit, K. Truffin, B. Gilles, F. Nicoud, A dynamic procedure for advanced subgrid-scale models and wall-bounded flows, Seventh International Symposium on Turbulence and Shear Flow Phenomena, Begel House Inc., 2011.
[56] F. Charlette, C. Meneveau, D. Veynante, A power-law flame wrinkling model for LES of premixed turbulent combustion part I: non-dynamic formulation and initial tests, Combust. Flame 131 (2002) 159–180.
[57] M. Ihme, H. Pitsch, Modeling of radiation and nitric oxide formation in turbulent nonpremixed flames using a flamelet/progress variable formulation, Phys. Fluids 20 (2008) 055110.
[58] S. Weise, D. Messig, B. Meyer, C. Hasse, An abstraction layer for efficient memory management of tabulated chemistry and flamelet solutions, Combust. Theory Model. 17 (2013) 411–430.
[59] H.G. Weller, G. Tabor, H. Jasak, C. Fureby, A tensorial approach to computational continuum mechanics using object-oriented techniques, Comput. Phys. 12 (1998) 620–631.